Atomic-scale friction study on Au(111) under electrochemical conditions

Dissertation
zur
Erlangung des Doktorgrades (Dr. rer.nat)
der
Mathematisch-Naturwissenschaftlichen Fakultät
der
Rheinischen Friedrich-Wilhelms-Universität Bonn

vorgelegt von

Inhee Park

aus
Nonsan, Republic of Korea

Bonn，2022

Atomic-scale friction study on Au(111) under electrochemical conditions

Dissertation
zur
Erlangung des Doktorgrades (Dr. rer.nat)
der
Mathematisch-Naturwissenschaftlichen Fakultät
der
Rheinischen Friedrich-Wilhelms-Universität Bonn

vorgelegt von

Inhee Park

aus
Nonsan, Republic of Korea

Bonn，2022

Angefertigt mit Genehmigung der Mathematisch-Naturwissenschaftlichen Fakultät
der Rheinischen Friedrich-Wilhelms-Universität Bonn

Promotionskommission

Erster Gutachter: Prof. Dr. Helmut Baltruschat
Zweiter Gutachter: Prof. Dr. Thomas Bredow
Fachnaher Gutachter: Prof. Dr. Sigurd Höger
Fachfremder Gutachter: Prof. Dr. Thorsten Geisler-Wierwille

Tag der mündlichen Prüfung: 01.09.2022

Erscheinungsjahr: 2022

Energy and persistence conquer all things.

(Benjamin Franklin)

Abstract

In this study, lateral force microscopy (LFM) has been employed to investigate the frictional behavior on the surface of an electrode and the role of adsorbates. In order to focus on the frictional behavior, it is advantageous to choose well known electrochemical systems and the metal underpotential deposition (UPD) is a suitable candidate. Basically, the UPD of a foreign metal on an electrode occurs due to the strong interaction between foreign metal ion and the substrate. Thus, this reaction happens at a potential far positive of the Nernst equilibrium potential where the bulk deposition takes place.

The Ag UPD on Au(111) in aqueous electrolyte has been intensively studied due to the negligible mismatch between gold and silver. On the basis of what is already known from earlier works, using LFM, it was our aim to understand the influence of adsorbates on friction during Ag UPD. Using lateral force images, we observed a $(\sqrt{3} \times \sqrt{7})R19.1°$ structure ($\theta_{sulfate} = 0.2$) for the adsorbed sulfate on Au(111) prior to the Ag UPD. When the silver forms a complete monolayer or a bilayer, the adsorbed sulfate forms a $(\sqrt{3} \times \sqrt{3})R30°$ structure ($\theta_{sulfate} = 0.33$). The measurement of friction forces as function of potential also reveals the relation between the coverage and friction. Thus, friction increases with coverage of Ag until the coverage arrives at a critical value (0.27 V vs. Ag/Ag^+) and then decreases again as the coverage is getting close to 1. The re-plotted friction forces as function of normal load suggest that the tip penetrates into the adlayers, resulting in the steep increase of friction.

The Ag UPD on I-modified Au(111) in aqueous electrolyte showed a clear transition of iodine structures with potential caused by the changing coverage of silver. Observed lateral force images at low normal load showed that the iodine adlayer forms a $(\sqrt{3} \times \sqrt{3})R30°$ structure ($\theta_{sulfate} = 0.33$) prior to the Ag UPD. When the potential passes the 1st UPD peak, the structure changes to a $p(3 \times 3)$ structure ($\theta_{sulfate} = 0.44$). Even though negative of the 2nd UPD peak a $p(3 \times 3)$ structure ($\theta_{sulfate} = 0.44$) was maintained, the height difference between the maxima resulting from the coverage of Ag ($\theta_{Ag} = 0.44$) disappeared. The large scale topographic images show that the 3rd Ag UPD peak correlates with a bilayer formation. At high normal load, the revealed structures clearly demonstrate that the tip penetrates into the iodine adlayer and even into the silver layer when the coverage of silver is less than a critical value (0.30 V vs. Ag/Ag^+). At potentials negative of the 2nd and 3rd Ag UPD peaks, lateral force images demonstrate that the silver forms a monolayer and a bilayer. Force separation (FS) curves shows a dependence on potential, supporting an adsorption of silver ions on the iodine adlayer prior to the deposition on Au(111) as suggested previously in literature. Friction forces as function of potential suggest that at low normal load,

friction increases due to the increasing coverage of silver underneath the tip, but it decreases when the Ag coverage approaches 0.44, correspondingly to an ordered $p(3 \times 3)$ adlayer and the adsorbed iodine is ordered. At high normal load, the tip penetrates the iodine or even silver for $\theta_{Ag} = 0.44$, which causes a hysteresis between the cathodic and anodic sweeps. Friction forces as function of normal load clearly show that friction increases steeply in two cases: 1) when the tip penetrates the iodine adsorbed on silver layer and 2) when the tip penetrates silver adlayer where the coverage is less than a critical value. However, this dramatic increase is missing when the tip penetrates the iodine adsorbed on Au(111).

Furthermore, the frictional behavior during Cu UPD in aqueous electrolyte is investigated. The copper is deposited on Au(111), paralleled by the co-adsorption of anions (sulfate or iodine). At high normal load, friction as function of normal load shows that friction increases in order of Au(111) < Cu submonolayer < Cu monolayer. Moreover, as normal load increases, multiple stick-slips is observed on a Cu monolayer, independent of anions. Considering the large lattice mismatch (about 11%) between Cu(111) and Au(111), it is expected that the surface energy of Cu adlayer on Au(111) increases as the Cu coverage gets close to 1 and the adsorption of anions such as sulfate and iodine on Cu layer reduces this high surface energy. Therefore, the possible model to explain the frictional behavior during Cu UPD is that as normal load increases, the tip pushes away (or penetrates) adsorbed anions and this allows the tip to strongly interact with Cu adlayers, leading to multiple stick-slips.

Special attention was paid to the investigation of frictional behavior in aprotic electrolytes. FS curves observed in Li^+ containing tetraethylene glycol dimethyl ether (G4) on I-modified Au(111) show a reproducible step-wise behavior as separation decreases. Furthermore, FS curves on I-modified Au(111) in pure G4 resemble the results obtained in Li^+ containing G4. Therefore, the ordered layers consist of G4 molecules. As observed in aqueous electrolyte, the penetration into the iodine adsorbed on Au(111) has a minor effect on friction. This demonstrates that the iodine adsorbed on Au(111) can be pushed away without extra energy dissipation. During the Ag UPD in G4, as shown in aqueous electrolyte, when the tip penetrates into the iodine adsorbed on silver adlayer, friction increases steeply with normal load. This increase seems to depend on the concentration of water. However, when the concentration of water exceeds a critical value, the increase of friction resulting from the penetration remains constant. Based on our results, it is hypothesized that the water adsorbed on the tip interacts with the silver layer, resulting in the increase of friction. The number of water molecules which can be adsorbed on the tip is limited. Therefore, only before the saturation of the water on the tip, the concentration of water affects the friction. The results observed on I-modified Au(111) in Ag^+ containing propylene carbonate (PC) shows that there is no steep increase of friction on Ag adlayer after the penetration, which suggests

an effect of solvent.

In this study, it is clearly shown that the tip pushes away the adsorbed iodine as normal load increases above a threshold value and the adsorbed iodine quickly rearranges as the tip slides on the surface. In particular, this penetration explains the non-monotonic, step-wise increase of friction in friction vs. load curves. The transition of structures from the iodine to silver adlayers and vice versa represent a model for so-called reversible wear. Furthermore, the distinct atomic corrugation for the Ag monolayer at high normal load demonstrates that no irreversible wear occurs by the sliding tip. Since the penetration, the frictional behavior is closely related to the interaction between the tip and UPD layers. For Au(111), any changes such as the concentration of water, solvent do not affect the friction. For Ag adlayers, the influence of water or solvent dominate the friction, but for Cu adlayers, the coverage of copper has a significant influence on the friction. Multiple stick-slip events only observed on a Cu monolayer are probably related to the stretched Cu structure caused by the lattice mismatch between Cu and Au, which leads to a larger corrugation than in the Ag UPD system.

Contents

List of Figures

List of Abbreviations

WE	Working electrode	**FCC**	Face centered cubic
CE	Counter electrode	**Au**	Gold
RE	Reference electrode	**Ag**	Silver
CV	Cyclic voltammetry or voltammogram	**Cu**	Copper
DLVO	Derjaguin-Landau-Verway-Overbeek theory	**Pt**	Platinum
SFA	Surface forces apparatus	**UHV**	Ultra-high vacuum
PT	Prandtl-Tomlinson model	**UPD**	Underpotential deposition
MD	Moleculear dynamics	**EC-SPM**	Electrochemical scanning probe microscopy
OMCTS	Octamethylcyclotetrasiloxane	**STM**	Scanning tunneling microscopy
G4	Tetraethylene glycol dimethyl ether	**AFM**	Atomic force microscopy
PC	Propylene carbonate	**LFM**	Lateral force microscopy
ILs	Ionic liquids	**PSPD**	Position-sensitive photo diode
SILs	Solvated ionic liquids	**SHO**	Simple harmonic oscillation
FS	Force-separation	**FFT**	Fast Fourier Transform
pzc	Potential of zero charge	**COF**	Coefficient of friction
SC	Simple cubic	**HOPG**	Highly oriented pyrolytic graphite
BCC	Body centered cubic		

CHAPTER 1

INTRODUCTION

1.1 Motivation

An easy example of the interaction when a surface approaches to the other surface can be found in the classroom of the university. In the beginning of the semester, since we don't know each other, there is no interaction between students like the molecules in the bulk. When the teacher makes several small groups and gives a task, we start to introduce ourselves and exchange our phone numbers in a small group. This corresponds to the molecules approaching each other.

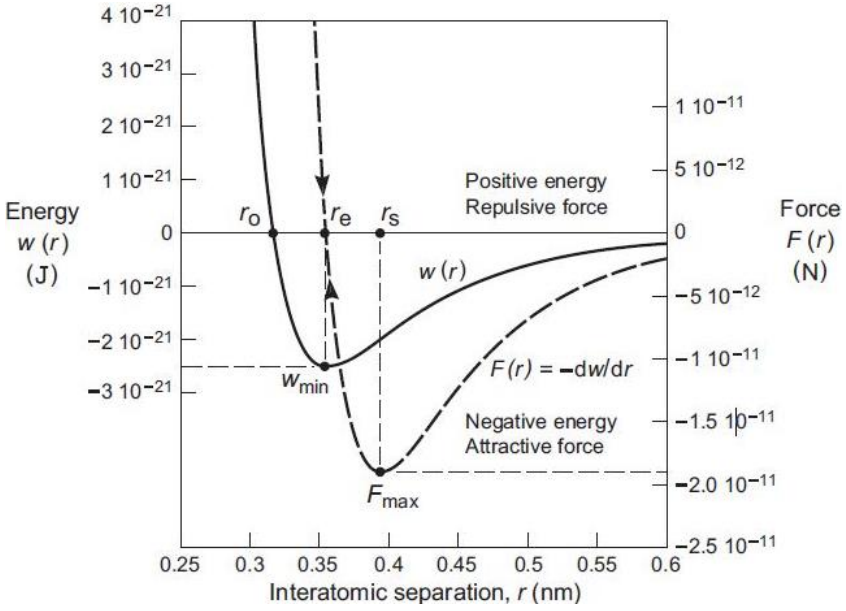

Figure 1.1 Typical van der Waals interaction energy (or potential) function *w(r)* and force function *F(r)* between two atoms, which are related by *F(r) = -dw/dr* [1].

Sometimes, we find a couple in the group after a task, meaning that a strong interaction grows between them. In the beginning, the strong attraction is dominant. However, when you get closes, the misunderstanding may grow. It represents the situation where the repulsion wins the attraction as the distance between the surface and molecules getting close. Figure 1.1 shows the typical van der Waals interaction energy function and force function between two atoms as a function of interatomic separation.

In sliding contacts, friction represents the energy loss and may lead to wear, which has been an attracting issue in various scientific fields and technological fields, ranging from physics to biology [2-7]. A simple example of the friction is writing with pencil on the paper and the written words on the paper are the result of wear. Classically, Amontons' law states that the frictional force *F* needed to slide one body laterally over another is independent of their macroscopic area of contact and proportional to the normal load *L* that presses them together [8, 9]. However, it is known that a macroscopic contact is rough and consists of a large number of smaller contacts called asperities. Hence, the real contact area is much smaller than the macroscopic contact area [10, 11]. Moreover, the adhesion between surfaces affects the deformation of asperities.

The Gouy-Chapmann-Stern theory explains the interactions between the electrode surface and ions (coordinated by solvent) in dilute electrolytes where ions with uniform charge density are dissolved in solvent and interact with each other via long-range Coulomb forces. The Derjaguin-Landau-Verway-Overbeek (DLVO) theory describes that the solid-liquid interaction is the sum of electrical double-layer repulsion and a van der Waals attraction [12]. Measurements using the surface forces apparatus (SFA) demonstrate the validity of the DLVO theory and the long-range repulsion, which demonstrates that as the surfaces are getting close up to 2 nm, a strong repulsive hydration force prevents attractive Van der Waals force in aqueous electrolyte [13]. Moreover, further decrease of separation below 1.5 nm causes oscillatory decay indicating the solvent structural effect and short-range interaction.

In order to investigate the atomic scale friction, lateral force microscopy (LFM) was introduced and the observed results using LFM often show the atomic stick-slip motion. Based on the Prandtl-Tomlinson (PT) model confirmed in LFM experiments, it is assumed that the average friction force (in the stick-slip regime) increases linearly with the ratio of the contact potential corrugation (E_0) to the measuring system stiffness combining the stiffness of the cantilever and the lateral stiffness of the contact [14-16].

Furthermore, friction with atomic resolution is ideally explored by LFM, which may provide the atomic mechanisms together with the results of Molecular dynamics (MD) simulations mimicking LFM [17-30]. MD simulations show that due to third body existing between sliding two bodies (e.g. adsorbate), Amontons' law is often not valid in atomic-scale friction where the interactions caused by the adsorbate such as adhesion is significant as mentioned above [9, 29, 31].

Numerous studies have shown that friction can depend dramatically on the chemical and atomic nature of surfaces and can be extremely sensitive even to submonolayers of adsorbed atoms or molecules. Therefore, it is advantageous to investigate the friction using the lateral force microscopy (LFM) under the electrochemical conditions in order to understand the fundamentals of friction.

1.2 Force-separation (FS) curves and tribology

FS curves

The surface forces apparatus (SFA) was pioneered by Tabor [32] and Israelachvili [33] to measure the van der Waals forces between two crossed cylindrical sheets of muscovite. Figure 1.2(a) shows a schematic drawing of a classical SFA [1]. The geometry of contact resembles the crossed cylinders which consist of a sphere (upper part) and a flat (lower part).

As mentioned above, DLVO theory describes the relationship between electrostatic (double-layer) repulsion and van der Waals attraction as the distance between two surfaces is getting close in the electrolyte (Figure 1.2(b)) [1]. For a highly charged surface in dilute electrolyte, there is a strong long-range repulsion that peaks at some distance, which forms the energy barrier. The magnitude of this energy barrier depends on the concentration of electrolyte (σ) as shown in Figure 1.2b. As the surface charge or potential approaches zero, the interaction curve approaches the pure van der Waals curve, meaning that the dominant interaction between two surfaces is attraction. Additionally, in short-range interaction, there is an oscillatory decay pointing out the structural effects of solvent (in dilute electrolytes) [13, 34-39] and ions [40-42].

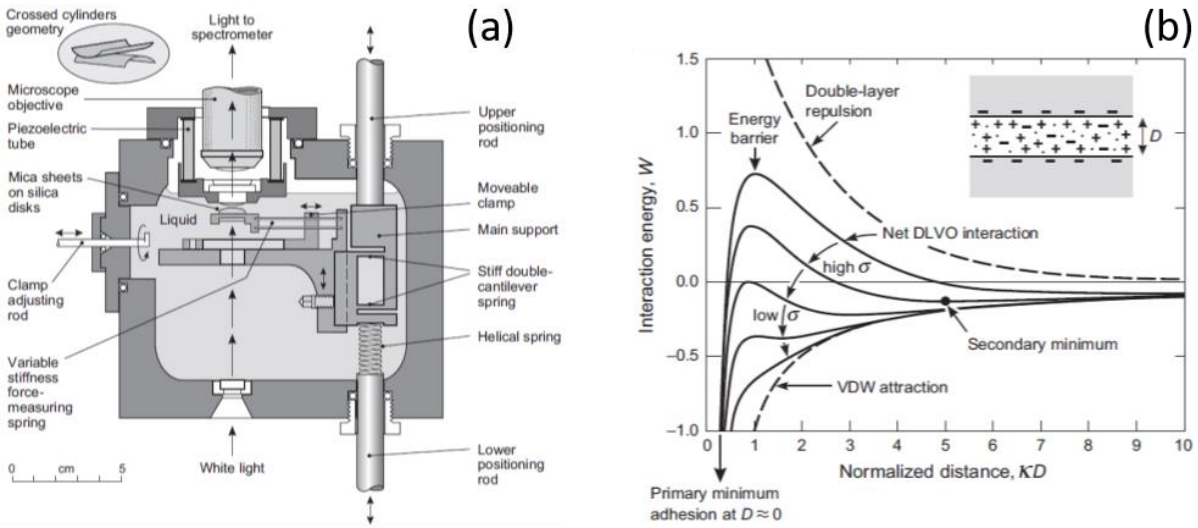

Figure 1.2 (a) Surface Forces Apparatus (SFA) for directly measuring the force-laws between surfaces in liquids or vapors level and (b) Schematic energy versus distance profiles of the DLVO interaction [1].

R. Horn et al. demonstrated the oscillatory decay using a SFA in octamethylcyclotetrasiloxane (OMCTS) and the influence of water on it [34]. They observed about 11 layers and the distance of layers slightly increases as the separation decreases, indicating that the molecules are more strongly bound near the surface. After the saturation of OMCTS with water (~240 ppm), the oscillations became more adhesive than that of pure OMCTS but the decay length was maintained. H. Christenson et al. observed the same behavior in cyclohexane and *n*-octane when they are saturated with water [35]. They suggested the possibility that water forms a bridge between the two surfaces in the contact region, which pulls them each other with a relatively large force. In addition, they measured the FS curves in a polar solvent, propylene carbonate (PC). Their results demonstrate that the polarity has not caused any major disruption to the packing effects reflected in the solvation force [37].

Ionic liquids (ILs) are composed entirely of charged ions but also are liquids at ambient temperature and pressure. Recent work has greatly progressed a fundamental understanding of ionic liquids [39-45]. A. Smith et al. showed the structural force in an ionic liquid mixed with PC using a surface force balance (SFB) [39]. In pure PC, the wavelength corresponds to the molecular size of PC, which indicates that PC molecules are ordered between two surfaces. When the 1-butyl-1-methylpyrrolidiniumbis[(trifluoromethane)sulfonyl]imide, $[C_4C_1Pyrr][NTf_2]$, was added in PC, the distance of oscillations changes from the size of a solvent molecule (PC) in a dilute ionic liquid solution to the size of a cation-anion pair in a concentrated solution. Thus, it

is demonstrated that the preference of interaction with surface changes as the concentration of $[C_4C_1Pyrr][NTf_2]$ increases.

In order to study nanometer-scale FS curves and tribology regarding contact asperity, lateral force microscopy (LFM) has been introduced [46-48]. A. Hillier et al. showed force-separation (FS) curves measured on gold surface using silica sphere tip (diameter: 10-20 μm) in air, deionized water, and electrolytes (10^{-3} M KCl, NaF, KBr, and KI and 10^{-2} M KCl) [48]. Due to the strength of the anion adsorption ($I^- > Br^- > Cl^- > F^-$), it is expected that the pzc is the most positive for F^- and the most negative for I^-. Furthermore, it is generally expected that the alkali metal cation has a much smaller influence on the pzc. The results indicate that negative of the potential of zero charge (*pzc*), there is a strong repulsion as surfaces getting close due to the absence of strong adsorption of cation. In contrast, at positive of *pzc*, with decreasing the separation, the strong attraction is observed. This demonstrate that in the electrolytes, the applied potential is important as well as the concentration of ions (DLVO theory) to understand the tendency of FS curves because the adsorption of ions on the electrode or localized ions near the electrode can influence the order of layers.

Furthermore, in ILs including solvated ionic liquids (SILs), force-separation curves observed using LFM show stepwise behavior in the boundary regime where the ions are ordered, in good agreement with the estimated size of ions as shown in the results observed using SFA [49-54]. These results directly show the dependence of potential, which demonstrates the preferred adsorption of cation or anion on applied potential. Thus, the interaction between the tip and the strongly bound ions or layers such as the formation of hydrogen bond is one of key factors to understand the atomic scale friction [52, 55].

Tribology

The friction measurements in ILs show that the coefficient of friction (COF) increases as the number of ordered layers between sliding surfaces decreases[41-43, 56]. A. Simith et al. showed this transition of friction with decreasing the number of ion layers near the surfaces in pure $[C_4C_1Pyrr][NTf_2]$[43]. Their results suggest that as the number of ordered layers decreases, ions are more ordered and have greater anion/cation excess concentration, which results in greater inter-layer attractions for the constant contact area.

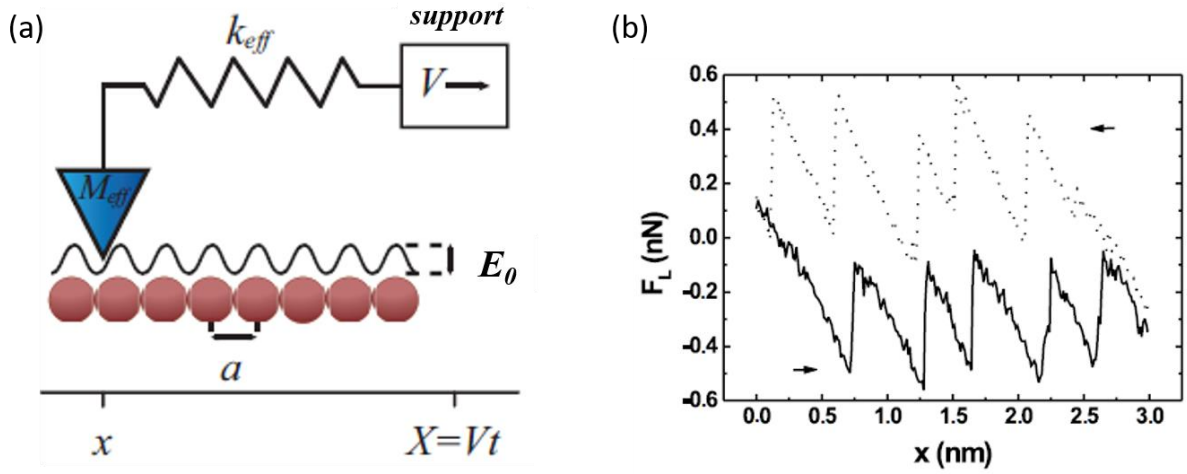

Figure 1.3 (a) LFM concentrates on the behavior of a single, contacting asperity with the indicated basic geometry of a local contact that is dragged through a corrugated potential energy landscape [16]. (b) atomic stick-slip loops observed on NaCl(001) usting LFM sliding in (100) direction. Applied normal load is 4.7 nN [15].

An interesting observation with LFM is the appearance of a regular atomic stick-slip, fitting perfectly with the lattice structure as shown in Figure 1.3. This atomic stick-slip can be simply explained by the Prandtl-Tomlinson (PT) model as mentioned above [14-16]. As shown in Figure 1.3 (a), in PT model, it is assumed that the tip is dragged over a lattice having a sinusoidal potential corrugation (E_0) with constant amplitude and periodicity (***a***). When the supporting body (V) moves, the spring between the tip and the body is extended in the stick region and relaxes in the slip region, respectively. Moreover, there is an influence of contact between the tip and the surface. Therefore, the effective stiffness (k_{eff}) is the combination between the stiffness of the cantilever and the lateral stiffness of the contact. This model predicts that the average friction force increases linearly with the ratio of the contact potential corrugation (E_0) to the effective stiffness. Thus, if there is a strong interaction between the tip and the surface resulting in the large increase of the potential corrugation, we can expect the steep increase of friction force. The contact potential corrugation can be calculated using eq.1.1[15], where F_L^{max} is the maximum friction value in the stick-slip loop.

$$E_0 = \frac{aF_L^{max}}{\pi} \qquad 1.1$$

F. Hausen et al. demonstrated the influence of adsorbates on Au(111) on friction under electrochemical conditions [21, 57]. They observed that the friction increases as the coverage of sulfate on Au(111) increases and at the maximum coverage of sulfate, the behavior of friction

depends on the normal load. Based on these results, W. Ouyang et al. performed MD simulations [29]. They suggest that as the coverage of adsorbate increases up to a critical value, the energy required to push away the adsorbate increases due to the van der Waals repulsion between adsorbates. However, when the coverage is above a critical value, it is energetically easier for the tip to slide on the adlayer than to push away the adsorbate. Therefore, when the tip slides on the adlayer, friction decreases. However, this model doesn't quite fit to the frictional behavior observed during the Cu underpotential deposition (UPD) on Au(111), showing that friction forces at the monolayer of copper is higher than that of submonolayer (θ = 0.67) [19, 21, 22].

Therefore, in the following chapters, using a LFM, the atomic scale frictional behavior under electrochemical conditions will be examined in order to shed some more light on the fundamental processes.

1.3 Single crystals

The study of the structure and dynamics of adsorption or deposition require well-defined surfaces as substrates. Therefore, single crystals are invariably used as substrates because they expose a specific crystal plane [58]. In this work, mainly a single crystal Au(111) was used as working electrode, Au has a face centered cubic (FCC) structure. Therefore, here cubic structures will be discussed.

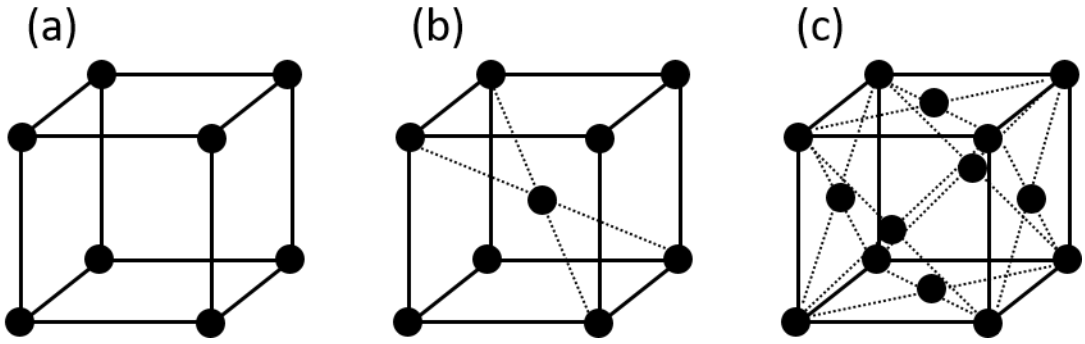

Figure 1.4 (a) Simple cubic (SC) structure, (b) Body centered cubic (BCC) structure, and (c) Face centered cubic (FCC) structure

Figure 1.4a shows the simple cubic (SC) structure. In the SC structure, 8 atoms are located at each corner in a cubic. When an atom is added in the center (or body) of the simple cubic structure, it becomes body centered cubic (BCC) structure as shown in Figure 1.4b. Some examples of metals that possess BCC include α phase of iron (α-Fe), chromium (Cr), tungsten (W), tantalum (Ta), and molybdenum (Mo). For face centered cubic (FCC) structure, six atoms are added in the simple cubic structure and they are located at each center of square in a cubic (Figure 1.4c). Aluminum (Al), Copper (Cu), silver (Ag), gold (Au), and platinum (Pt) belong to this structure.

The FCC lattice has three different low index crystal planes, (100), (110), and (111). In a (111) plane of FCC structure, there are three different positions for additional atoms: 1) atop site A, 2) 3-fold hollow sites B and C as shown in Figure 1.5a. Figure 1.5b shows the typical stacking order in (111) plane of FCC structure, ABC stack.

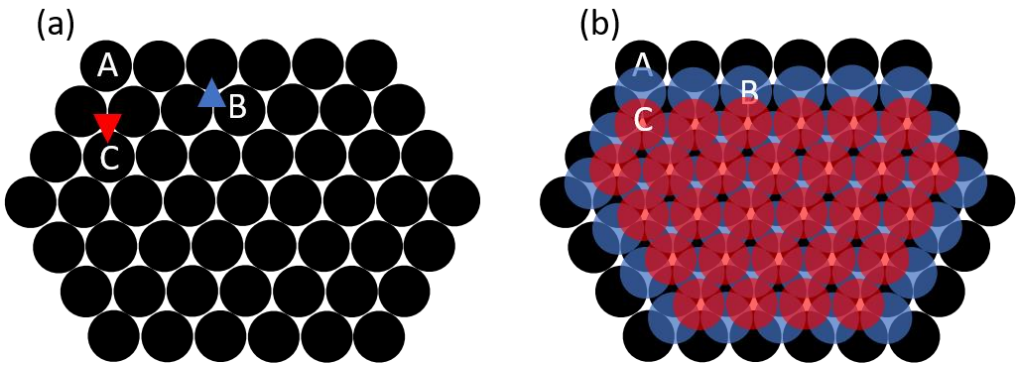

Figure 1.5 (a) The positions (A, B, and C) of atoms in (111) plane of FCC structure and (b) complete three layers of (111) plane of FCC structure

1.4 Adsorbate structures: iodide as an example

The Adsorption of ions on electrodes can modify the electronic, chemical, and even structural properties of the electrodes significantly [59]. Regarding these significant effects, it is important to understand and predict the thermodynamically stable structure of adsorbed ions as a function of environmental parameters such as ion concentration in the electrolyte and electrode potential. Therefore, structures of adsorbed halides on metal electrodes in aqueous electrolytes have been studied using a variety of methods [60-69].

On Pt(111), the adsorbed iodine in ultra-high vacuum (UHV) forms two possible structures, $(\sqrt{3} \times \sqrt{3})R30°$ and $(\sqrt{7} \times \sqrt{7})R19°$ [70]. In contrast, adsorbed iodine by dipping the electrode in 10^{-3} M KI solution leads to the formation of a (3×3) structure. Moreover, when the annealed Pt(111) is cooled down in an I_2-N_2 carrier gas stream showed, iodine forms a $(\sqrt{7} \times \sqrt{7})R19°$ structure and also a (3×3) structure by adjusting the distance between Pt(111) and the iodine crystals [60]. Therefore, it is assumed that the preparation conditions of adsorbed layers can influence the structure of adsorbate.

F. Lu et al. showed the structural transition of iodine adlattice on Pt(111) with potential in aqueous electrolyte [61]. As the potential is swept in anodic direction, iodide starts to substitute adsorbed hydrogen and forms a $(\sqrt{3} \times \sqrt{3})R30°$ structure. When a potential passes the spike, the first structural transition occurs from $(\sqrt{3} \times \sqrt{3})R30°$ structure to $(\sqrt{7} \times \sqrt{7})R19°$ structure. Further increase of potential causes the second structural transition from a $(\sqrt{7} \times \sqrt{7})R19°$ structure to a (3×3) structure, which is clearly visible in pH 10.

Figure 1.6 shows the reported three different structures of iodine on Pt(111). A $(\sqrt{3} \times \sqrt{3})R30°$ structure shows that iodine sits only on atop site of Pt(111) and the coverage of iodine (θ_I) is 0.33. The coverage of adsorbate is defined as written in eq. 1.1.

$$\theta = \frac{Number\ of\ sufrace\ sites\ occupied\ by\ adsorbate\ (N_s)}{Number\ of\ surface\ atoms\ of\ the\ substrate\ (N)} \qquad (1.1)$$

When the coverage reaches 1 ($\theta = 1$), it is called monolayer. In the case of a $(\sqrt{7} \times \sqrt{7})R19°$ structure, iodine atoms sitting on atop site form a unit cell and others are sitting on 3-fold hollow sites. Considering the unit cell, the coverage of iodine (θ_I) is 3/7 = 0.43. Similarly, in the case of a (3×3) structure, iodine atoms consisting of a unit cell sit on atop site and others occupy on 2-fold bridge site, corresponding to the coverage of 4/9 = 0.44 (θ_I).

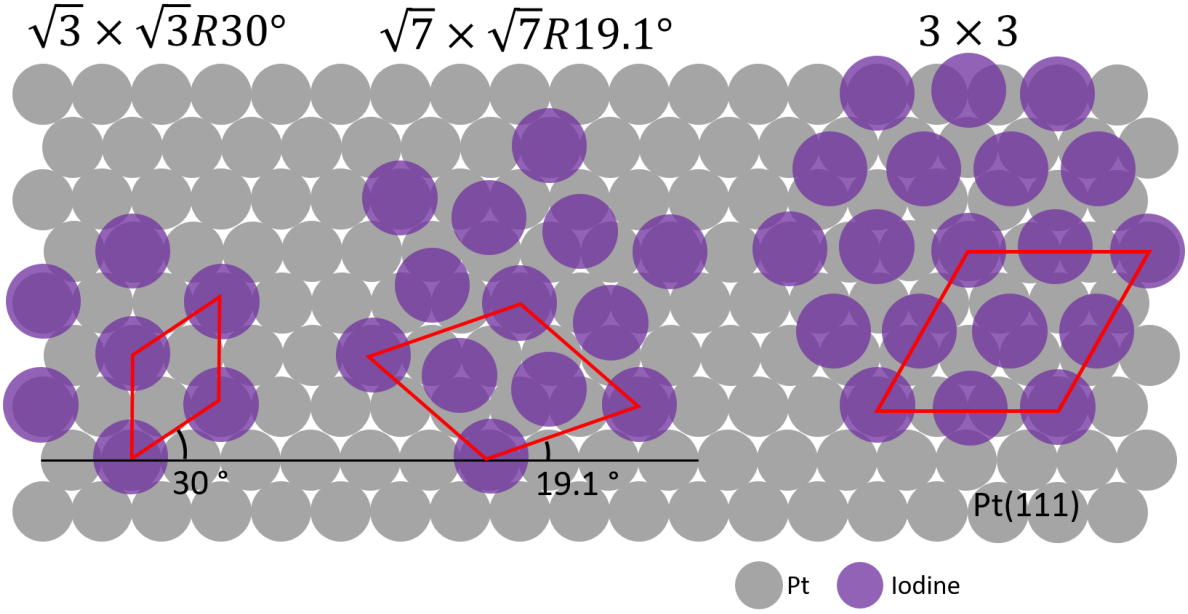

Figure 1.6 Structure of adsorbed iodide on Pt(111) in aqueous electrolyte

On Au(111), the adsorbed iodine in ultra-high vacuum (UHV) has been investigated by Cochran and Farrell [71]. They used low-energy electron diffraction technic and three different LEED patterns were observed as the coverage of iodine (θ_I) increases. The first pattern fits to a $\left(\sqrt{3} \times \sqrt{3}\right)R30°$ structure ($\theta_I = 0.33$) and with increasing exposure of I_2, the $\sqrt{3}$ spots splits into 'triad' ($0.33 < \theta_I < 0.48$) and 'rosettes' ($\theta_I \cong 0.48$). This result indicates that the increase of I_2 pressure leads to densely packed structure of iodine on Au(111).

X. Gao et al. examined the coverage of iodine (θ_I) using scanning tunneling microscopy (STM) in 0.5 mM KI/0.1 M $HClO_4$ [62]. As a potential is swept in anodic direction, the reconstructed Au(111) exhibiting the $\left(\sqrt{3} \times 22\right)$ structure is lifted by strongly adsorbed iodide and at -0.3 V (vs. SCE), iodide forms a $\left(\sqrt{3} \times \sqrt{3}\right)R30°$ structure ($\theta_I = 0.33$). As the potential slightly increases to a more positive potential, iodide intermediately forms a $\left(8 \times \sqrt{3}\right)$ structure and then, transforms to a $\left(5 \times \sqrt{3}\right)$ structure ($\theta_I = 0.4$). These results demonstrate that the iodine layer is continuously compressed with increasing potential to achieve higher coverage. Positive of the spike (E > 0.2 V vs. SCE), the observed structure shows a near-hexagonal array where the distance between iodides is about 4.4 - 4.5 Å. Moreover, a longer-range z corrugation is also observed as hexagonal pattern whose periodicity is about 19 – 22 Å. The corresponding coverage of iodine (θ_I) is about 0.44, which indicates that the adlayer structure approaches to the close-packed limit ($\theta_I \approx 0.45$) determined by the iodine van der Waals diameter, 4.3 Å.

Adsorbed iodine on Au(111) shows a relatively high tolerance to experimental handling due to strong interaction between Au and iodine . Therefore, in this thesis, iodine is pre-adsorbed on Au(111) by cooling it in the I_2 atmosphere after the flame annealing procedure (see chapter 2) in many experiments.

1.5 Underpotential deposition (UPD) of metals

The underpotential deposition (UPD) is the process where the first or second monolayer of another metal are deposited on the substrate at potentials positive of the reversible equilibrium potential of the respective bulk deposition, the Nernst potential [72]. This indicates that the interaction between deposited foreign metal and substrate is stronger than that between the atoms of the deposited metal.

Cu underpotential deposition (UPD) on Au(111)

Cu UPD on bare Au(111) is a system which has been intensively studied using structural sensitive techniques such as electrochemical scanning probe microscopy (EC-SPM) [74-86]. It has been observed that the presence of specifically adsorbing anions (e.g. SO_4^{2-} , Br^-, Cl^-, I^-) has a significant effect on the process of Cu UPD on Au(111), e.g. the rate of deposition. Z. Shi et al. showed that the potential for the onset of Cu UPD varies with anions [83]. The onset of Cu UPD on Au(111) decreases in order of $Br^- \approx Cl^- > SO_4^{2-}$. Considering the onset of anion adsorption on Au(111), the strength of anion adsorption decreases in order of ($Br^- > Cl^- > SO_4^{2-}$) and the rate of the copper deposition is closely related to the strength of anion adsorption on Au(111). In addition, the Cu UPD takes places in 2 steps in the presence of Cl^- and SO_4^{2-} but it takes places in about 5 steps in the presence of Br^-, which supports that the anions coadsorb with the deposited metal adatoms. They estimated the coverage of copper and anions depending on potential using measured charge density.

Batina's group examined the results of Cu UPD on I-modified Au(111) in 0.05 M H_2SO_4 [87, 88]. In contrast to other halides present in the electrolyte, the onset of Cu UPD on I-modified Au(111)

is slightly shifted in negative direction compared to that in sulfuric acid. This is a contrasting influence compared to that in the presence of Cl^- and Br^-.

Therefore, the frictional behavior during the Cu UPD on bare Au(111) in the presence of sulfate and on I-modified Au(111) will be discussed in this thesis (see chapter 5).

Ag underpotential deposition (UPD) on Au(111)

It is well known that the lattice misfit between silver and gold ($a_{Ag} = 4.08$ Å, $a_{Au} = 4.07$ Å) is negligible. Therefore, much attention has been focused on Ag UPD [89-97]. In sulfuric acid, M. Esplandiu et al. observed the structural transitions as the coverage of silver increases [89]. At potentials far positive of the 1st Ag UPD peak, they observed the structure of sulfate forming a $(\sqrt{3} \times \sqrt{7})R19.1°$ structure. When the potential passes the 1st Ag UPD peak, they observed a $(\sqrt{3} \times \sqrt{3})R30°$ structure at 0.5 V (vs. Ag/Ag^+), (3×3) structure at 0.45 V, and distorted hexagonal structure at 0.4 V in a relatively short potential range. When the potential is near the 2nd Ag UPD peak, they observed the growing islands with height of 0.09 nm due to the transition of Ag structures from (3×3) to(1×1). Therefore, it is suggested that the silver completes a monolayer at potentials slightly negative of the 2nd Ag UPD peak. In contrast to Cu UPD, silver forms a bilayer on Au(111) before the bulk deposition.

To better understand the potential dependence of the Ag coverage and of the structure, LFM images during the Ag UPD on bare Au(111) in aqueous electrolyte have been studied and will be discussed in this thesis (see chapter 3), along with the frictional behavior, i.e. dependence of friction on other parameters such as normal load.

S. Sugita et al. showed the effect of iodine adlayer adsorbed on Au(111) on Ag UPD [97]. Iodine is adsorbed by dipping Au(111) in the iodide containing electrolyte. They observed $(5 \times \sqrt{3})$ structure ($\theta_I = 0.4$) at potentials positive of the 1st Ag UPD peak. At potentials slightly negative of the 1st peak, iodine forms a (3×3) structure ($\theta_I = 0.44$) and there were some pits where the coverage of iodine is lower than 0.44 due to the lack of iodine. As the potential is passing the 2nd Ag UPD peak, the iodine maintains a (3×3) structure. At potentials slightly negative of the 2nd Ag UPD peak, the coverage of silver at the pits seems slightly higher than 0.44, indicating that the further Ag deposition is occurred on the areas having lower iodine coverage.

Based on the previous study, the Ag UPD on I-modified Au(111) in aqueous electrolyte (see chapter 4) will be discussed in following chapter. Furthermore, the Ag UPD on I-modified Au(111) in aprotic electrolytes (see chapter 7) is also on subject of research in this thesis.

Reference

[1] J. N. Israelachvili, Intermolecular and surface forces, Academic press, **2011**.

[2] P. Steiner, R. Roth, E. Gnecco, A. Baratoff, S. Maier, T. Glatzel, E. Meyer *Phys. Rev. B.* **2009**, *79*, 045414.

[3] M. Urbakh, J. Klafter, D. Gourdon, J. Israelachvili *Nature*. **2004**, *430*, 525-528.

[4] S. Iqbal, S. Wezisla, N. Podgaynyy, H. Baltruschat *Electrochimica Acta*. **2015**, *186*, 427-435.

[5] S. G. Balakrishna, A. S. de Wijn, R. Bennewitz *Phys. Rev. B.* **2014**, *89*, 245440.

[6] J. N. Panda, E. Y. Orquera, A. A. Mohanty, P. Egberts *Tribology International*. **2021**, *161*, 107066.

[7] M. Palacio, B. Bhushan *Adv. Mater. (Weinheim, Ger.).* **2008**, *20*, 1194-1198.

[8] F. P. Bowden, D. Tabor, The friction and lubrication of solids, Oxford university press, **1958**.

[9] G. He, M. H. Müser, M. O. Robbins *Science*. **1999**, *284*, 1650-1652.

[10] Y. Mo, K. T. Turner, I. Szlufarska *Nature*. **2009**, *457*, 1116-1119.

[11] I. Szlufarska, M. Chandross, R. W. Carpick *J. Phys. D-Appl. Phys.* **2008**, *41*, 123001.

[12] B. Derjaguin, L. Landau *Acta Physicochim. URSS*. **1941**, *14*, 58.

[13] J. N. Israelachvili, R. M. Pashley *Nature*. **1983**, *306*, 249-250.

[14] E. Gnecco, R. Bennewitz, T. Gyalog, E. Meyer *J. Phys.-Condens. Matter*. **2001**, *13*, R619-R642.

[15] A. Socoliuc, R. Bennewitz, E. Gnecco, E. Meyer *Physical review letters*. **2004**, *92*, 134301.

[16] S. Y. Krylov, J. W. M. Frenken *physica status solidi (b)*. **2014**, *251*, 711-736.

[17] I. Park, H. Baltruschat *ChemPhysChem*. **2021**, *7*, 1-9.

[18] M. Nielinger, F. Hausen, N. Podghainiy, H. Baltruschat in *Nanotribology at electrodes: Influence of adsorbates and potential on friction forces studied with atomic force microscopy, Vol.* (Eds.: A. Fischer, K. Bobzin), Wiley-VCH, Weinheim, **2009**, pp.178-184.

[19] N. Podgaynyy, S. Wezisla, C. Molls, H. Baltruschat *BEILSTEIN JOURNAL OF NANOTECHNOLOGY*. **2015**, *6*, 820-830.

[20] N. Podgaynyy, S. Iqbal, H. Baltruschat *Surf. Sci.* **2015**, *631*, 67-72.

[21] F. Hausen, M. Nielinger, S. Ernst, H. Baltruschat *Electrochimica Acta*. **2008**, *53*, 6058-6063.

[22] M. Nielinger, H. Baltruschat *Phys Chem Chem Phys*. **2007**, *9*, 3965-3969.

[23] R. Bennewitz, E. Gnecco, T. Gyalog, E. Meyer *Tribol. Lett.* **2001**, *10*, 51-56.

[24] A. Socoliuc, E. Gnecco, S. Maier, O. Pfeiffer, A. Baratoff, R. Bennewitz, E. Meyer *Science*. **2006**, *313*, 207-210.

[25] J. Hoth, F. Hausen, M. H. Muser, R. Bennewitz *J. Phys.-Condens. Matter*. **2014**, *26*.

[26] F. Hausen, N. N. Gosvami, R. Bennewitz *Electrochimica acta*. **2011**, *56*, 10694-10700.

[27] A. Labuda, F. Hausen, N. N. Gosvami, P. H. Grütter, R. B. Lennox, R. Bennewitz *Langmuir*. **2011**, *27*, 2561-2566.

[28] A. S. d. Wijn, A. Fasolino, A. E. Filippov, M. Urbakh *Physical Review Letters*. **2014**, *112*, 055502-055501 - 055502-055505.

[29] W. Ouyang, A. S. de Wijn, M. Urbakh *Nanoscale*. **2018**, *10*, 6375-6381.

[30] W. Ouyang, S. N. Ramakrishna, A. Rossi, M. Urbakh, N. D. Spencer, A. Arcifa *Physical Review Letters*. **2019**, *123*, 116102.

[31] J. Gao, W. D. Luedtke, D. Gourdon, M. Ruths, J. N. Israelachvili, U. Landman in Frictional forces and Amontons' law: from the molecular to the macroscopic scale, Vol. (Ed.^Eds.: Editor), ACS Publications, City, **2004**.

[32] D. Tabor, R. H. S. Winterton *Proceedings of the Royal Society of London. A. Mathematical and Physical Sciences*. **1969**, *312*, 435-450.

[33] J. N. Israelachvili, D. Tabor *Proceedings of the Royal Society of London. A. Mathematical and Physical Sciences*. **1972**, *331*, 19-38.

[34] R. G. Horn, J. N. Israelachvili *J. Chem. Phys.* **1981**, *75*, 1400-1411.

[35] H. Christenson, R. Horn, J. Israelachvili *J. Colloid Interface Sci.* **1982**, *88*, 79-88.

[36] H. K. Christenson, R. G. Horn *J. Colloid Interface Sci.* **1985**, *103*, 50-55.

[37] H. Christenson, R. Horn *Chem. Phys. Lett.* **1983**, *98*, 45-48.

[38] H. K. Christenson, C. E. Blom *J. Chem. Phys.* **1987**, *86*, 419-424.

[39] A. M. Smith, S. Perkin *Physical review letters*. **2017**, *118*, 096002.

[40] S. Perkin, T. Albrecht, J. Klein *Phys Chem Chem Phys*. **2010**, *12*, 1243-1247.

[41] A. M. Smith, M. A. Parkes, S. Perkin *J. Phys. Chem. Lett.* **2014**, *5*, 4032-4037.

[42] C. S. Perez-Martinez, S. Perkin *Langmuir*. **2019**, *35*, 15444-15450.

[43] A. M. Smith, K. R. J. Lovelock, N. N. Gosvami, T. Welton, S. Perkin *Phys Chem Chem Phys*. **2013**, *15*, 15317-15320.

[44] R. Espinosa-Marzal, A. Arcifa, A. Rossi, N. Spencer *The journal of physical chemistry letters*. **2014**, *5*, 179-184.

[45] R. Espinosa-Marzal, A. Arcifa, A. Rossi, N. Spencer *J. Phys. Chem. C*. **2014**, *118*, 6491-6503.

[46] G. Binnig, C. F. Quate, C. Gerber *Physical review letters*. **1986**, *56*, 930.

[47] C. M. Mate, G. M. McClelland, R. Erlandsson, S. Chiang *Physical Review Letters*. **1987**, *59*, 1942-1945.

[48] A. C. Hillier, S. Kim, A. J. Bard *J. Phys. Chem.* **1996**, *100*, 18808-18817.

[49] H. Li, F. Endres, R. Atkin *Phys Chem Chem Phys*. **2013**, *15*, 14624-14633.

[50] B. McLean, H. Li, R. Stefanovic, R. J. Wood, G. B. Webber, K. Ueno, M. Watanabe, G. G. Warr, A. Page, R. Atkin *Phys Chem Chem Phys*. **2015**, *17*, 325-333.

[51] A. Cook, K. Ueno, M. Watanabe, R. Atkin, H. Li *J. Phys. Chem. C*. **2017**, *121*, 15728-15734.

[52] H. Li, T. Niemann, R. Ludwig, R. Atkin *The journal of physical chemistry letters*. **2020**, *11*, 3905-3910.

[53] R. Atkin, N. Borisenko, M. Drüschler, S. Z. El Abedin, F. Endres, R. Hayes, B. Huber, B. Roling *Phys Chem Chem Phys*. **2011**, *13*, 6849-6857.

[54] T. Cui, A. Lahiri, T. Carstens, N. Borisenko, G. Pulletikurthi, C. Kuhl, F. Endres *J. Phys. Chem. C*. **2016**, *120*, 9341-9349.

[55] H. Li, M. W. Rutland, M. Watanabe, R. Atkin *Faraday Discuss.* **2017**, *199*, 311-322.

[56] R. Lhermerout, S. Perkin *Phys Chem Chem Phys*. **2020**, *22*, 455-466.

[57] R. Bennewitz, K. Broermann, P. Egberts, N. N. Gosvami, F. Hausen, C. Held *Adv. Eng. Mater.* **2010**, *12*, 362-367.

[58] G. A. Attard, C. Barnes, Surfaces, Oxford University Press Inc., New York, **1998**.

[59] X. Lin, F. Gossenberger, A. Groß *Industrial & Engineering Chemistry Research*. **2016**, *55*, 11107-11113.

[60] B. C. Schardt, S. L. Yau, F. Rinaldi *Science*. **1989**, *243*, 1050-1053.

[61] F. Lu, G. N. Salaita, H. Baltruschat, A. T. Hubbard *J. Electroanal. Chem.* **1987**, *222*, 305-320.

[62] X. P. Gao, M. J. Weaver *J. Am. Chem. Soc.* **1992**, *114*, 8544-8551.

[63] N. J. Tao, S. M. Lindsay *J. Phys. Chem.* **1992**, *96*, 5213-5217.

[64] B. M. Ocko, J. Wang, G. M. Watson *J. Phys. Chem.* **1994**, *98*, 897-906.

[65] K. Itaya, N. Batina, T. Yamada *J. Phys. Chem.* **1995**, *99*, 8817-8823.

[66] J. Inukai, Y. Osawa, K. Itaya *Journal of Physical Chemistry B*. **1998**, *102*, 10034-10040.

[67] P. Broekmann, M. Wilms, M. Kruft, C. Stuhlmann, K. Wandelt *J. Electroanal. Chem.* **1999**, *467*, 307-324.

[68] D. W. Suggs, A. J. Bard *J. Phys. Chem.* **1995**, *99*, 8349-8355.

[69] M. L. Foresti, G. Aloisi, M. Innocenti, H. Kobayashi, R. Guidelli *Surface Science*. **1995**, *335*, 241-251.

[70] T. E. Felter, A. T. Hubbard *J. Electroanal. Chem.* **1979**, *100*, 473-491.

[71] S. A. Cochran, H. H. Farrell *Surface Science*. **1980**, *95*, 359-366.

[72] D. Kolb. **1978**, *11*, 125.

[73] E. Budevski, G. Staikov, W. J. Lorenz, Electrochemical Phase Formation and Growth, VCH, Weinheim, **1996**.

[74] O. M. Magnussen, J. Hotlos, R. J. Nichols, D. M. Kolb, R. J. Behm *Phys. Rev. Lett.* **1991**, *64*, 2929.

[75] T. Hachiya, H. Honbo, K. Itaya *J Electroanal. Chem.* **1991**, *315*, 275-291.

[76] D. M. Kolb, U. Retter, M. H. Hölzle *J. Electroanal. Chem.* **1994**.

[77] W. Haiss, R. J. Nichols, J.-K. Sass *Surface Science*. **1997**, *388*, 141-149.

[78] N. Batina, T. Will, D. M. Kolb *Faraday Discussions*. **1992**, *94*, 93-106.

[79] F. Möller, O. M. Magnussen, R. J. Behm *Electrochimica Acta*. **1995**, *40*, 1259-1265.

[80] N. Ikemiya, S. Miyaoka, S. Hara *Surface Science*. **1994**, *311*, L641-L648.

[81] M. S. Zei, G. Qiao, G. Lehmpfuhl, D. M. Kolb

Berichte der Bunsen-Gesellschaft für Physikalische Chemie. **1987**, *91*, 349-353.

[82] L. J. Wu S. *Prog. Surf. Sci.* **1995**.

[83] Z. Shi, S. Wu, J. Lipkowski *Electrochimica Acta*. **1995**, *40*, 9-15.

[84] D. Kolb *Schering Lecture*. **1991**, *1*, 1-35.

[85] Y. Nakai, M. S. Zei, D. M. Kolb, G. Lehmpfuhl *Ber. Bunsen-Ges. Phys. Chem. Chem. Phys.* **1984**, *88*, 340-345.

[86] O. M. Magnussen *Chemical Reviews*. **2002**, *102*, 679-725.

[87] A. Martínez-Ruíz, M. Palomar-Pardavé, J. Valenzuela-Benavides, M. H. Farías, N. Batina *The Journal of Physical Chemistry B*. **2003**, *107*, 11660-11665.

[88] A. Martinez-Ruiz, J. Valenzuela-Benavides, L. M. de la Garza, N. Batina *Surf. Sci.* **2001**, *476*, 139-151.

[89] M. Espladiu, M. Schneeweiss, D. Kolb *Phys Chem Chem Phys*. **1999**, *1*, 4847-4854.

[90] T. Hachiya, K. Itaya *Ultramicroscopy*. **1992**, *42*, 445-452.

[91] K. Ogaki, K. Itaya *Electrochimica acta*. **1995**, *40*, 1249-1257.

[92] C. H. Chen, S. M. Vesecky, A. A. Gewirth *Journal of the American Chemical Society*. **1992**, *114*, 451-458.

[93] P. Mrozek, Y.-e. Sung, M. Han, M. Gamboa-Aldeco, A. Wieckowski, C.-h. Chen, A. A. Gewirth *Electrochimica acta*. **1995**, *40*, 17-28.

[94] V. Rooryck, F. Reniers, C. Buess-Herman, G. A. Attard, X. Yang *Journal of electroanalytical chemistry*. **2000**, *482*, 93-101.

[95] M. Azhagurajan, T. Itoh, K. Itaya *J. Phys. Chem. C*. **2016**, *120*, 16221-16227.

[96] T. Kondo, J. Morita, M. Okamura, T. Saito, K. Uosaki *Journal of Electroanalytical Chemistry*. **2002**, *532*, 201-205.

[97] S. Sugita, T. Abe, K. Itaya *J. Phys. Chem.* **1993**, *97*, 8780-8785.

CHAPTER 2

EXPERIMENTAL METHODS

2.1 The three electrode arrangement

Commonly, a three electrode arrangement is used in electrochemical experiments. In this three electrode configuration, two electrodes are used to apply a current through the system and one electrode is used to determine the potential of the working electrode [1, 2]. Thus, the connection between counter electrode (CE) and working electrode (WE) allows a current to flow through electrolyte and a reaction occurs on the WE. Since the potential of the reference electrode (RE) remains constant, it serves to measure the applied potential at the WE. The feedback circuit of the potentiostat allows to adjust a desired potential at the WE by applying the necessary voltage (and current) between CE and WE. Figure 2.1 shows the common design of electrochemical glass cell, the so-called H-cell, often used in the electrochemical experiments and used in this study. To prevent the ohmic potential drop between the WE and RE, the RE is located in a separate compartment and a so-called *Luggin capillary* connects the WE and the RE compartments. In addition, during the electrochemical experiments, WE compartment of the cell is purged with pure Ar.

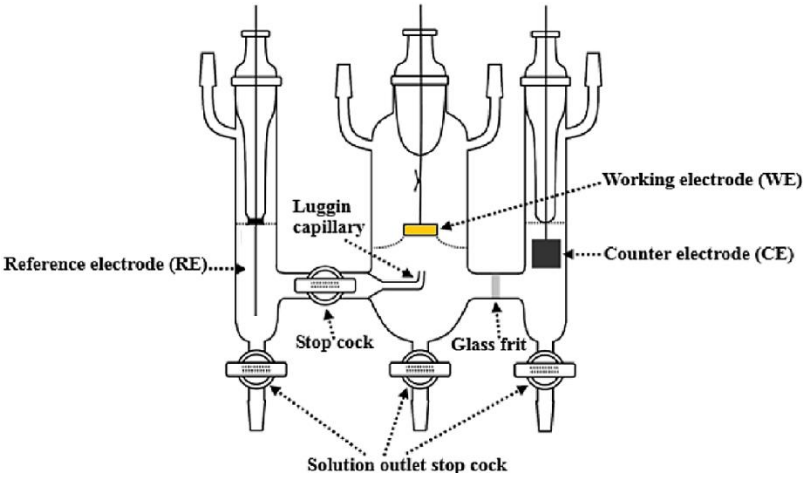

Figure 2.1 Design of an electrochemical glass cell, H-cell, used in this study.

2.2 The preparation of single crystals

Single crystal electrodes are prepared such that they expose a particular crystal plane. Due to thermodynamic reactions (minimization of the surface energy) the surface is prone to be contaminated by adsorbates. Therefore, the single crystal should be cleaned properly.

The surface of the single crystal electrode was prepared by the flame annealing method developed by J. Clavilier [3]. This flame annealing serves to remove contaminants such as organic molecules on the surface and flattens the surface on the atomic scale [4]. In the case of strong contamination, the single crystal is additionally oxidized at 5 V (vs. RHE) and then, oxides including contaminants are directly dissolved in concentrated HCl. After the annealing process, the single crystal is cooled down above the Milli-Q water in the H-cell purged with Ar and when reaching a temperature slightly below the 100 °C, it is contacted with water ("quenching"). In order to check the cleanness and the size of terrace after the flame annealing and cooling procedure, the cyclic voltammogram (CV) is checked in 0.1 M H_2SO_4 as shown in Figure 2.2. J is the current density and it is obtained by dividing the observed current with the geometric surface area (0.785 cm^2).

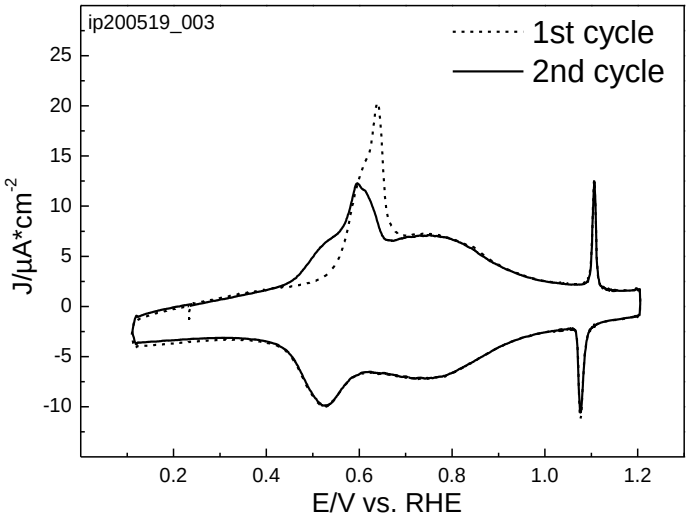

Figure 2.2 Cyclic voltammogram in H-cell for Au(111) in 0.1 M H_2SO_4 after the flame annealing and cooling process. The sweep rate is 50 mV/s.

An iodine-CO replacement method has been reported as an alternative to the flame annealing and quenching method for Pt single crystal [5]. In this study, the annealed single crystal Au(111) is cooled down above iodine crystals to get the monolayer of iodine on Au(111). It means that the Au(111) is cooled down in the I_2 vapor atmosphere. Due to this method, large terraces are observed as well as the step bunching.

2.3 Scanning probe microscopy (SPM)

2.3.1 Scanning tunneling microscopy (STM)

To study surface properties of materials from the micrometer scale all the way down to the atomic level, scanning tunneling microscopy (STM) was invented in 1981 at IBM Zurich [6]. The probe in an STM is a conducting sharp tip made from tungsten or platinum-iridium. A bias voltage is applied between the tip and the sample. When the tip approaches to the surface, from the certain distance close enough to the surface, electron begins to 'tunnel' through the gap. Depending on the polarity of the applied bias (+,-), electron tunnels from the tip to surface or vice versa. When the tip is scanning on the surface, due to the piezo material in the scanner, the variation of the magnitude of this current thus reflects the topography of the sample. In addition, there is a feedback control ensuring that the probe accurately tracks the surface topography,

which reduces the damage of sample by tip. This feedback control compares continuously the detected signal to the setpoint and adjusts the voltage applied to the scanner when it is not equal.

2.3.2 Atomic force microscopy (AFM)

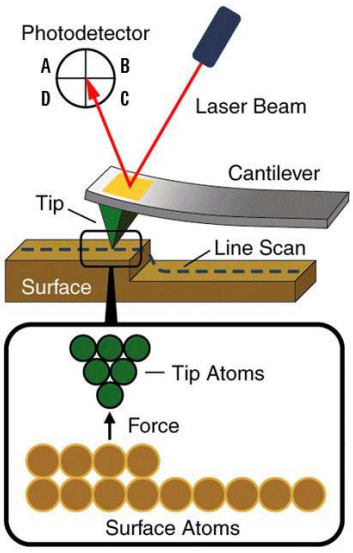

Figure 2.3 Basic AFM principle [10]

The atomic force microscopy (AFM) is a variant form of STM allowing also to study surfaces of non-conducting materials such as insulators and semiconductors [7]. As the scanner scans the surface of the sample, the contact force causes the cantilever to bend according to the change in topography of the sample. A Laser is focused on the cantilever, reflected to the position-sensitive photodiode (PSPD) detector as shown in Figure 2.3 [8]. Thus, a detector measures the deflection of cantilever as the tip scans the surface of sample. There are 3 different modes to operate AFM: 1) contact mode, 2) non-contact mode, and 3) tapping mode. In contact mode, AFM tip is brought to the surface in contact with the surface of sample. The contact force causes the cantilever to perpendicularly bend (short range repulsive force), which provides the topography of the surface. Since the tip is in contact with the sample, there is a risk of damaging the sample.

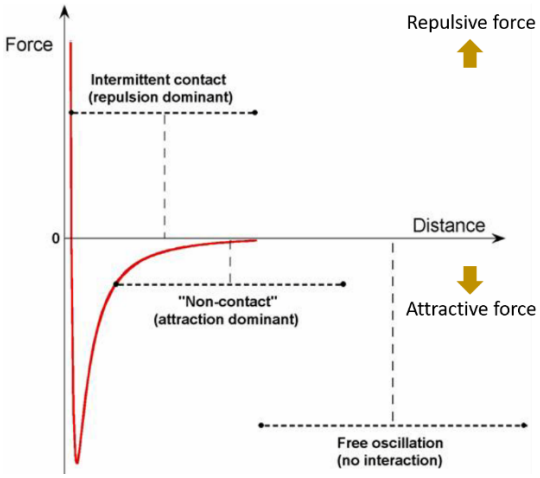

Figure 2.4 Zones of interaction as the tip approaches the sample [8]

In non-contact mode, the cantilever vibrates with a certain frequency near the surface of the sample in the non-contact zone (Figure 2.4) and the cantilever bends due to the long range

attractive force. Thus there is no direct contact between tip and the surface. In contrast, in tapping mode, an oscillating tip intermittently taps the surface of the sample to map the topography. In this tapping mode, the amplitude of oscillation of cantilever is very sensitive and can be modified, which reflects the topography of the sample.

2.3.3 Lateral force microscopy (LFM)

Lateral force microscopy (LFM) works in contact mode of AFM and maps relative differences in vertical deflection (topography) and torsional deflection resulting from the twist of the cantilever in scan direction. Figure 2.5 shows that the torsional deflection depends on the scan directions, trace and retrace, which results in the different sign of the values.

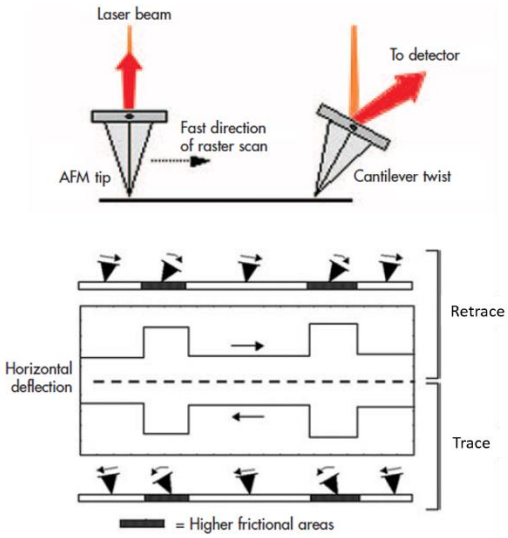

Figure 2.5 Lateral force measurement [9]

Calibration of the cantilever

The deflection of the cantilever spring is directly proportional to the tip-sample interaction force. For LFM measurement, the vertical deflection of the cantilever, the normal spring constant (k_N), is monitored for the topography based on the applied normal force. Moreover, the torsional deflection, the torsional spring constant (k_T), of cantilever related to the applied torque to the angle of twist of cantilever is important. For calibrating the normal and torsional spring

constants, the Sader method is used [10, 11]. In this method, the dimensions of the rectangular cantilever (length and width) and the resonant frequencies for normal and torsional motions are required. The resonant frequencies (w_r) can be easily obtained using non-contact mode of AFM. Furthermore, the quality factor (Q) for the resonant frequencies are obtained by fitting a curve of resonant frequency to the equation of simple harmonic oscillation (SHO) as shown in eq. 2.1.

$$A_{white} + \frac{A_0 w^4}{(w^2 - {w_r}^2)^2 + \frac{w^2 {w_r}^2}{Q^2}} \qquad 2.1$$

The observed values of resonance frequencies and Q factors were inserted in the program maintained by J. Sader[12].

The lateral spring constant (k_L) used to calculate the friction, is obtained by dividing the torsional spring constant (k_T) with the square of the tip height. The tip height from the provider of the cantilever is in the range between 10 to 15 µm, independent of the type of cantilevers. In this thesis, it was assumed that the tip height is 13.5 µm.

Conversion of normal load and friction

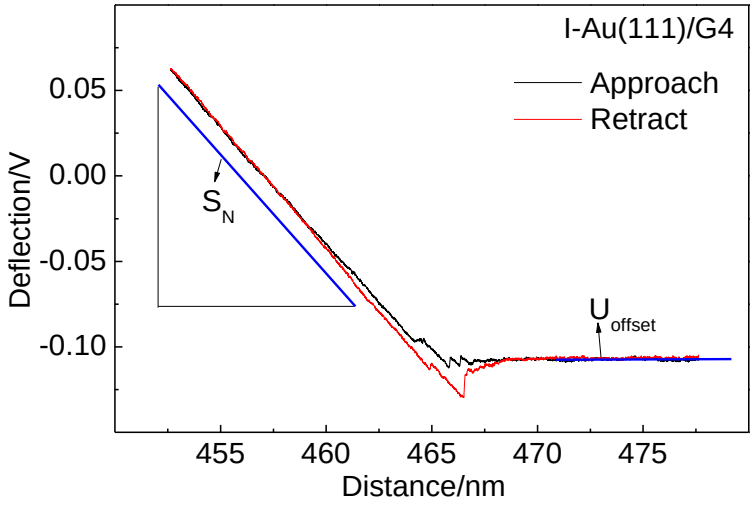

Figure 2.6 Plot of approach (black) and retract (red) curves on I-modified Au(111) in pure tetraglyme (G4). The gradient chosen for sensitivity measurements and the baseline offset for the deflection are both marked on this plot.

Figure 2.6 shows the raw data for cantilever deflection in displayed in Volt when the cantilever approaches the surface (black curve) and retracts from the surface (red curve). The applied normal load, F_N, can be calculated using eq. 2.2, which states

$$F_N[N] = k_N \left[\frac{N}{m}\right] \times S_N \left[\frac{m}{V}\right] \times (U_N - U_{offset})[V] \quad 2.2$$

Where k_N is the normal spring constant determined by the Sader method, S_N and U_{Offset} are the deflection sensitivity and baseline offset where the tip retracts, respectively, shown in Figure 2.6, and U_N is the applied voltage on the cantilever.

Lateral forces, F_L, can be calculated using eq. 2.2, which states

$$F_L[N] = (\frac{3}{2} \times \frac{h}{L} \times k_L \left[\frac{N}{m}\right] \times S_N \left[\frac{m}{V}\right]) \times U_L[V] \quad 2.3$$

Where h and L are the height and length of cantilever, respectively, k_L is the lateral spring constant, S_N is the deflection sensitivity, and U_L is the torsional deflection in Volt. Twisting of the cantilever usually arises from the friction on the scanned surface and from topography. Thus, there is an influence of topography on the raw data and it is the topographic effect (T). Thus, in our system, the retrace and trace data contain T+F and T-F, respectively. The torsional deflection, U_L, in the eq. 2.3 is obtained by subtracting the trace data from the retrace data and dividing it by 2 to eliminate topographic effect [13].

Force-separation (FS) curves

The deflection of the cantilever is shown in units of Volt, as shown in Figure 2.6. First, this value in y-axis should be converted in units of length by multiplying it with the deflection sensitivity, S_N. The distance in x-axis corresponds to the piezo height. When the cantilever deflects towards the sample (attractive interaction), the separation between the tip and the surface will be less than the piezo height. Since the cantilever deflection and position are available in the same unit, this can be easily corrected by subtracting the cantilever deflection from it as written in eq. 2.4.

$$Separation = piezo\ height - (deflection \times Deflection\ sensitivity) \quad 2.4$$

In eq. 2.4, the units of deflection and deflection sensitivity are Volt, V and meter per Volt, m/V, respectively.

This subtraction leads to the gradient of the approach curve becoming vertical as shown in Figure 2.7. This indicates that once the tip is in contact with the surface of sample, the tip-sample distance remains at zero while the force still increases due to the cantilever pushing towards the surface.

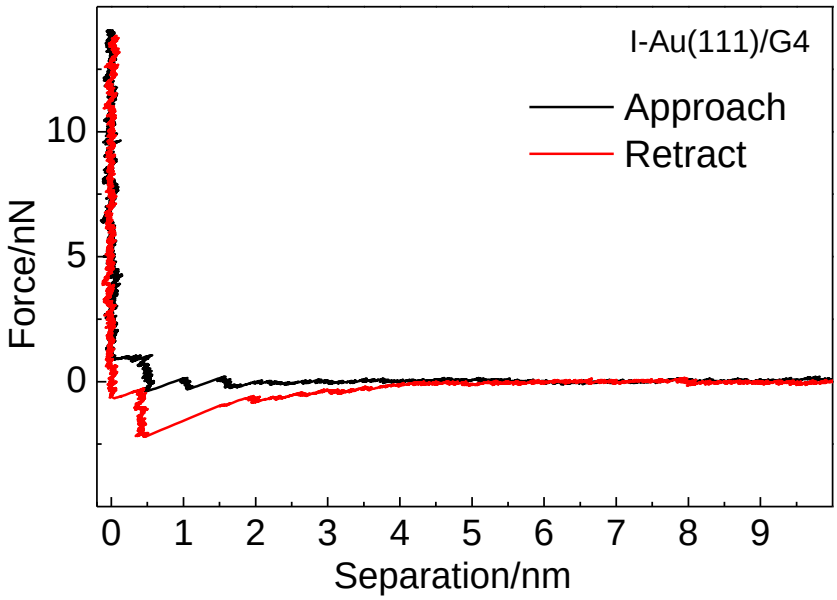

Figure 2.7 Force-separation plot for the data shown in Figure 2.6

2.3.4 Atomic corrugation and thermal drift correction

Thermal drift in slow scan direction is a general problem for the measurement using scanning probe microscope (SPM). It is problematic especially for atomically resolved images. Calculations are performed to correct the thermal drift, based on the paper by S. Iqbal et al. [14] and his doctorate thesis [15].

Figure 2.8 and 2.9 show topography images and lateral force maps observed on highly oriented pyrolytic graphite (HOPG) in air using PPP-CONTSC (k_N = 0.15 N/m), which show the negligible discrepancy of atomic structures between them. In this thesis, we study the structure of adsorbates (e.g. iodine, sulfate, Ag, and Cu) and substrate using lateral force maps. Furthermore, the observed lattice parameters of HOPG were approx. 10 % larger than the theoretical value, 0.246 nm. Therefore, we assume that the experimental value contains basically ± 10 % error and it might be slightly larger under electrochemical conditions.

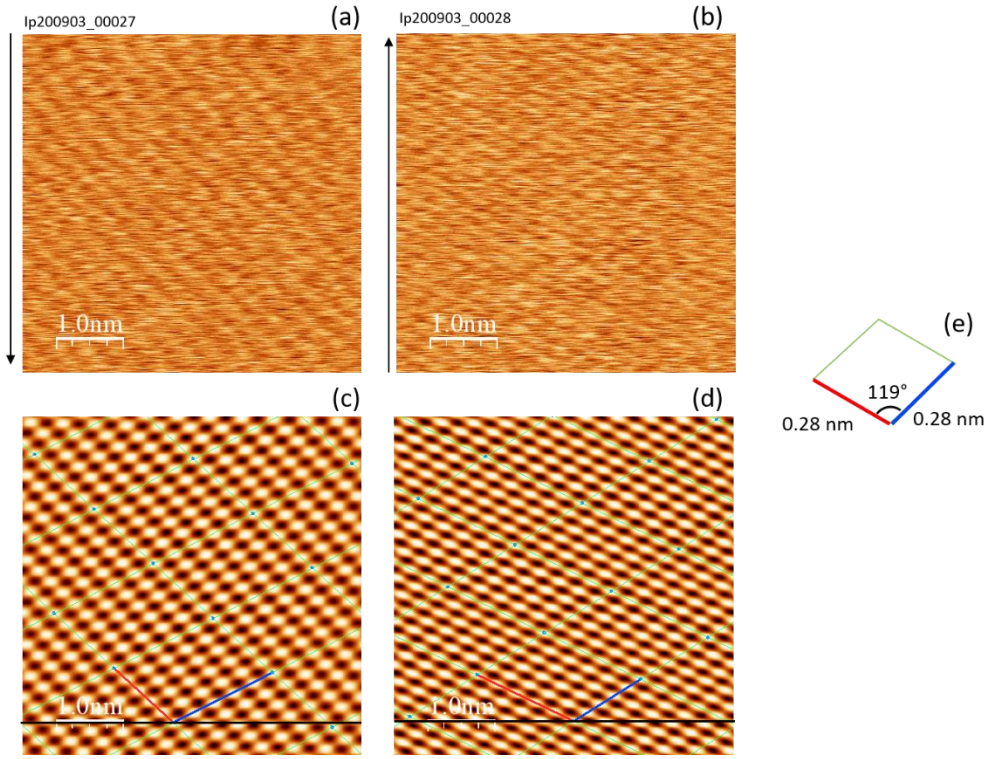

Figure 2.8 Topography images on HOPG in (a) downward scan and (b) upward scan. Black arrow indicates the scan direction. (c) and (d) are the lattice images after Fast Fourier Transform (FFT) of (a) and (b), respectively. (e) is the lattice vector after the correction of thermal drift. Applied normal load is 50 nN.

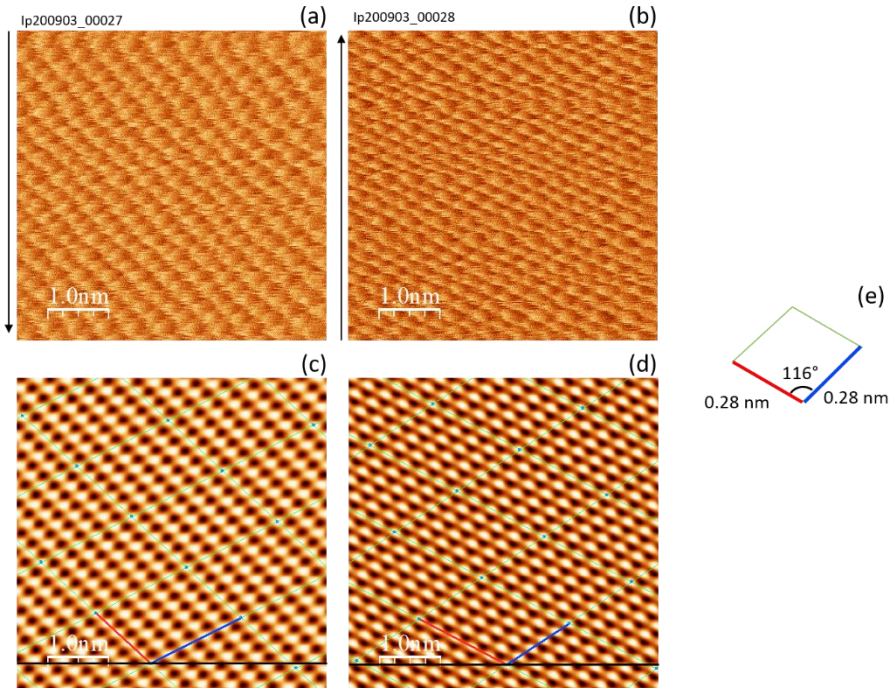

Figure 2.9 Lateral force maps on HOPG in (a) downward scan and (b) upward scan. Black arrow indicates the scan direction. (c) and (d) are the lattice images after Fast Fourier Transform (FFT) of (a) and (b), respectively. (e) is the lattice vector after the correction of thermal drift. Applied normal load is 50 nN.

2.3.5 Z-axis calibration

Figure 2.10 shows mono-atomic steps observed on Au(111) at open circuit potential (OCP), 0.11 V (vs. Pt/PtO) in 0.1 M $Ca(ClO_4)_2$/DMSO. It is noteworthy that after the subtraction of background, there is still the effect of background, which affects the value of mono-atomic step. Nevertheless, this result confirms that the observed values are close to the theoretical value (0.2 nm) for a mono-atomic step of Au(111).

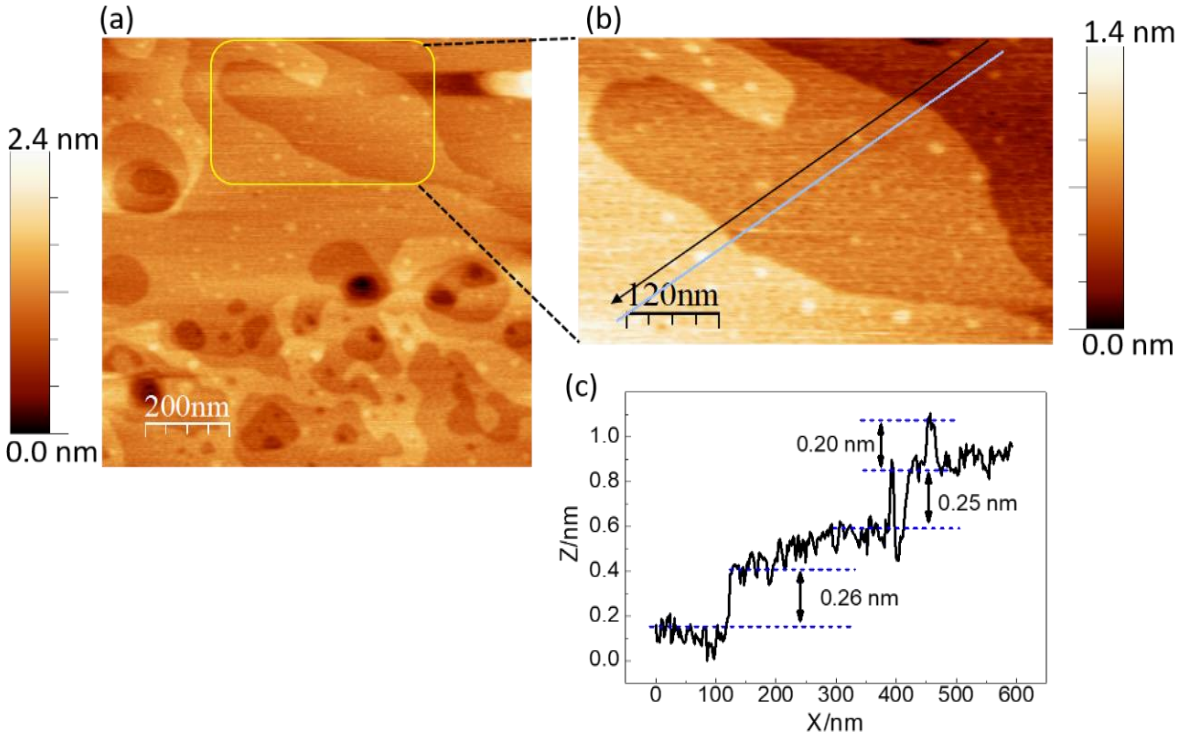

Figure 2.10 (a) Topography images on Au(111) at 0.11 V (vs. Pt/PtO) in 0.1 M Ca(ClO4)2/DMSO. To subtract the background, partial image (b) was taken where the size of terraces are relatively large. (c) is the line profile marked on (b). The scan direction is downward.

2.3.6 Electrochemistry in the AFM cell

Figure 2.10 shows a design of an electrochemical AFM-cell assembled with a sample stage of AFM. This home built AFM-cell is made of polychlorotrifluoroethylene (PCTFE), Kel-F. Differently from the H-cell described above, the AFM-cell is composed of two separate compartments. The WE and CE are located in a large compartment and the RE is located in a small compartment connected to a large compartment via small hole, which avoids the contamination of the RE. Due to the limitations of this cell design, in this work the electrolyte for the RE-compartment is identical to that for the WE-compartment. Therefore, a Ag or Cu wires were used as the RE for this study.

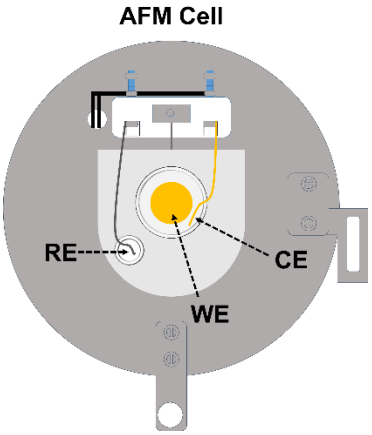

Figure 2.11 Design of an electrochemical AFM-cell, used in this study.

Reference

[1] W. Schmickler, S. E., Interfacial Electrochemistry, springer, Berlin, **2010**.

[2] A. J. Bard, L. R. Faulkner, Electrochemical Methods: Fundamentals and Applications, John Wiley & Sons Inc., New York, Weinheim, **2001**.

[3] J. Clavilier, R. Faure, G. Guinet, R. Durand *J. Electroanal. Chem.* **1980**, *107*, 205-209.

[4] M. H. Dishner, M. M. Ivey, S. Gorer, J. C. Hemminger, F. J. Feher *J. Vac. Sci. Technol. A-Vac. Surf. Films*. **1998**, *16*, 3295-3300.

[5] D. Zurawski, L. Rice, M. Hourani, A. Wieckowsi *J. Electroanal. Chem.* **1987**, *230*, 221-231.

[6] G. Binnig, H. Rohrer *Surface Science*. **1983**, *126*, 236-244.

[7] G. Binnig, C. F. Quate, C. Gerber *Physical review letters*. **1986**, *56*, 930.

[8] A. Technologies in Agilent Technologies 5500 Scanning Probe Microscope, Vol. (Ed.^Eds.: Editor), City.

[9] Veeco in A Practical Guide to SPM: Scanning Probe Microscopy, Vol. (Ed.^Eds.: Editor), City.

[10] J. E. Sader, J. W. M. Chon, P. Mulvaney *Rev. Sci. Instrum.* **1999**, *70*, 3967-3969.

[11] C. P. Green, H. Lioe, J. P. Cleveland, R. Proksch, P. Mulvaney, J. E. Sader *Review of Scientific Instruments*. **2004**, *75*, 1988-1996.

[12] J. Sader *https://www.ampc.ms.unimelb.edu.au/afm/calibration.html*. **2003**.

[13] S. Sundararajan, B. Bhushan *J. Appl. Phys.* **2000**, *88*, 4825-4831.

[14] S. Iqbal, L. Zan, E. Nardi, H. Baltruschat *Phys. Chem. Chem. Phys.* **2018**, *20*, 6176-6186.

[15] S. Iqbal, Rheinischen Friedrich-Wilhelms-Universität Bonn, **2015**.

CHAPTER 3

Silver underpotential deposition (UPD) on Au(111) in aqueous electrolyte

Inhee Park[1] and H. Baltruschat[1*]

[1]Institut für Physikalische und Theoretische Chemie, Universität Bonn, Römerstraße 164, D-53117 Bonn, Germany

*Corresponding Author: Baltruschat@uni-bonn.de

Reproduced with the permission from:

I. Park and H. Baltruschat, *ChemPhysChem*, **2021**, 22, 1-9,

DOI: 10.1002/cphc.202100130 ©2021 The Authors. ChemPhysChem published by Wiley-VCH GmbH

3.1 Abstract

The electrodeposition of silver on Au(111) was investigated using lateral force microscopy (LFM) in the Ag^+ containing sulfuric acid. Friction force images show that adsorbed sulfate forms the $\left(\sqrt{3} \times \sqrt{7}R19.1°\right)$ structure ($\theta_{sulfate} = 0.2$) on Au(111) prior to Ag upd and the ($\sqrt{3} \times \sqrt{3}R30°$) structure ($\theta_{sulfate} = 0.33$) on a complete monolayer of Ag and also on the complete bilayer on Au(111). Variation of friction with normal load shows a non-monotonous dependence, which is caused by increasing penetration of the tip into the sulfate adlayer. In addition, the friction force is influenced by the varying coverage and mobility of Ag atoms on the surface: Before the coverage of Ag reaches the critical value, the deposited silver atoms may be mobile enough to be dragged by the movement of AFM tip. Possible penetration of the tip into the UPD layer at very high loads is discussed as a model for self-healing wear. However, when the coverage of Ag is close to 1, the deposited Ag atoms are tight enough to resist the influence of the AFM tip and the tip penetrates only into the sulfate adlayer.

KEYWORDS: Ag underpotential deposition, Lateral force microscopy (LFM), Adsorbate coverage, Friction, Tribology

3.2 Introduction

Silver electrodeposition on Au(111) has been the subject of numerous studies because the interaction between foreign metal and substrate is very strong and the lattice mismatch is negligible[1-9]. The Ag UPD occurs in at least three different steps on Au(111) in sulfuric acid. Itaya et al. and Kolb et al. reported the structures of surface during Ag UPD in sulfuric acid using STM [1-3, 8]. They observed the ($\sqrt{3} \times \sqrt{7}R19.1°$) structure at the most positive potential, which indicates that sulfate/bisulfate is adsorbed and forms ordered structure. At a potential

negative of the 1st Ag UPD peak, Itaya and coworkers observed a $(\sqrt{3} \times \sqrt{3}R30°)$ structure but Kolb and coworkers observed a $(\sqrt{3} \times \sqrt{3}R30°)$ structure, a striped compressed structure and a $p(3 \times 3)$ structure down to potentials close to 0.25 V. There, a very small peak in the CV indicates further Ag deposition and the start of the completion of the 1st Ag monolayer ($p(3 \times 3)$ to (1×1) transition). No well-resolved atomic-scale image was observed at the potential near the 2nd Ag UPD peak, only a slight increase in height was observed. Results of surface X-ray scattering (SXS) shows that the Ag completes a monolayer at the potentials after the 2nd Ag UPD; a bilayer forms at the potential of 3rd Ag UPD [6, 7]. Although in situ STM and related techniques could reveal the atomic-level deposition/dissolution process, the Ag UPD process before the completion of Ag monolayer is still not sufficiently understood.

The lateral force microscope (LFM) is used to address frictional forces on the nanometer scale or even in single asperity contact. The strength of interaction between surface and AFM strongly depends on the species adsorbed on the surface. Thus, adsorbed molecules on substrates play a crucial role in adhesion, friction and wear behaviors[10-22]. Interestingly, molecular dynamics (MD) simulation demonstrated that for given external conditions, such as normal load, temperature and adsorbate surface coverage, the observed regime of friction is determined by the strength of the adsorbate-substrate interaction[23-25].

Ionic liquids (ILs) form layered structures at electrode surfaces, as revealed by tip approach curves; friction measurements indicate that the outer layers are penetrated by the tip and only the boundary ion layers, which are in touch with the surface, are closely related with the friction behavior that can be modified by the applied potential [16-18, 22]. Furthermore, smooth layers lead to lower friction values than those with a larger corrugation. In aqueous electrolytes, the surface of Au(111) can be reversibly modified by anions and cations. Our group also has studied the influence of several adlayers on Au(111) on friction force under electrochemical condition[11-14]. For sulfate ions on Au(111) the friction starts to increase at the potential where the lifting of reconstruction of Au(111) occurs and continuously increases with increasing sulfate coverage until the potential arrives at the spike, which indicates the transition of disordered to ordered sulfate adlayer. [12] For low normal loads, friction decreases slightly upon ordering, whereas for high normal load ordering rather leads to a further friction increase. In the case of Cu UPD in sulfuric acid solution, we observed that when a potential approaches the onset of 1st Cu UPD, COF shows the lowest value, resulting from the decreasing anion coverage. Negative of the 1st Cu UPD peak, the copper forms a $(\sqrt{3} \times \sqrt{3}R30°)$ structure with 2/3 coverage, resulting in the increase of the COF. When a Cu monolayer is completed, sulfate ions are adsorbed on Cu(111)

and the interaction between sulfate ions and copper substrate leads to the double slip on relatively high loads. Atomic stick slip, which for an electrode surface had first been observed by Labuda et al.[26], has also be observed at a regularly stepped Au(665) electrode [27]. Friction considerably increases and stick-slip becomes irregular upon oxidation of a Au(111) surface.[28]

In this study, we investigate the dependence of friction force on applied potentials during Ag UPD on Au(111) in sulfuric acid. On the basis of what is already known from earlier results, it was our aim to understand the influence of adsorbed anions and the coverage of silver during Ag UPD and thus to substantiate and generalize our previous findings on the effects of adsorbates and possible tip penetration.

3.3 Experimental

A disc type of Au(111) single crystal(diameter: 10mm and thickness: 3mm) purchased from MaTecK GmbH was used as working electrode. It was annealed by flame and cooled down above water purged with Ar to get clean surface. Gold and silver wires were used as counter and reference electrodes, respectively. For electrolytes, 1mM Ag_2SO_4 were dissolved in 0.05M H_2SO_4.

Lateral (frictional) force measurements were performed using Agilent 5500 AFM, combined with glass chamber. Silicon tips (PPP-FM and and PPP-CONTSC, NANOSENSORS, tip radius <10nm) were used and the spring constants were determined to be 0.95±0.05 N/m (PPP-FM, 'hard') and 0.1±0.05 N/m (PPP-CONTSC, 'soft'). Normal and torsional resonance frequency of AFM tips were measured by AFM (Agilent 5500/AC mode). Q factor for theses resonance frequencies was obtained using the equation of simple harmonic oscillation (SHO). Normal and torsional force constants were calculated using the Sader method[29, 30] and the lateral spring constant was obtained by dividing torsional spring constant with the square of the tip height. A homemade AFM cell was used, which contains a three-electrode assembly and Ar was purged through the glass chamber. The lateral force vs. normal load and potential curves were measured with a scan size of 20 x 20 nm^2 and a scan rate of 0.47nm/s.

When the AFM tip scans the surface, friction (F) makes it twist, which we obtain as the deflection of the laser beam. The sign of the deflection depends on the scan direction. In addition, the deflection of the laser is caused by topography (T) (e.g. steps on the surface), this effect does not depend on scan direction. Thus, the forward image and backward image contain [T+F] and [T-F], respectively. Friction force data was obtained by subtracting the backward data from the forward data and dividing it by 2 to eliminate topographic effects [31].

3.4 Results and discussion

3.4.1 Cyclic voltammetry (CV)

Figure 3.1(a) shows the cyclic voltammetry obtained in H-cell filled with 1mM Ag_2SO_4/0.05M H_2SO_4. Three major peaks, C_1, C_2, and C_3, with a number of small peaks corresponding to the Ag UPD were observed in agreement with previous reports [1-5].In the AFM-cell resolution is lower and only three major peaks were visible (Figure 3.1b). In order to understand the charges associated with peaks, we vary the potential regions (I, II, II´, III, and IV) referring to three major peaks. Region II´ corresponds to the potential range where Gewirth et al. observed no atomic structure due to the some type of rapid exchange process with the electrolyte [4]. The charge densities corresponding to the first (II), second (II´+III), and third (IV) UPD peaks/regions in H-cell are 65 (C_1) + 51, 34 + 57, and 178 µC/cm², respectively.

Regarding the charge density and the results of surface X-ray scattering (SXS)[6, 7], silver completes a monolayer at slightly negative potential of C_2 and peak C_3 is related with a bilayer formation. The total charge for completion of the first monolayer (region II-III, 207 µC/cm²) is less than the theoretical charge (222 µC/cm²) which is explained by the shift of the pzc upon deposition of Ag, which on Ag is 1 V more negative than that of Au, and the corresponding anionic charge flow [3]. The charge flow in the broad region II and II´ may indicate that the silver is continuously deposited on the surface as shown in results of the electrochemical quartz crystal microbalance (EQCM) [32].

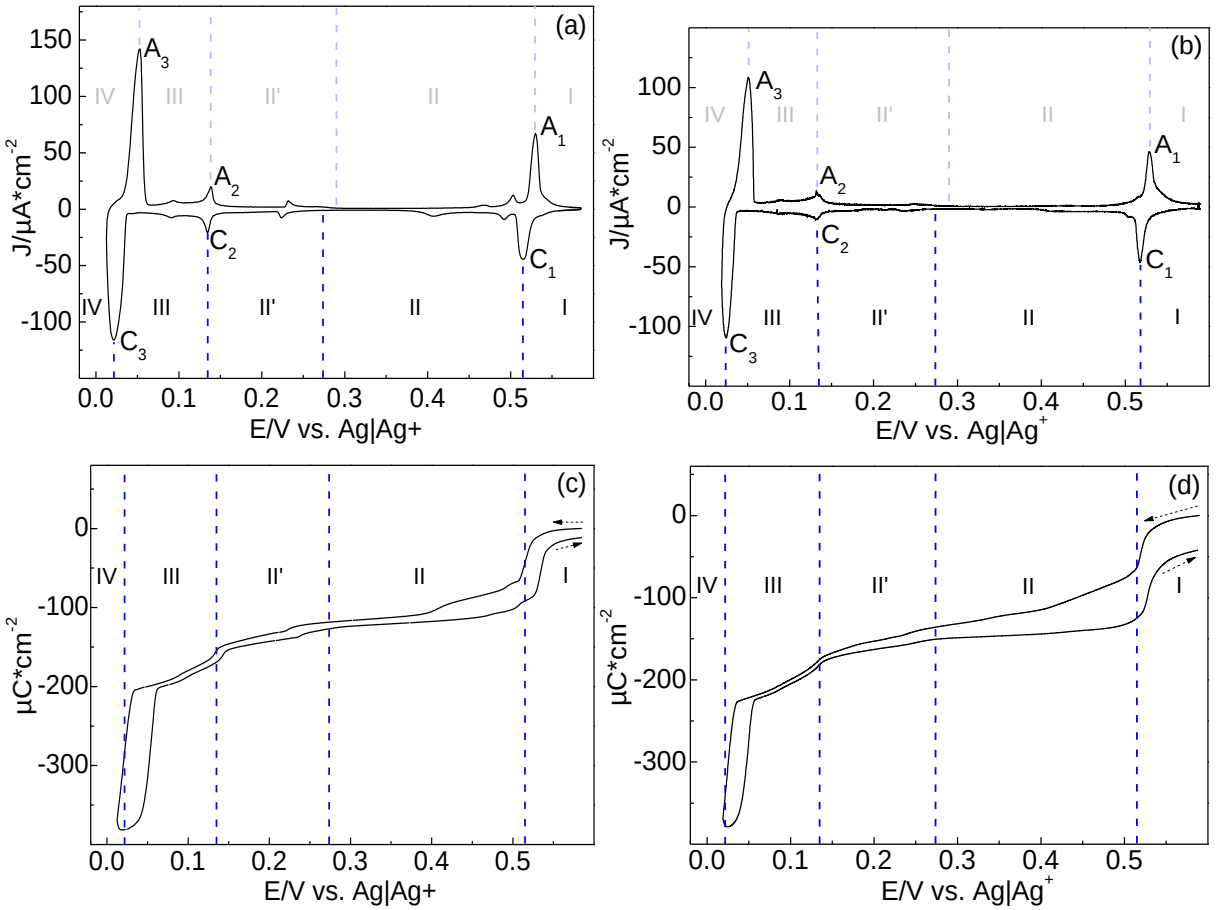

Figure 3.1 Cyclic voltammetry and coulometric curve in (a) and (c) H-cell and (b) and (d) AFM-cell for the Au(111) in 1mM Ag_2SO_4/0.1M H_2SO_4. The sweep rate is 10mV/s.

3.4.2 Atomic corrugation in friction

We investigated structures depending on potentials using atomic corrugation in friction images to get the information for the coverage of adsorbates (sulfate and Ag). To get clear lattice image we used fast Fourier transform (FFT) filtering and corrected for thermal drift [33]. As shown in Figure S3.1, we observed the well-known ($\sqrt{3} \times \sqrt{7}R19.1°$) structure of the ordered sulfate/bisulfate layer on Au(111) at 0.57 V. At potentials between the 1st and 2nd Ag UPD peaks (region II and II'), it was not easy to get atomically well resolved images, which may be due to the fact that several structures seem to coexist in this potential region and their instability[1-5].

Sometimes, we observed the $(\sqrt{3} \times \sqrt{3}R30°)$ structure at 0.33 V as shown in Figure S3.2. At 0.0 V, where we assume that silver completes a Ag bilayer, we easily observed the $(\sqrt{3} \times \sqrt{3})R30°$ structure as shown in Figure 3.3. In anodic sweep, at slightly positive of peak A_3, 0.09 V, where a monolayer exists after the dissolution of a Ag bilayer, the $(\sqrt{3} \times \sqrt{3})R30°$ structure was also observed (Figure 2). It supports the previous results of EQCM that the amount of adsorbed sulfate is rather constant during the Ag UPD (region II-IV) [32].

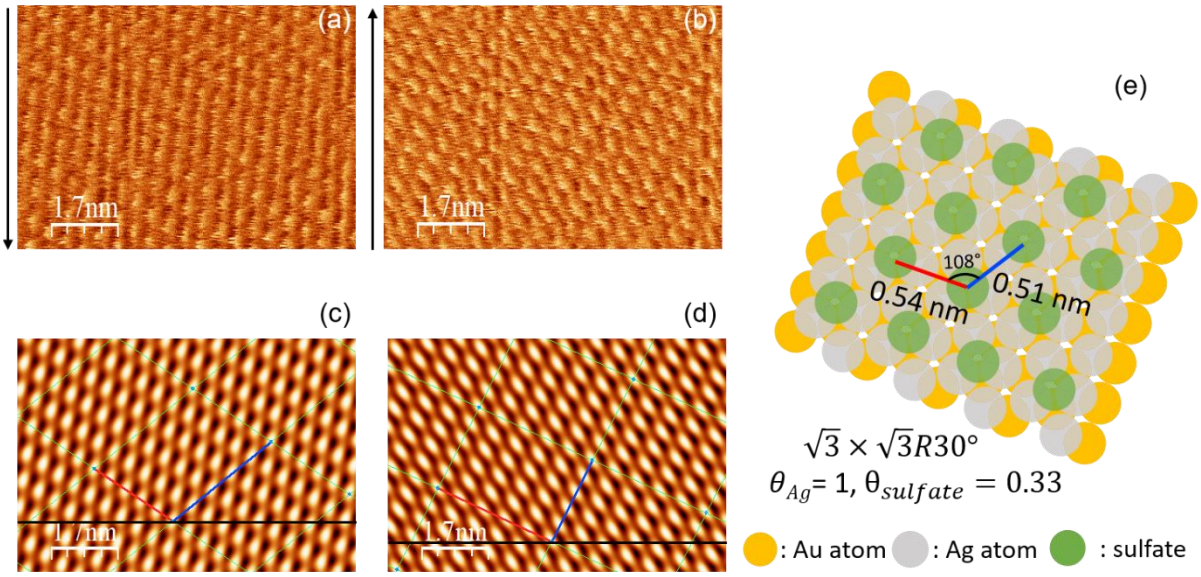

Figure 3.2 Lateral force maps at 0.09V (vs. Ag/Ag+) in anodic sweep during (a) downward scan and (b) upward scan. Black arrow indicates scan direction. (c) and (d) are the lattice images after FFT filtering of (a) and (b), respectively. (e) is the illustration of the real lattice with lattice parameters after the correction of thermal drift. PPP-FM was used (k_N = 0.95±0.05 N/m). Applied normal load is 8 nN.

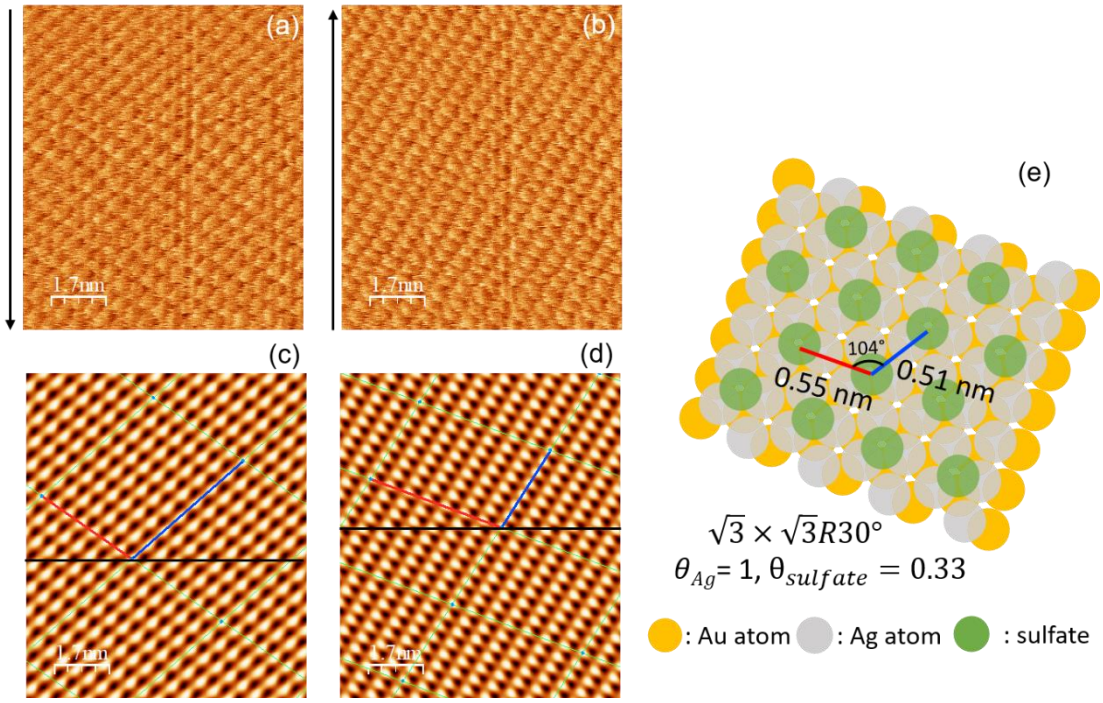

Figure 3.3 Lateral force maps at 0.02V (vs. Ag/Ag+) in cathodic sweep during (a) downward scan and (b) upward scan. Arrow indicates scan direction. (c) and (d) are the lattice images after FFT filtering of (a) and (b), respectively. (e) is the illustration of the real lattice with lattice parameters after the correction of thermal drift. PPP-FM was used (k_N = 0.95±0.05 N/m). Applied normal load is 8 nN.

3.4.3 Friction force dependence on potential

Figure 3.4 shows the dependence of friction on potential. In this measurement, the sweep rate of CV was set as 14 mV/s, which fits the speed for the completion of a lateral force map. When a potential arrives at about 0.02V in cathodic sweep, one friction image was recorded at 0.02V for the complete Ag bilayer before starting the anodic sweep; the corresponding friction is marked as green dots in Figure 3.4.

When the applied normal load is below 5 nN, no friction change is observed. Above this minimal load, the friction shows strong dependence on the coverage of adsorbates. When the applied potential is more positive than the 1st Ag UPD peak, region I, the sulfate/bisulfates are

adsorbed on Au(111) and form the $(\sqrt{3} \times \sqrt{7})R19.1°$ structure ($\theta_{sulfate} = 0.2$). Friction therefore is dominated by the interaction between AFM tip and the sulfate layer.

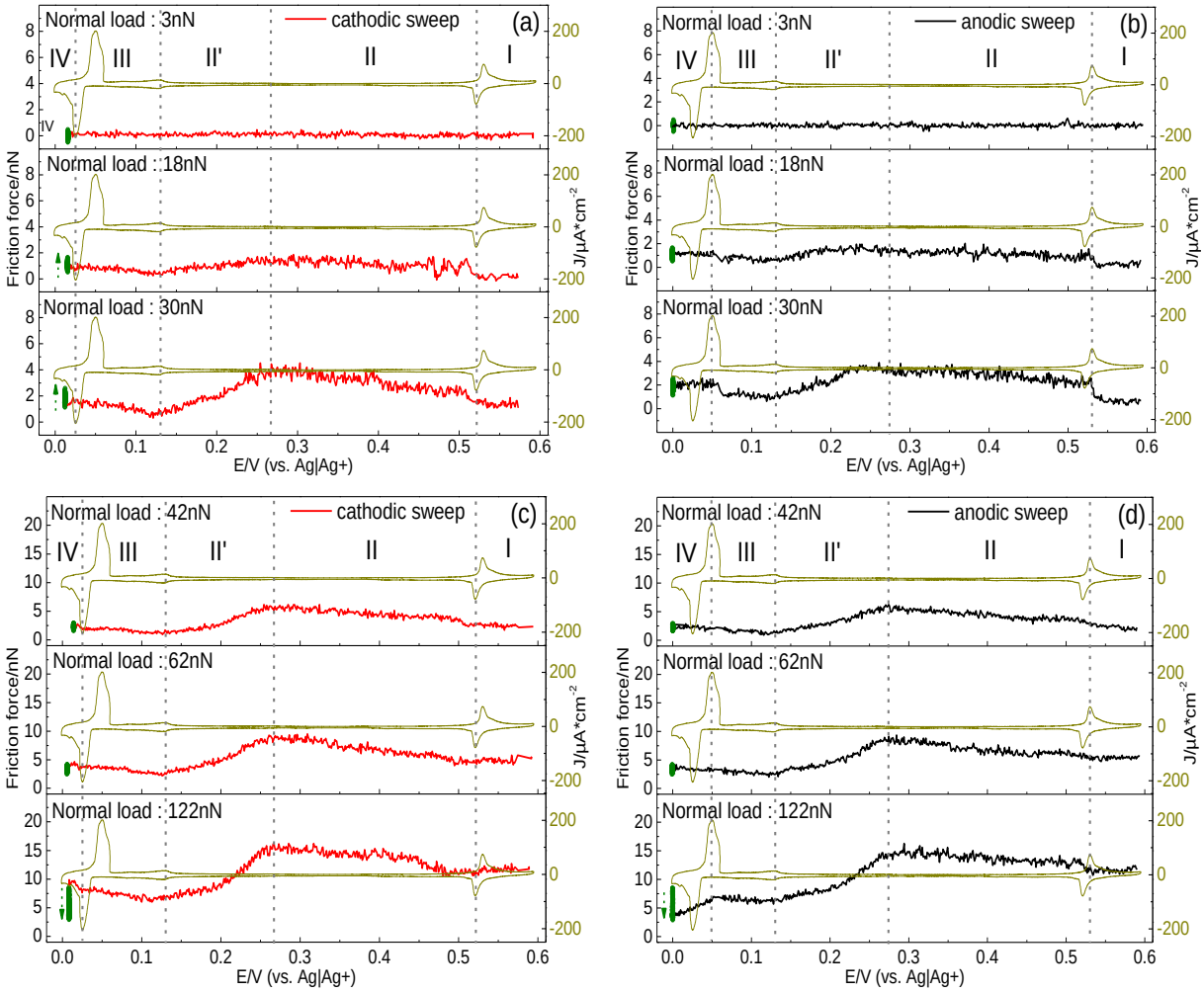

Figure 3.4 Friction force on potential at fixed normal loads during (a) and (c) cathodic sweep and (b) and (d) anodic sweep. PPP-FM was used (k_N = 0.95±0.05 N/m). The scan rate and size of AFM images were 0.47nm/s and 20X20nm², respectively.

Slightly negative of the 1st Ag UPD peak, the deposition of silver causes a sudden increase in friction. Moreover, friction continuously increases with decreasing potential in region II. In this region, Kolb et al. observed three different structures by STM (a $(\sqrt{3} \times \sqrt{3})R30°$, compressed $(\sqrt{3} \times \sqrt{3})R30°$, and, predominantly, a $p(3 \times 3)$ structure) in region II [3], whereas Itaya [1, 2] mainly found the $(\sqrt{3} \times \sqrt{3})R30°$ structure and Gewirth [4, 5], by AFM, only the $p(3 \times 3)$ structure. Since we observed the $(\sqrt{3} \times \sqrt{3})R30°$ structure at 0.33 V, 0.09V, and 0.0 V, we

speculate that sulfate constantly forms this structure after the 1st Ag UPD peak, at least in some domains, independent of the overall coverage of silver. The deposition of Ag induces a higher coverage by sulfates due to the change of the pzc, thus partially compensating the charge density of the 1st Ag UPD. The transition of sulfate structures from the $(\sqrt{3} \times \sqrt{7})R19.1°$ to the $(\sqrt{3} \times \sqrt{3})R30°$ structure leads to a change in coverage of $\Delta\theta_{sulfate}$ = 0.2 – 0.33, corresponding to a change of charge density of anions during the 1st Ag UPD of 29 µC/cm² in good agreement with our experimental value of about 24 µC/cm². Thus, depending on imaging conditions, either this sulfate structure is observed or that of the underlying Ag adlattice with a possible $p(3 \times 3)$ structure. A corresponding structure model for the $(\sqrt{3} \times \sqrt{3})R30°$ structure of sulfate layer on the $p(3 \times 3)$ structure of silver layer is shown in Fig S3. We explain the continuously increasing Ag coverage over the large potential range II and the obvious instability of the structures by the simultaneous change of the pzc with increasing Ag coverage, which is shifting in negative direction; on a rational potential scale (referenced with respect to the pzc), the potential is becoming more positive with increasing Ag coverage. The increase of friction in region II suggests that the adsorbate layers (sulfate and Ag) are highly mobile on the surface. We observed such an increasing high friction on Au(111) in pure sulfuric acid, when with increasing potential the sulfate coverage increases, as long as the adlattice is disordered below the potential of the well-known spike indicating the phase transition to the ordered $(\sqrt{3} \times \sqrt{7})$ structure [12]. Similarly, in 0.4 mM $CuSO_4$/0.05 M H_2SO_4, friction decreases when sulfate is desorbed upon a potential sweep in negative direction reaching a minimum before Cu sets in [13]. Such a dependence of friction on coverage by a mobile phase is also in agreement with the MD simulation of Ouyang et al. [25]. This continuous increase of friction is different from the case of Cu UPD, where friction is independent of potential when the copper forms the immobile honeycomb structure as shown in Figure S3.4 [34].

The sudden increase of friction is delayed at higher normal load of 62 nN and even more 122 nN. This may be due to the AFM tip penetrating the incomplete Ag-submonolayer at high normal loads and thus pushing away the silver ions near the tip, which locally leads to the negative shift of the potential for the adsorption of silver ions [12].

At 0.27 V friction starts to decrease. This is the potential where the transition to the (1×1) adlayer starts (region II´) [3], because the (3×3) adlayer with a coverage of 0.45 is completed and therefore silver is no longer mobile. After penetration of the sulfate adlayer it pushes the ions on a fairly smooth Ag layer or slides on the layer. Friction further decreases when the

potential approaches the second Ag UPD peak at about 0.1 V because the completed (1×1) Ag layer is even smoother.

Negative of peak C_2 (region III) friction slightly increases again; this is paralleled by a fairly large current the origin of which is not discussed in previous papers [3]. This charging and friction increase might indicate deposition of further, disordered and fluctuating Ag ad-atoms initializing deposition of the 2nd layer and adsorption of sulfate.

Negative of peak C_3, where a bilayer forms, friction force changes with time (cf. green dots in Fig. 4). The direction of this change shows a dependence on normal load: At low normal load (10 nN < F_N < 40 nN) friction increases with time; when the normal load exceeds 40 nN, this behavior disappears. Astonishingly, at 122 nN, friction decreases with time. Moreover, in anodic sweep, the friction increases when the potential approaches and passes peak A_3. On the contrary, at low normal loads (30 nN), friction drops after passing peak A_3. According to Kolb et al., formation of the 2nd layer in the peak C_3 does not immediately lead to a smooth surface. Rather, a rough, dynamic 2nd layer only slowly transforms into a complete, smooth 2nd Ag layer after waiting several minutes close to 0 V. It is tempting to assume that the time dependent change of friction at this potential is related to this slow deposition process.

Our results presented above showed that sulfate forms the $(\sqrt{3} \times \sqrt{3})R30°$ structure ($\theta_{sulfate} = 0.33$) both on the Ag bilayer and the completed Ag–monolayer, i.e. on both sides of peak C_3/A_3. However, one may presume that sulfate on the bilayer is more strongly bound, since the pzc of the bilayer can be assumed to be nearly identical to that of bulk Ag whereas that of a monolayer might be up to 200 mV more positive[35]. This could lead to a higher friction for the monolayer once the tip is penetrating the sulfate layer. The very high normal load of 122 nN, on the other hand, might locally prevent deposition of the 2nd adlayer, but why this could lead to a reduced friction remains completely unclear at this point.

3.4.4 Friction dependence on normal load

The data of Figure 3.4 are replotted as a function of load in Figure 3.5 (also cf. Figure S3.5). For the friction at 0.016 V, data in the anodic sweep was used because of the time dependence. Interestingly, friction versus load shows at least three different sections or regimes, depending on different extents of penetration. For very low normal loads (F_N < 14 nN), the COF is low for all potentials. We assume that here the tip is sliding above any adsorbate layer. The COF then increases above a critical load, which depends on potential (regime α). We had observed this effect before for the Cu-upd system and also for sulfate on Au(111) and tentatively ascribed it to penetration of the tip into the sulfate adlayer [12, 13], where more and more adsorbate species interact with the tip and have to be pushed away. For higher normal loads, as suggested also by the modelling in [25], the adsorbate is completely squeezed out from the confined region underneath the tip, "and the number of particles in contact with the tip levels off. In this second regime, the main contribution to the frictional energy dissipation comes from the adsorbates pushed by the tip along the surface. This contribution depends weakly on the normal load, leading to a low friction coefficient" [25] (the plateau of regime β). Thereafter, in regime γ friction increases linearly with normal load (Amontons' behavior); this friction force adds to the force necessary for displacement of the adsorbate species of regime β. Since the tip penetrates into the adsorbate layer, we presume that the interaction between adsorbate and substrate is an important factor for the COF and additionally, the interaction between tip and substrate (e.g. hydrogen bond, covalent bond) might have influence on it [36]. This behavior shall now be discussed separately for the different potential regions. At 0.57 V where the sulfate forms the $(\sqrt{3} \times \sqrt{7})R19.1°$ structure, the friction increases with increasing normal loads at low normal loads (15 nN < F_N < 30 nN) and high normal load (38 nN < F_N), indicating regime α and γ, respectively. The COFs for regime α and γ are 0.09 and 0.12, respectively. Before the transition from regime α to regime γ, the friction shows a plateau, regime β. We may infer that in accordance with the modelling of ref [25] with increasing normal loads the tip starts to penetrate into sulfate layer resulting in the increase of friction (regime α). At certain normal load the tip penetrates into sulfate layer and pushes away the adsorbed sulfates (regime β), which does not depend much on load. Considering COFs at high normal load (regime γ), where presumably the tip is in direct contact with the Au substrate, we suggest that the multiple interactions between tip, sulfate, and the surface of Au(111) have an effect on this regime.

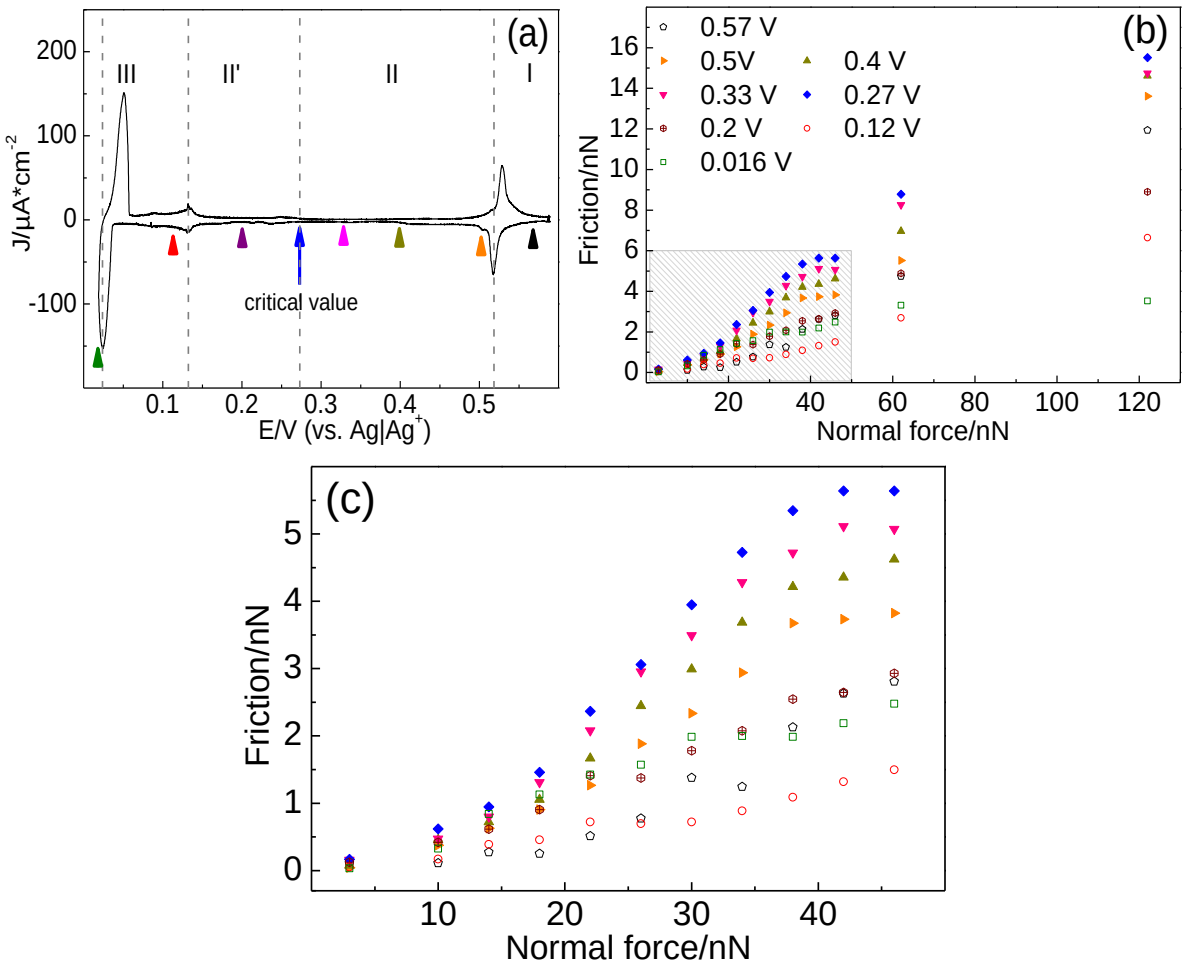

Figure 3.5 (a) CV obtained in AFM-cell and (b) data from Figure 3.4 plotted as function of normal load during Ag UPD. (c) shaded area of (b). Potentials are remarked with same colored arrows in the CV.

At potentials in region II, where the adsorbates (sulfate and Ag) form instable structures, the friction shows a dramatic increase with increasing normal loads in regime α (18 nN < FN < 38 nN). Moreover, the COF increases with decreasing potentials (0.14 (0.5 V), 0.16 (0.4 V), 0.17 (0.33 V), and 0.2 (0.27 V)). It resembles the friction results for Au(111) in 0.1 M H_2SO_4 from Hausen et al. where the COF increases with increasing the coverage of sulfate when the sulfate is disordered (Figure S3.6) [12]. Considering the instable structure of adsorbates including frizzy nature of monoatomic steps on Ag(111) surfaces [37, 38] and the continuously increasing Ag coverage, we envisage two possibilities: Either the tip penetrates only the sulfate adlayer. Continuous displacement and pushing sulfate upon scanning may require more energy on a disordered Ag layer, which strengthens the resistance against the sliding of the tip [28]. Or, the tip penetrates into the sulfate layer as well as the Ag layer. At this point, we cannot really separate

the contribution of sulfate and Ag layers in regime α; considering the atomic stick-slip at 0.27 V (Figure S3.7), the penetration into Ag layer might be dominant influence. The friction increase with decreasing potential is due to the increasing number of Ag atoms which have to be moved or which are hindering the movement of sulfate in front of the tip. In regime β, the friction shows a clear plateau, as discussed above. At high normal loads (regime γ, 46 nN < F_N), the friction increases linearly and the COF is constantly 0.12, resulting from the multiple interactions between tip, adsorbates (sulfate and Ag), and the surface of Au(111).

At 0.2 V (potential region II'), the COFs (0.08) in regime α and γ are lower than all the values in region II, whereas the extensions of regime α and γ are same as for region II. This indicates that beyond a critical value for the Ag coverage (E < 0.27 V), where according to ref.[3] the amount of deposited Ag exceeds the coverage of 0.45 corresponding to the $p(3 \times 3)$ Ag adlayer and where thus the transition to (1×1) adlayer starts, the tip only penetrates into sulfate layer. Therefore, the tip is sliding on a smooth, probably well - ordered $p(3 \times 3)$ Ag adlayer and therefore the COF is reduced.

At 0.12 V (region III), where we assume the formation of a complete Ag monolayer, the COF in regime α (10 nN < F_N < 24 nN) and in regime γ (30 nN < F_N) is further decreased to 0.04 and 0.07, respectively. This may be due to the much smoother Ag(1×1) adlayer, on which the tip is sliding after displacement of sulfate. At 0.016V where a bilayer completes, the COF in regime α (10 nN < F_N < 30 nN) and in regime γ (38 nN < F_N) are 0.07 and 0.02, respectively. Considering the ordered structure of sulfate ($(\sqrt{3} \times \sqrt{3})R30°$), the slight increase of COF in regime α is reasonable as discussed above, whereas an explanation of the independence of friction from normal load in regime γ might indicate the penetration of the tip into the 2nd (top) Ag-adlayer (as discussed before for sulfate). However this as well as the observed time dependence in this potential region needs further consideration. In a similar way we can interpret the results of ref. [12] (together with Figure S3.6): the higher the sulfate coverage, the larger the normal load for penetration of the tip has to be. Upon ordering, this necessary load is further increased, and therefore ordering leads to increased friction for high normal loads as opposed to low normal loads, for which ordering seems to lead to an easier sliding of the tip above the sulfate.

We should add that at the high normal loads used in regime γ one might expect the occurrence of wear. We did not find any indication for that. We had observed previously that for the Au(111)/Cu UPD system local alloy formation induced by wear was only observed when a Pt

covered tip was used and the normal load was 1 μN [39] or, for several UPD systems, when scanning with an STM tip under conditions where a quantum nano-contact is formed [40-42]. But it is also clear that if the tip penetrates the Ag adlayer this is already the first stage of wear; tip induced displacement or local dissolution of Ag, however, does not lead to a structural change, this kind of wear is self-healing.

3.5 Conclusion

Friction force images show clearly resolved structures for sulfate adsorbed on a densely packed Au(111) substrate positive of Ag UPD $\left(\sqrt{3}\times\sqrt{7}R19.1°\right)$ ($\theta_{sulfate}=0.2$), and also on the complete monolayer or complete bilayer of Ag on Au(111) ($\sqrt{3}\times\sqrt{3}R30°$) ($\theta_{sulfate}=0.33$). However, in the whole potential range where the Ag monolayer is not completed a clear structure could not reproducibly observed, despite of the observed atomic stick-slip. This is certainly due to the high mobility of Ag in such an open structure and also the interaction with the tip. The dependence of friction on potential reflects the complexity of this UPD system. Friction increases with coverage of Ag until the coverage arrives at a critical value (0.27V) and then decreases again when due to more Ag deposition the formation of the monolayer is initiated and probably the mobility of Ag atoms on the surface is reduced. The friction forces plotted as function of load demonstrate once again a non-monotonic dependence of the friction force on the coverage of adsorbates (sulfate and Ag). In general, the behavior of friction on normal load can be divided into three regimes; in the process of penetration into adsorbate layer (regime α), after the penetration (regime β), and interaction with metal substrates (Au and Ag) (regime γ). The coverage and stability of adsorbates are determining factors for the COF in regime α. In general, the higher the coverage, the larger the normal load necessary for complete penetration of the tip seems to be. In regime β, the tip pushes away a load independent (but potential dependent) number of adsorbed species; it would be interesting to elucidate the dependence of this behavior on surface mobility of an adsorbate in further studies. Thus, the change of friction on normal load is negligible in this regime. At high normal load (regime γ), additional interaction between tip and substrate results in linear increase of friction on normal load.

Atomic-scale friction force measurements under electrochemical condition thus provide a way to understand the interaction between the surface and a single asperity. Further work would be necessary to elucidate and separate the effects of surface charge and double layer, which are screened in the present work by the strong adsorption (including their partial discharge) of silver and sulfate.

Acknowledgment

The authors gratefully acknowledge the DFG (Deutsche Forschungsgemeinschaft) for funding this work (BA1008/21-1).

3.6 Supporting information

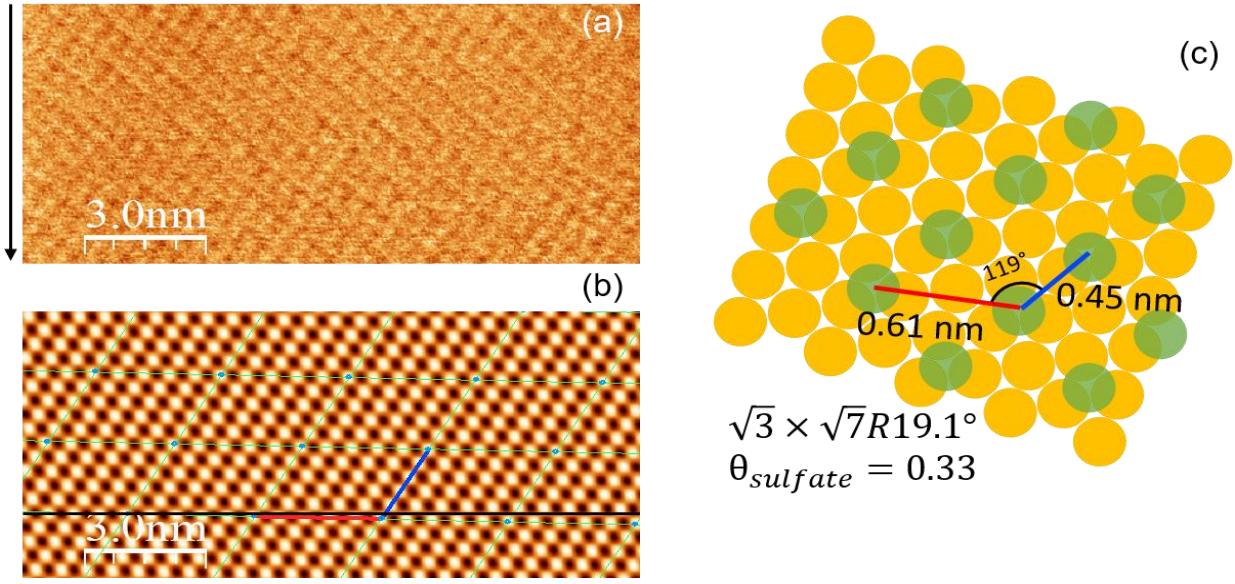

Figure S3.1 (a) Lateral force maps at 0.57V (vs. Ag/Ag+) during downward scan. Black arrow indicates scan direction. (b) is the lattice image after FFT filtering of (a). (c) is the illustration of the real lattice with lattice parameters after the correction of thermal drift. PPP-FM was used (k_N = 0.95±0.05 N/m). The scan rate and size of (a) is 0.47 nm/s and 20X20 nm². Applied normal load is 14 nN.

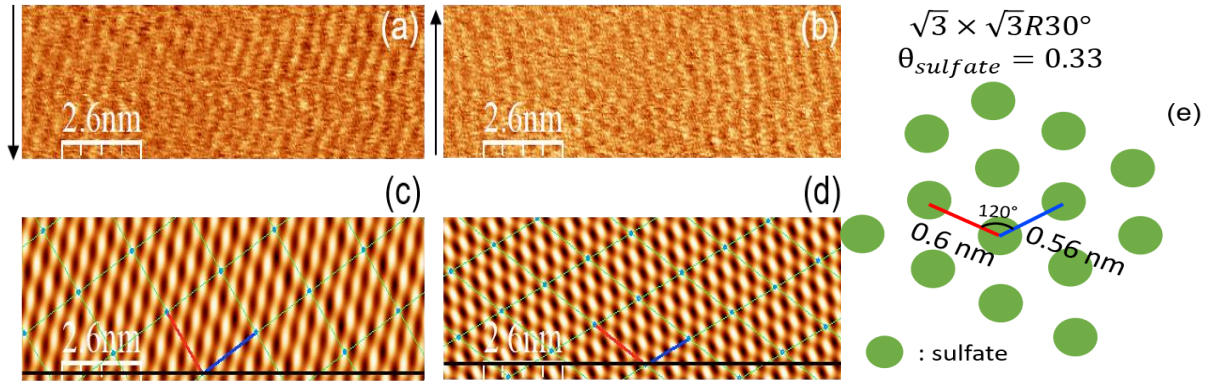

Figure S3.2 Lateral force maps at 0.33V (vs. Ag/Ag+) in cathodic sweep during (a) downward scan and (b) upward scan. Black arrow indicates scan direction. (c) and (d) are the lattice images after FFT filtering of (a) and (b), respectively. (e) is the illustration of the real lattice with lattice parameters after the correction of thermal drift. PPP-FM was used (k_N = 0.95±0.05 N/m). Applied normal load is 16 nN

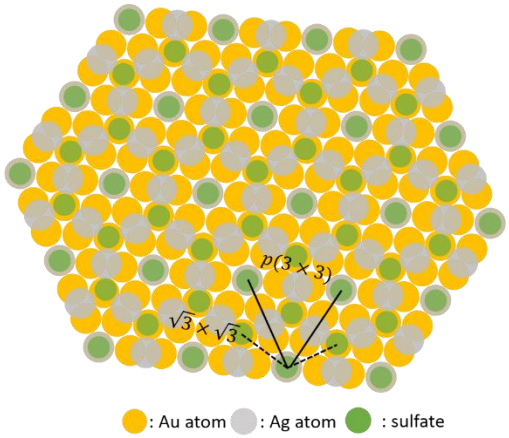

Figure S3.3 Schematic representation of the $p(3 \times 3)$ structure for the silver and the $(\sqrt{3} \times \sqrt{3})R30°$ structure for the sulfate.

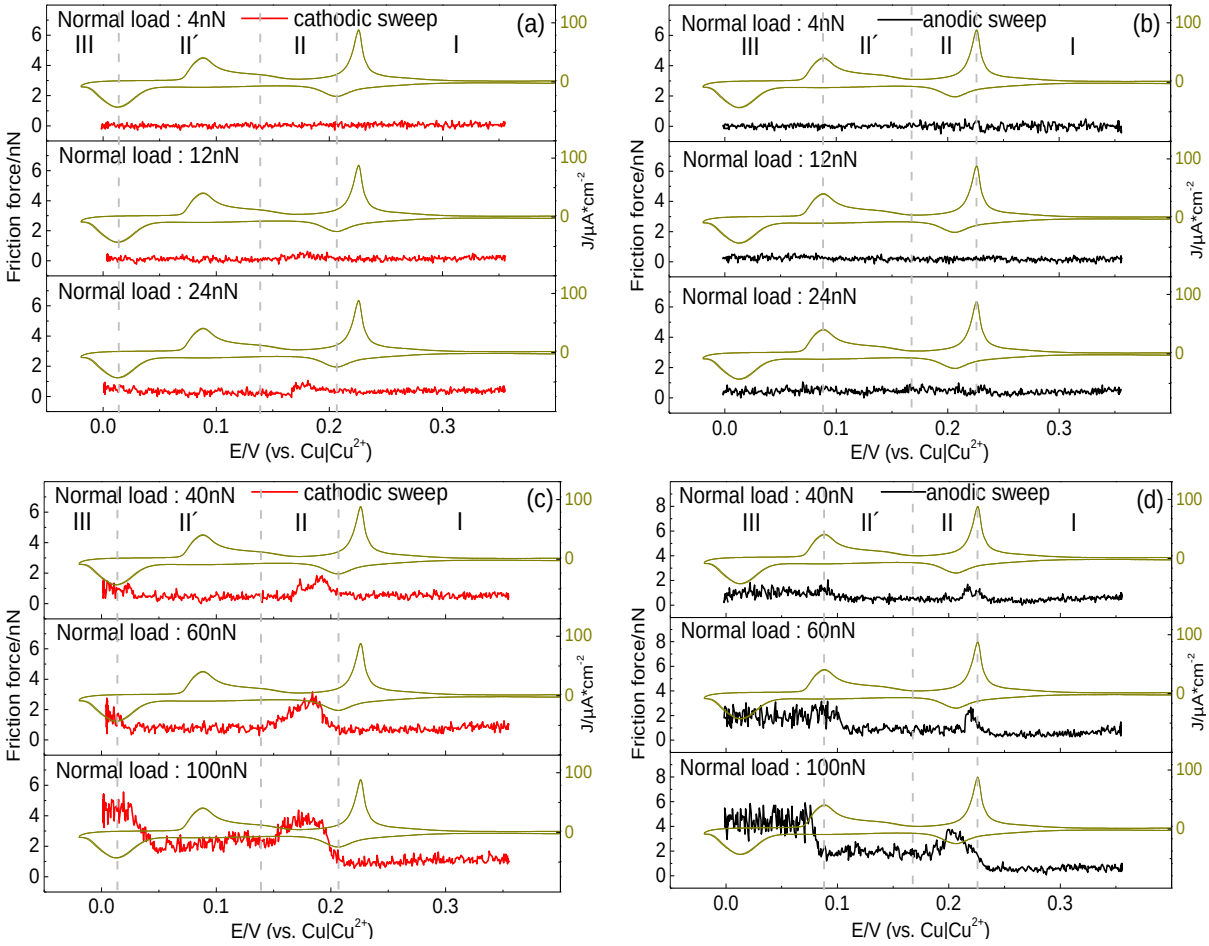

Figure S3.4 Friction forces on potential during Cu UPD on Au(111) in (a) and (c) cathodic sweep and (b) and (d) anodic sweep. PPP-FM was used (k_N = 0.95±0.05 N/m). The scan rate and size of AFM images were 0.47nm/s and 20X20nm², respectively.

Figure S3.4 shows the friction results on potential in Cu^{2+} containing electrolyte. These data reproduce the data of ref. [13], but are more detailed. In region I, with decreasing the potential (cathodic sweep) disordered sulfate is desorbed, which resulting in the decrease of friction. It is in good agreement that the pure Au(111) (E = 0.22 V) shows the lowest friction [13]. Further decrease of potential causes the deposition of Cu on Au(111), which leads to the increase of friction (region II). Thus, the friction increases dramatically due to the increasing the coverage of Cu. Whenever the copper forms honeycomb structure ($\left(\sqrt{3}\times\sqrt{3}\right)R30°$ and $\theta_{Cu} = 2/3$), friction is independent of potential (region II´).

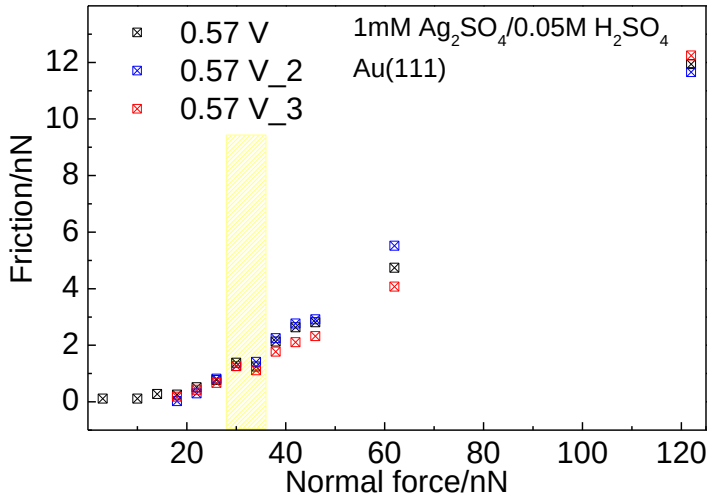

Figure S 3.5 Data as in Figure 3.5, plotted as function of normal load at 0.57 V. Three different areas in lateral map were chosen to make clear the behavior of plateau (shaded area) indicating the regime β.

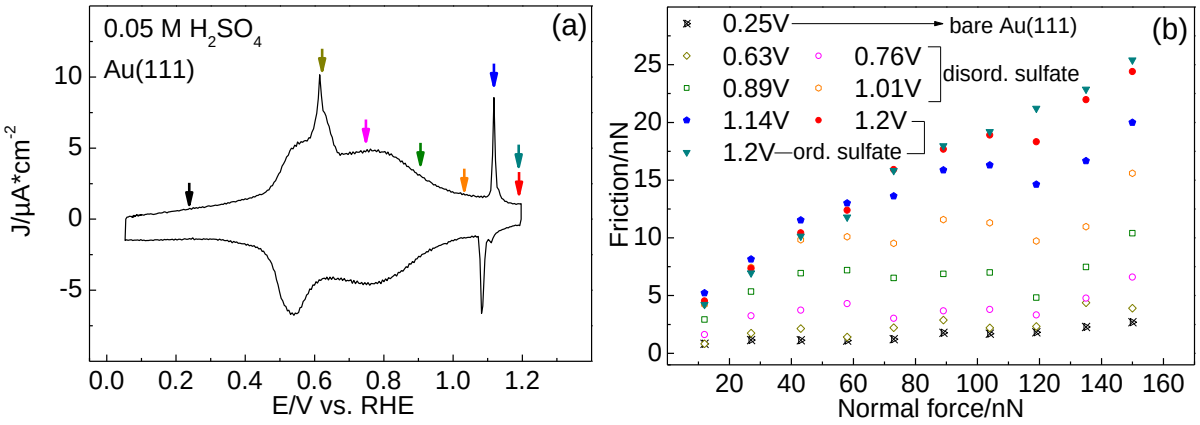

Figure S 3.6 Paper from Hausen et al. [12] CV obtained on Au(111) in 0.05 M H_2SO_4. (b) Friction as function of potential was replotted as function of normal load. The potential stopped at 1.20; therefore, data at 1.20 V represent changes with time.

Figure S3.6 shows the results replotted as function of normal load from the data in the paper from Hausen et al [12]. At 0.63 V where sulfate is adsorbed on Au(111) and lifting the reconstruction of Au(111), the friction on normal load still behaves similarly as observed on bare Au(111) (0.25 V). At 0.76 V, at low normal load (F_N < 60 nN), with increasing normal load friction increases slightly. It indicates that in regime α (F_N < 60 nN) friction is due to the penetration into adsorbed sulfate layer. The COF in regime α is 0.06. At high normal load (120 nN < F_N) friction increases again with increasing normal load. It indicates regime γ where the interaction with gold surface is dominating. Between regime α and γ, the friction shows plateau and it indicates regime β. When the potential approaches to 0.89 V, the COF in regime α increases to 0.12. It indicates that the COF in regime α is closely related with the coverage of sulfate if it is disordered. When the sulfate is ordered (1.20 V), the range of regime β seems to be reduced meaning that the dependence of friction on normal load is rather linear.

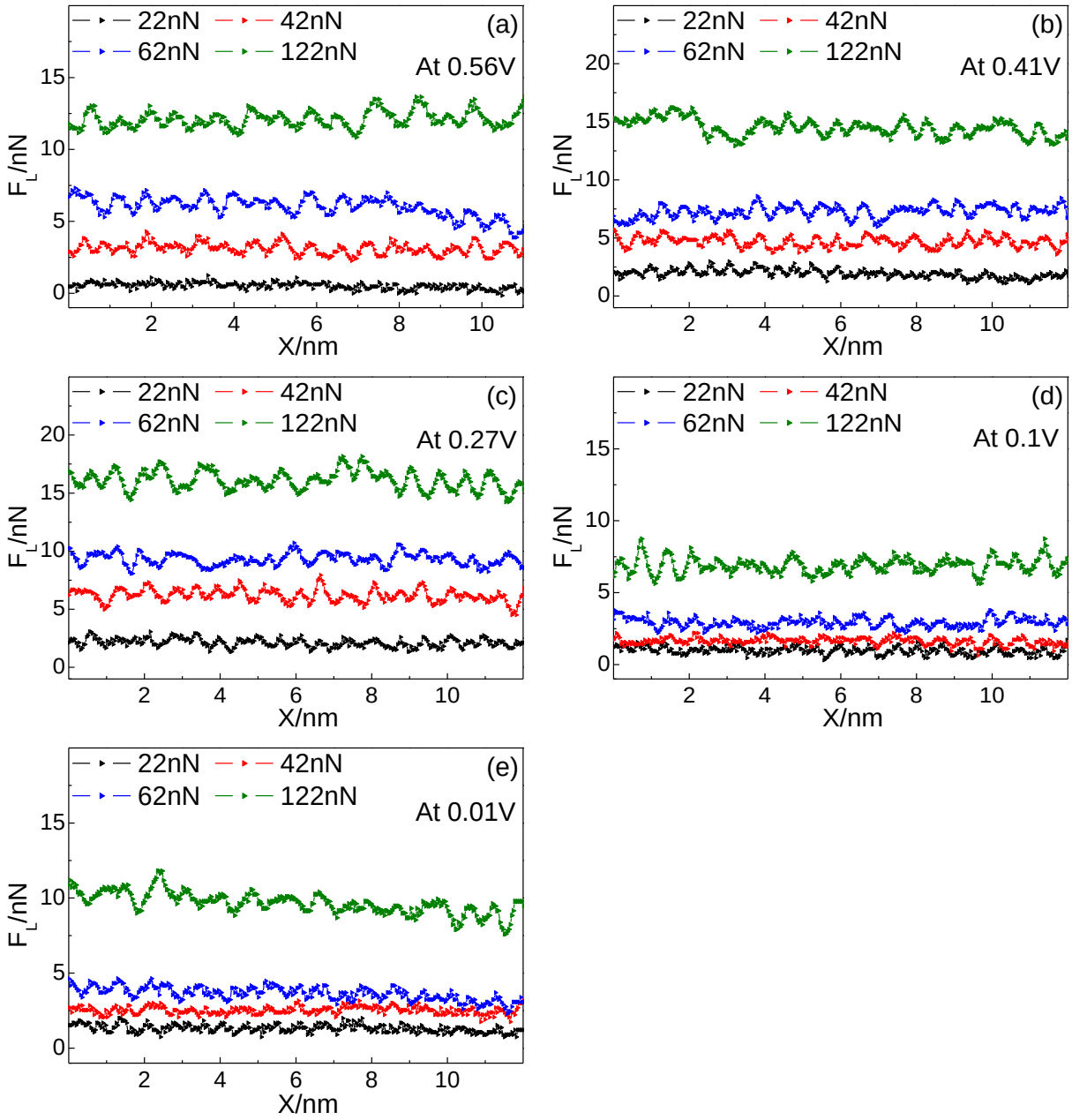

Figure S 3.7 Atomic stick-slip during Ag UPD at (a) 0.56 V, (b) 0.41V, (c) 0.27V, (d) 0.1V, and (d) 0.01V on Au(111) at normal load 22, 42, 62, and 122nN. PPP-FM (k_N = 0.95±0.05 N/m) was used.

Figure S3.7 shows the atomic stick-slip depending on potential. At 0.56 V where the adsorbed sulfate forms the $(\sqrt{3} \times \sqrt{7})R19.1°$ structure, no clear atomic stick-slip is observed at 22nN but at the normal load above 40nN, identical atomic stick-slips are obtained. The distance between sticks is about 0.7 nm. We assume that the adsorbed sulfate forms instable structure at 0.41 V and 0.27 V (potential region II), which might cause the atomic stick-slip at lower normal

load. The distance between sticks is about 0.7 nm. The atomic stick-slip at 0.1 V and 0.01 V look similar and it might result from the same coverage of Ag ($\theta_{Ag} = 1$).

Reference

[1] T. Hachiya, K. Itaya *Ultramicroscopy*. **1992**, *42*, 445-452.

[2] K. Ogaki, K. Itaya *Electrochimica acta*. **1995**, *40*, 1249-1257.

[3] M. Espladiu, M. Schneeweiss, D. Kolb *Physical Chemistry Chemical Physics*. **1999**, *1*, 4847-4854.

[4] C. H. Chen, S. M. Vesecky, A. A. Gewirth *Journal of the American Chemical Society*. **1992**, *114*, 451-458.

[5] P. Mrozek, Y.-e. Sung, M. Han, M. Gamboa-Aldeco, A. Wieckowski, C.-h. Chen, A. A. Gewirth *Electrochimica acta*. **1995**, *40*, 17-28.

[6] T. Kondo, J. Morita, M. Okamura, T. Saito, K. Uosaki *Journal of Electroanalytical Chemistry*. **2002**, *532*, 201-205.

[7] N. Sisson, Y. GruÌˆnder, C. A. Lucas *The Journal of Physical Chemistry C*. **2016**, *120*, 16100-16109.

[8] M. Azhagurajan, T. Itoh, K. Itaya *The Journal of Physical Chemistry C*. **2016**, *120*, 16221-16227.

[9] V. Rooryck, F. Reniers, C. Buess-Herman, G. A. Attard, X. Yang *Journal of electroanalytical chemistry*. **2000**, *482*, 93-101.

[10] H. I. Kim, T. Koini, T. R. Lee, S. S. Perry *Langmuir*. **1997**, *13*, 7192-7196.

[11] M. Nielinger, H. Baltruschat *Physical Chemistry Chemical Physics*. **2007**, *9*, 3965-3969.

[12] F. Hausen, M. Nielinger, S. Ernst, H. Baltruschat *Electrochimica Acta*. **2008**, *53*, 6058-6063.

[13] N. Podgaynyy, S. Wezisla, C. Molls, H. Baltruschat *BEILSTEIN JOURNAL OF NANOTECHNOLOGY*. **2015**, *6*, 820-830.

[14] S. Iqbal, S. Wezisla, N. Podgaynyy, H. Baltruschat *Electrochimica Acta*. **2015**, *186*, 427-435.

[15] F. Hausen, N. N. Gosvami, R. Bennewitz *Electrochimica acta*. **2011**, *56*, 10694-10700.

[16] A. Elbourne, J. Sweeney, G. B. Webber, E. J. Wanless, G. G. Warr, M. W. Rutland, R. Atkin *Chem. Commun.* **2013**, *49*, 6797-6799.

[17] H. Li, M. W. Rutland, R. Atkin *Physical Chemistry Chemical Physics*. **2013**, *15*, 14616-14623.

[18] H. Li, M. W. Rutland, M. Watanabe, R. Atkin *Faraday discussions*. **2017**, *199*, 311-322.

[19] N. N. Gosvami, P. Egberts, R. Bennewitz *The Journal of Physical Chemistry A*. **2011**, *115*, 6942-6947.

[20] L. Pashazanusi, M. Oguntoye, S. Oak, J. N. L. Albert, L. R. Pratt, N. S. Pesika *Langmuir*. **2018**, *34*, 801-806.

[21] A. J. Barthel, A. Al-Azizi, N. D. Surdyka, S. H. Kim *Langmuir*. **2014**, *30*, 2977-2992.

[22] O. Y. Fajardo, F. Bresme, A. A. Kornyshev, M. Urbakh *Scientific Reports*. **2015**, *5*, 6.

[23] G. He, M. H. Müser, M. O. Robbins *Science*. **1999**, *284*, 1650-1652.

[24] M. H. Müser, M. O. Robbins *Phys. Rev. B*. **2000**, *61*, 2335.

[25] W. Ouyang, A. S. de Wijn, M. Urbakh *Nanoscale*. **2018**, *10*, 6375-6381.

[26] A. Labuda, W. Paul, B. Pietrobon, R. B. Lennox, P. H. Grutter, R. Bennewitz *Review of Scientific Instruments*. **2010**, *81*, 083701.

[27] N. Podgaynyy, S. Iqbal, H. Baltruschat *Surface Science*. **2015**, *631*, 67-72.

[28] A. Labuda, F. Hausen, N. N. Gosvami, P. H. Grütter, R. B. Lennox, R. Bennewitz *Langmuir*. **2011**, *27*, 2561-2566.

[29] J. E. Sader, J. W. M. Chon, P. Mulvaney *Rev. Sci. Instrum.* **1999**, *70*, 3967-3969.

[30] R. Espinosa-Marzal, A. Arcifa, A. Rossi, N. Spencer *The journal of physical chemistry letters*. **2014**, *5*, 179-184.

[31] S. Sundararajan, B. Bhushan *J. Appl. Phys.* **2000**, *88*, 4825-4831.

[32] H. Uchida, M. Miura, M. Watanabe *J. Electroanal. Chem.* **1995**, *386*, 261-265.

[33] S. Iqbal, L. Zan, E. Nardi, H. Baltruschat *Phys. Chem. Chem. Phys.* **2018**, *20*, 6176-6186.

[34] J. G. Gordon, O. R. Melroy, M. F. Toney *Electrochimica Acta*. **1995**, *40*, 3-8.

[35] T. Langkau, H. Baltruschat *Electrochimica Acta*. **2002**, *47*, 1595 - 1599.

[36] W. Ouyang, S. N. Ramakrishna, A. Rossi, M. Urbakh, N. D. Spencer, A. Arcifa *Physical Review Letters*. **2019**, *123*, 116102.

[37] M. Poensgen, J. Wolf, J. Frohn, M. Giesen, H. Ibach *Surface Science*. **1992**, *274*, 430-440.

[38] H. W. Cheng, P. Stock, B. Moeremans, T. Baimpos, X. Banquy, F. U. Renner, M. Valtiner *Advanced Materials Interfaces*. **2015**, *2*, 1500159.

[39] M. Nielinger, F. Hausen, N. Podghainiy, H. Baltruschat in *Nanotribology at electrodes: Influence of adsorbates and potential on friction forces studied with atomic force microscopy, Vol.* (Eds.: A. Fischer, K. Bobzin), Wiley-VCH, Weinheim, **2009**, pp.178-184.

[40] P. Berenz, PhD, Rheinische Friedrich-Wilhelms-Universität Bonn, **2002**.

[41] P. Berenz, X. Xiao, H. Baltruschat *Journal of Physical Chemistry B*. **2002**, *106*, 3673-3680.

[42] M. Nielinger, P. Berenz, X. Y. Xiao, H. Baltruschat *Surf. Sci.* **2005**, *597*, 1-10.

CHAPTER 4

Silver underpotential deposition (UPD) on I-modified Au(111) in aqueous electrolyte

4.1 Abstract

The underpotential deposition (UPD) of Ag on an I-modified Au(111) surface has been examined in perchloric acid solution by electrochemical lateral force microscopy (LFM). The observed structural transitions demonstrate that the structure of iodine is very sensitive to the coverage of silver and the AFM tip penetrates the adlayers as normal load increases. At potentials positive of the 1st Ag UPD peak, the iodine forms a $(\sqrt{3} \times \sqrt{3})R30°$ structure ($\theta_I = 0.33$) on Au(111). As the potential passes the 1st Ag UPD peak, the iodine forms a $p(3 \times 3)$ structure ($\theta_I = 0.44$) and silver also forms a $p(3 \times 3)$ structure ($\theta_I = 0.44$). At potentials slightly negative of the 2nd Ag UPD peak, even though the iodine structure is maintained as a $p(3 \times 3)$ structure ($\theta_I = 0.44$), the atomic corrugations observed at high normal load indicate that silver completes a monolayer. The large-scale images clearly show that a Ag bilayer is formed at the 3rd Ag UPD peak. When the Ag bilayer completes, the iodine forms a $(\sqrt{3} \times \sqrt{3})R30°$ structure ($\theta_I = 0.33$). The frictional transition is observed with increasing normal load. At potentials positive of the 1st Ag UPD, even though atomic corrugations clearly demonstrate that the tip penetrates into the iodine adlayer, no corresponding frictional increase is observed. In contrast, at potentials negative of 1st Ag UPD peak, friction increases steeply with normal load when the tip starts to penetrate the iodine adlayer. Furthermore, at 0.33 V, a further increase of friction with increasing normal load is observed, resulting from the penetration into the Ag adlayer where the Ag coverage is sub-monolayer.

4.2 Introduction

Friction at electrode surfaces has long been a topic [1]. The invention of the AFM made it possible to also study friction on the atomic scale [2, 3]. Friction with atomic resolution is ideally explored by lateral force microscopy (LFM), which reveals the tribological behavior corresponding to the real contact area [4, 5]. In LFM experiments under electrochemical condition, it is possible to monitor the interfacial interactions occurring between tip and the surface for which the surface chemistry (e.g. adsorption, adhesion, and oxidation) plays a crucial role [6-13]. Hausen et al. reported that the AFM tip might penetrate into the sulfate adlayer and the required force for the penetration is closely related to the coverage of sulfate [11]. Ouyang et al. suggested the multiple dissipative mechanisms obtained using molecular dynamics (MD) simulations, which directly predicts that a non-monotonic dependence of the friction force is strongly related with the surface coverage of adsorbate showing the possible penetration of the AFM tip into the adlayer [14]. Recently, Park et al. reported that the coverage of Ag on Au(111) during the Ag UPD is a decisive factor for the penetration of the AFM tip into adlayers, which has a great influence on the friction behavior (see chapter 3) [13]. In an aprotic electrolyte (chapter 6), a structure change in the LFM image indicated penetration of the tip into the adsorbed iodine layer upon increasing normal load, but no change of the friction coefficient was found; this was ascribed to the high mobility of the otherwise strongly adsorbed iodine atoms. LFM may therefore also help in understanding the interaction of ions and surface beyond the models suggested by MD simulations.

The underpotential deposition (UPD) of silver occurring at potentials more positive than the Nernst equilibrium potential has often been studied on gold in aqueous electrolytes. It is a model system for UPD studies since the lattice constants of silver and gold are nearly identical ($a_{Ag} = 4.08$ Å, $a_{Au} = 4.07$ Å) [15-22]. The previous works show that the UPD process is very sensitive to the presence of adsorbed anions (e.g. SO_4^{2-} , ClO_4^-). Itaya et al. reported the transition of iodine structures during the Ag UPD on I-modified Au(111) using scanning tunneling microscopy [23]. Their CVs show that the Ag UPD occurs in three different steps on I-modified Au(111), which resembles the results on Au(111) in sulfuric acid. However, they found that a large amount of charge (ca. 65μC/cm²) is consumed prior to the 1st Ag UPD peak, which might suggest that the mechanism of Ag UPD on I-modified Au(111) is different due to the interaction between iodine and silver ions. Regarding the atomic structures, pre-adsorbed iodine forms a $(5 \times \sqrt{3})$

structure ($\theta_I = 0.4$) on Au(111) and it changes to a $p(3 \times 3)$ structure ($\theta_I = 0.44$), where the potential passes the 1st Ag UPD peak. The $p(3 \times 3)$ structure even remains at potentials negative of the 2nd Ag UPD peak. When the potential approaches to the 3rd Ag UPD peak, the iodine structure changes to a $(\sqrt{3} \times \sqrt{3}R30°)$ structure.

In this chapter, we present a study of atomic-scale friction on I-modified Au(111) during Ag UPD. By introducing the stable iodine adlayer, it was our aim to understand the influence of adsorbates layers as well as the tip penetration on friction behavior during Ag UPD. Thus, in this chapter, we intend to clarify: 1) the influence of the iodine adlayer on Ag structures, 2) the influence of the hydrophobicity on friction, 3) the required condition for the tip penetration, and 4) the influence of the penetration on friction.

4.3 Experimental

A disc type of Au(111) single crystal (diameter: 10 mm and thickness: 3 mm) purchased from MaTecK GmbH was used as working electrode. It was annealed by flame and cooled down above iodine crystals purged with Ar to get a monolayer of iodine on clean surface [24]. Gold and silver wires were used as counter and reference electrodes, respectively. For electrolytes, 2 mM $AgClO_4$ were dissolved in 0.1 M $HClO_4$.

Lateral (frictional) force measurements were performed using an Agilent 5500 AFM, combined with atmosphere chamber. Silicon tips from NANOSENSORS (PPP-FM, k_N =1.10±0.05 N/m and PPP-CONTSC, k_N = 0.1±0.05 N/m, hereafter called hard and softer cantilevers for PPP-FM and PPP-CONTSC, resp., both with a tip radius < 10 nm) were used. Normal and torsional resonance frequency of AFM tips were measured by AFM (Agilent 5500/AC mode). Q factor for theses resonance frequencies was obtained using the equation of simple harmonic oscillation (SHO). Normal and torsional spring constants were calculated using the Sader method [25, 26] and the lateral spring constant was obtained by dividing torsional spring constant with the square of the tip height. During the measurement, a homemade AFM cell was used, which contains a three-electrode assembly and Ar was purged through the atmosphere chamber.

To get the clear lattice image, we used fast Fourier transform (FFT) filtering and thermal drift was corrected as described in [27]. The model illustrations are the real lattice based on the values after the thermal drift correction.

When the AFM tip scans the surface, friction (F) makes it twist, leading to a deflection of the laser beam. The sign of the deflection depends on the scan direction. In addition, the deflection of the laser in the same direction is caused by topography (T) (e.g. steps on the surface); hence, the sign does not depend on scan direction. Thus, the forward image and backward image contain [T+F] and [T-F], respectively. Friction force data were obtained by subtracting the backward data from the forward data and dividing it by 2 to eliminate such topographic effects [28].

4.4 Results and discussion

4.4.1 Cyclic voltammetry (CV)

Figure 4.1a and b show cyclic voltammetry (CV) for I-modified Au(111) obtained in the H-cell and the AFM-cell containing 2 mM $AgClO_4$/0.1 M $HClO_4$. As reported by K. Itaya et al.[23], we observed three peaks for the Ag UPD on I-modified Au(111), C_1, C_2, and C_3. The charge densities corresponding to the first (C_1), second (C_2), and third (C_3) UPD peaks in H-cell are 96, 32, and 178 µC/cm², respectively. Moreover, about 30 µC/cm² and 22 µC/cm² were consumed prior to the first and third Ag UPD peaks, as already observed in the above paper by Itaya et al., who ascribed it to the adsorption of Ag^+ on the iodine adlayer prior to the Ag deposition on Au(111). The total charge density prior to the onset of the peak C_3 is ≈ 210 µC/cm², closed to the charge required for the deposition of a complete Ag monolayer (220 µC/cm²). This together with the relatively large current between C_2 and C_1 suggests that the Ag monolayer is only completed just before the onset of the deposition of the second Ag adlayer. In the AFM-cell, slightly larger charge densities for the 1st and 2nd Ag UPD peaks were observed. The same result as in perchloric acid is obtained in sulfuric acid for I-modified Au(111), where only the peaks are a little sharper (Figure S4.1).

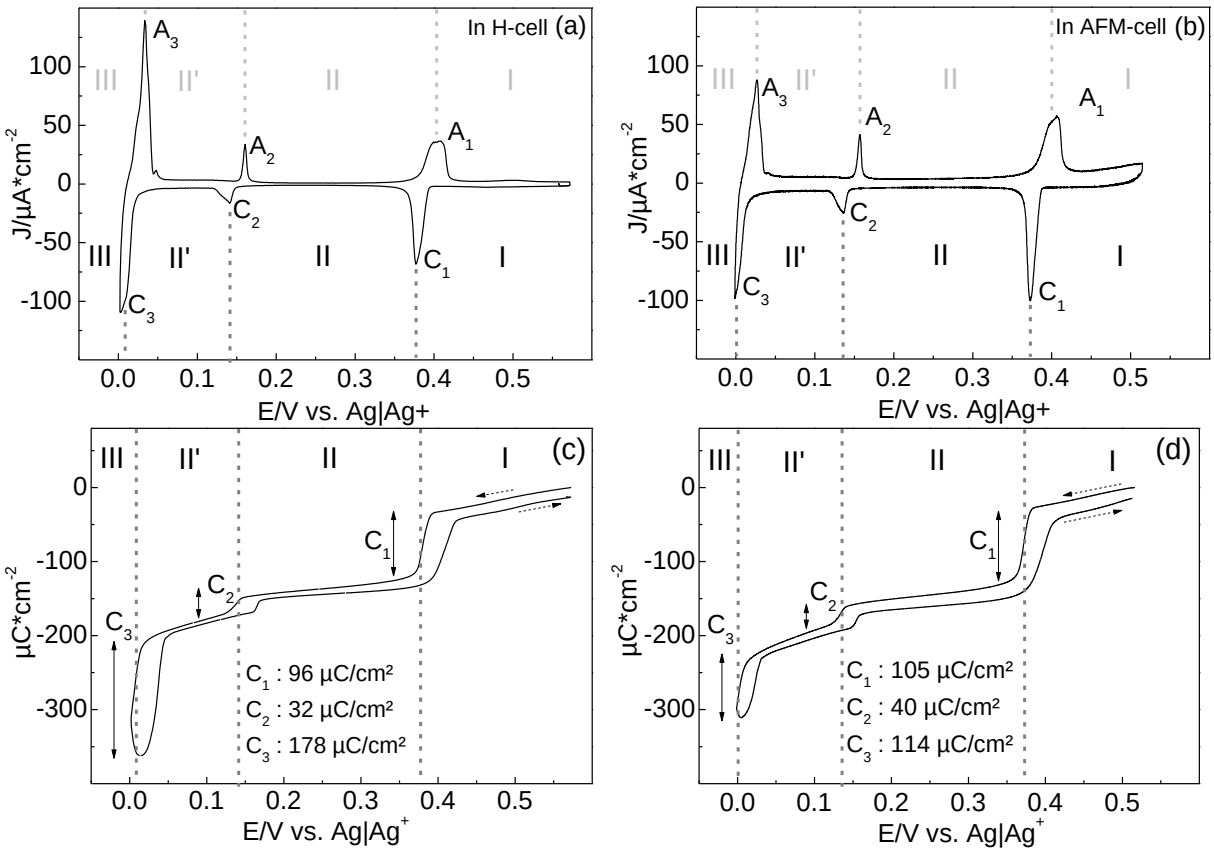

Figure 4.1 Cyclic voltammetry and coulometric curve in (a) and (c) H-cell and (b) and (d) AFM-cell for the I-modified Au(111) in 2mM $AgClO_4$/0.1M $HClO_4$. The sweep rate in H-cell and AFM-cell is 10mV/s and 12.5 mV/s, respectively.

Figure S4.2 and S4.3 show the large scale morphology and lateral force images during cathodic and anodic sweeps, respectively. After the first deposition peak (region II) both the topography and the friction image become somewhat blurred until the onset of peak C_2. This suggests that the Ag adlayer in potential region II is incomplete and probably mobile, in agreement with the charge of the peak C_1 corresponding to less than half a monolayer. More important, at least more eye-catching, is the fact that the commonly observed increase of friction at the steps caused by the Schwoebel-barrier [29-31] is hardly visible in this potential region. Interestingly, they become visible again in peak C_2 when the first monolayer is nearly completed. Close to the peak C_3, the surface appears rougher due to the start of further Ag deposition. As the potential was maintained at 0.0 V, i. e. negative of C_3 (region III), the terraces first appear noisy in the friction image, then partially incomplete terraces appear due to the slow formation of a second Ag layer (Figure S4.3a and c); they appear much smoother. These incomplete terraces disappear with time when the bilayer is completed. Therefore, peak C_3 corresponds to the deposition of a second layer of Ag, resembling the results of the Ag UPD on bare Au(111) in sulfuric acid [13, 22, 32]. Upon dissolution (Figure S4.3b and d), some dark spots indicating very

high friction appear – they might be due to the formation of 2D holes in the layer during dissolution. Opposite to the cathodic sweep, no change is visible in the image during the anodic sweep when the potential passes A_2. The original shape is regained after Ag dissolution in peak A_1.

4.4.2 Atomic corrugation during Ag UPD

The structure of iodine adlayer on Au(111) has been previously studied using STM measurements in UHV [33] and under electrochemical conditions [34, 35]. Based on this literature, in iodide containing solution electrochemically adsorbed iodide forms a $(\sqrt{3} \times \sqrt{3})R30°$ structure ($\theta_I = 0.33$) at potentials slightly positive of the lifting of the Au(111) reconstruction. With increasing potential, the coverage of iodide increases, which introduces the distortion of the $(\sqrt{3} \times \sqrt{3})R30°$ structure. Thus, iodide forms a $(5 \times \sqrt{3})$ structure ($\theta_I = 0.4$). Further increase of potential beyond the small spike makes iodide form again hexagonal array ($\theta_I = 0.45$), but the d_{I-I} is smaller than the $\sqrt{3}$ distance. Different coverages and structures have been reported in literature for iodine on Au(111) in iodide free solutions. Itaya et al. observed a $(5 \times \sqrt{3})$ structure ($\theta_I = 0.4$) after dipping the gold crystal in 1 mM KI electrolyte [23]. Bard et al. observed a $(\sqrt{3} \times \sqrt{3})R30°$ structure when dipping the single crystal Au(111) in 10 mM KI electrolyte [36]. Furthermore, the coverage of iodide on Pt(111) is quite sensitive and varies with the concentration of iodide in the solution and the method (e.g. dipping the crystal in an iodide containing electrolyte or cooling down the crystal in I_2 containing gas stream) [37]. Therefore, the exact initial coverage of iodine on Au(111) seems to strongly depend on details of the adsorption process.

Lateral force maps showing atomic corrugation were used here to study the structure of iodine as function of potential in the presence of Ag. Figure 4.2 shows that the iodine forms a $(\sqrt{3} \times \sqrt{3})R30°$ structure on Au(111) in region I, which indicates that the coverage of iodine is 0.33 under our preparation conditions. The lattice vector is slightly larger than the theoretical value (0.5 nm), which is due to some experimental error.

At 0.25 V, region II, the structure of iodine changes to the $p(3 \times 3)$ structure meaning that the coverage of iodine increases to 0.44 (Figure 4.3) and we assume that the silver adlayer forms the same $p(3 \times 3)$ structure as reported by Itaya et al. [23]. The lateral force image reveals two different height maxima corresponding to different positions of the iodine atoms. Figure S4.4 shows two different ball models for the $p(3 \times 3)$ structure of iodine. In both cases, Ag atoms sit on atop and bridge sites of Au(111). In Figure S4.4a and b, the iodine sits on atop site and 3-fold hollow site of the silver adlayer, respectively. Considering the height difference, even though it is unideal, the ball model in Figure S4.4a for the $p(3 \times 3)$ structure is used in this chapter. Due to the transition of iodine coverages (0.4→0.44) in the STM images, Itaya et al. observed pits where the coverage of iodine is still low and not uniform. However, we didn't observe any pits at potentials in region II, although the coverage change is even larger.

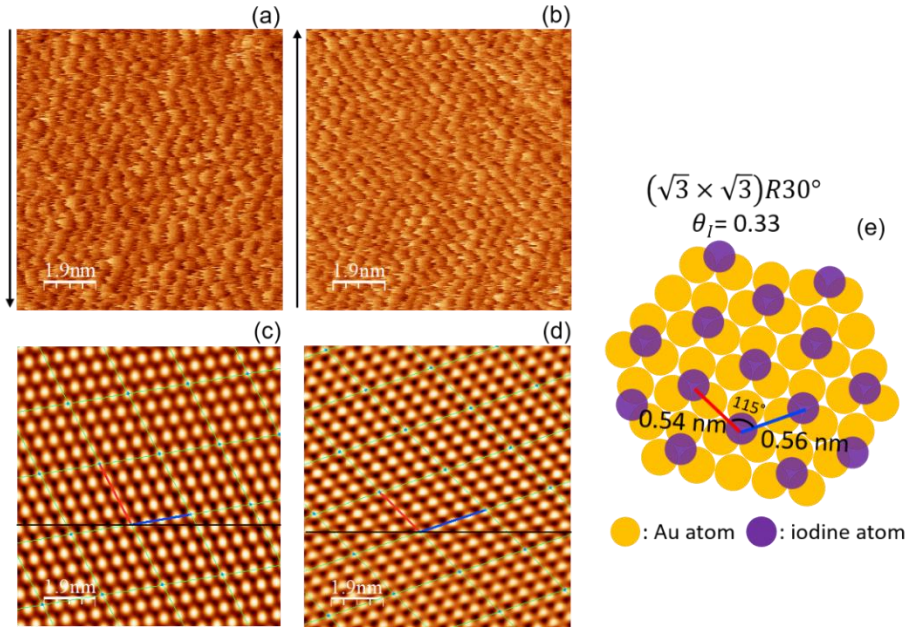

Figure 4.2 Lateral force maps for I-modified Au(111) in 2 mM $AgClO_4$/0.1 M $LiClO_4$ at 0.45 V (vs. Ag/Ag+) in cathodic sweep during (a) downward scan and (b) upward scan. Arrow indicates scan direction. (c) and (d) are the lattice images after the Fast Fourier Transform (FFT) filtering of (a) and (b), respectively. (e) is the illustration of the real lattice with lattice parameters after the correction of thermal drift. Soft cantilever was used and applied normal load is 4 nN.

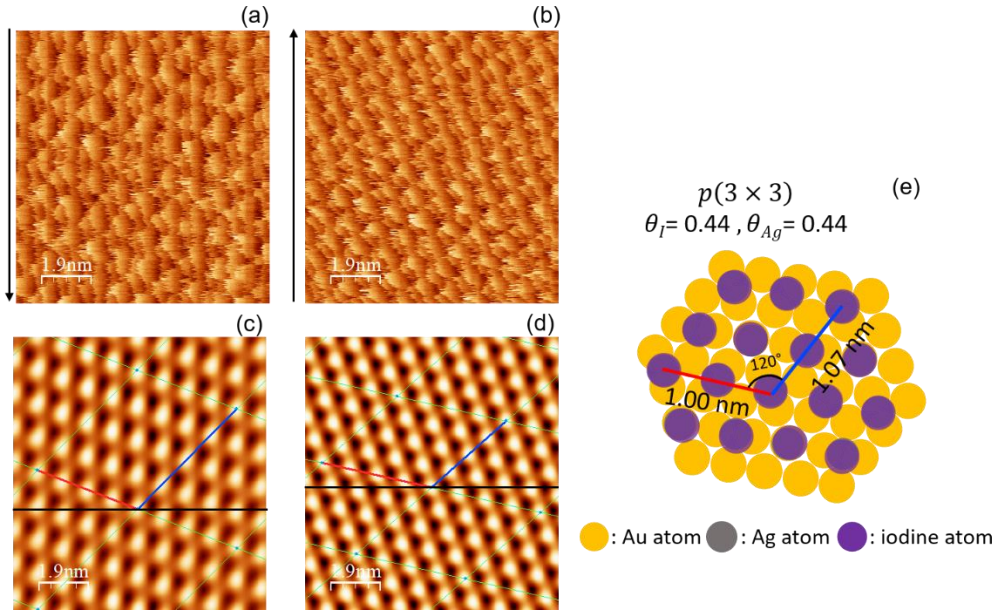

Figure 4.3 Lateral force maps for I-modified Au(111) in 2 mM $AgClO_4$/0.1 M $LiClO_4$ at 0.25 V (vs. Ag/Ag+) in cathodic sweep during (a) downward scan and (b) upward scan. Arrow indicates scan direction. (c) and (d) are the lattice images after the Fast Fourier Transform (FFT) filtering of (a) and (b), respectively. (e) is the illustration of the real lattice with lattice parameters after the correction of thermal drift. Soft cantilever was used and applied normal load is 4 nN.

As the potential passes the 2nd Ag UPD peak, C_2, a different $p(3 \times 3)$ structure for the iodine is observed (Figure S4.5 and S4.6). At 0.07 V (region II´), all atoms appear with an identical height, and which had not been observed by Itaya et al. [23] (Figure 4.4). As revealed in Figure S4.5 and S4.6, the lattice vectors do not change at all during this transition. The Ag monolayer certainly completes slightly negative of the second Ag UPD peak, C_2 (region II´), which sitting on the 3-fold hollow site of gold. It is hypothesized that the iodine sits on atop and 2-fold bridge sites of silver but due to the dominant bridge site, the iodine atoms show an identical height. With further decrease of potential to region III (0.003 V), where silver forms a bilayer, the $(\sqrt{3} \times \sqrt{3})R30°$ structure is obtained again (Figure 4.5).

In the anodic sweep (Figure S4.7-9), the transitions of iodine structures correspond to the transitions of structures observed in cathodic sweep.

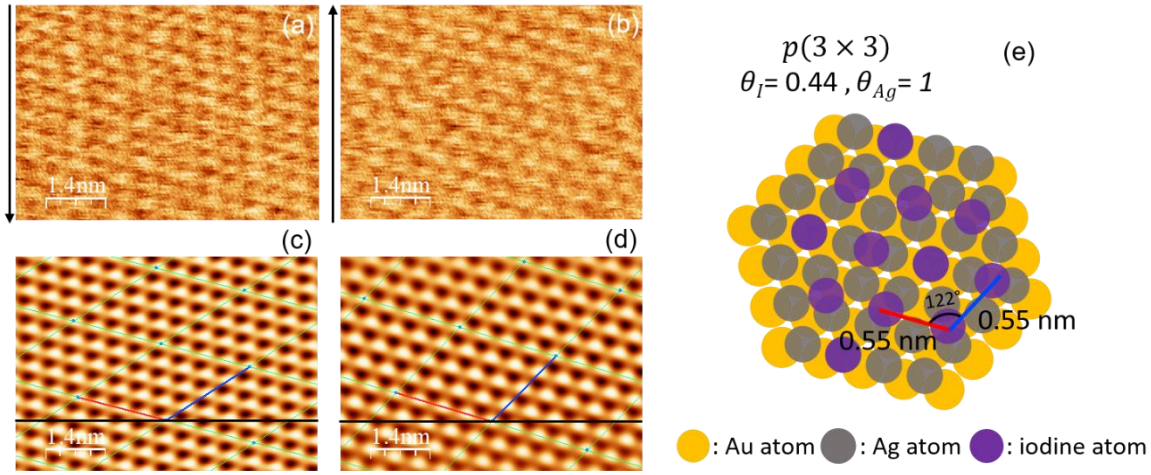

Figure 4.4 Lateral force maps for I-modified Au(111) in 2 mM $AgClO_4$/0.1 M $LiClO_4$ at 0.07 V (vs. Ag/Ag+) in cathodic sweep during (a) downward scan and (b) upward scan. Arrow indicates scan direction. (c) and (d) are the lattice images after the Fast Fourier Transform (FFT) filtering of (a) and (b), respectively. (e) is the illustration of the real lattice with lattice parameters after the correction of thermal drift. Soft cantilever was used and applied normal load is 4 nN.

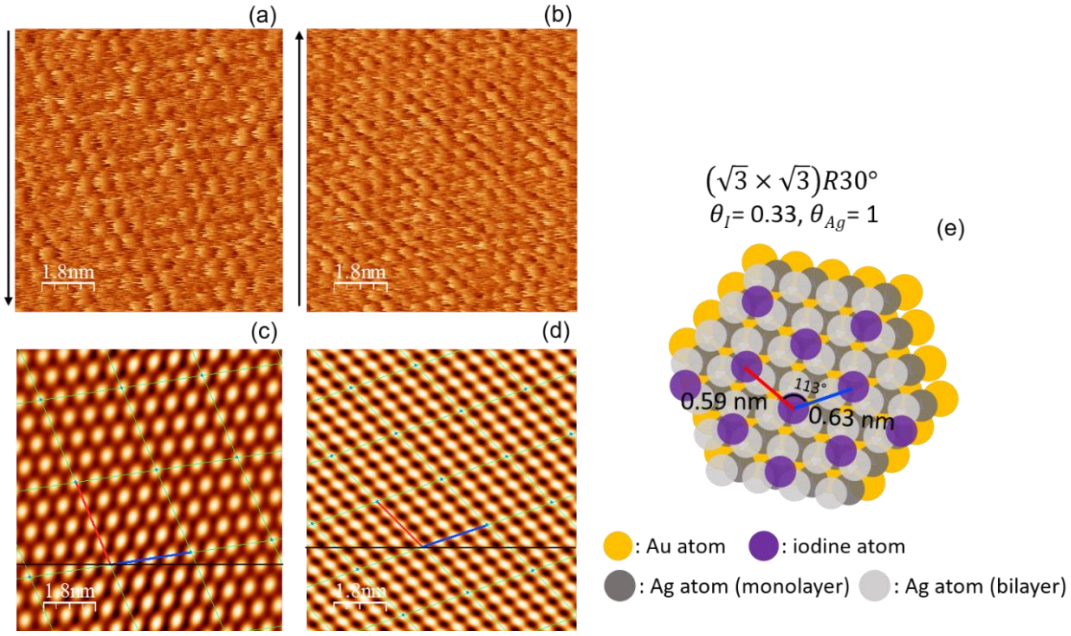

Figure 4.5 Lateral force maps for I-modified Au(111) in 2 mM $AgClO_4$/0.1 M $LiClO_4$ at 0.003V in cathodic sweep (vs. Ag/Ag+) during (a) downward scan and (b) upward scan. Arrow indicates scan direction. (c) and (d) are the lattice images after Fast Fourier Transform (FFT) of (a) and (b), respectively. (e) is the illustration of the real lattice with lattice parameters after the correction of thermal drift. Soft cantilever was used and applied normal load is 4 nN.

4.4.3 Force-separation (FS) curve: interfacial structure

FS curves should reveal a possible layering of the solvent molecules as previously reported for ILs and, in particular, reveal a possible displacement of the adsorbed iodine and/or silver. Figure 4.6 shows force versus separation (FS) curves for the I-modified Au(111) depending on the potential during Ag UPD. FS curves were measured using soft and hard cantilevers but discrete steps indicating structured layers near the surface were only measurable with a soft cantilever. Therefore, we present here the results observed using a soft cantilever. Based on the atomic structures of iodine observed at the normal load of 4 nN, we presume that the iodine layer is bound so strongly that it resists its displacement by the tip during the FS measurement.

Figure 4.6a and e show FS curves in region I and II´, respectively. Both FS curves show two distinct layers. Interestingly, the thickness of layers and the corresponding push-through forces are similar in both cases. However, at 0.31 V and -0.001 V, representing potential region II and III, FS curves show only one layer, which might result from the weakly adsorbed water on the iodine adlayer. As mentioned above, the consumed charge in potential region I and II´ suggests that the silver ions are adsorbed on the iodine adlayer prior to the Ag deposition on gold surface [23]. Therefore, it is reasonable that the innermost layer in potential region I and II´ results from a partially solvated Ag ions attached to the iodine adlayer.

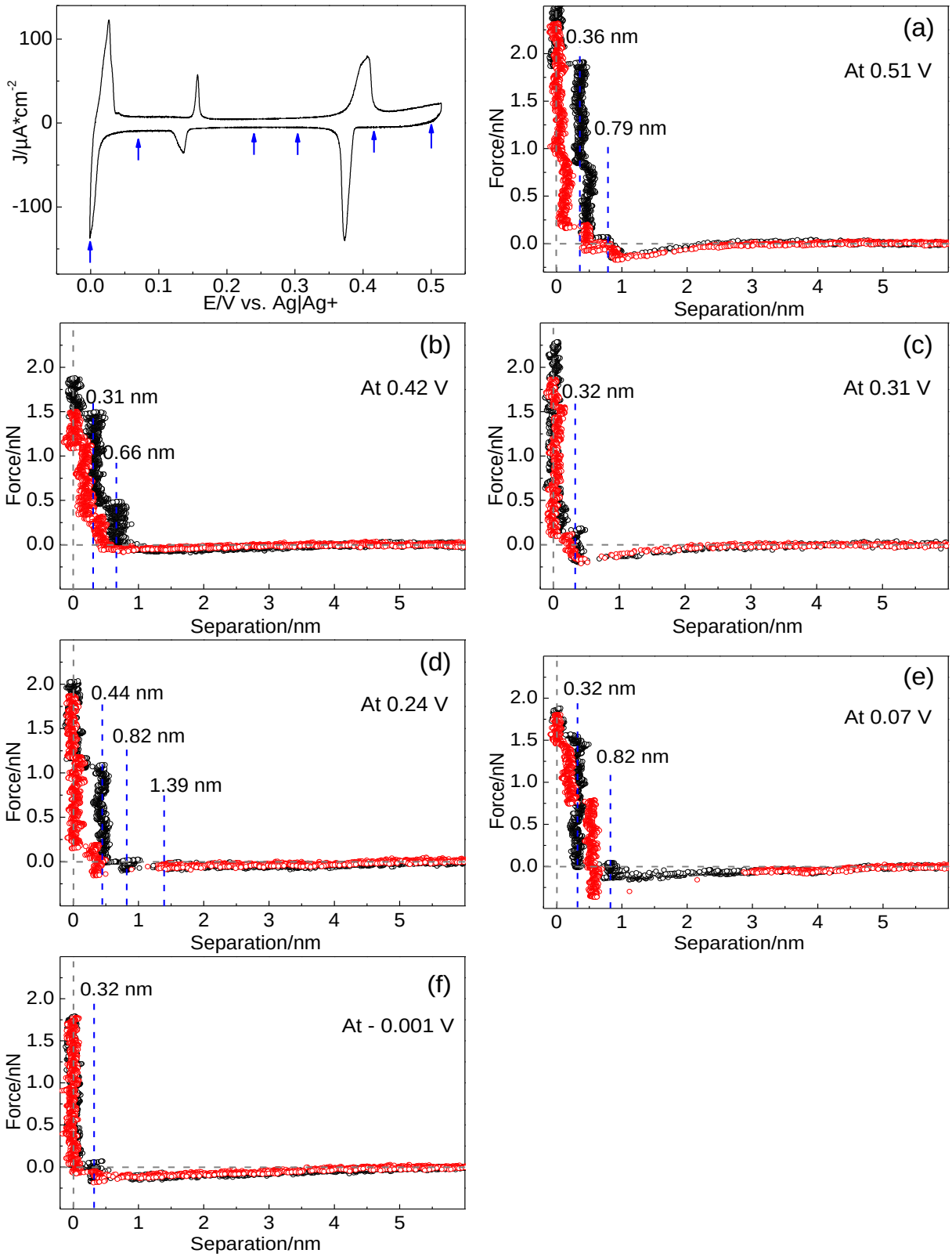

Figure 4.6 Force separation profiles obtained in cathodic sweep at the potential of (a) 0.51 V, (b) 0.42 V, (c) 0.31 V, (d) 0.24 V, (e) 0.07 V, (f) - 0.001 V for the I-modified Au(111) in 2mM $AgClO_4$/0.1M $HClO_4$. All profile shows approaching (black) and retracting (red) curves and the approaching speed is ~50 nm/s. Soft cantilever was used.

4.4.4 Friction forces depending on potential

The relation between electrochemical potential, I-modified gold surface, and friction has been studied using both the hard and soft cantilevers. Since overall the results show a similar behavior, we will present here the results obtained using hard cantilever (Figure 4.7) and the results obtained using a soft cantilever will be presented in the supporting information (Figure S4.10).

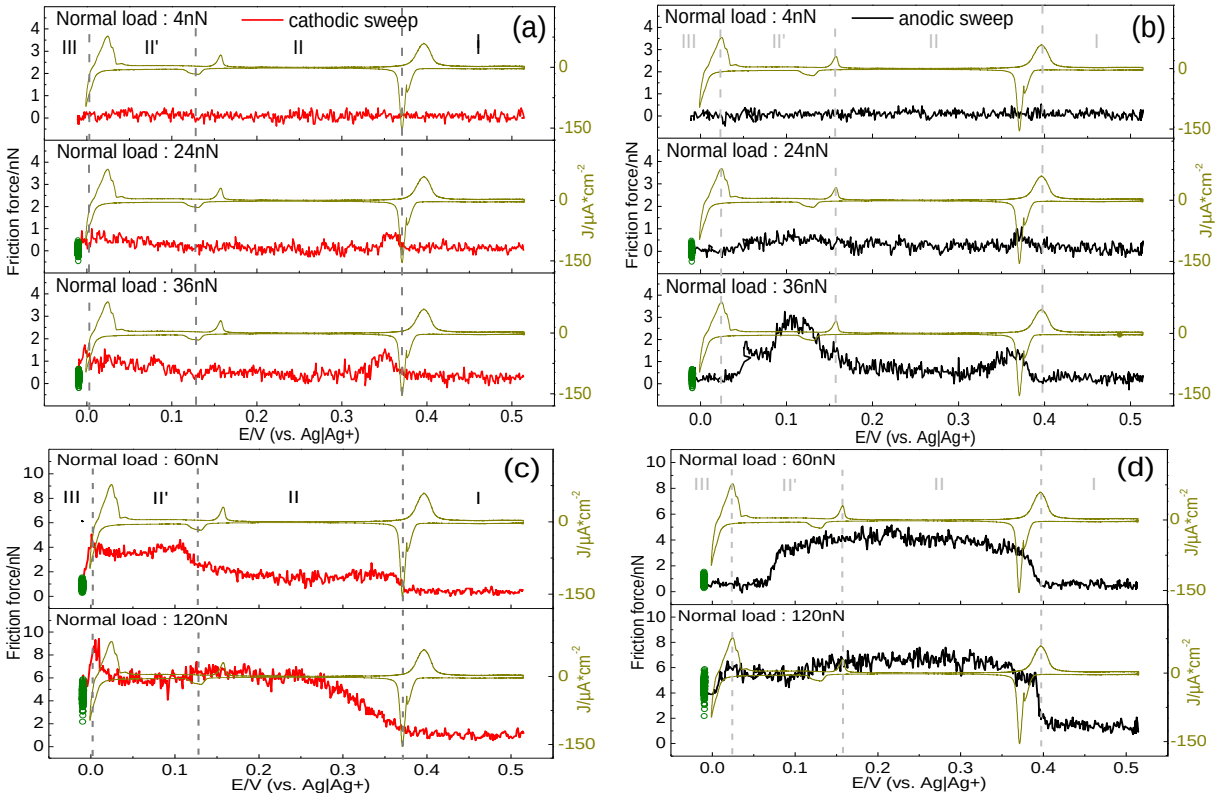

Figure 4.7 Friction force on potential at fixed normal loads during (a) and (c) cathodic sweep and (b) and (d) anodic sweep. Before the anodic sweep, at -0.002 V, observed friction force is shown as green curve. Hard cantilever was used. The scan rate of AFM image was 0.47 nm/s.

For very low normal load (F_N < 10nN), friction is close to zero for all potentials, indicating a minimal load is required to obtain friction distinguishable from the noise. Interestingly, above this critical load, the friction shows the dependence on potential (region I, II, II´, and III) as well as on normal load.

At low loads (10 nN < F_N < 35 nN), friction in the cathodic sweep increases sharply when the potential passes the peak C_1 (region II), but it decreases again negative of 0.33 V. The 1st Ag UPD ($\theta_{Ag} = 0.44$) is followed by a transition of iodine structures from the $\left(\sqrt{3} \times \sqrt{3}\right)R30°$

structure to $p(3 \times 3)$ structure as shown in atomic corrugation (Figure 4.2 and 3). Therefore, the transition of iodine structures and the increasing Ag coverage lead to an increase of friction probably caused by the transitory disorder. In region II´, even though there is a slight change in $p(3 \times 3)$ structure and an increase of the Ag coverage, friction hardly changes. This suggests that adsorbed iodine forming $p(3 \times 3)$ structure is quite mobile during the deposition of silver underneath it. Thus, the tip slides on the iodine adlayer at low normal loads. In region III, where a bilayer forms, friction initially is slightly higher than in region II´ due to transitory disorder caused by continuously adsorbed silver adatoms, and decreases with time upon completion of the 2nd Ag layer. Steps on the incomplete Ag bilayer contribute to the increase of friction as described by the Schwoebel-barrier [29-31]. Moreover, the continuously adsorbed silver ions, i.e. the effect of coverage, contributes to the increase of friction. To ensure the completion of the Ag bilayer, the potential was maintained at -0.002 V for a lateral map scan shown as green dots in Figure 4.7, replotted in Figure S4.11 as a function of time. As soon as the deposited silver atoms completes a bilayer, iodine forms the $(\sqrt{3} \times \sqrt{3})R30°$ structure (cf. Figure 4.5), which results in the decrease of friction. This decreased friction in areas where the 2nd Ag layer is deposited is also obvious in Figure S4.3c. In the anodic sweep, friction slightly increases again in region II´ after the dissolution of Ag bilayer.

A large hysteresis was observed for the friction between the cathodic and the anodic sweeps at the normal load of 36 nN and 60 nN, confirmed for three different positions (Figure S4.12). Whereas for 36 nN in the cathodic sweep, the transition of friction is similar to that at 24 nN, in anodic direction, a large friction increase occurs in region II`, but decreases again before reaching region II. As will be shown and discussed in more detail below, at this normal load of 36 nN the tip starts to penetrate into the iodine adlayer, which is the reason for a step-wise increase of friction in friction vs. normal load curves. The exact value at which this penetration starts may depend on many factors such as potential and exact coverage by Ag and iodine. In addition, a shielding effect of the tip may lead to a delayed deposition or dissolution of Ag and thus causes the hysteresis. It is noteworthy that at 0.1 V, about the same value of friction force observed in the anodic sweep at 36 nN as at 60 nN in the cathodic sweep and again in the subsequent anodic sweep. This supports the assumption of a penetration of the tip; higher friction values indicating continuous penetration are observed as the normal load increases, clearer at 120 nN. Therefore, it is hypothesized that when the Ag forms a monolayer, the adsorption of iodine is relatively weak due to the adsorption (or desorption) of silver ions for a Ag bilayer, which temporarily allows the tip to penetrate the iodine adlayer. While the tip

penetrating into the iodine layer, the contact area increases, which results in the increase of friction [14].

As shown in the SI, the required normal load to penetrate the iodine adlayer is estimated from the adsorption strength and the coverage of adsorbed iodine, showing that the required normal load turns out to be 123 nN. Therefore, the normal load of 120 nN is sufficient for the tip penetration into the iodine adlayer regardless of potential. Also, at 120 nN, the increase of friction in region II takes place over broader potential range in cathodic sweep compares to that at low normal loads. This might indicate that the tip penetrates even into Ag adlayer because the Ag coverage is below a critical value. In region II´, the friction slightly decreases with decreasing the potential to 0.05 V and then, shows sharp increases when the potential approaches to the 3rd Ag UPD peak, C_3 as the formation of a Ag bilayer starts [38]. At the potential of the 3rd Ag UPD peak, friction slightly decreases with time (Figure S4.12) is clear at 120 nN compare to low normal load, which demonstrates that the 2nd Ag layer completes. At 120 nN where the tip penetrates into the iodine adlayer regardless of potential, the friction on Ag adlayer is higher than that on Au(111), which might indicate that the adsorbed iodine is less mobile on Ag adlayer than on Au(111).

4.4.5 Friction forces depending on normal load

In order to understand the influence of the adsorbates (e.g. coverage and the strength of interaction with tip and substrate) under steady state on friction, we have investigated the dependence of friction on normal load at constant potential. The following data are taken from lateral force maps with scan size and scan rate were 20 x 20 nm² and 0.47nm/s, respectively. A hard cantilever was used.

Compared to the regimes suggested in our previous study observed on Au(111) during Ag UPD (cf. chapter 3) [13], friction forces vs. normal load behaves quite differently on I-modified Au(111), which results from the penetration into the iodine adlayer. Therefore, considering the

effect of the penetration into the iodine adlayer, the regimes (α, β, and γ), where the coefficient of the friction (COF) changes, are classified again as shown in Figure 4.8b.

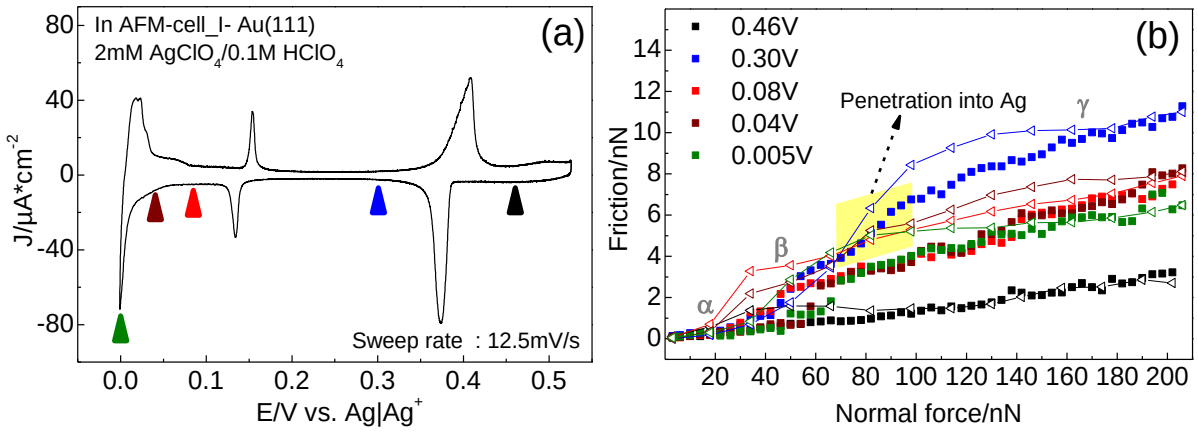

Figure 4.8 (a) Cyclic Voltammetry on I-modified Au(111) in AFM-cell filled with 2mM $AgClO_4$/0.1M $HClO_4$. (b) Friction on normal load obtained using hard cantilever at fixed potentials marked on (a) with same color. Solid and hollow symbols indicate friction forces observed during increasing and decreasing load, respectively. The scan size and rate are 20x20 nm^2 and 0.47 nm/s, respectively.

At low normal load (F_N < 20 nN (0.46 V), F_N < 30 nN (0.30 V and 0.08V), and F_N < 50 nN (0.04 V and 0.005 V)) indicating regime α, the COF is low for all potentials (COF: ~ 0.02). The changes of the observed atomic structures with increasing load (Figure S4.13-17) is convincing evidence showing that the AFM tip slides on iodine layer in this regime.

At 0.46 V, i.e. in potential region I, friction is independent of load even though the transition of atomic corrugations (Figure S4.13) clearly shows the penetration into the iodine adlayer. A similar behavior was observed for iodine covered Au(111) in a tetraglyme electrolyte (see chapter 6) [39]. Obviously, the friction coefficient is similarly low for Au(111) and the iodine covered surface. Therefore, it is assumed that the iodine atoms on the surface of Au(111) are so mobile that they have no influence on the tip movement, despite of their strong adsorption on Au(111).

For the other potentials, the lateral force steeply increases above a certain normal load and this indicates regime β. Within regime β, friction increases stepwise. At 0.08 V, 0.04 V, and 0.005 V, lateral force maps (Figure S4.15-17) in plateau area of regime β show that the atomic corrugation for the iodine layer is slightly enhanced compared to that at regime α. With further increase of load, the lateral maps reveal two different lattices (Figure S4.15c, S4.16d, and

S4.17d), which demonstrate that the AFM tip starts to penetrate into iodine adlayer. The penetration results in the steep increase of friction on load (COF: 0.01 (0.46V), 0.14 (0.08 V and 0.005 V), and 0.23 (0.04 V)).

It is remarkable that at 0.3 V, two plateaus at about 40 nN and 60 nN are observed in regime β. Figure S4.14 shows that the atomic corrugation for the $p(3 \times 3)$ structure slightly changes at 54 nN. At high loads (134 nN), the $p(3 \times 3)$ structure disappears and smaller lattice than the $p(3 \times 3)$ structure is observed even though it less clear than that observed at 0.46 V. On the basis of our data (e.g. charge density, atomic structure, friction as function of potential) we suggest that silver forms a $p(3 \times 3)$ structure and due to the adsorbed site of silver on Au(111), atop or 2-fold bridge sites, adsorbed iodine shows clear height difference in $p(3 \times 3)$ structure (Figure S4.14a and b). With increasing the pressure (30 nN < F_N < 50 nN), the AFM tip penetrates into the iodine adlayer (COF: 0.14) and slightly modifies the position of silver atoms, which results in the even height between silver atoms in $p(3 \times 3)$ structure (Figure S4.14d and e). Further increase of load allows the AFM tip to penetrate the silver layer (COF: 0.1) meaning that the AFM tip slides on the surface of Au(111) as shown in Figure S4.13f.

In regime γ for all potential regions, friction increases linearly with normal load (Amontons' law); this friction force adds to the force necessary for the displacement of the adsorbate species of regime β. Since the AFM tip entirely penetrates adsorbates layers, the interaction between iodine and substrate is an important factor for the COF and additionally, the interaction formed with tip might have influence on it (COF: 0.02 (0.46 V), 0.04 (0.3 V and 0.04 V), and 0.03 (0.08 V and 0.005 V)) [40].

As suggested by A. Socoliuc et al. [41], it is expected that the interaction between the tip and the surface has an influence on the E_0. Therefore, the corrugation of the surface potential, E_0, is calculated depending on potential in regime γ, 134 nN, where the tip penetrates the iodine adlayer (or even Ag adlayer). Figure 4.9a shows a stick-slip curve at 0.46 V. Figure 4.9b demonstrates that the E_0 increases a lot as the tip slides on Ag adlayer compared to that on Au(111), marked as ΔE_0. The E_0 increases as the tip penetrates the iodine adlayer, ΔE_0 and it increases again at 0.3 V as the tip penetrates the Ag adlayer, $\Delta E_0'$. Our results suggest that the interaction between the tip and the surface increases on silver adlayer compared to that on Au(111), but the Ag coverage is insignificant on the increase of E_0, ΔE_0. Furthermore, at 0.3 V, the E_0 increases with increasing the normal load from regime β to regime γ, which results from the penetration of tip into the silver adlayer.

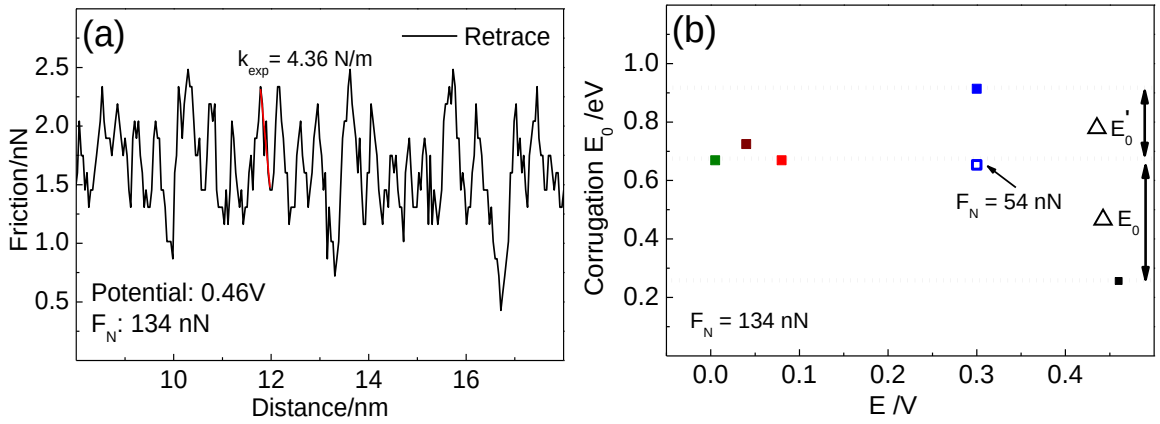

Figure 4.9 (a) stick-slip curve on I-modified Au(111) at 0.46 V. (b) the corrugation of the surface potential E_0 as function of potential. Solid symbols are observed at the normal load of 134 nN in regime γ. In addition, the hollow symbol is observed at the normal load of 54 nN in regime β.

4.4.6 Ag UPD in 0.1 mM $AgClO_4$/0.05 M $HClO_4$

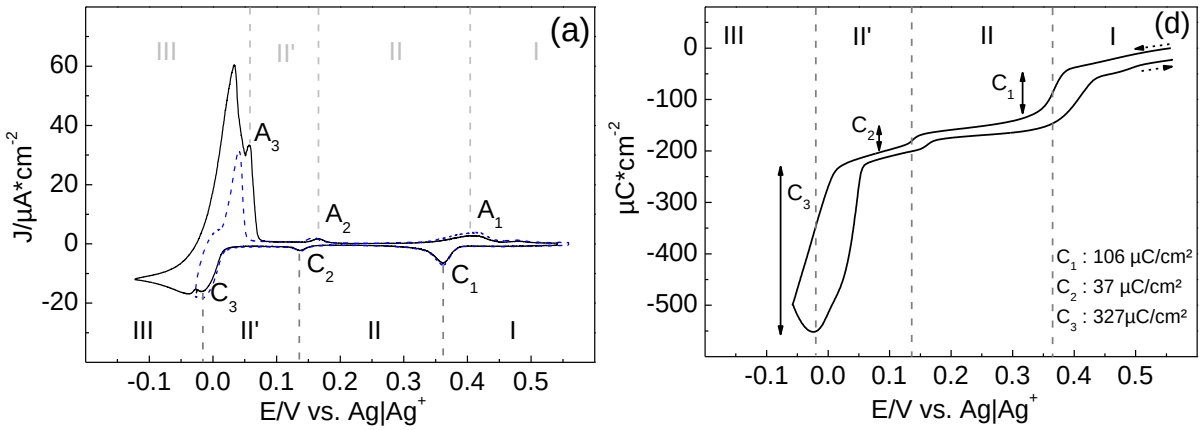

Figure 4.10 (a) Cyclic voltammetry and (b) coulometric curve in H-cell recorded with the sweep rate of 1 mV/s for I-modified Au(111) in 0.1 mM $AgClO_4$/0.05 M $HClO_4$.

Figure S4.18a shows CV in H-cell recorded with the sweep rate of 10 mV/s for the I-modified Au(111) in 0.1 mM $AgClO_4$/ 0.05 M $HClO_4$. Since the Ag^+ concentration is 10 time lower than above results, the Ag deposition slows down in this case resulting in broad peaks for the Ag UPD. Therefore, we recorded the CV with sweep rate of 5 mV/s as shown in Figure S4.18b. In

both cases we observed two peaks for the Ag UPD, C_1/A_1 and C_2/A_2, corresponding to the formation of the Ag monolayer. Due to the low concentration of silver ions, negative of the peak C_3 the Ag bilayer is formed followed by the Ag bulk deposition. When the sweep rate is further reduced to 1 mV/s (Figure 4.10), the potential for the Ag bilayer formation can be distinguished from the bulk deposition. The charge densities for the first (C_1), second (C_2), and third (C_3) UPD peaks in H-cell (1 mV/s) are 109, 46, and 259 μC/cm², respectively. However, in AFM-cell, even with the sweep rate of 1 mV/s, Ag bilayer is not separated from the Ag bulk deposition. Therefore, we divide the potential range into 4 different potential regions.

Figure 4.11 shows the friction results obtained as function of normal load for the I-modified Au(111) in 0.1 mM $AgClO_4$/0.05 M $HClO_4$. At 0.51 V, before the Ag deposition, the friction results quite resembles the results obtained in 2 mM $AgClO_4$/ 0.1 M $HClO_4$, which is reasonable. At 0.257 V (potential region II), based on the structure of iodine at 12 nN (Figure 4.12), we presume that the Ag coverage reaches 0.44. However, the friction starts to increase at about 60 nN, which indicates that the required normal load to penetration into iodine adlayer increased. Figure 4.12 shows the transition of atomic corrugations at 0.257 V with increasing normal load. The highly mobile Ag atoms can move flexibly during the AFM scan. Thus, it is hard to separate the penetration into iodine layer and silver layer but based on the atomic corrugation, at high load (130 nN < F_N), the tip penetrates submonolayer of silver and interacts with the surface of Au(111).

At 0.07 V (potential region II'), the atomic corrugation at 12 nN (Figure 4.12) shows that the iodine maintains as a $p(3 \times 3)$ structure. At high load (60 nN < F_N), a transition of atomic structures is observed, indicating that the AFM tip penetrates the iodine layer as normal load increases and silver completes a monolayer at this potential.

At -0.12 V (potential region III), the atomic corrugation at 12 nN (Figure 4.13) shows that the iodine forms a $(\sqrt{3} \times \sqrt{3})R30°$ structure on the Ag adlayer. With increasing normal load, the observed lattice demonstrates that the AFM tip penetrates the iodine layer and interacts with the silver layer. However, at about 136 nN, we observed another transition of structures from Ag(111) to the $(\sqrt{3} \times \sqrt{3})R30°$ structure. This structure transition is reproducible but the required normal load is not identical. A possible explanation is that at relatively high normal loads, the Ag deposition might be disturbed by the sliding tip, which results in somewhat irregular time required to complete Ag bilayer. After the completion of Ag bilayer, the *pzc* of Ag(111) is achieved. Because the *pzcs* of Au(111) and Ag(111) differ by 1 V [42], it is expected

that the iodine is adsorbed more strongly on the Ag bilayer than Au(111). Therefore, it is reasonable to assume that the second transition of structures results from the iodine adsorption after the completion of Ag bilayer.

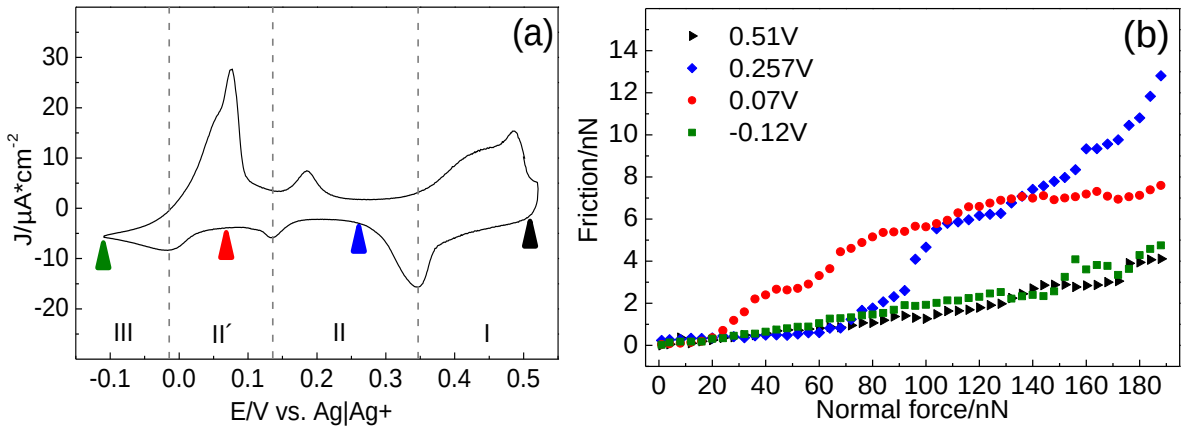

Figure 4.11 (a) Cyclic Voltammetry on I-modified Au(111) in H-cell filled with 0.1 mM $AgClO_4$/0.05 M $HClO_4$. (b) Friction on normal load obtained using hard cantilever at fixed potentials marked on (a) with same color. The sweep rate for the CV is 10mV/s. The scan size and rate for the friction measurement are 20x20 nm² and 0.47 nm/s, respectively.

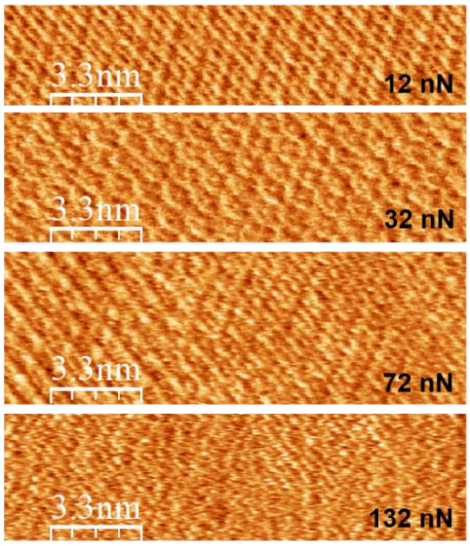

Figure 4.12 Lateral force map depending on normal load at 0.257 V in 0.1 mM $AgClO_4$/0.05 M $HClO_4$. Hard cantilever was used.

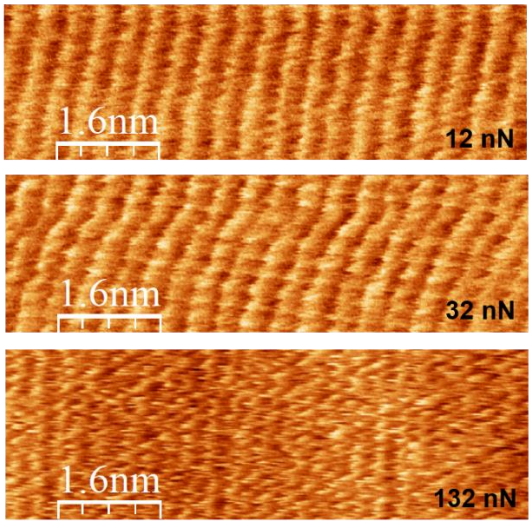

Figure 4.13 Lateral force map depending on normal load in 0.1 mM $AgClO_4$/0.05 M $HClO_4$ at 0.07 V. The scan size and rate are 10 nm x10 nm and 0.235 nm/s, respectively.

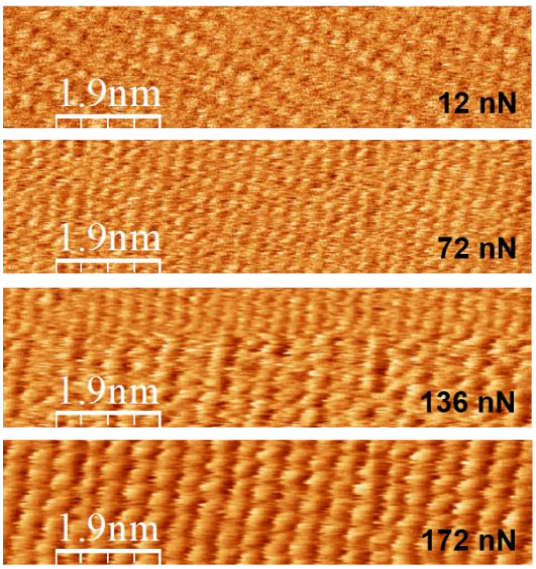

Figure 4.14 Lateral force map depending on normal load in 0.1 mM $AgClO_4$/0.05 M $HClO_4$ at V -0.12 V. The scan size and rate are 10 nm x10 nm and 0.235 nm/s, respectively.

4.5 Conclusion

We investigated the structural transition on I-modified Au(111) in 2 mM Ag^+ containing electrolyte as the coverage of silver increases. At potentials positive of Ag UPD, the atomic corrugations showed that the iodine forms the $(\sqrt{3} \times \sqrt{3})R30°$ structure ($\theta_I = 0.33$) on Au(111). This structure is transformed into the $p(3 \times 3)$ structure ($\theta_I = 0.44$) when the potential passes the 1st Ag UPD peak. Considering the clear height difference in the atomic corrugations, it is assumed that the Ag atoms forming a $p(3 \times 3)$ structure e.g. occuping atop and 2-fold bridge sites of Au(111) and the iodine also forms $p(3 \times 3)$ structure sitting on atop site of the silver adlayer. Interestingly, the $p(3 \times 3)$ structure is maintained at slightly negative of the 2nd Ag UPD peak but the height difference disappears. This demonstrates again that the coverage of silver directly influence the structure of iodine. When the silver forms a bilayer, the structure of iodine changes to the $(\sqrt{3} \times \sqrt{3})R30°$ structure.

FS curves in 2 mM Ag^+ containing electrolyte together with the result of charge density suggest a possible adsorption of silver ions on the iodine adlayer prior to the deposition.

The friction forces as function of potential in 2 mM Ag^+ containing electrolyte show the dependence on potential as well as applied normal load. At low normal load above a minimal load (10 nN < F_N < 35 nN) the change of friction force closely correlates with the transient fluctuation of the iodine adlayer due to the increasing Ag coverage. Thus, as the potential passes the 1st Ag UPD peak, it is expected for the iodine adlayer to be disordered due to the deposition of silver. This disorder of the iodine adlayer allows the friction to increase with increasing the coverage of silver from 0 to 0.44. When the coverage of silver arrives at 0.44, the iodine forms a $p(3 \times 3)$ structure according to the structure of silver, which results in the decrease of friction. At the normal of 36 nN and 60 nN a large hysteresis between cathodic and anodic sweeps appears. Thus, there is a clear transition of friction between potential region III and II, which starts at 0.1 V. Therefore, even though it is hard to clarify the exact conditions (e.g. the coverages of Ag and I), the penetration of the tip occurs at the normal load of 36 nN and 60 nN when the Ag forms a monolayer. At high normal load, 120 nN, as expected by our approximate calculation, the penetration into the iodine adlayer occurs independent of potential.

As observed on I-modified Au(111) in tetraglyme electrolyte [39], no significant energy is required to push away the adsorbed iodine on Au(111). After the deposition of silver, the

friction forces on normal load in 2 mM Ag^+ containing electrolyte show three different regimes (α, β, and γ regimes) where the COFs change. The transition of atomic corrugations with increasing the normal load demonstrates that the transition of friction results from the penetration into the iodine adlayer. In α regime, the tip slides on the iodine adlayer, resulting in low friction regardless of potential. Friction increases steeply in β regime because the tip penetrates into the iodine adlayer. Furthermore, before the coverage of silver reaches a critical value, possibly at the 0.33 V, further increase of normal load after the penetration into the iodine adlayer causes the penetration into the silver adalyer. In γ regime where the applied normal load is strong enough to penetrate into the adlayer, the tip slides on the metal surfaces and friction shows moderate increase. This indicates that there is no additional dynamic interaction between tips and the surface.

The results (e.g. CV, atomic corrugations, friction vs. normal load) in 0.1 mM Ag+ containing electrolyte quite resemble that in 2 mM Ag+ containing electrolyte except for the formation of Ag bilayer. Thus, due to reduced concentration of silver ions in the electrolyte, at 0.12 V, the formation of Ag bilayer is followed by the Ag bulk deposition. Astonishingly, during the measurement of friction as function of normal load, at 0.12 V, the transition of atomic corrugations from Ag(111)(1x1) to the $(\sqrt{3} \times \sqrt{3})R30°$ structure at high normal load, which has no influence on friction. This might result from the continuous deposition of silver.

Acknowledgment

The authors gratefully acknowledge the DFG (Deutsche Forschungsgemeinschaft) for funding this work (BA1008/21-1).

4.6 Supporting Information

4.6.1 1 mM Ag_2SO_4/0.05 M H_2SO_4

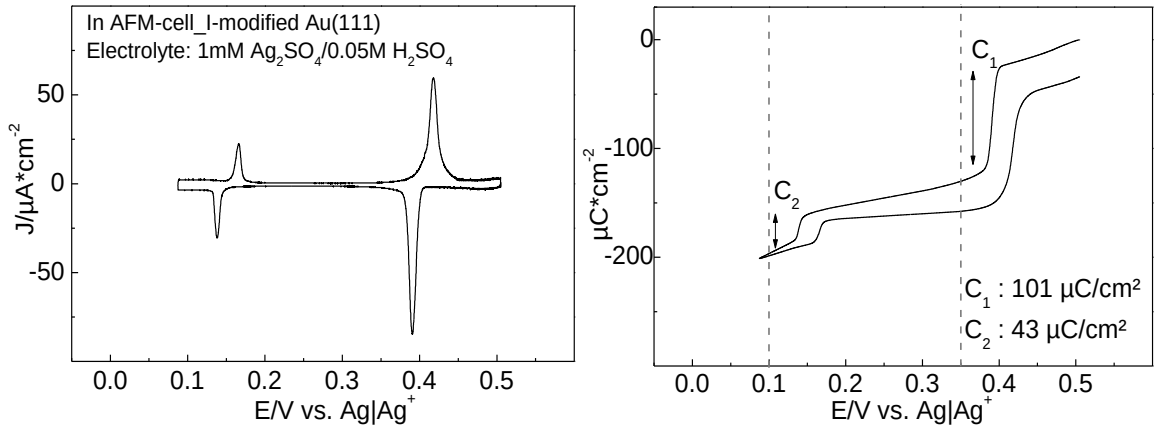

Figure S4.1 (a) Cyclic voltammetry and (b) coulometric curve in AFM-cell for the I-modified Au(111) in 1 mM Ag_2SO_4/0.05 M H_2SO_4.

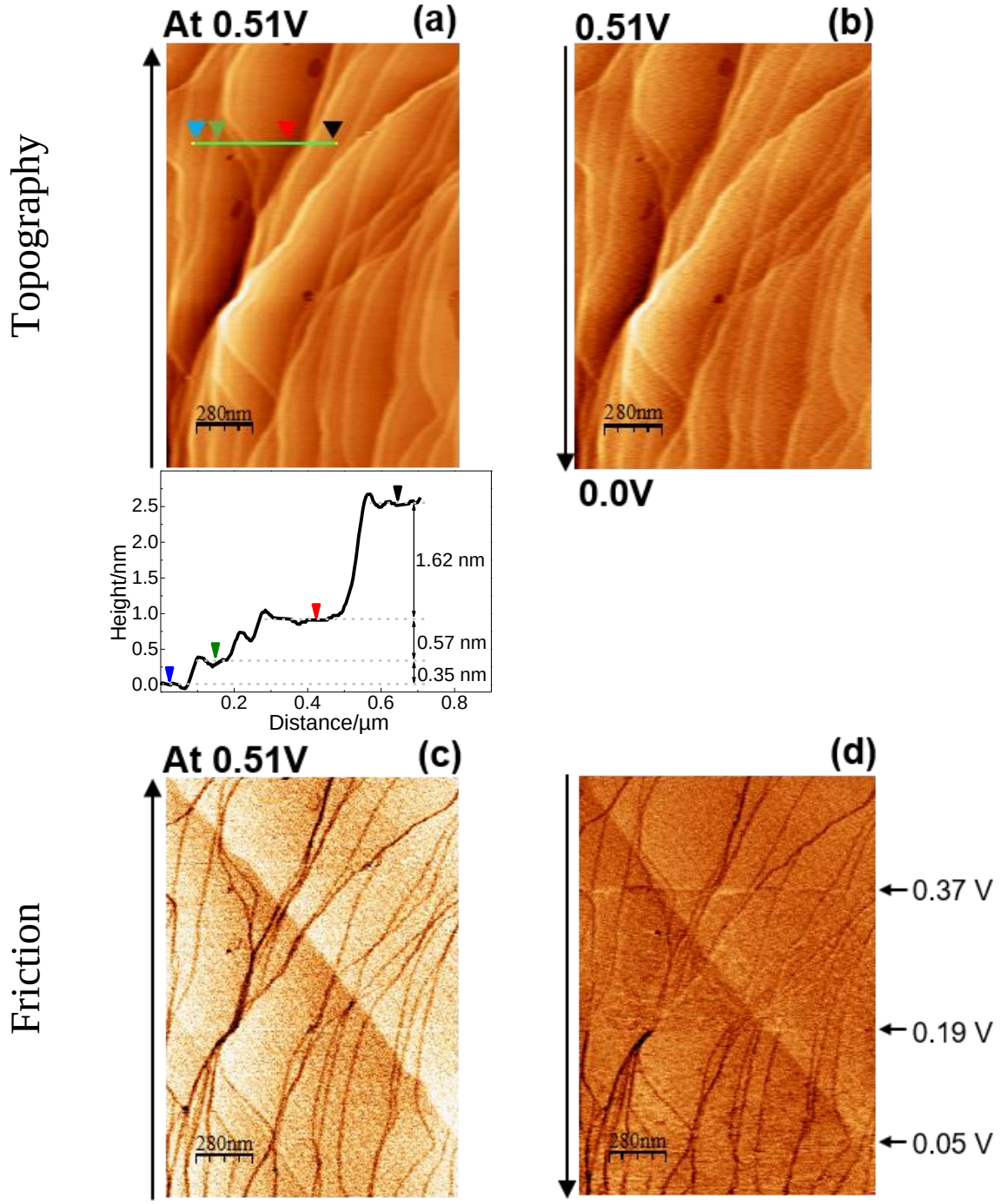

Figure S4.2 Topography obtained (a) at 0.51V (vs. Ag/Ag^+), (b) during cathodic sweep (0.51 V→0.0 V). Lateral force maps (c) at 0.51 V and (d) during the cathodic sweep. Arrow indicates the scan direction of AFM images (topography and friction image). The scan direction corresponds to the potential sweep direction for (b) and (d). Below mage of (a) shows line profile of the position marked in (a). The scan size and rate are 2x2 μm² and 47 nm/s, respectively. Hard cantilever was used and applied normal load is 28 nN. Friction image is the backward scan meaning that the dark color indicates high friction.

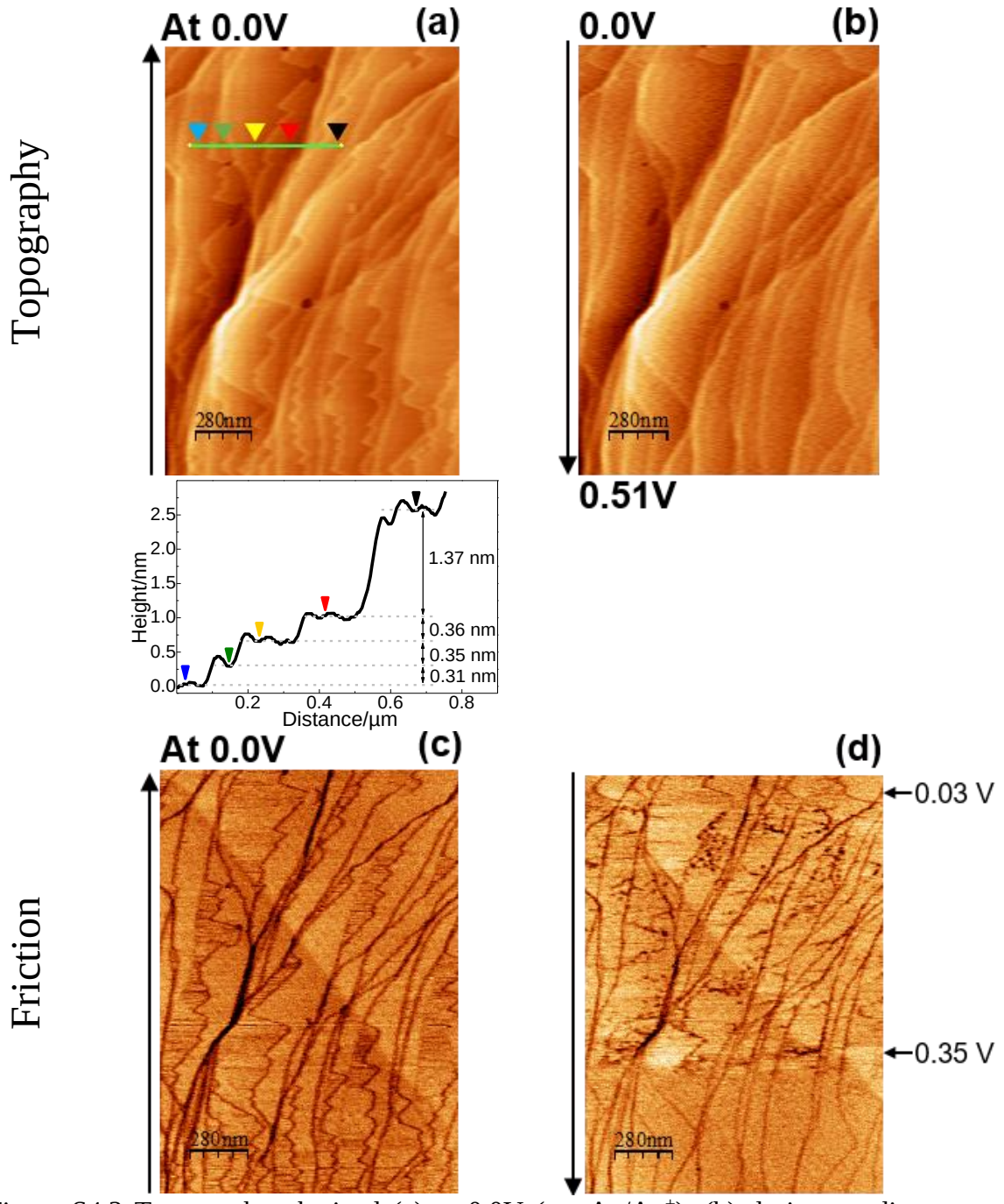

Figure S4.3 Topography obtained (a) at 0.0V (vs. Ag/Ag^{+}), (b) during anodic sweep (0.0 V→0.51 V). Lateral force maps (c) at 0.0 V and (d) during the anodic sweep. Arrow indicates the scan direction of AFM images (topography and friction image). The scan direction corresponds to the potential sweep direction for (b) and (d). Below image of (a) shows line profile of the position marked in (a). The scan size and rate are 2x2 μm² and 47 nm/s, respectively. Hard cantilever was used and applied normal load is 28 nN. Friction image is the backward scan meaning that the dark part indicate high friction.

The morphological changes on the surface of I-modified Au(111) were recorded by using in situ AFM measurements during the cathodic and anodic sweeps as shown in Figure S4.2 and S4.3, respectively. The scan size of AFM images (topography and friction) was 2x2 μm² but

due to oscillations upon reversal of scan direction, the images were cut off to about 600 nm in x direction. The images below Figure S4.2a and S4.3a indicate the height profiles along the green line marked in Figure S4.2a and S4.3a, respectively. Figure S4.2a shows the surface of I-modified Au(111) before the Ag UPD (potential region I). Even though it is slightly larger than theoretical value (0.2 nm), monoatomic step (~ 0.35 nm) is observed between blue and green arrows. The step bunching shown between red and black arrows is caused by the cooling process of single crystal in the iodine atmosphere [43, 44]. It is noteworthy that the error between theoretical and observed values of a monoatomic step results from the background subtraction of the image. Due to the step bunching at the surface, it is more difficult to determine a correct background. During the cathodic sweep, in topography (Figure S4.2b) no morphological change is detected but the friction (Figure S4.2d) shows clear dependence on potential. When the potential is maintained at 0 V (region III) as shown in Figure S4.3a and c, partially incomplete terraces appear. The height of incomplete terraces marked as yellow and red arrows show monoatomic step, which confirms that a bilayer is formed during the 3rd Ag UPD. The friction image indicates that the friction is lower and in particular less noisy on the Ag bilayer than on a monolayer. It might be related to desorption of iodine due to the ongoing Ag deposition on a monolayer or different surface energy.

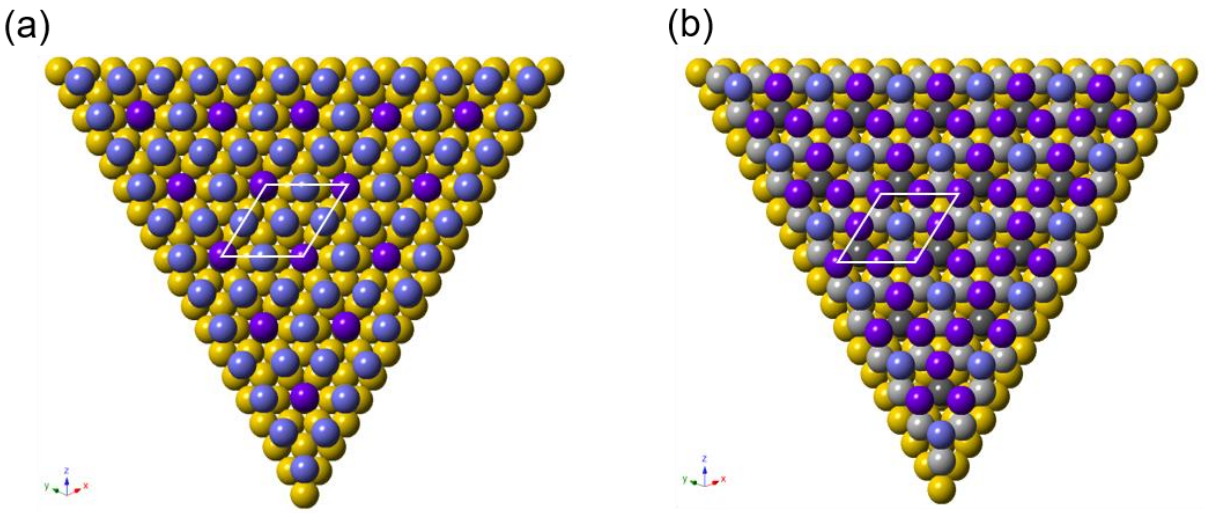

Figure S 4.4 Ball models of the $p(3 \times 3)$ structure depending on the occupying site of iodine. Silver atoms sit on atop and bridge sites of Au(111) and iodine sits on (a) atop site or (b) 3-fold hollow site of silver adlayer.

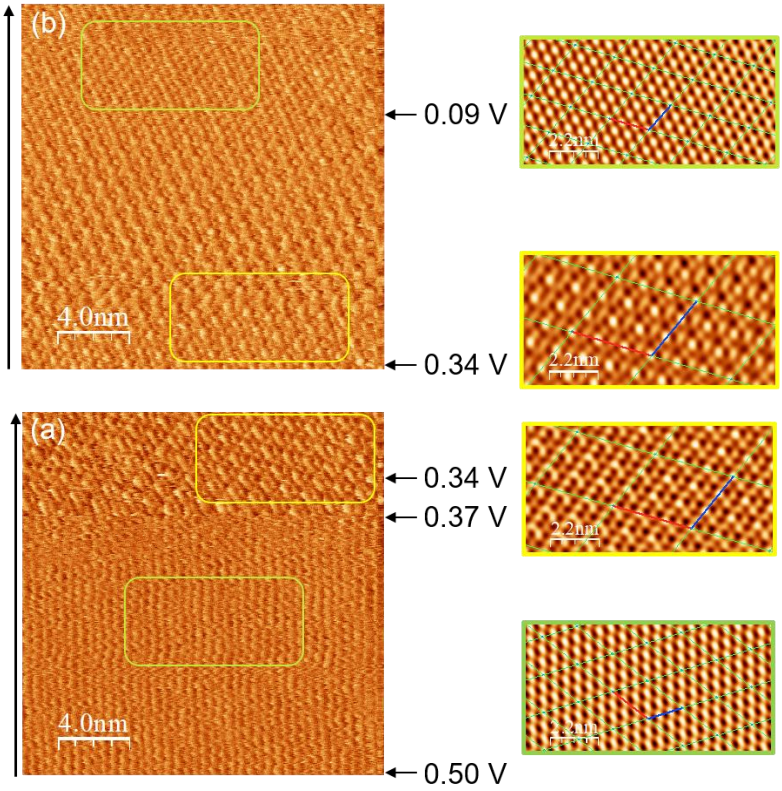

Figure S4.5 Lateral force maps showing the transition of iodine structures (a) from the $(\sqrt{3} \times \sqrt{3})R30°$ structure to the $p(3 \times 3)$ structure (0.50 V→ 0.34 V), (b) from the $p(3 \times 3)$ structure to the $(\sqrt{3} \times \sqrt{3})R30°$ structure in cathodic sweep (0.34 V → 0.09 V). The black arrow indicates the scan direction and sweep direction of potential. Soft cantilever was used and applied normal load is 4 nN.

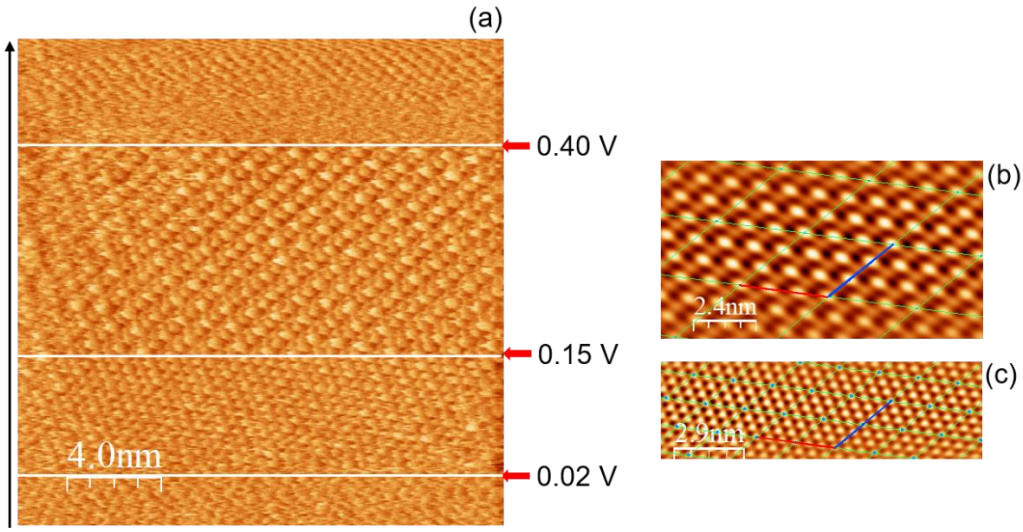

Figure S4.6 (a) Lateral force map during anodic sweep from 0.0 V to 0.50 V. (b) and (c) are the lattice images after Fast Fourier Transform (FFT) for the potential region II and II´, respectively. Black arrow indicates scan and sweep (CV) direction. Soft cantilever was used and applied normal load is 4 nN.

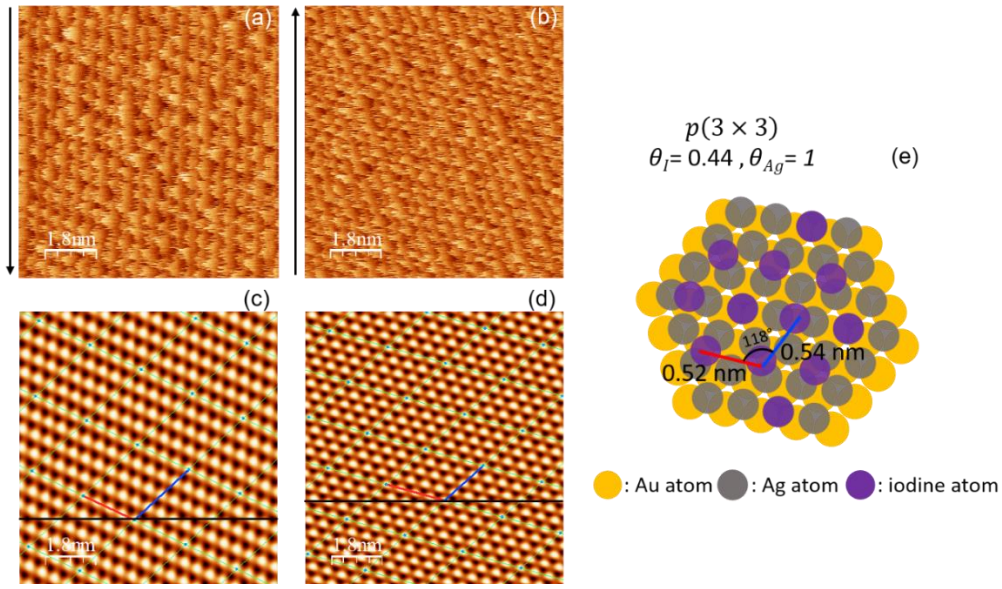

Figure S4.7 Lateral force maps for I-modified Au(111) in 2 mM $AgClO_4$/0.1 M $LiClO_4$ at 0.1V (vs. Ag/Ag+) in anodic sweep during (a) downward scan and (b) upward scan. Arrow indicates scan direction. (c) and (d) are the lattice images after Fast Fourier Transform (FFT) of (a) and (b), respectively. (e) is the illustration of the real lattice with lattice parameters after the correction of thermal drift. Soft cantilever was used and applied normal load is 4 nN.

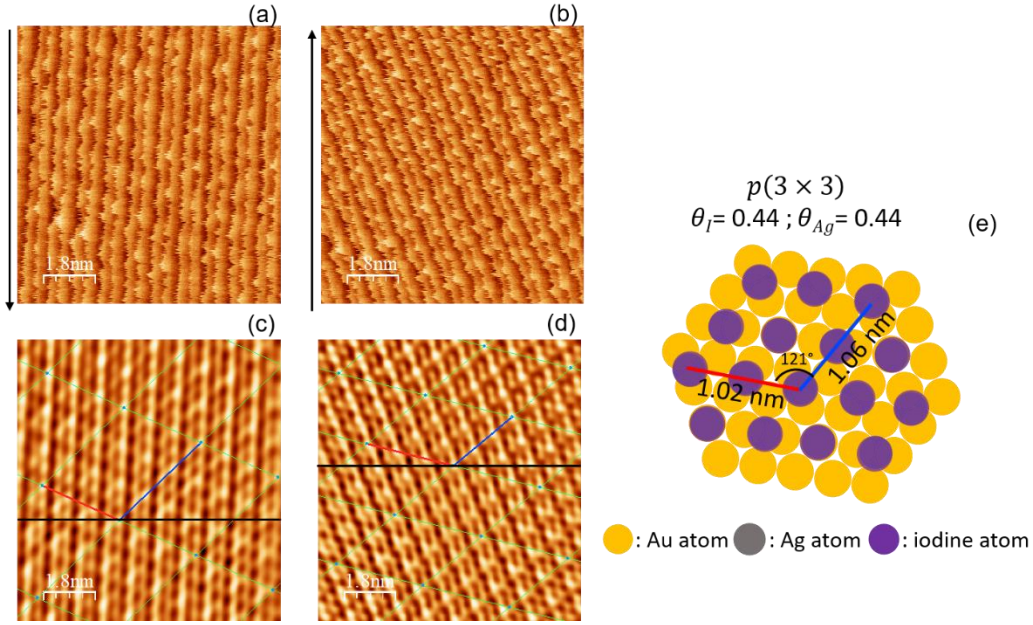

Figure S4.8 Lateral force maps for I-modified Au(111) in 2 mM $AgClO_4$/0.1 M $LiClO_4$ at 0.25V (vs. Ag/Ag+) in anodic sweep during (a) downward scan and (b) upward scan. Arrow indicates scan direction. (c) and (d) are the lattice images after Fast Fourier Transform (FFT) of (a) and (b), respectively. (e) is the illustration of the real lattice with lattice parameters after the correction of thermal drift. Soft cantilever was used and applied normal load is 4 nN.

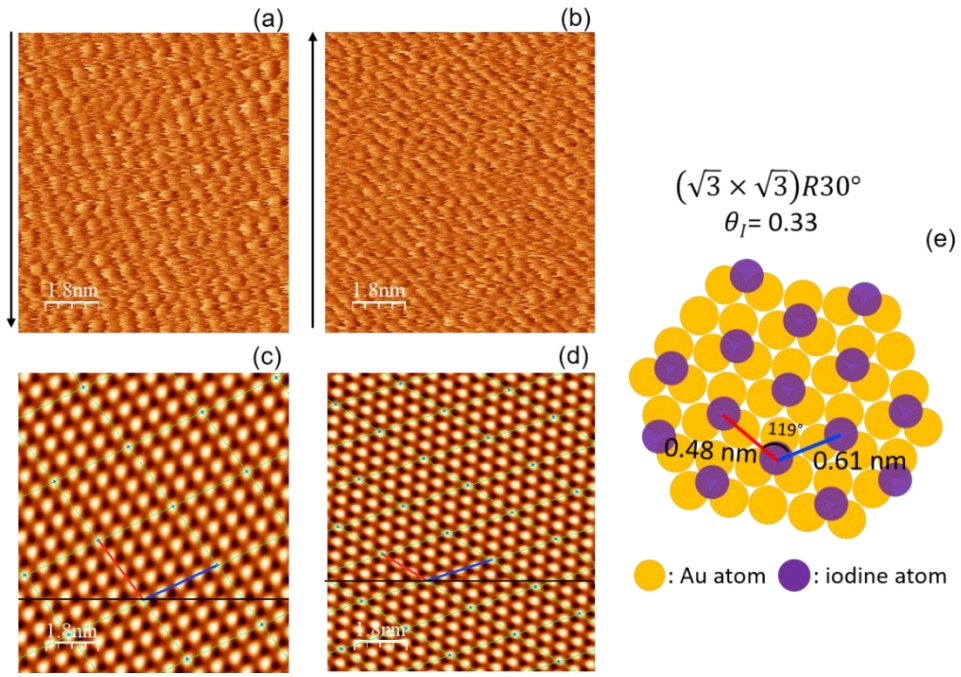

Figure S4.9 Lateral force maps for I-modified Au(111) in 2 mM $AgClO_4$/0.1 M $LiClO_4$ at 0.49 V (vs. Ag/Ag+) in anodic sweep during (a) downward scan and (b) upward scan. Arrow indicates scan direction. (c) and (d) are the lattice images after Fast Fourier Transform (FFT) of (a) and (b), respectively. (e) is the illustration of the real lattice with lattice parameters after the correction of thermal drift. Soft cantilever was used and applied normal load is 4 nN.

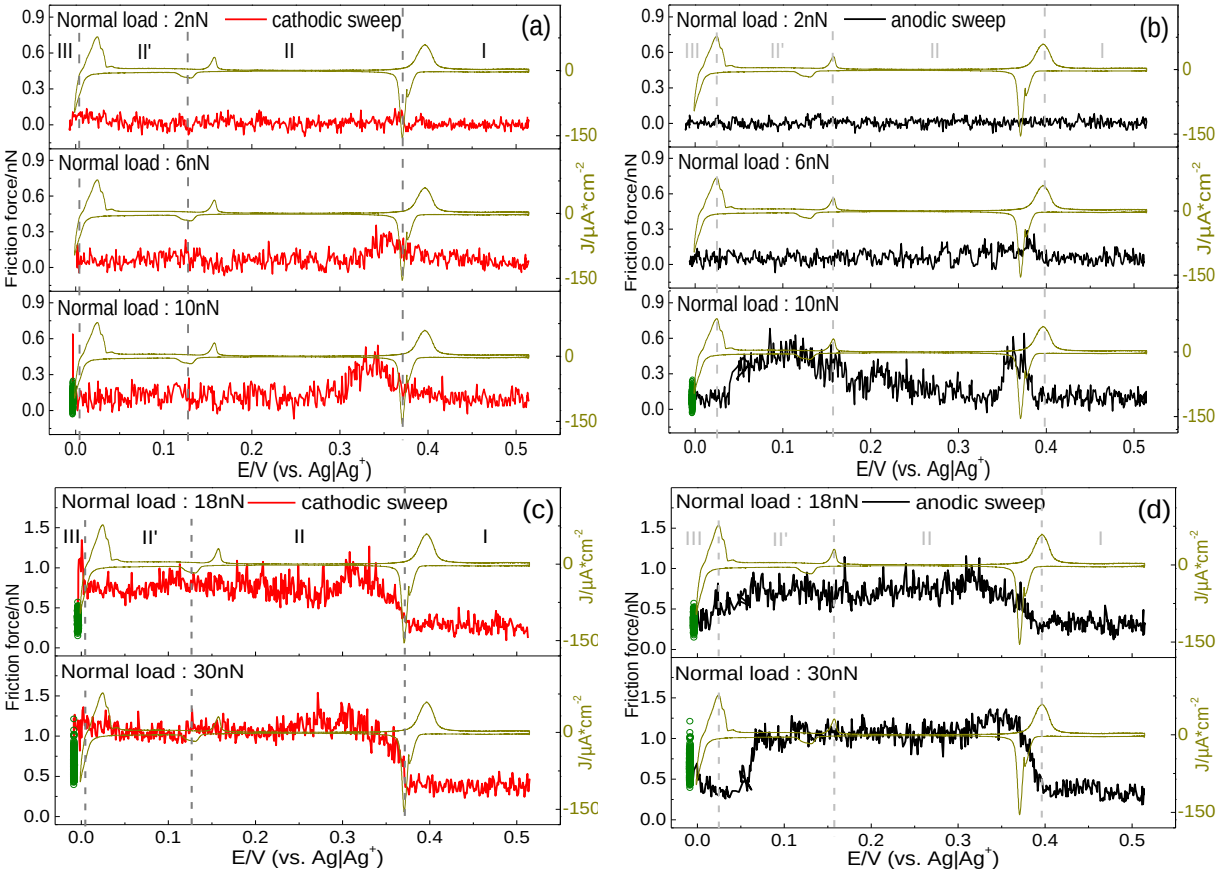

Figure S4.10 Friction force on potential at fixed normal loads during (a) and (c) cathodic sweep and (b) and (d) anodic sweep. Before the anodic sweep, at -0.002 V, observed friction force is shown as green curve. The soft cantilever was used and the spring constant is 0.1±0 05 N/m. The scan rate of AFM image was 0.47 nm/s. Integral and proportional gains were 8 and 13, respectively.

Figure S4.10 shows the dependence of friction on potentials at fixed normal load obtained using soft cantilever. The results show similar behavior as observed using a hard cantilever (Figure 4.7). For too low normal load (F_N < 4nN), no friction change is observed, indicating a minimal load is required to obtain such friction. The hysteresis of friction between cathodic and anodic sweeps appears at the normal load of 10 nN, which indicates that the AFM tip starts to penetrate into iodine layer temporarily when the silver ions are desorbed after the dissolution of Ag bilayer. Due to the mechanical limitation (max. normal load for soft cantilever: ~30 nN), we couldn't observe the friction behavior in region III after the penetration into the iodine layer.

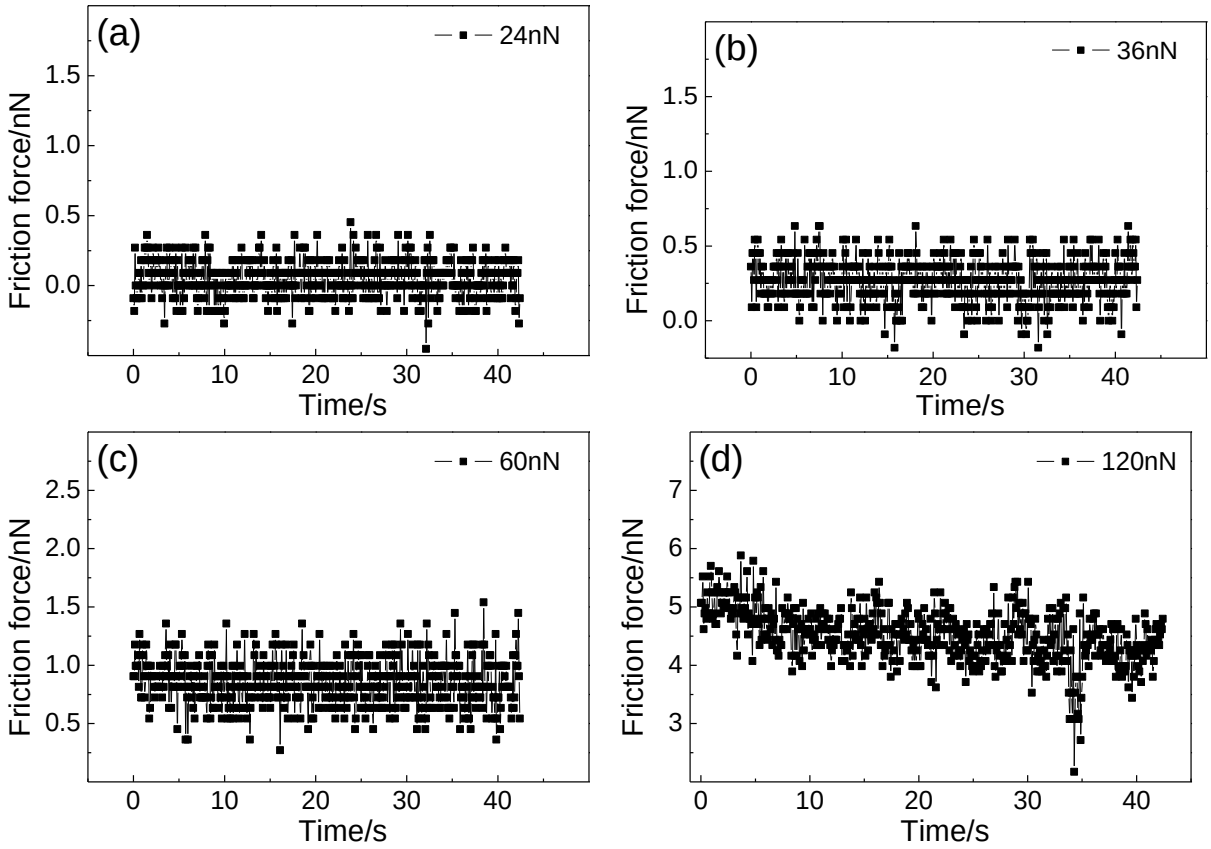

Figure S 4.11 Friction forces as function of time at the 3rd Ag UPD peak, -0.002 V at the normal load of (a) 24 nN, (b) 36 nN, (c) 60 nN, and (d) 120 nN.

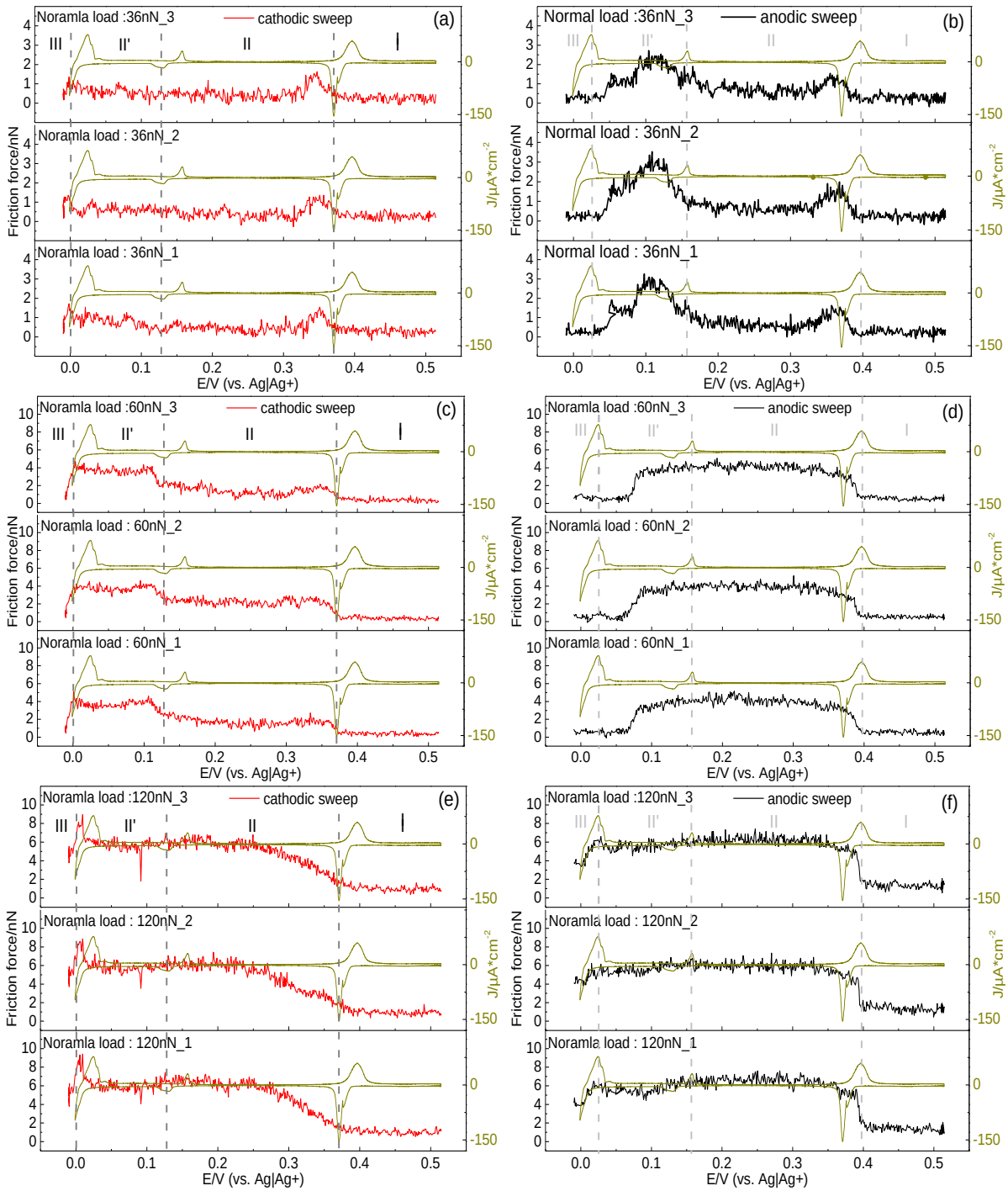

Figure S4.12 Friction force on potential at the fixed normal load at 36 nN during (a) cathodic sweep and (b) anodic sweep, at 60 nN during (c) cathodic sweep and (d) anodic sweep, and at 120 nN during (e) cathodic sweep and (f) anodic sweep. Three different lines were selected to get the friction values.

Calculation of the required normal load to penetrate into the iodine adlayer

We can estimate the penetration force regarding the coverage and strength of iodine layer. The difference of the iodine coverage calculated from obtained structures is around 0.1. Since the difference is not large, we assume that the effect of iodine coverage is same in all potentials. The potential where the iodide starts to adsorb on Au(111) is around -0.2 V(vs. RHE) [45] and the most positive potential during Ag UPD on I-modified Au(111) is around 0.7 V (vs. RHE). Considering that the iodide adsorption is one electron process, the strength of iodine on Au(111) at 0.7 V is 0.9 eV. The iodide forms on Ag(111) a $(\sqrt{3} \times \sqrt{3})R30°$ structure at about - 0.47V (vs. RHE) [46]. Therefore, after the 1st Ag UPD at 0.5 V and 2nd Ag UPD at 0.3V, the strengths of iodide on silver adlayers are around 0.97 eV and 0.77 eV, respectively. Hence, we assume that the average strength of iodine on Au(111) and silver adlayers is about 1 eV to estimate whether the applied force can penetrate into the iodine layer under the AFM tip as shown in eqn (1).

$$V \cdot \Delta p = \frac{F}{A} \cdot V = F \cdot h = 1\ eV\ \times n \tag{1}$$

F is the normal load applied on the AFM tip, A and V are the area and volume where the force applied, respectively. Since we assume that the AFM tip penetrates under the iodine layer, h is the height of iodine monolayer, 0.4 nm. 1eV is $1.602 \cdot 10^{-19}(N \cdot m)$, n is the number of iodine atoms under the AFM tip. If we assume that the contact radius of tip is 4 nm, the number of iodine atoms under the tip is 230 ($\theta_I = 0.33$) and 307 ($\theta_I = 0.44$). Therefore, the required force to penetrate into 307 iodine atoms is about 123 nN.

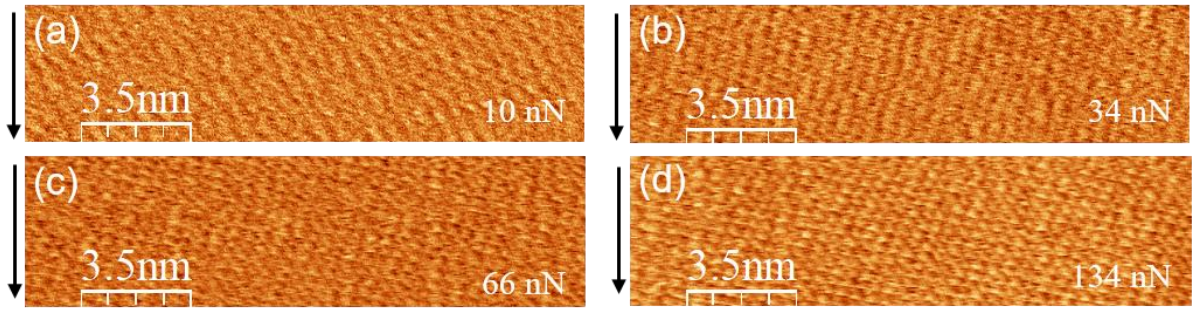

Figure S4.13 Lateral force maps recorded at 0.46 V on I-modified Au(111) in 2 mM $AgClO_4$/ 0.1M $HClO_4$ at different loads: (a) 14 nN, (b) 24 nN, (c) 34 nN, and (d) 74 nN. Iodine structure is observed in (a) and (b). The mixed structure is found in (c) and the structure of Au(111) is observed in (d). The scan size and rate were 20x20 nm² and 0.47 nm/s, respectively.

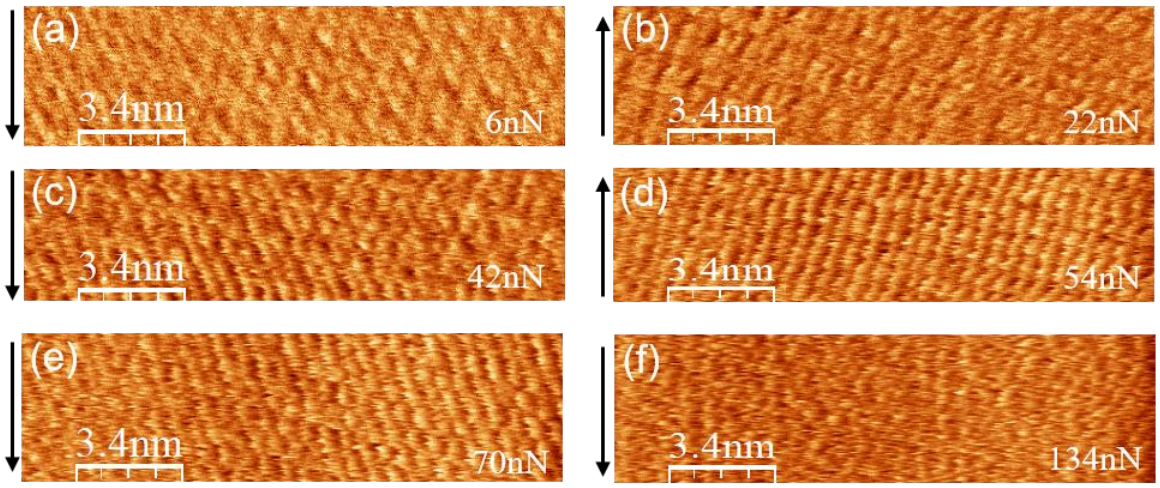

Figure S4.14 Lateral force maps recorded at 0.30 V on I-modified Au(111) in 2 mM $AgClO_4$/ 0.1M $HClO_4$ at different loads: (a) 6 nN, (b) 22 nN, (c) 42 nN, (d) 54 nN, (e) 70 nN, and 134 nN. Iodine structure is observed in (a)-(c). The silver structure is found in (d) and (e). The structure of Au(111) is observed in (f). The scan size and rate were 20x20 nm^2 and 0.47 nm/s, respectively.

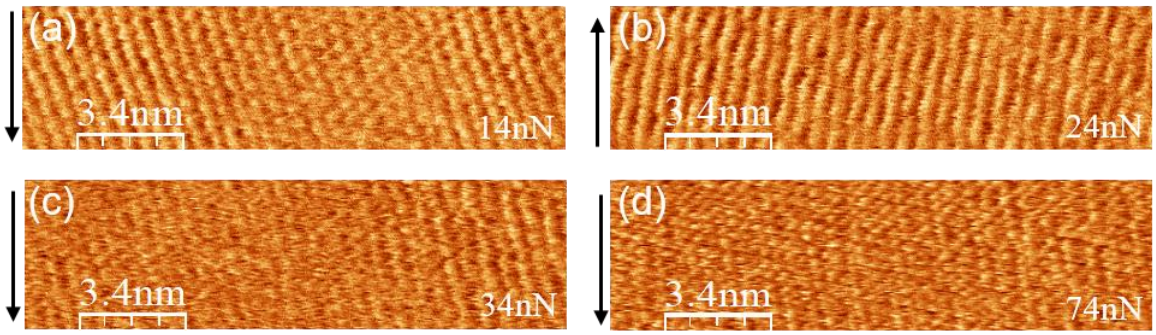

Figure S4.15 Lateral force maps recorded at 0.08 V on I-modified Au(111) in 2 mM $AgClO_4$/ 0.1M $HClO_4$ at different loads: (a) 14 nN, (b) 24 nN, (c) 34 nN, and (d) 74 nN. Iodine structure is observed in (a) and (b). The mixed structure is found in (c) and the Ag (111)(1x1) is observed in (d). The scan size and rate were 20x20 nm^2 and 0.47 nm/s, respectively.

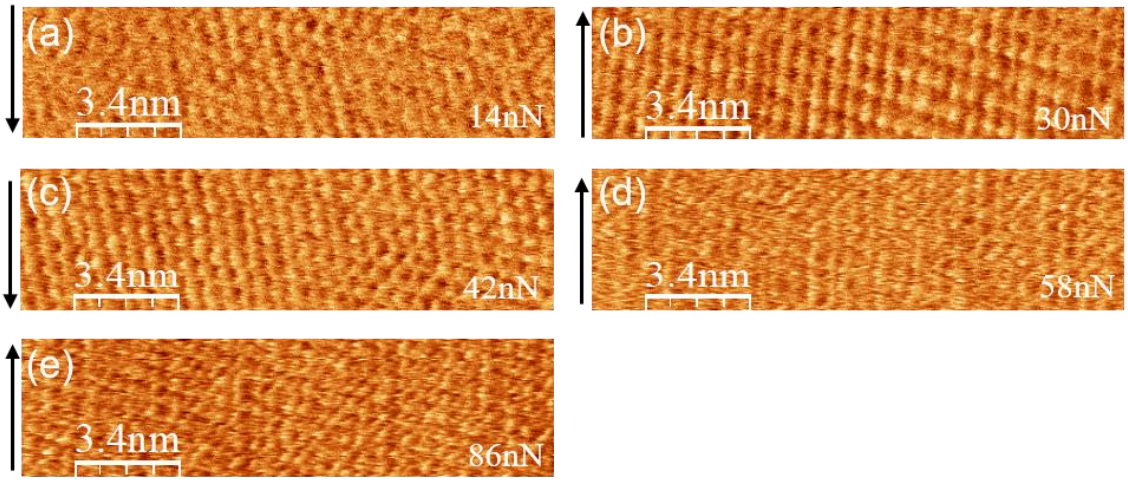

Figure S4.16 Lateral force maps recorded at 0.04 V on I-modified Au(111) in 2 mM $AgClO_4$/ 0.1M $HClO_4$ at different loads: (a) 14 nN, (b) 30 nN, (c) 42 nN, (d) 58 nN, and (e) 86 nN. Iodine structure is observed in (a)-(c). The mixed structure is found in (d) and the Ag (111)(1x1) structure is observed in (e). The scan size and rate were 20x20 nm^2 and 0.47 nm/s, respectively.

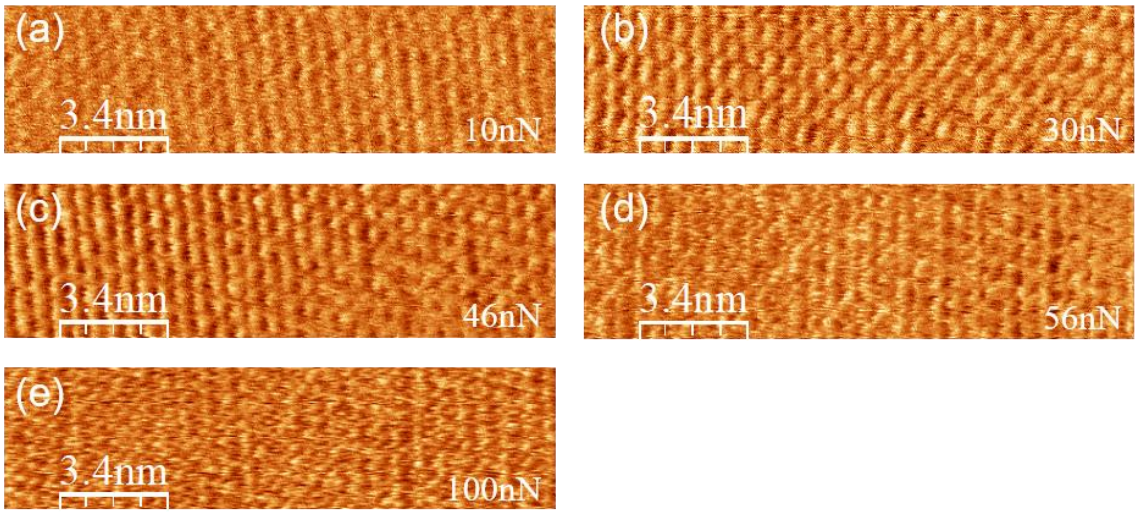

Figure S4.17 Lateral force maps recorded at 0.005 V on I-modified Au(111) in 2 mM $AgClO_4$/ 0.1M $HClO_4$ at different loads: (a) 10 nN, (b) 30 nN, (c) 46 nN, (d) 56 nN, and (e) 100 nN. Iodine structure is observed in (a)-(c). The mixed structure is found in (d) and the Ag bilayer, Ag (111)(1x1) structure is observed in (e). The scan size and rate were 20x20 nm^2 and 0.47 nm/s, respectively.

4.6.2 0.1 mM Ag_2SO_4/0.05 M H_2SO_4

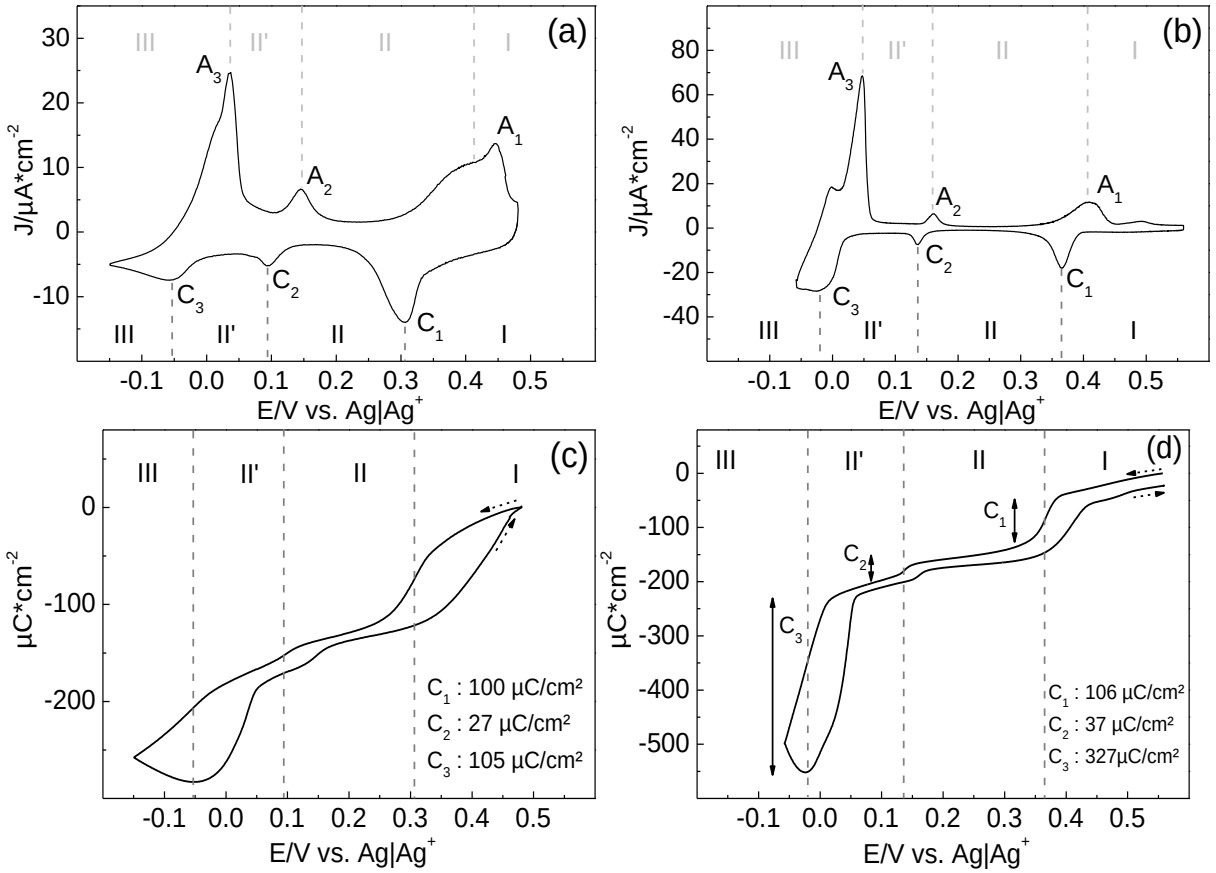

Figure S4.18 Cyclic voltammetry and coulometric curve in H-cell recorded with the sweep rate of (a) 10 mV/s and (b) 5 mV/s for I-modified Au(111) in 0.1 mM $AgClO_4$/0.05 M $HClO_4$.

Reference

[1] J. E. Dubois, P. C. Lacaze, R. Courtel, C. C. Herrmann, D. Maugis *J. Electrochem. Soc.* **1975**, *122*, 1454-1460.

[2] G. Binnig, C. F. Quate, C. Gerber *Physical review letters*. **1986**, *56*, 930.

[3] C. M. Mate, G. M. McClelland, R. Erlandsson, S. Chiang *Physical Review Letters*. **1987**, *59*, 1942-1945.

[4] Y. Mo, K. T. Turner, I. Szlufarska *Nature*. **2009**, *457*, 1116-1119.

[5] I. Szlufarska, M. Chandross, R. W. Carpick *J. Phys. D-Appl. Phys.* **2008**, *41*, 123001.

[6] N. N. Gosvami, T. Filleter, R. Bennewitz *Tribol. Lett.* **2010**, *39*, 19-24.

[7] N. N. Gosvami, P. Egberts, R. Bennewitz *The Journal of Physical Chemistry A*. **2011**, *115*, 6942-6947.

[8] F. Hausen, N. N. Gosvami, R. Bennewitz *Electrochimica acta*. **2011**, *56*, 10694-10700.

[9] A. Labuda, F. Hausen, N. N. Gosvami, P. H. Grütter, R. B. Lennox, R. Bennewitz *Langmuir*. **2011**, *27*, 2561-2566.

[10] M. Nielinger, H. Baltruschat *Physical Chemistry Chemical Physics*. **2007**, *9*, 3965-3969.

[11] F. Hausen, M. Nielinger, S. Ernst, H. Baltruschat *Electrochimica Acta*. **2008**, *53*, 6058-6063.

[12] N. Podgaynyy, S. Wezisla, C. Molls, H. Baltruschat *BEILSTEIN JOURNAL OF NANOTECHNOLOGY*. **2015**, *6*, 820-830.

[13] I. Park, H. Baltruschat *ChemPhysChem*. **2021**, *7*, 1-9.

[14] W. Ouyang, A. S. de Wijn, M. Urbakh *Nanoscale*. **2018**, *10*, 6375-6381.

[15] M. Espladiu, M. Schneeweiss, D. Kolb *Physical Chemistry Chemical Physics*. **1999**, *1*, 4847-4854.

[16] T. Hachiya, K. Itaya *Ultramicroscopy*. **1992**, *42*, 445-452.

[17] K. Ogaki, K. Itaya *Electrochimica acta*. **1995**, *40*, 1249-1257.

[18] C. H. Chen, S. M. Vesecky, A. A. Gewirth *Journal of the American Chemical Society*. **1992**, *114*, 451-458.

[19] P. Mrozek, Y.-e. Sung, M. Han, M. Gamboa-Aldeco, A. Wieckowski, C.-h. Chen, A. A. Gewirth *Electrochimica acta*. **1995**, *40*, 17-28.

[20] V. Rooryck, F. Reniers, C. Buess-Herman, G. A. Attard, X. Yang *Journal of electroanalytical chemistry*. **2000**, *482*, 93-101.

[21] M. Azhagurajan, T. Itoh, K. Itaya *The Journal of Physical Chemistry C*. **2016**, *120*, 16221-16227.

[22] T. Kondo, J. Morita, M. Okamura, T. Saito, K. Uosaki *Journal of Electroanalytical Chemistry*. **2002**, *532*, 201-205.

[23] S. Sugita, T. Abe, K. Itaya *The Journal of Physical Chemistry*. **1993**, *97*, 8780-8785.

[24] D. Zurawski, L. Rice, M. Hourani, A. Wieckowski *J. Electroanal. Chem.* **1987**, *230*, 221-231.

[25] J. E. Sader, J. W. M. Chon, P. Mulvaney *Rev. Sci. Instrum.* **1999**, *70*, 3967-3969.

[26] R. Espinosa-Marzal, A. Arcifa, A. Rossi, N. Spencer *The journal of physical chemistry letters*. **2014**, *5*, 179-184.

[27] S. Iqbal, L. Zan, E. Nardi, H. Baltruschat *Phys. Chem. Chem. Phys.* **2018**, *20*, 6176-6186.

[28] S. Sundararajan, B. Bhushan *J. Appl. Phys.* **2000**, *88*, 4825-4831.

[29] E. Meyer, R. Luthi, L. Howald, M. Bammerlin, M. Guggisberg, H. J. Guntherodt *J. Vav. Sci. Technol. B*. **1996**, *14*, 1285-1288.

[30] T. Müller, M. Lohrmann, T. Kässer, O. Marti, J. Mlynek, G. Krausch *Physical review letters*. **1997**, *79*, 5066.

[31] H. Hoelscher, D. Ebeling, U. D. Schwarz *PHYSICAL REVIEW LETTERS*. **2008**, *101*, 246105.

[32] N. Sisson, Y. GruÌˆnder, C. A. Lucas *The Journal of Physical Chemistry C*. **2016**, *120*, 16100-16109.

[33] K. Itaya, N. Batina, T. Yamada *Journal of Physical Chemistry*. **1995**, *99*, 8817-8823.

[34] W. Haiss, J. K. Sass, X. Gao, M. J. Weaver *Surf. Sci.* **1992**, *274*, L593-L598.

[35] X. P. Gao, M. J. Weaver *J. Am. Chem. Soc.* **1992**, *114*, 8544-8551.

[36] R. L. McCarley, A. J. Bard *J. Phys. Chem.* **1991**, *95*, 9618-9620.

[37] N. Batina, J. W. McCargar, G. N. Salaita, F. Lu, L. Lagurendavidson, C. H. Lin, A. T. Hubbard *Langmuir*. **1989**, *5*, 123-128.

[38] H. W. Cheng, P. Stock, B. Moeremans, T. Baimpos, X. Banquy, F. U. Renner, M. Valtiner *Advanced Materials Interfaces*. **2015**, *2*, 1500159.

[39] I. Park, H. Baltruschat. **In process**.

[40] H. K. Christenson *The Journal of chemical physics*. **1983**, *78*, 6906-6913.

[41] A. Socoliuc, R. Bennewitz, E. Gnecco, E. Meyer *Physical review letters*. **2004**, *92*, 134301.

[42] G. Valette *J. Electroanal. Chem.* **1989**, *269*, 191-203.

[43] B. C. Schardt, S. L. Yau, F. Rinaldi *Science*. **1989**, *243*, 1050-1053.

[44] R. Vogel, I. Kamphausen, H. Baltruschat *Ber. Bunsenges. Phys. Chem.* **1992**, *96*, 525.

[45] B. M. Ocko, J. Wang, G. M. Watson *J. Phys. Chem.* **1994**, *98*, 897-906.

[46] A. T. Hubbard, G. N. Salaita, F. Lu, L. Laguren-Davidson *J. Electroanal. Chem.* **1987**, *229*, 1-17.

CHAPTER 5

Copper underpotential deposition (UPD) on Au(111) and I-modified Au(111) in aqueous electrolyte

5.1 Introduction

The deposition of foreign metals on a metal substrate often starts at more positive potential than the equivalent bulk deposition, called underpotential deposition (UPD) [1]. The Cu UPD on gold electrode has been studied exhaustively using various techniques, which reveals that this is strongly influenced by the co-adsorbed anions (e.g. Br^-, Cl^-, SO_4^{2-}) [2-10]. A. Martíubez-Ruíz et al. have reported that on I-modified Au(111) the deposition mechanism is different compared to the case on bare Au(111) in Cu^{2+} containing sulfuric acid [11, 12]. The structure or the coverage of Cu UPD layer on Au(111) has been investigated by STM measurements [13-15], electrochemical quartz crystal microbalance (EQCM) [16], extended X-ray adsorption fine structure (EXAFS) [17], and ex-situ electron diffraction [6]. Commonly, a $(\sqrt{3} \times \sqrt{3})R30°$ structure is observed slightly negative of the 1st Cu UPD peak, C_2, which indicates the 2/3 coverage of Cu monolayer and 1/3 coverage of sulfate.

Friction forces obtained using lateral force microscope (LFM) under electrochemical conditions give us hints to understand the interfacial interaction between sliding tip and the surface where electrochemical reactions occur (e.g. adsorption (or desorption) of ions, deposition of foreign metals). M. Nielinger et al. have shown frictional changes during Cu UPD on Au(111) [18]. At low normal load, up to 30 nN, friction increases as Cu forms 2/3 ML but there is no frictional

change between Cu 2/3 ML and a Cu monolayer. However, at high normal load (F_N > 75 nN), friction force shows further increase as the coverage of Cu increases from 2/3 to 1. They assumed that the tip invades (or penetrates) into the sulfate adlayer on 2/3 ML and a monolayer of Cu, which results in the steep increase of friction with normal load as Cu coverage increases from 2/3 ML to 1 ML. At 0.35 V vs. Cu/Cu^{2+}, positive of Cu UPD, where sulfate is not adsorbed on Au(111), there is no steep increase of friction with normal load, which leads to low friction compared to friction on Cu adlayer. R. Bennewitz et al. have examined the frictional behavior as function of potential during Cu UPD on Au(111) at three different normal loads [19]. They showed that the friction increases as copper is deposited on Au(111) but when copper forms 2/3 ML followed by the adsorption of sulfate forming a $(\sqrt{3} \times \sqrt{3})R30°$ structure, the observed friction forces are lower than that on Au(111). This is contradiction to the results by M. Nielinger et al., but when the coverage of Cu increases from 2/3 to 1, they observed further increase of the friction as also observed by M. Nielinger et al. N. Podgaynyy et al. have reported friction as function of normal load during Cu UPD on Au(111). They observed that friction increases steeply at about 20 nN when the copper forms 2/3 ML and a monolayer. For Cu 2/3 ML, at the normal load above 150 nN, friction forces seem to increase steeply again and for a monolayer of copper, friction forces increase dramatically again at about 70 nN. Interestingly, they observed multiple stick-slips with increasing normal load when the copper forms a monolayer. F. Hausen et al. [20] and A. Labuda et al. [21] have studied the effect of trace amount of chloride on friction during Cu UPD. A. Labuda et al. observed similar Cu lattice constant of 3.67 Å, confirming that the chloride forms the so-called (5×5) structure in the electrolyte containing trace amount of chloride (10^{-5} M) [22]. They observed relatively low friction with normal load compared to the results during the Cu UPD in sulfuric acid, which might result from the co-adsorbed chloride.

Based on previous friction studies, we re-investigate the frictional behavior on Au(111) with potential in Cu^{2+} containing sulfuric acid. Furthermore, we present here the friction forces as function of potential on I-modified Au(111) during Cu UPD and compare it to our previous work on Ag UPD on (I-) Au(111).

5.2 Experimental

A disc type Au(111) single crystal(diameter: 10mm and thickness: 3mm) purchased from MaTecK GmbH was used as working electrode. It was annealed by flame and cooled down above Milli-Q water to get the clean surface. For a monolayer of iodine, the annealed crystal was cooled down above iodine crystals purged with Ar. Gold and copper wires were used as counter and reference electrodes, respectively. For electrolytes, 1mM $CuSO_4$ and 0.05M H_2SO_4 were dissolved in Milli-Q water.

Lateral (frictional) force measurements were performed using the Agilent 5500 AFM, combined with an atmosphere chamber. Silicon tips (PPP-FM and PPP-CONTSC, NANOSENSORS, tip radius <10nm) were used and the normal force constants were 1.13 N/m and 0.1±0.05 N/m. Normal and torsional resonance frequency of AFM tips were measured by AFM (Agilent 5500/AC mode). The Q factor for theses resonance frequencies was obtained using the equation of simple harmonic oscillation (SHO) [23]. Normal and torsional force constants were calculated using the Sader method and the lateral force constant was obtained by dividing torsional force constant with the square of the tip height [23, 24]. During the measurement, a homemade AFM cell was used, which contains a three-electrode assembly and Ar was purged through the atmosphere chamber.

We investigated structures using atomic corrugation observed in lateral force maps and PPP-CONTSC (k_N = 0.1±0.05 N/m) was used. To get the clear lattice image, fast Fourier transform (FFT) was used and thermal drift was corrected [25]. The illustration contains the lattice parameter after the correction of thermal drift.

When the AFM tip scans the surface, friction (F) makes it twist, leading to the deflection of the laser beam. The sign of the deflection depends on the scan direction. In addition, the deflection of the laser is caused by topography (T) (e.g. steps on the surface) and does not depend on scan direction. Thus, the forward image and backward image contain [T+F] and [T-F], respectively. Friction force data was obtained by subtracting the backward data from the forward data and dividing it by 2 to eliminate topographic effects [26].

In measurements of friction forces as function of potential, PPP-CONTSC (k_N = 0.1±0.05 N/m), soft cantilever, and PPP-FM (k_N = 1.13), hard cantilever, were used. The scan size and scan rate of lateral force map were 20nm² and 0.47 nm/s, respectively.

5.3 Results and discussion

5.3.1 Cyclic voltammetry (CV)

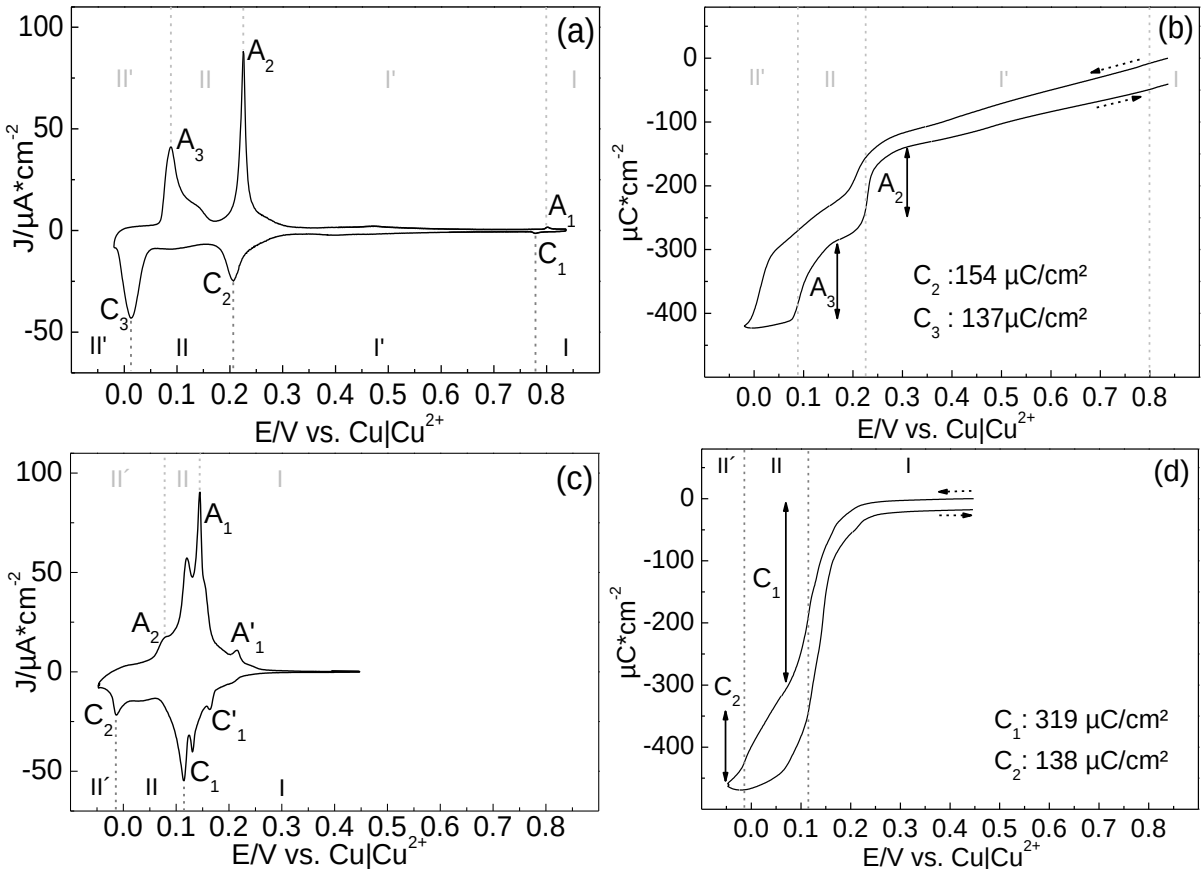

Figure 5.1 (a) Cyclic voltammetry in H-cell and (b) coulometric curve for Au(111) in 2mM $CuSO_4$/0.05M H_2SO_4. (c) Cyclic voltammetry in H-cell and (d) coulometric curve for I-modified Au(111) in 2 mM $CuSO_4$/0.05 M H_2SO_4. The sweep rate was 9 mV/s.

Figure 5.1a shows cyclic voltammetry (CV) for the bare Au(111) electrode in 2 mM $CuSO_4$/ 0.05M H_2SO_4. The peak appearing at about 0.8 V (vs. Cu/Cu^{2+}), C_1/A_1, is the spike for the indication of ordered sulfates on Au(111) , a $(\sqrt{3} \times \sqrt{7})R19.1°$ structure. As reported before [13-15, 27, 28], we observed two peaks for the Cu UPD, C_2/A_2 and C_3/A_3 corresponding to the formation of 2/3 ML and full monolayer, respectively. The peak A_3 depends sensitively on the quality of the crystal surface, meaning that well-prepared surfaces lead to a sharp peak A_3 [27]. The peak C_2 is much smaller than A_2, which is due to the slow rate of the Cu UPD on Au(111) [13]. Regarding the status of adsorbates (SO_4^{2-} and Cu), we distinguish 4 different regions (I, I´, II, and II´).

Figure 5.1c shows the cyclic voltammetry for the I-modified Au(111) in 2 mM $CuSO_4$/ 0.05 M H_2SO_4. N. Batina et al. reported that Cu underpotential deposition (UPD) on I-modified Au(111) ($\theta_I = 0.37$) takes place in a two-step process and kinetics of Cu UPD on I-modified Au(111) is lower than for Cu UPD on clean Au(111) [11, 12]. Comparable to this observation, we observed two sets of the Cu UPD peaks together with small peaks, C_1/A_1, C_2/A_2. As shown in Figure 5.1d, the coulometric curve on I-modified Au(111) shows that the copper is continuously deposited on I-modified Au(111) with decreasing potential. The charge densities for the peak C_1 and C_2 are approx. 319 and 138 µC/cm², indicating that slightly negative of the 1st Cu UPD peak C_1, the coverage of Cu is 2/3 ML and a Cu monolayer is completed negative of the 2nd Cu UPD peak, C_2. Considering the UPD process, we divide the potential range into 3 different regions (I, II, and II´).

5.3.2 The structure: atomic corrugation in friction

At 0.14 V (region II) where copper forms 2/3 ML, in agreement with the previous literature[13-15], lateral force images show a $(\sqrt{3} \times \sqrt{3})R30°$ structure (Figure 5.2). At about 0 V (region II´), it is known that copper completes a monolayer and a $(\sqrt{3} \times \sqrt{7})$ structure is observed (Figure S5.1). It was not easy to get well resolved atomic corrugations at this potential due to the disturbance of multiple stick-slips with normal load. During the anodic sweep, the structure of copper at 0.15 V (region II) shows the same structure as observed in the cathodic sweep as shown in Figure 5.3.

Figure 5.4 shows the structure of iodine adlayer on Au(111) at 0.32 V, before the deposition of copper (region I). It reveals that the iodine forms a $(\sqrt{3} \times \sqrt{3})R30°$ structure ($\theta_I = 0.33$). When the potential is swept to 0.15 V, the structure changes to the $p(3 \times 3)$ structure as shown in Figure 5.5. As the potential decreases further down to 0.09 V (region II), the $p(3 \times 3)$ structure transforms to the $(\sqrt{3} \times \sqrt{3})R30°$ structure (Figure 5.6). When the potential approaches the peak C_2 ($\theta_{Cu} \approx 1$), it was hard to get well resolved atomic corrugation.

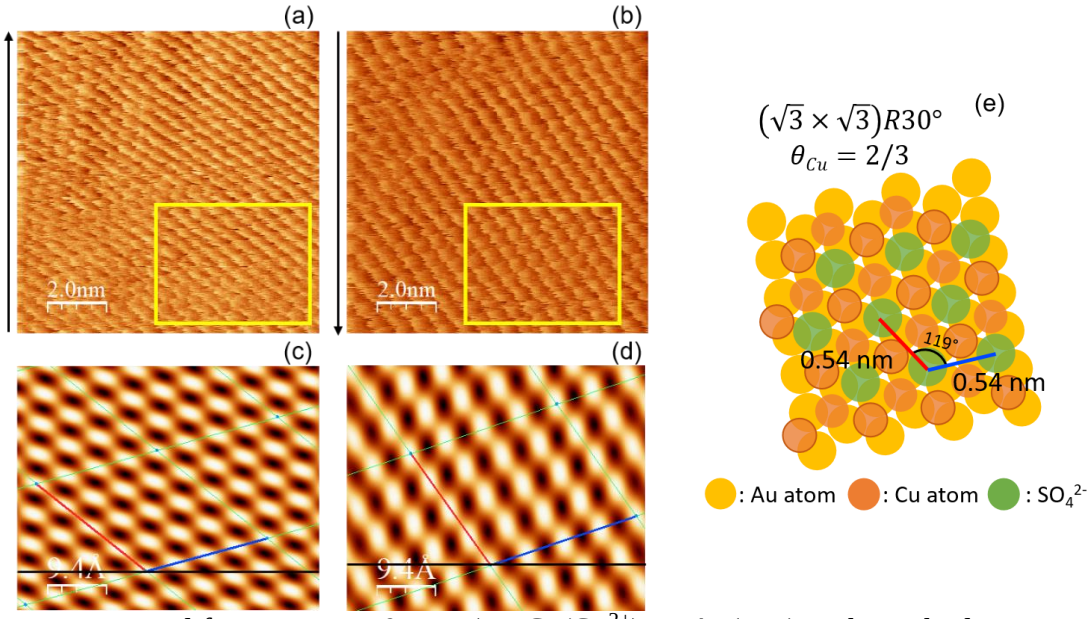

Figure 5.2 Lateral force maps at 0.14V (vs. Cu/Cu^{2+}) on Au(111) in the cathodic sweep during (a) upward scan and (b) downward scan. Arrow indicates scan direction. (c) and (d) are the lattice images after Fast Fourier Transform (FFT) of (a) and (b), respectively. (e) is the illustration of the real lattice with lattice parameters after the correction of thermal drift. Soft cantilever (k_N = 0.1±0.05 N/m) is used and applied normal load is 5nN.

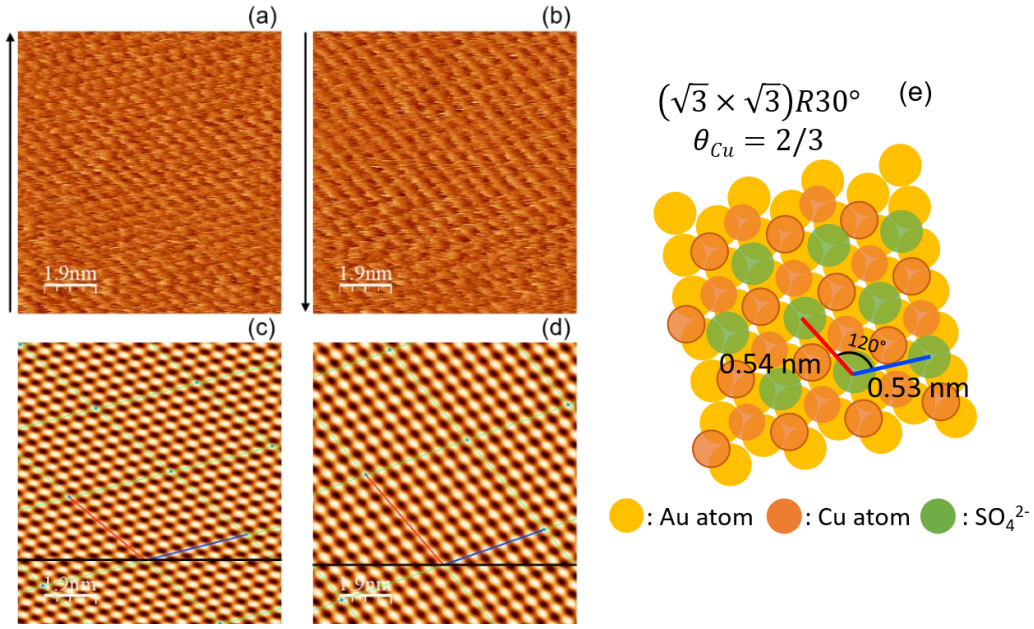

Figure 5.3 Lateral force maps at 0.15V (vs. Cu/Cu^{2+}) on Au(111) in the anodic sweep during (a) upward scan and (b) downward scan. Arrow indicates scan direction. (c) and (d) are the lattice images after Fast Fourier Transform (FFT) of (a) and (b), respectively. (e) is the illustration of the real lattice with lattice parameters after the correction of thermal drift. Soft cantilever (k_N = 0.1±0.05 N/m) is used and applied normal load is 5nN.

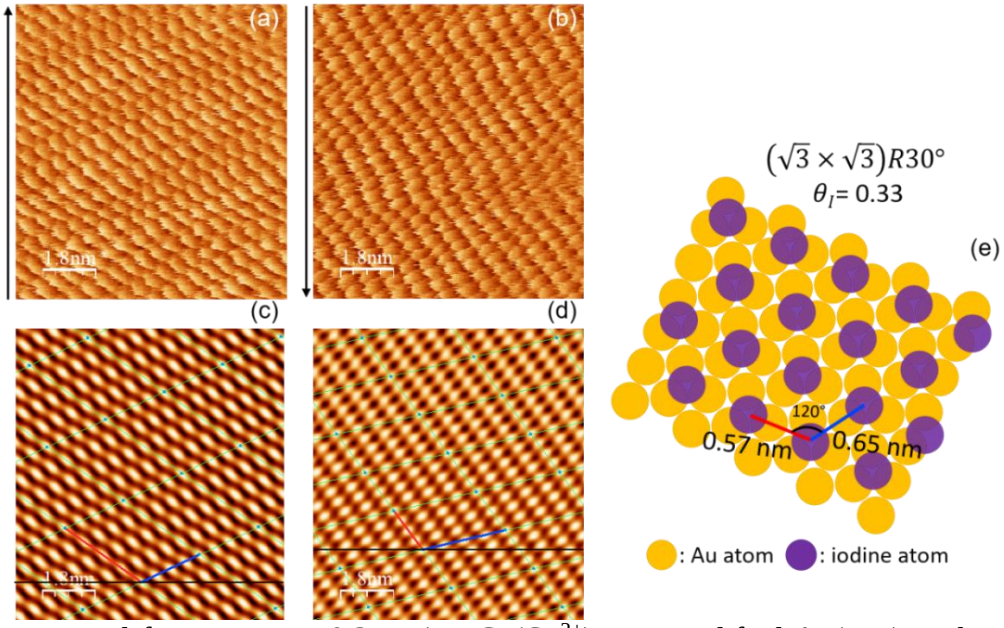

Figure 5.4 Lateral force maps at 0.32V (vs. Cu/Cu^{2+}) on I-modified Au(111) in the cathodic sweep during (a) upward scan and (b) downward scan. Arrow indicates scan direction. (c) and (d) are the lattice images after Fast Fourier Transform (FFT) of (a) and (b), respectively. (e) is the illustration of the real lattice with lattice parameters after the correction of thermal drift. Soft cantilever (k_N = 0.1±0.05 N/m) was used. Applied normal load is 4nN.

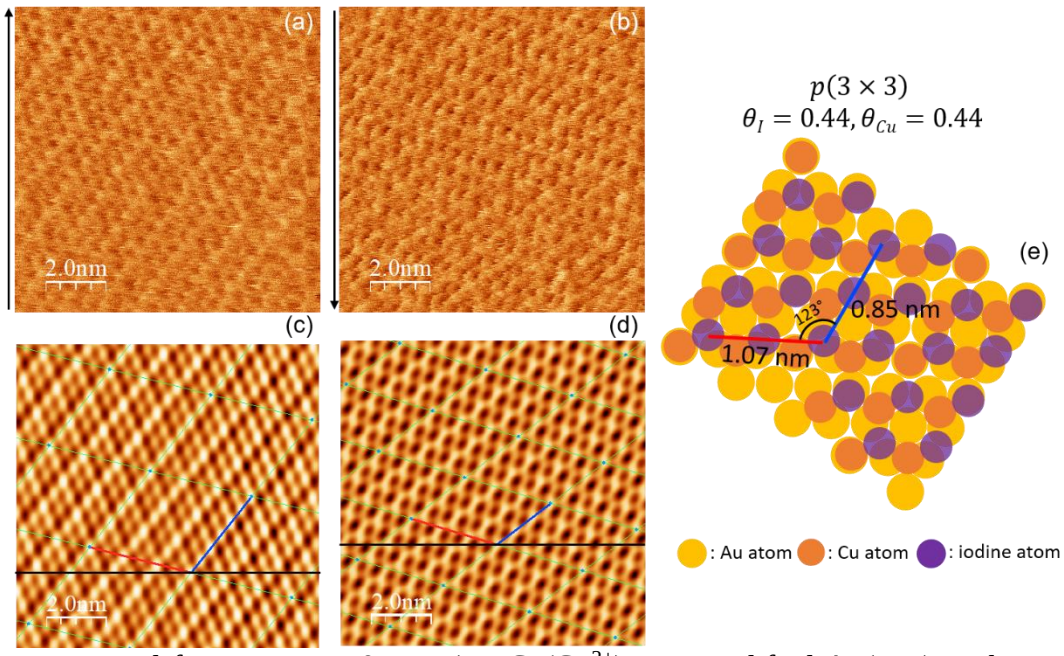

Figure 5.5 Lateral force maps at 0.15V (vs. Cu/Cu^{2+}) on I-modified Au(111) in the cathodic sweep during (a) upward scan and (b) downward scan. Arrow indicates scan direction. (c) and (d) are the lattice images after Fast Fourier Transform (FFT) of (a) and (b), respectively. (e) is the illustration of the real lattice with lattice parameters after the correction of thermal drift. Soft cantilever (k_N = 0.1±0.05 N/m) was used. Applied normal load is 4nN.

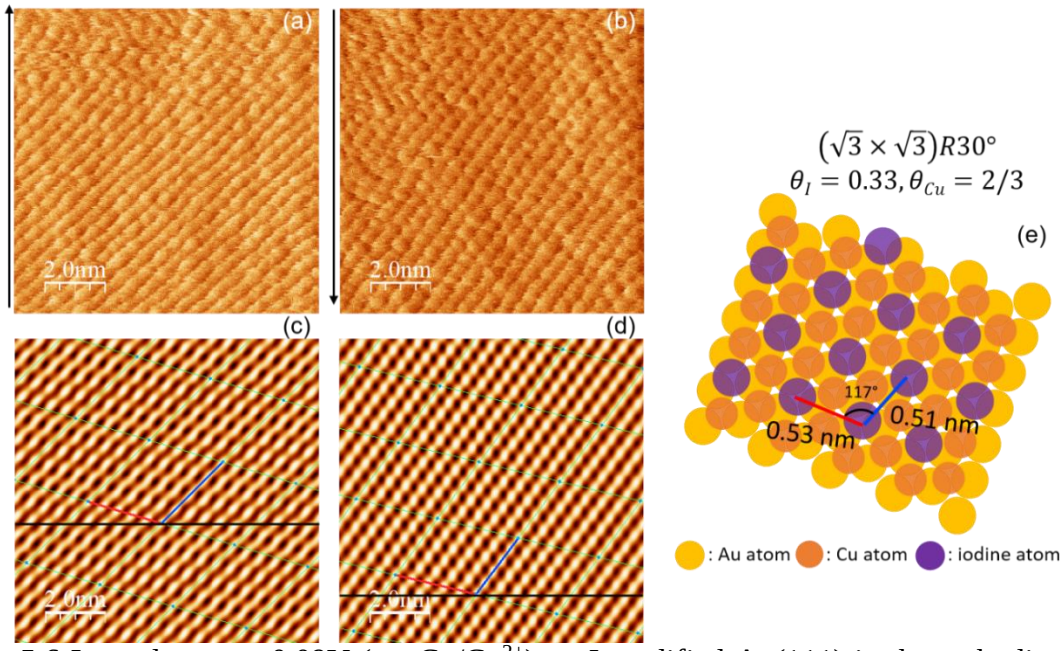

Figure 5.6 Lateral map at 0.09V (vs. Cu/Cu^{2+}) on I-modified Au(111) in the cathodic sweep during (a) upward scan and (b) downward scan. Arrow indicates scan direction. (c) and (d) are the lattice images after Fast Fourier Transform (FFT) of (a) and (b), respectively. (e) is the illustration of the real lattice with lattice parameters after the correction of thermal drift. Soft cantilever (k_N = 0.1±0.05 N/m) was used. Applied normal load is 4nN.

Atomic corrugation in lateral force maps was observed during the cathodic sweep in order to examine the transition of structures as the coverage of copper changes. Figure S5.2 shows the clear transition of iodine structures with potential. As mentioned above, the iodine forms a $(\sqrt{3} \times \sqrt{3})R30°$ structure on Au(111) in the beginning of the potential region I. In contrast, A. Martínez-ruíz et al. observed a $c(p \times \sqrt{3}R30°)$ structure before Cu UPD on I-modified Au(111) [11, 12]. Considering that they prepared the iodine adlayer by dipping the Au(111) in the iodine containing electrolyte, the initial structure of the iodine is closely related to the preparation of iodine adlayer. When the potential passes the peak C_1' at about 0.17 V, a $p(3 \times 3)$ structure is observed (Figure S5.2, ii). Considering the charge density at 0.12 V (195 µC/cm²), it is suggested that the coverage of copper is about 0.44 and copper forms a $p(3 \times 3)$ structure, resulting in same structure for the iodine adlayer as the case of Ag UPD on I-modified Au(111) (see chapter 4). A. Martínez-ruíz et al. observed the transition of iodine structures from a $c(p \times \sqrt{3}R30°)$ structure to a $p(3 \times 3)$ structure ($d_{I\text{-}I}$: 0.43 nm) at potentials between 0.3 V and 0.24 V (vs. Cu/Cu^{2+}) even though the consumed charge is very small [11, 12]. Furthermore, they observed a complete hexagonal but compressed structure ($d_{I\text{-}I}$: 0.41 nm) at 0.12 V. As the potential passes the peak C_1, the clear height difference in a $p(3 \times 3)$ structure disappears but the angle of the lattice structure is still same with a $p(3 \times 3)$ structure (Figure S5.2, iii). It is

noteworthy that at a constant potential, 0.09 V (Figure 5.6), the observed lattice corresponds to a $(\sqrt{3} \times \sqrt{3})R30°$ structure. This indicates that the further deposition of copper causes a transitorily dense $p(3 \times 3)$ structure due to relatively short time for the relaxation or rearrangement of iodine on Cu adlayer. Together with charge density, it is therefore expected that the copper forms a graphite-like honeycomb structure ($\theta_{Cu} = 0.67$) at 0.09 V [29] and after certain time, the iodide is situated on the vacancies of copper as the case of sulfate on the Cu 2/3 ML. When a potential swept further (Figure S5.2, iv), the angle of observed lattice resembles a $(\sqrt{3} \times \sqrt{3})R30°$ structure, in agreement with the results from A. Martínez-ruíz et al. [12]. Therefore, it is reasonable to assume that the iodine forms a $(\sqrt{3} \times \sqrt{3})R30°$ structure on a Cu monolayer.

5.3.3 Friction force as function of potential

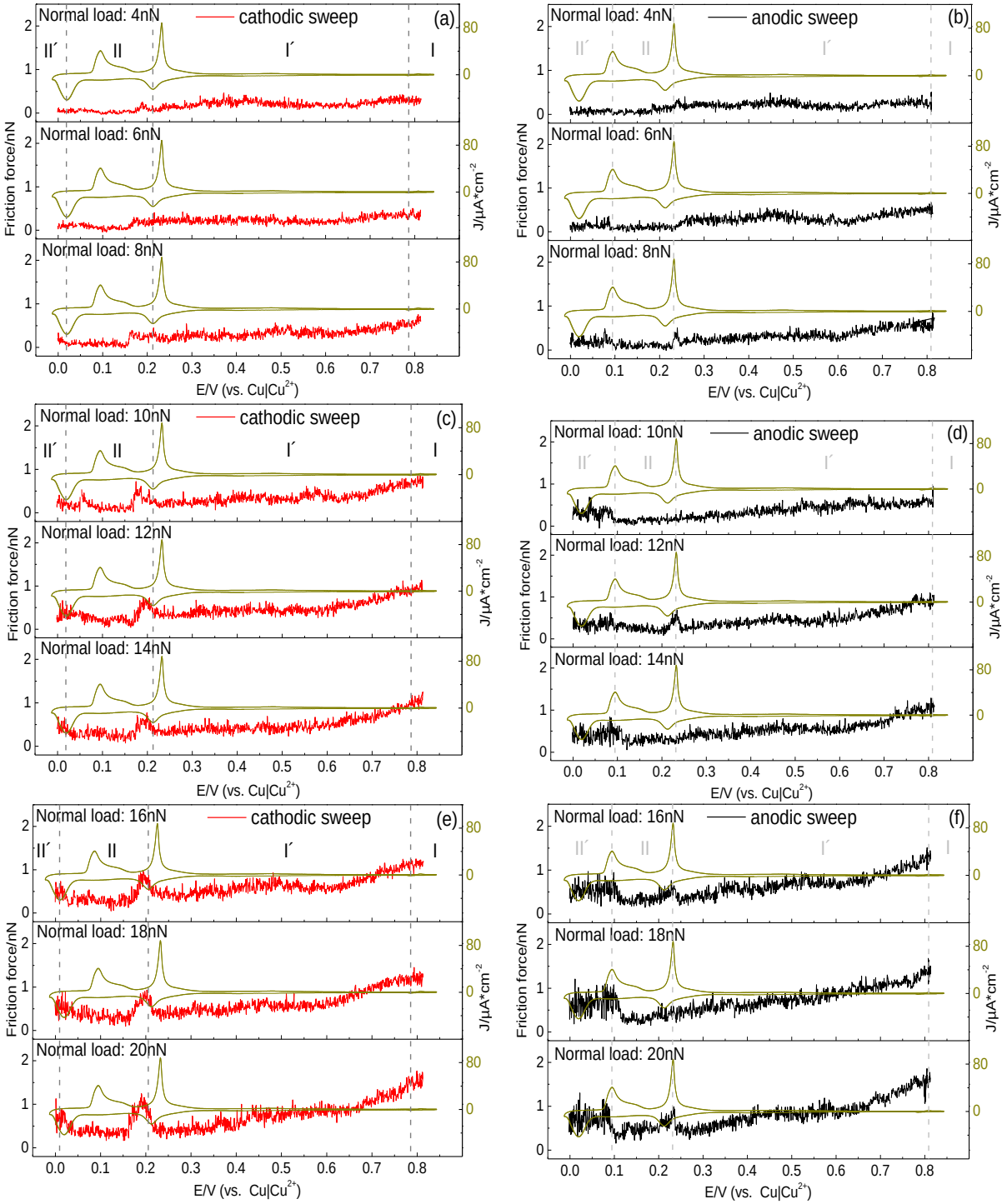

Figure 5.7 Friction forces on potential for Au(111) at fixed normal loads during (a), (c), and (e) cathodic sweep and (b), (d), and (f) anodic sweep. Soft cantilever (k_N = 0.1±0.05 N/m) was used. The scan rate of AFM image was 0.47nm/s.

We have studied the dependence of friction force on normal load during Cu UPD on Au(111) [18, 20, 28]. These results show that the frictional behavior strongly depends on the coverage of the

copper and adsorbed anions. Here, we extended the study to the friction change when a potential swept to investigate the influence of adsorbates on the friction during Cu UPD in more detail. The results obtained by hard cantilever are given in the Supporting information (Figure S5.3-4).

Figure 5.7 shows the dependence of friction on potential. In region I, the adsorbed sulfate forms a $\left(\sqrt{3} \times \sqrt{7}\right)R19.1°$ structure ($\theta = 0.22$) on Au(111). When the potential is swept to region I´, adsorbed sulfate is disordered and the coverage decreases with decreasing potential. As reported in our previous paper [20], the coverage of sulfate on Au(111) is a key factor to understand the frictional behavior in potential region I and I´. Thus, friction decreases with decreasing the coverage of sulfate.

When the potential passes the peak C_2, 1st Cu UPD, friction forces sharply increase for normal loads above a minimum load (F_N > 8 nN). However, friction forces decreases again negative of the peak C_2 upon completion of the 2/3 Cu adlayer. As in the case of the adsorbed sulfate on Au(111), increasing the coverage of copper on Au(111) causes the increase of friction when the potential passes the peak C_2. Whenever the coverage of copper reaches 2/3 ML and sulfate sits on the hollow site of the honeycomb structure, friction forces decrease again. In the potential region II´ where the copper forms a monolayer, friction forces are higher than that for Cu 2/3 ML (region II), which is more clearly observed in the anodic sweep as observed in previous papers from our group [20, 28]. Furthermore, as reported by N. Podgaynyy et al.[28], the multiple stick-slips are observed only on a Cu monolayer as normal load increases (Figure 5.8). At the normal load of 4 nN where the single stick-slip occurs, the distance between sticks is approx. 0.76 nm, in agreement with one of mean distances in the $\left(\sqrt{3} \times \sqrt{7}\right)$ structure ($\sqrt{3} \cdot d_{Au} = 0.5, \sqrt{7} \cdot d_{Au} = 0.76$). With increasing the normal load, the distance of sticks increases to about 1.4 nm, corresponding to double slip. These multiple stick-slips are clearer in the results observed using the hard cantilever (Figure S5.4) and triple slip is also observed.

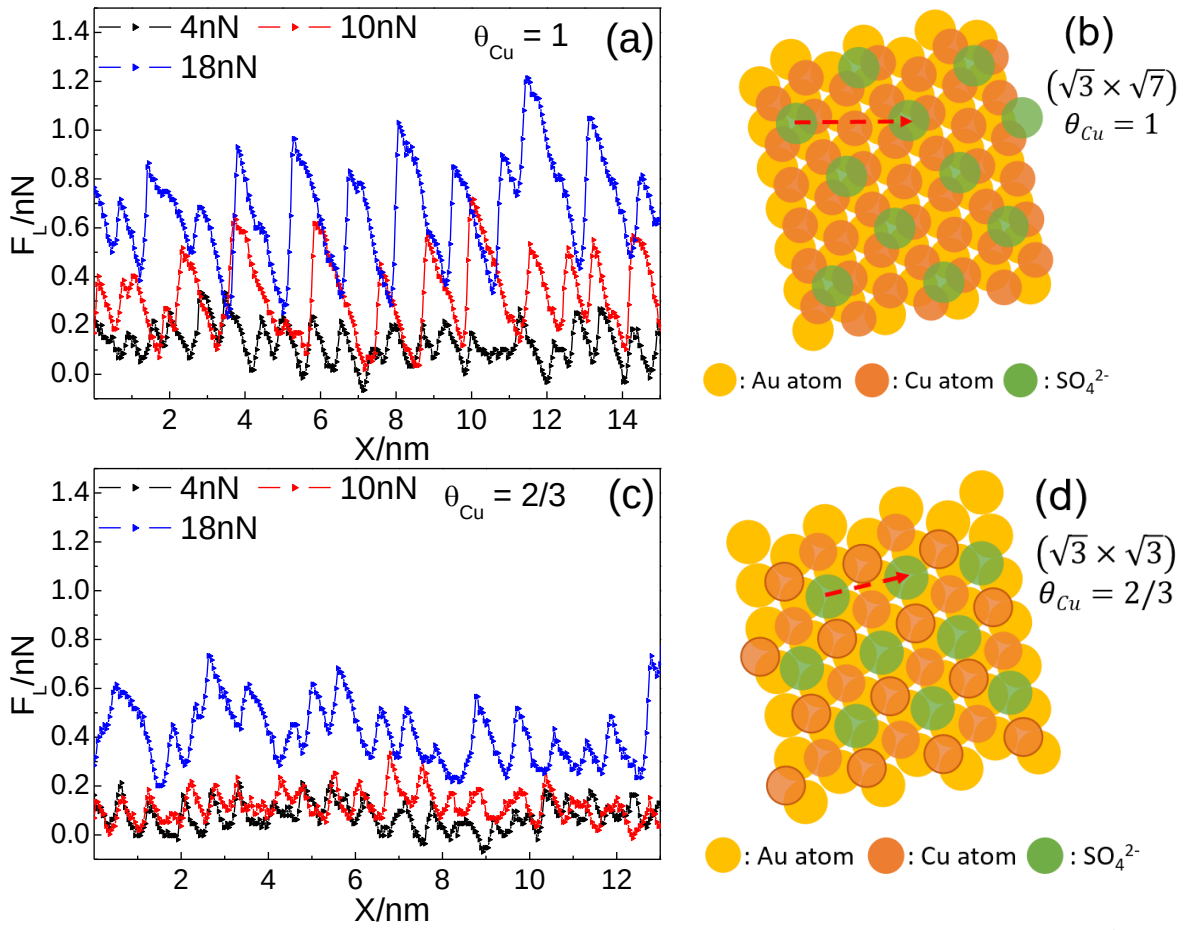

Figure 5.8 Atomic stick-slip when the Cu forms (a) a monolayer (E = 0.05 V vs. Cu/Cu^{2+}) and (c) a 2/3 monolayer (E = 0.125 V) on Au(111) at normal loads of 4, 10, and 18nN. Schematic illustration of the sulfate structure (b) $(\sqrt{3} \times \sqrt{7})$ on the Cu monolayer and (d) $(\sqrt{3} \times \sqrt{3})$ on 2/3 Cu monolayer. Red arrow in (b) and (d) indicate the possible way for the atomic stick-slip. Soft cantilever (k_N = 0.01±0.05 N/m) was used.

The results observed using the hard cantilever also show a similar behavior when the potential passes the 1st Cu UPD peak for normal loads below 60 nN (Figure S5.3). At high normal load with the hard cantilever, 100 nN, friction shows a plateau and the decrease of friction seems to be slightly delayed, which might indicate the time effect or potential effect on Cu UPD. Thus, it is reasonable to expect that the deposition of Cu paralleled by the adsorption of sulfate is hindered at high normal load, which might require longer time or more negative potential to reach the coverage 2/3 ML. In addition, compared to the results observed using the soft cantilever (Figure 5.7), at 100 nN, the friction increases in order of Au(111) < Cu 2/3 ML < Cu monolayer. This cannot be explained by the results observed during Ag UPD (see chapter 3)[30]. The lattice constant of Au(111) is about 11 % larger than Cu(111), a much larger difference than that between Au(111) and Ag(111). Therefore, it is expected that this large mismatch

increases the surface energy of the Cu adlayer on Au(111) due to the residual stress [31] and the adsorption of sulfate is expected to reduce the high surface energy of the Cu adlayer. However, at high normal load, the sliding tip might modify the position of sulfate or penetrate the sulfate, which consequently increases friction.

Figure 5.9 shows the friction as function of potential during Cu UPD on I-modified Au(111) observed using the hard cantilever (k_N =1.13 N/m).

When the potential passes the 1st Cu UPD peak, C_1, at low normal load (10 nN < FN < 40 nN), friction increases steeply as the potential passes about 0.12 V. With increasing normal load to 60 nN, it is clear that in the potential region II, the friction slightly decreases with decreasing potential from 0.1 V to 0.06 V. As confirmed by the transition of atomic corrugations (Figure S5.2), at 0.12 V, the coverage of copper increases. Therefore, we suggest that the increasing coverage of copper mainly results in the increase of friction at 0.12 V. As mentioned in the case of Cu UPD on Au(111) in sulfuric acid, the decrease of friction at slightly negative of the peak C_1 indicates that copper and co-adsorbed iodine form ordered structure. At high normal load, 100 nN, it seems that the deposition of copper paralleled by the rearrangement of iodine is hindered by the sliding tip at about 0.07 V. The sudden increase of friction appears at about 0.05 V and it is maintained beyond peak C_2. Hence, it is reasonable to assume that the coverage of copper underneath the tip is already 1 at 0.05 V and the transition of friction is caused by the coverage of copper. It is remarkable that in the potential region II´, as the case of Cu UPD on Au(111) in sulfuric acid (Figure 5.8 and Figure S5.4), multiple stick-slip also appears with increasing normal load when copper forms a monolayer (Figure 5.10a) on I-modified Au(111). When the applied normal load is above 25nN, clear atomic stick-slip appears and the distance between sticks are about 0.83 nm (red curve in Figure 5.10a). Considering the iodine structure, the possible path for the stick-slip is shown in Figure 5.10b. The distance between sticks increases to 1.66 nm at 60nN and 2.88 nm at 100 nN, which indicates double and triple slip, respectively.

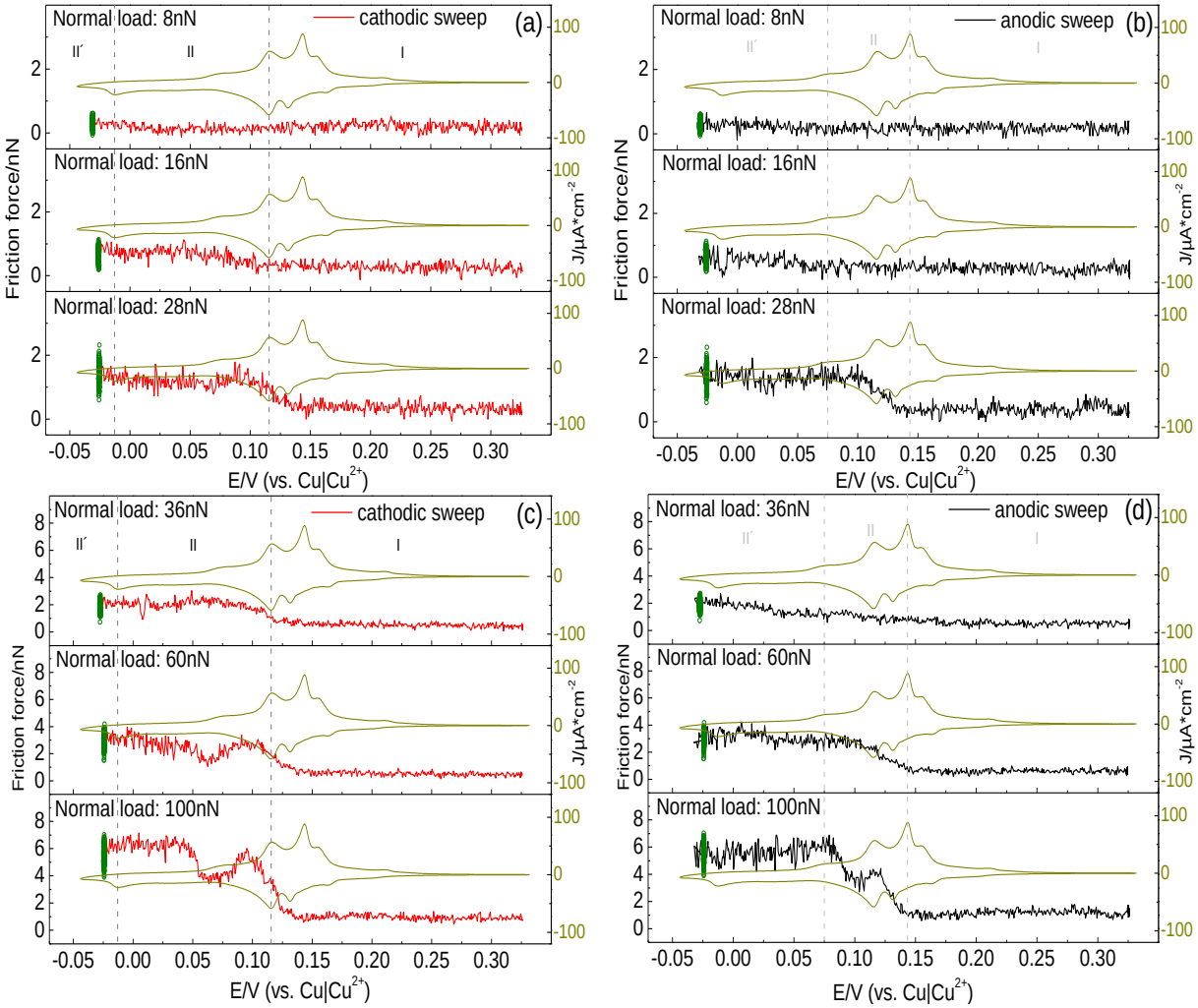

Figure 5.9 Friction forces on potential during Cu UPD on I-Au(111) in (a) and (c) cathodic sweep and (b) and (d) anodic sweep. Hard cantilever (k_N = 1.13) is used. The scan rate and size of AFM images were 0.47nm/s and 20X20nm², respectively.

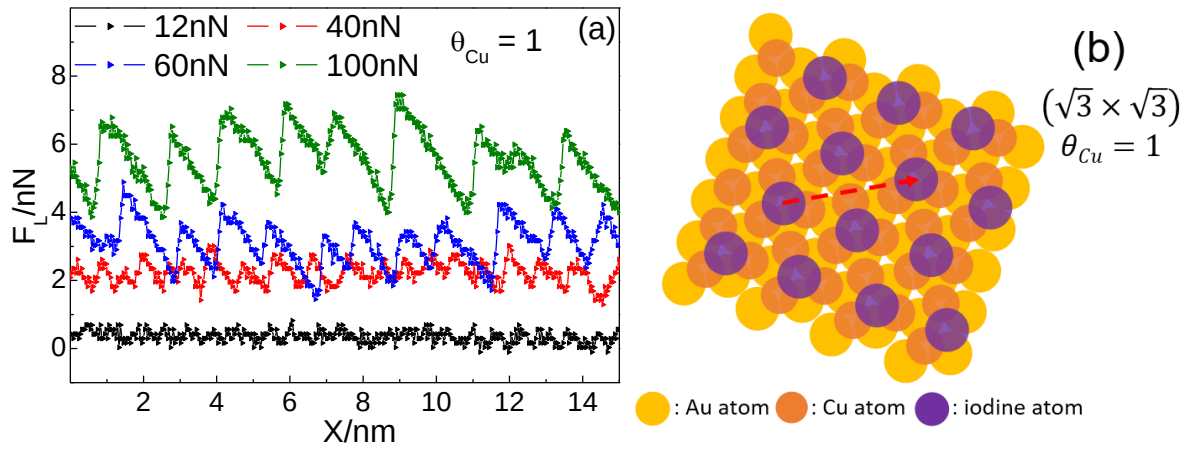

Figure 5.10 (a) Atomic stick-slip when the Cu forms a monolayer (E = 0.01 V vs. Cu/Cu^{2+}) on I-modified Au(111) at normal loads of 12, 40, 60, and 100nN. (b) Schematic illustration of the iodine structure ($\sqrt{3} \times \sqrt{3}$) on the Cu monolayer. Red arrow in (b) indicate the possible way for the atomic stick-slip. Hard cantilever (k_N = 1.13 N/m) is used.

Based on the Prandtl-Tomlinson model [32, 33], the tip slides and interacts with the substrate lattice, which results in a periodic sinusoidal potential energy. The total potential energy consists of the sum of all periodic tip-surface interactions. Therefore, our results convince that the strong interaction between a copper monolayer and the tip causes multiple stick-slips regardless of anions. Here, we suggest two possible scenarios for the origin of the strong interaction. The first is that the height of the potential barrier increases mechanically, meaning that due to the lattice mismatch between copper and gold, the potential wall gets deeper. The second is that the height of the potential barrier increases chemically. When the coverage of copper approaches one, the surface energy of copper increases due to the mismatch but it is stabilized by the co-adsorption of anions. As the normal load increases, the tip can slightly push away (or penetrate into) the co-adsorbed anions and the copper surface is exposed to the tip. Thus, the tip chemically interacts with bare copper surface and it is stronger with increasing normal load because the area where the co-adsorbed anions are pushed away increases.

Astonishingly, Hausen et al. reported that there is no frictional change during Cu UPD on Au(111) when a trace amount of Cl^- (4×10^{-4} M) is present in the electrolyte [20]. A. Labuda et al. [21] have observed the so-called (5 × 5) structure of chloride ($d_{Cl-Cl} \approx 3.7$ Å) when copper is deposited on Au(111) in the electrolyte in presence of even small amounts of chloride (10^{-5} M). Therefore, it is expected that the coverage of chloride approached a maximum independent of the concentration of chloride in electrolyte, more than sulfate and pre-adsorbed iodine.

Apparently, the coverage of co-adsorbed anions decides whether the tip can push away the co-adsorbed anions.

5.3.4 Friction forces as function of normal load

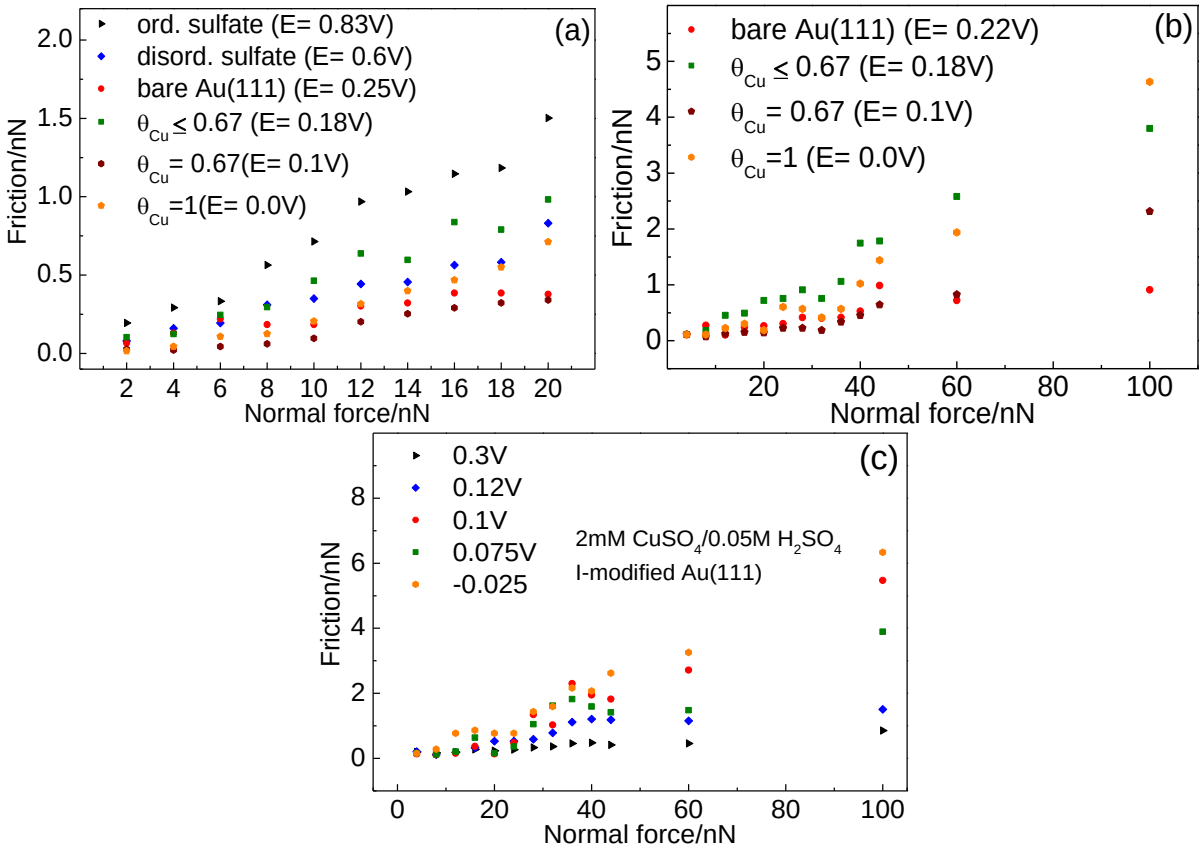

Figure 5.11 Friction as function of normal load replotted from (a) Figure 5.7, (b) Figure S5.3 during Cu UPD on Au(111), and (c) Figure 5.9 during Cu UPD on I-modified Au(111) in the cathodic sweep.

The data of Figure 5.7, Figure S5.3, and Figure 5.9 are replotted as a function of normal load in Figure 5.11a, b, and c respectively. Figure 5.11a shows that the friction closely correlates with the coverage of sulfate, in good agreement with the results from Hausen et al. [20]. Figure 5.11b obviously shows the dependence of friction on the coverage of Cu. As shown in previous papers by our group [18, 20, 28], friction forces increase at normal load between 30 and 40 nN and above

60 nN. Moreover, friction forces with normal load on I-modified Au(111) resembles the results on Au(111).

5.3.5 Force-separation curve: interfacial structure

The force separation curve was measured using hard cantilever (k_N= 1.13) as shown in Figure 5.12. The black and red curves indicate approach and retract curves, respectively. The force is constant at separations greater than 2 nm and this force is set to zero. During the approach, the ordered layers are observed as steps due to the repulsion. If the force is enough to break through the layer, then it jumps to the next one and the force increases again [34]. The distance of layers is in the range between 0.3 nm and 0.4 nm. We speculate that the sulfate ions, water molecules, and Cu^{2+} located near the electrode surface work in combination to form the ordered layer on the surface.

During retracting the tip, an adhesion force appears at 0.34 V and 0.045V, where the sulfate is mostly disordered. Serafin et al. has reported that the adhesion force decreases when the coverage of copper is 2/3 and sulfate form ordered structure ($(\sqrt{3} \times \sqrt{3})$) [35]. Therefore, the disappearance of the adhesion at 0.15V might be due to the strongly adsorbed sulfate.

Figure 5.13 shows FS curves on I-modified Au(111) obtained using the soft cantilever (0.1±0.05 nN). Compared to the case on Au(111), it was hard to observe stepwise behavior using the hard cantilever on I-modified Au(111). Therefore, it is assumed that water or Cu^{2+} are more weakly adsorbed on I-modified Au(111) , which might be due to the pre-adsorbed iodine. Moreover, at 0.1 V and - 0.01 V after the Cu deposition, a thick layer (~ 3 nm) is observed. This suggests that there are a relatively dense layer near the electrode surface compared to bulk electrolyte, which consists of water and ions together.

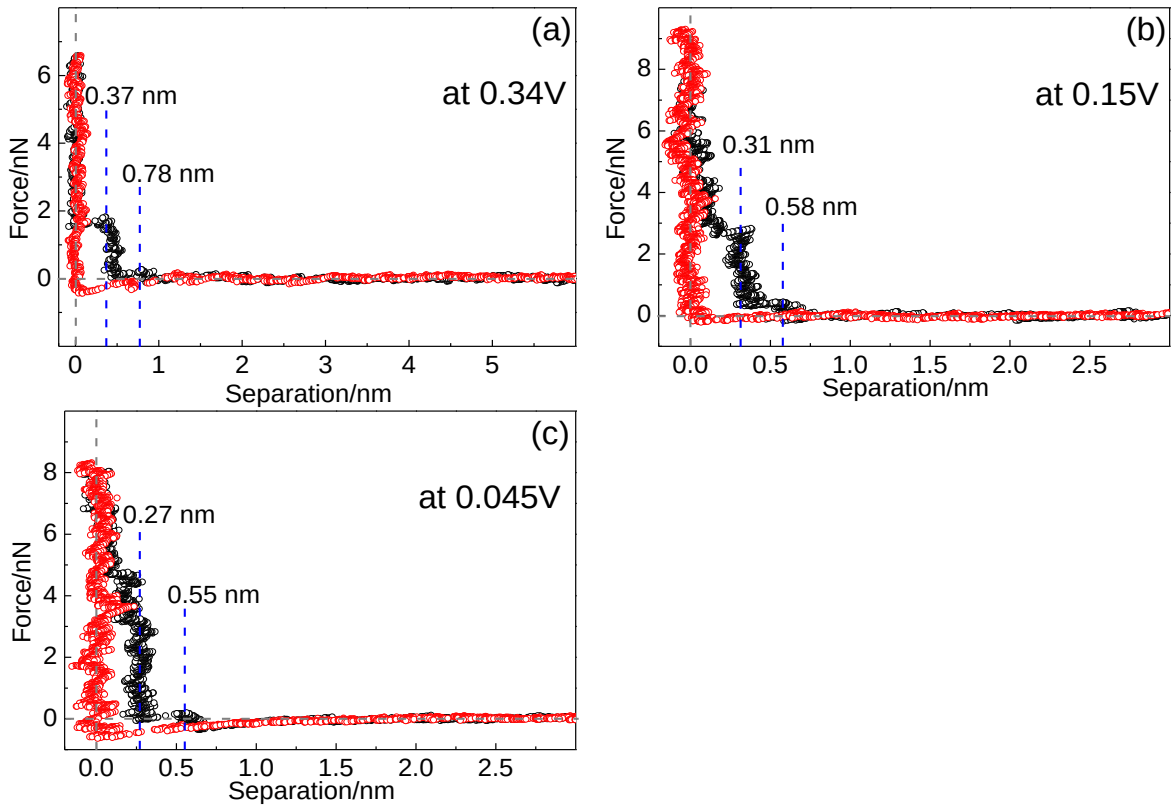

Figure 5.12 Force separation profiles obtained on Au(111) at the potential of (a) 0.34 V, before Cu UPD, (b) 0.15 V, after the 1st Cu UPD, (c) 0.045V, after the 2nd Cu UPD. All profiles show the approach (black) and retract (red) of AFM tip and the approaching (retracting) speed is 50nm/s. Hard cantilever (k_N =1.13 N/m) was used.

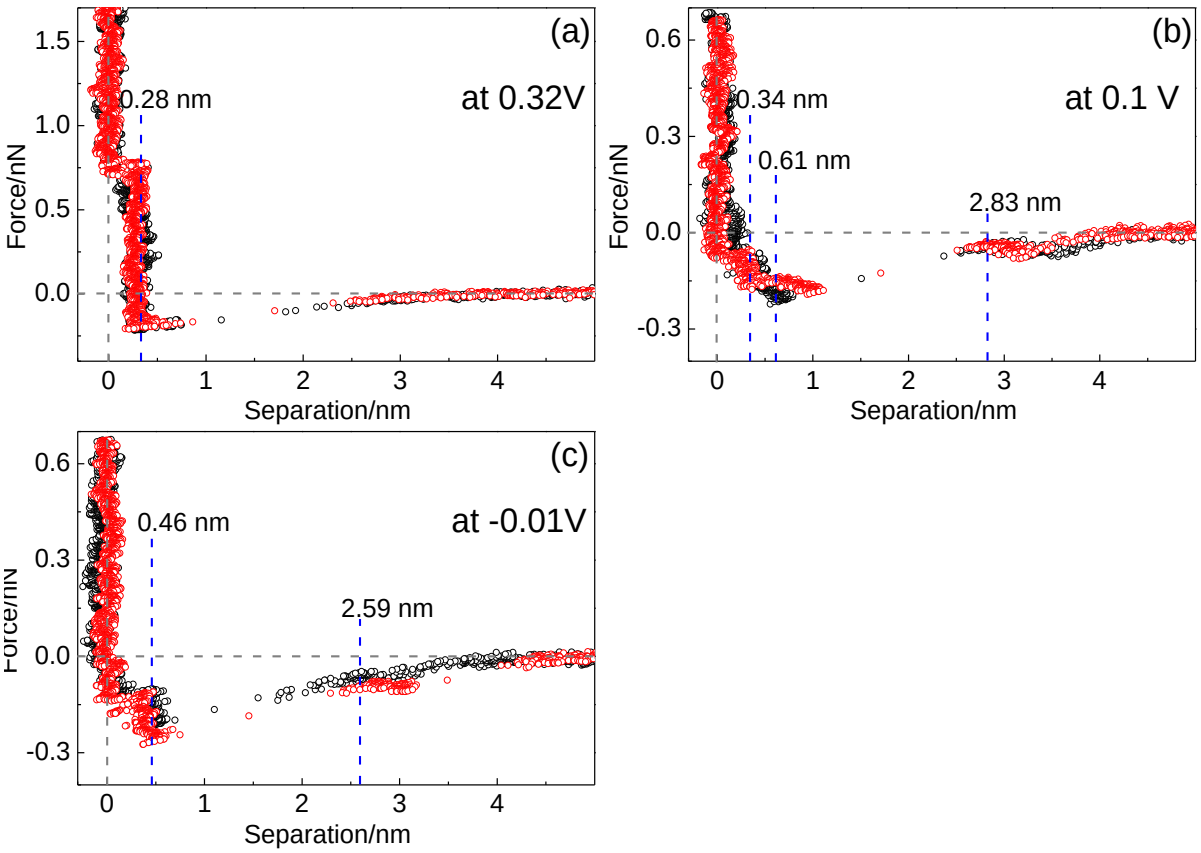

Figure 5.13 Force separation profiles obtained on I-modified Au(111) at the potential of (a) 0.32 V, before Cu UPD, (b) 0.1 V, after the 1st Cu UPD, (c) - 0.01V, after the 2nd Cu UPD. All profiles show the approach (black) and retract (red) of AFM tip and the approaching (retracting) speed is 25 nm/s. Soft cantilever (k_N =0.1±0.05 N/m) was used.

5.4 Conclusion

Friction force images confirm previous findings that the sulfate forms the smooth $(\sqrt{3} \times \sqrt{3})R30°$ structure on the Cu 2/3 ML at about 0.15 V (region II), with situated at the hollow site of the honeycomb $(\sqrt{3} \times \sqrt{3})R30°$ structure of Cu adlayer. At about 0.0 V, where the copper completes a monolayer and the $(\sqrt{3} \times \sqrt{7})$ structure is observed for sulfate. The dependence of friction on potential reflects the status of adsorbates (e.g. ordered or disordered structures, coverage, and roughness). In potential region I, sulfate ions form the $(\sqrt{3} \times \sqrt{7})$ structure on Au(111), which indicates that the coverage of sulfate is maximum ($\theta_{sulfate} = 0.22$). Furthermore, multiple stick-slips are observed on a Cu monolayer as normal load increases. On I-modified Au(111), the structure of iodine also depends on the Cu coverage. Before Cu deposition, iodine forms a $(\sqrt{3} \times \sqrt{3})$ structure on Au(111). This structure is changed to a $p(3 \times 3)$ structure when the potential is swept to 0.12 V, resulting from the deposition of Cu. Therefore, it is reasonable to assume that copper deposited underneath the iodine adlayer forms a $p(3 \times 3)$ structure, same structure with iodine. At 0.09 V, forms a $(\sqrt{3} \times \sqrt{3})$ structure but the rearrangement of iodine requires more time than other structures. The charge density at 0.09 V corresponds to Cu 2/3 ML, suggesting that the iodine sits on the hollow site of Cu honeycomb $(\sqrt{3} \times \sqrt{3})$ structure. The transition of lattice angle confirms that the iodine forms a $(\sqrt{3} \times \sqrt{3})$ structure on a Cu monolayer. It is noteworthy that multiple stick-slips with normal load are also observed as a Cu monolayer completes on I-modified Au(111). This suggests that the origin of multiple stick-slips result from the interaction between the tip and a Cu monolayer.

Friction as function of potential show the dependence of friction on the coverage of adlayers, the interaction between the tip and surface, and the normal load. On Au(111), as the potential is swept from 0.8 V to 0.22 V, the friction decreases due to 1) the decreasing coverage of sulfate and 2) the transition of structures from the ordered state to disordered state. When the potential passes the 1st Cu UPD peak C_1, friction forces increase dramatically, which corresponds to the increase of Cu coverage approaching 2/3 ML. After the coverage reaches 2/3 ML paralleled by the adsorption of sulfate, friction decreases again. In potential region II´ where the copper completes a monolayer, friction is higher than the friction on Cu 2/3 ML at high normal loads. On I-modified Au(111), it is astonishing that the increase of friction starts at 0.12 V where the coverage of copper changes from 0.44 to 0.67. Thus, there is no change of friction while the

coverage of Cu reaches 0.44. This might indicate that the effect of the lattice mismatch is significant above a certain coverage. As the Cu coverage approaches to 2/3 ML paralleled by the rearrangement of iodine, friction decreases slightly at high normal load (60 nN $\leq F_N$). When the copper completes a monolayer, the friction increases again and friction on a Cu monolayer is higher than that on sub-monolayer. Friction on a Cu monolayer and multiple stick-slips independent of co-adsorbed anions suggest that there is a strong interaction between the tip and a Cu monolayer, which results from the large lattice mismatch between Au(111) and Cu(111). The dependence of multiple stick-slips on normal load suggests that as normal load increases, the tip pushes away the adsorbed anions, allowing the tip to interact with the tip.

Acknowledgement

The authors gratefully acknowledge the DFG (Deutsche Forschungsgemeinschaft) for funding this work (BA1008/21-1).

5.5 Supporting information

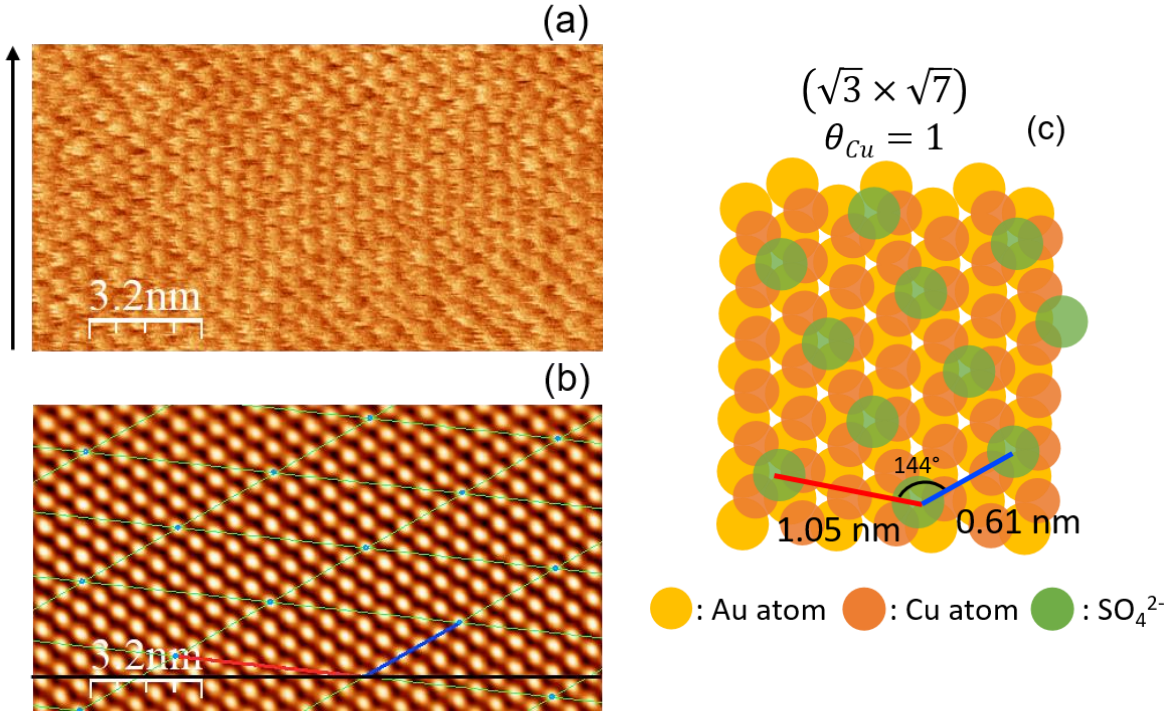

Figure S 5.1 Lateral force map on Au(111) in in 2 mM $CuSO_4$/0.05 M H_2SO_4 at 0.0V (vs. Cu/Cu^{2+}) in (a) upward scan. (b) is the lattice images after Fast Fourier Transform (FFT) of (a). (c) is the illustration of the real lattice with lattice parameters after the correction of thermal drift. Hard cantilever (k_N = 1.13 N/m) is used and applied normal load is 24nN.

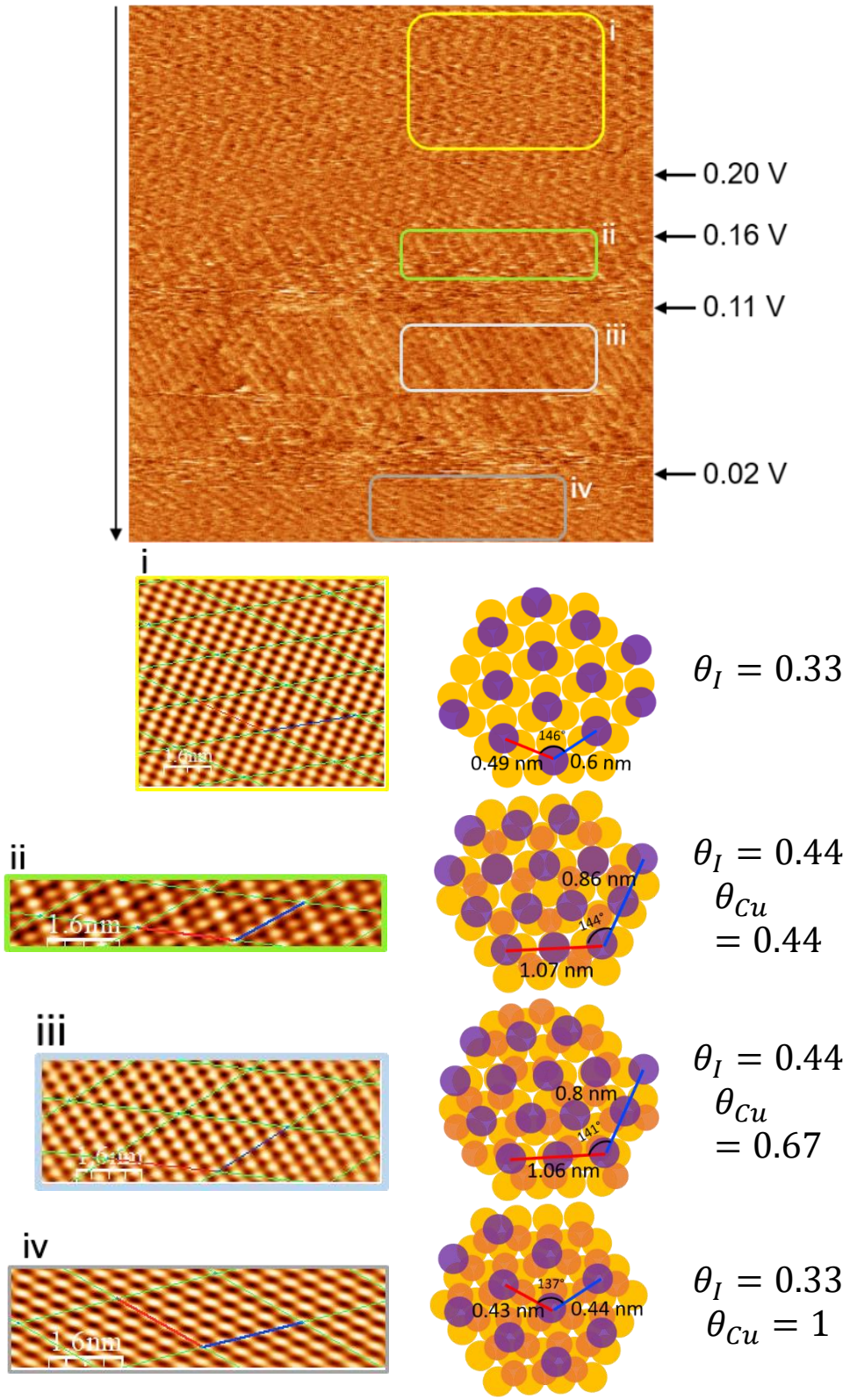

Figure S5.2 (a) lateral force map, filtered image using FFT, and illustrations with lattice parameter at 4 different potentials during cathodic sweep on I-modified Au(111) in 2 mM $CuSO_4$/0.05 M H_2SO_4. Soft cantilever (k_N = 0.1±0.05 N/m) was used and the applied normal load was 2 nN.

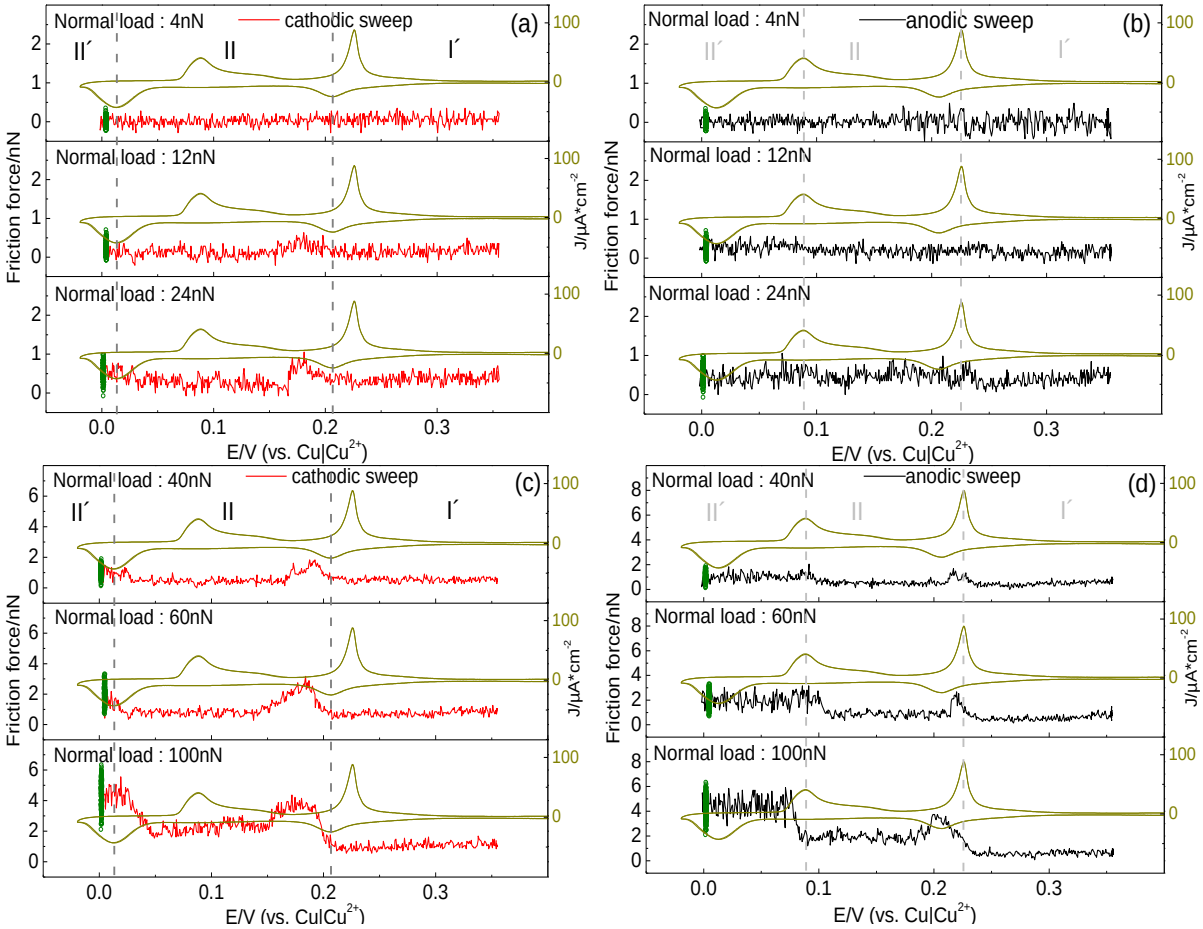

Figure S 5.3 Friction forces on potential during Cu UPD on Au(111) in (a) and (c) cathodic sweep and (b) and (d) anodic sweep. Hard cantilever (k_N = 1.13) is used. The scan rate and size of AFM images were 0.47nm/s and 20X20nm², respectively.

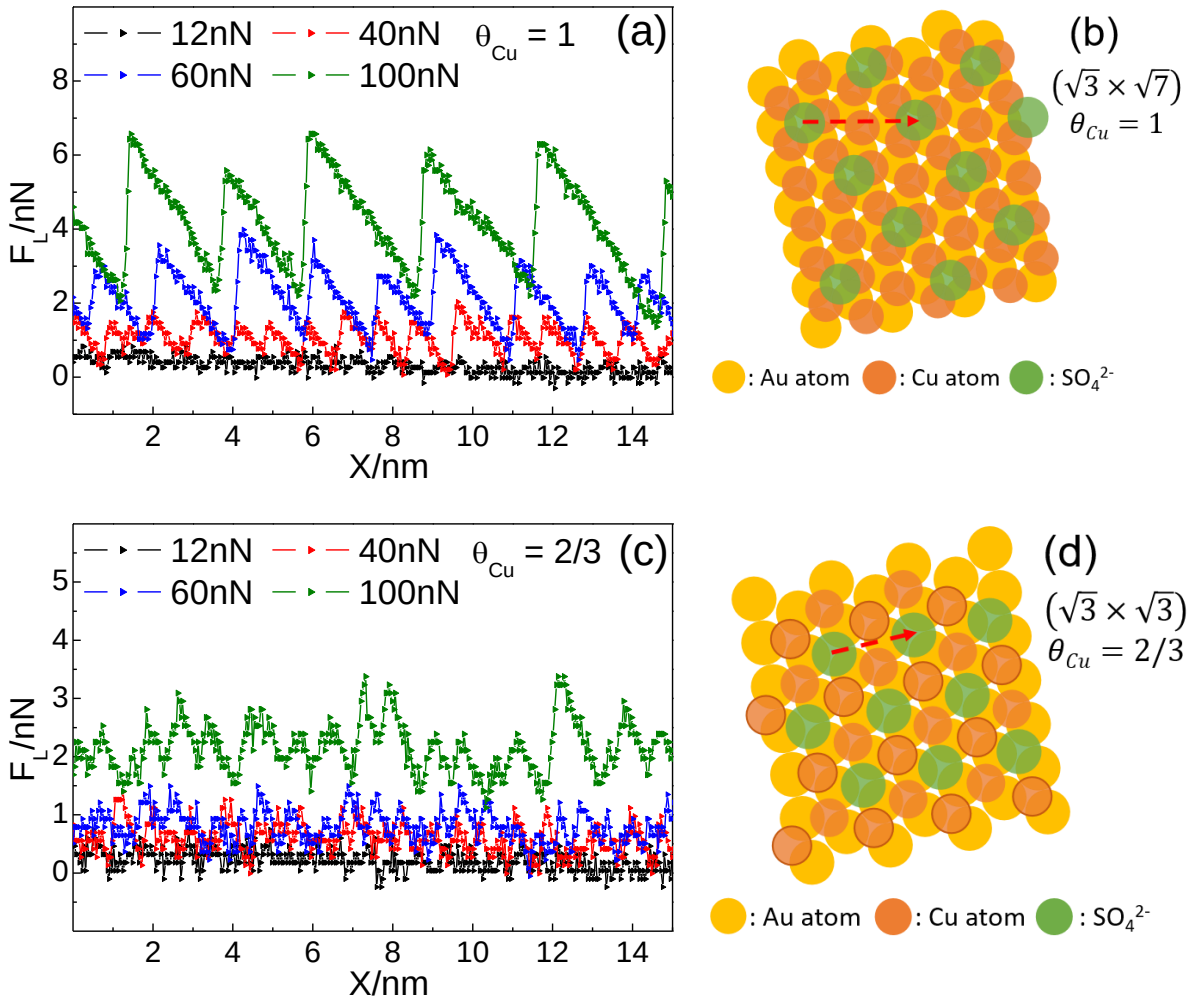

Figure S 5.4 Atomic stick-slip when the Cu forms (a) a monolayer (E = 0.01 V vs. Cu/Cu^{2+}) and (c) a 2/3 monolayer (E = 0.17 V) on Au(111) at normal loads of 12, 40, 60, and 100nN. Schematic illustration of the sulfate structure (b) $(\sqrt{3} \times \sqrt{7})$ on the Cu monolayer and (d) $(\sqrt{3} \times \sqrt{3})$ on 2/3 Cu monolayer. Red arrow in (b) and (d) indicate the possible way for the atomic stick-slip. Hard cantilever (k_N = 1.13 N/m) is used.

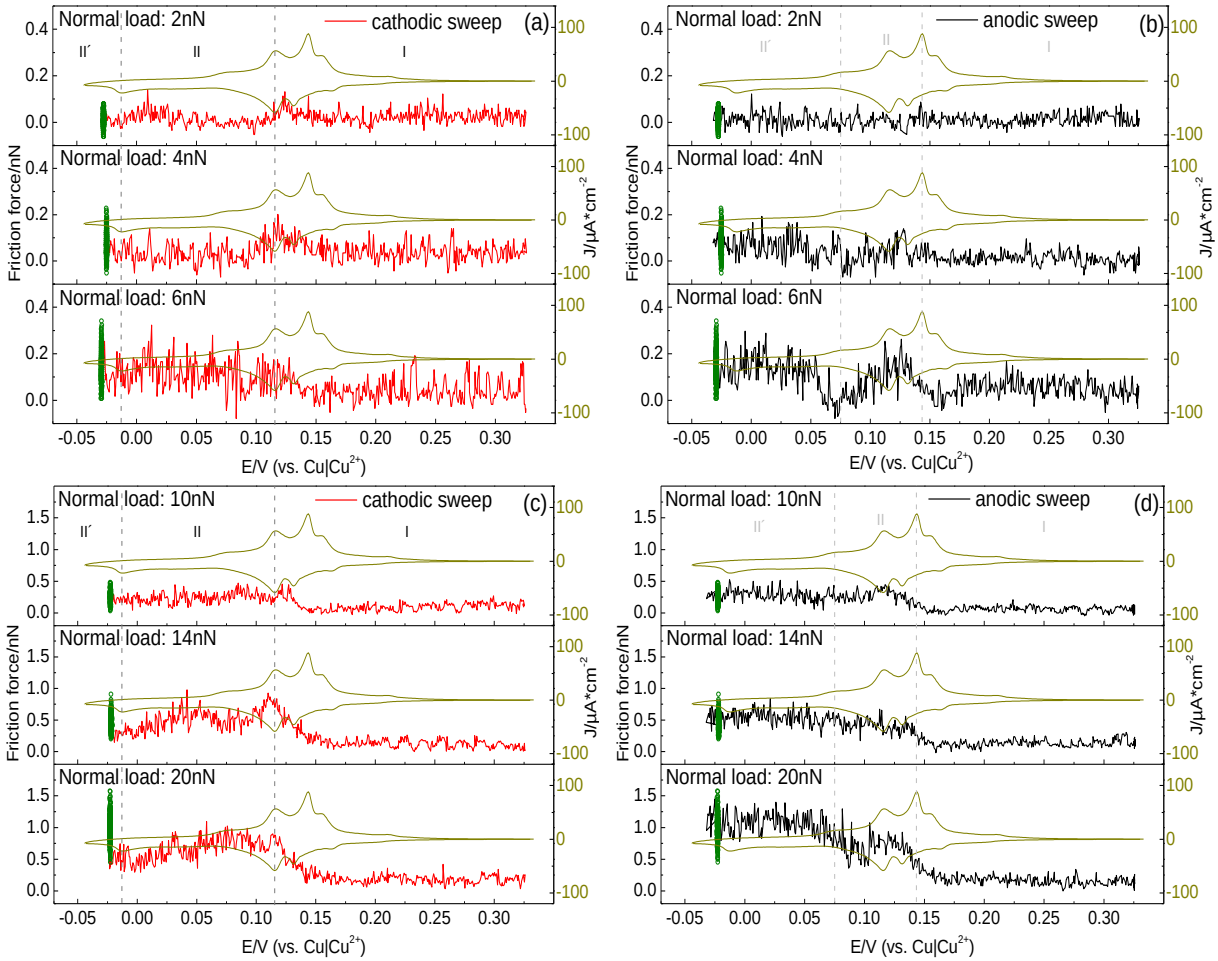

Figure S 5.5 Friction forces on I-modified Au(111) as function of potential at fixed normal loads during (a) and (c) cathodic sweep and (b) and (d) anodic sweep. Soft cantilever (k_N = 0.1±0.05 N/m) was used. The scan rate and size of AFM image was 0.47nm/s and 20X20 nm², respectively.

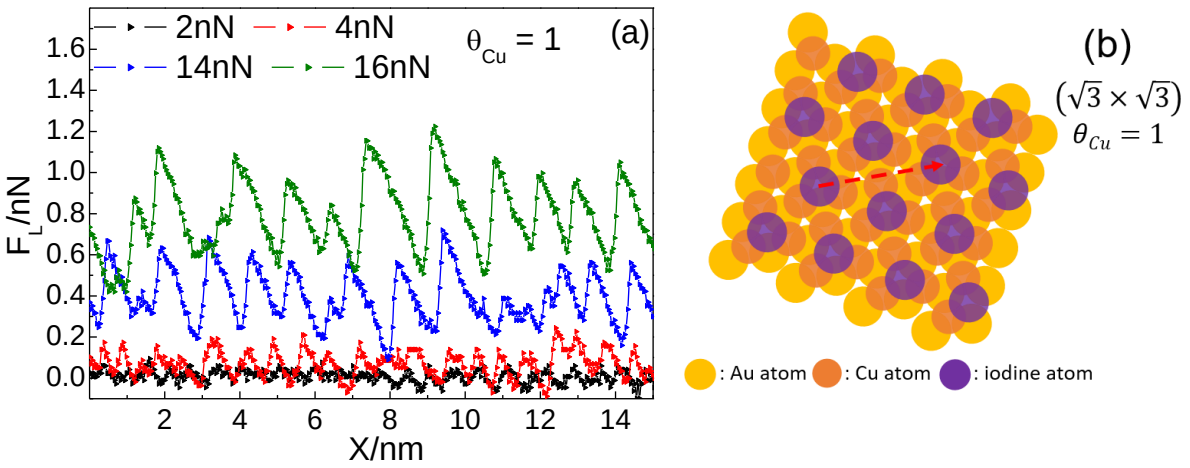

Figure S 5.6 Atomic stick-slip when the Cu forms a monolayer (E = 0.01 V vs. Cu/Cu^{2+}) on I-modified Au(111) at normal loads of 2, 4, 12, and 16nN. (b) Schematic illustration of the iodine structure $(\sqrt{3} \times \sqrt{3})$ on the Cu monolayer. Red arrow in (b) indicate the possible way for the atomic stick-slip. Soft cantilever (k_N = 0.1±0.05 N/m) is used.

Reference

[1] D. Kolb. **1978**, *11*, 125.

[2] O. M. Magnussen, J. Hotlos, R. J. Nichols, D. M. Kolb, R. J. Behm *Phys. Rev. Lett.* **1991**, *64*, 2929.

[3] N. Batina, T. Will, D. M. Kolb *Faraday Discussions*. **1992**, *94*, 93-106.

[4] F. Möller, O. M. Magnussen, R. J. Behm *Electrochimica Acta*. **1995**, *40*, 1259-1265.

[5] N. Ikemiya, S. Miyaoka, S. Hara *Surface Science*. **1994**, *311*, L641-L648.

[6] M. S. Zei, G. Qiao, G. Lehmpfuhl, D. M. Kolb

Berichte der Bunsen-Gesellschaft für Physikalische Chemie. **1987**, *91*, 349-353.

[7] L. J. Wu S. *Prog. Surf. Sci.* **1995**.

[8] Z. Shi, S. Wu, J. Lipkowski *Electrochimica Acta*. **1995**, *40*, 9-15.

[9] D. Kolb *Schering Lecture*. **1991**, *1*, 1-35.

[10] Y. Nakai, M. S. Zei, D. M. Kolb, G. Lehmpfuhl *Ber. Bunsen-Ges. Phys. Chem. Chem. Phys.* **1984**, *88*, 340-345.

[11] A. Martínez-Ruíz, M. Palomar-Pardavé, J. Valenzuela-Benavides, M. H. Farías, N. Batina *The Journal of Physical Chemistry B*. **2003**, *107*, 11660-11665.

[12] A. Martinez-Ruiz, J. Valenzuela-Benavides, L. M. de la Garza, N. Batina *Surface science*. **2001**, *476*, 139-151.

[13] T. Hachiya, H. Honbo, K. Itaya *J Electroanal. Chem.* **1991**, *315*, 275-291.

[14] O. M. Magnussen, J. Hotlos, R. J. Nichols, D. M. Kolb, R. J. Behm *Physical Review Letters*. **1990**, *64*, 2929-2932.

[15] B. Madry, K. Wandelt, M. Nowicki *Applied Surface Science*. **2016**, *388*, 678-683.

[16] M. Watanabe, H. Uchida, M. Miura, N. Ikeda *J. Electroanal. Chem.* **1995**, *384*, 191-195.

[17] R. Melroy, M. G. Samant *Langmuir*. **1988**.

[18] M. Nielinger, H. Baltruschat *Physical Chemistry Chemical Physics*. **2007**, *9*, 3965-3969.

[19] R. Bennewitz, F. Hausen, N. N. Gosvami *J. Mater. Res.* **2013**, *28*, 1279.

[20] F. Hausen, M. Nielinger, S. Ernst, H. Baltruschat *Electrochimica Acta*. **2008**, *53*, 6058-6063.

[21] A. Labuda, W. Paul, B. Pietrobon, R. B. Lennox, P. H. Grutter, R. Bennewitz *Review of Scientific Instruments*. **2010**, *81*, 083701.

[22] J. Hotlos, O. M. Magnussen, R. J. Behm *Surface Science*. **1995**, *335*, 129-144.

[23] J. E. Sader, J. W. M. Chon, P. Mulvaney *Rev. Sci. Instrum.* **1999**, *70*, 3967-3969.

[24] C. P. Green, H. Lioe, J. P. Cleveland, R. Proksch, P. Mulvaney, J. E. Sader *Review of Scientific Instruments*. **2004**, *75*, 1988-1996.

[25] S. Iqbal, L. Zan, E. Nardi, H. Baltruschat *Phys. Chem. Chem. Phys.* **2018**, *20*, 6176-6186.

[26] S. Sundararajan, B. Bhushan *J. Appl. Phys.* **2000**, *88*, 4825-4831.

[27] M. H. Holzle, U. Retter, D. M. Kolb *J. Electroanal. Chem.* **1994**, *371*, 101-109.

[28] N. Podgaynyy, S. Wezisla, C. Molls, H. Baltruschat *BEILSTEIN JOURNAL OF NANOTECHNOLOGY*. **2015**, *6*, 820-830.

[29] J. Xu, X. Wang *Surface Science*. **1998**, *408*, 317-325.

[30] I. Park, H. Baltruschat *ChemPhysChem*. **2021**, *7*, 1-9.

[31] W. Haiss, J. Sass *J. Electroanal. Chem.* **1995**, *386*, 267-270.

[32] L. Prandtl *Z. Angew. Math. Mech*. **1928**, *8*, 85-106.

[33] G. Tomlinson *Phil. Mag.* **1929**, *7*, 905.

[34] T. Niemann, H. Li, G. G. Warr, R. Ludwig, R. Atkin *The journal of physical chemistry letters*. **2019**, *10*, 7368-7373.

[35] J. M. Serafin, S.-J. Hsieh, J. Monahan, A. A. Gewirth *Journal of Physical Chemistry B*. **1998**, *102*, 10027-10033.

CHAPTER 6

Friction force on I-modified Au(111) in a Tetraglyme electrolyte

Inhee Park[1], Florian Hausen[2,3], and Helmut Baltruschat[1*]

[1]Institut für Physikalische und Theoretische Chemie, Universität Bonn, Römerstraße 164, D-53117 Bonn, Germany[2]Forschungszentrum Jülich GmbH, Institute of Energy and Climate Research, IEK-9 – Fundamental Electrochemistry, 52425 Jülich, Germany

[3]RWTH Aachen University, Institute of Physical Chemistry, Landoltweg 2, D- 52074 Aachen, Germany

*Corresponding Author: Baltruschat@uni-bonn.de

Reproduced with the permission from:

Inhee Park, Florian Hausen, and Helmut Baltruschat, *ChemElectroChem*, **2022**

DOI: 10.1002/celc.202101660 ©2022 ChemElectroChem published by Wiley-VCH GmbH

6.1 Abstract

In situ electrochemical lateral force microscopy (EC-LFM) has been employed to study the ordered structure of Li^+ containing tetraglyme (G4) in front of I-modified Au(111) and its influence on friction as function of normal load. Since the effect of water in aprotic electrolytes is a critical issue, the influence of water on the ordered structure and friction was also been investigated. Lateral force maps recorded at low normal load (F_N < 30 nN) show that the adsorbed iodine forms a $(\sqrt{3} \times \sqrt{3})$R30° structure ($\theta_I = 0.33$) independent of potential. With increasing normal load, observed atomic corrugations at both potentials (0.45 V and -0.4 V) are in agreement with the Au(111) (1×1) structure while returning to a $(\sqrt{3} \times \sqrt{3})$R30° structure with decreasing normal load. Thus we conclude that the AFM tip penetrates into the iodine adlayer without irreversible wear. Astonishingly, no clear friction increase was observed upon penetration into the iodine adlayer; also no corresponding step was found in force separation (FS) curves.

On the other hand, FS curves for I-modified Au(111) in pure G4 solvent and Li^+ containing electrolyte clearly showed several steps suggesting that G4 molecules are forming up to five ordered layers. It is noteworthy that we observed two different push-through forces for the innermost layers. Considering the higher reproducibility of FS curves on I-modified Au(111) compared to bare Au(111) we assume that the low surface energy of the iodine monolayer leads to negligible interaction between G4 molecules and iodine adlayer, resulting in less perturbations of the structure by the solid phase and also an increase of push-through force. Charts of friction forces vs. normal load are found to be independent of applied potential and the concentration of water.

KEYWORDS: Electrolyte structure, Tribology, Atomic force microscopy (AFM), Lateral force microscopy (LFM), Force separation (FS) curve

6.2 Introduction

Friction between two surfaces is an important issue in everyday life and is the ultimate cause of all mechanical energy dissipation. Understanding its origin, finding factors that influence it, and ways to reduce it is therefore of extreme importance. Friction often occurs in a liquid environment (or wet or lubricated surfaces) and hence, electrochemistry is involved. Here we will study the interaction between a sliding or static AFM tip serving as a model for a single asperity and an iodine covered Au(111) surface in an aprotic tetraglyme electrolyte. Since iodine is known to be very strongly adsorbed, the latter is an ideal, comparatively simple model system.

Numerous studies of atomic scale friction employed atomic force microscopy or lateral force microscopy (AFM or LFM) [1-12], a technique that is also well suited to elucidate the lateral atomic structure [13]. As compared to the electrochemical scanning tunneling microscopy (EC-STM) [14, 15], it has the disadvantage of a typically lower lateral resolution. However, AFM has the advantage that, by recording tip approach curves (force separation (FS) curves), also information on structuring of the electrolyte or solvent normal to the surface can be obtained [16-19]. Such an information on both lateral and vertical structure is important for an understanding of all kinds of electrode processes and catalytic reactions. It is also obvious that vertical interaction potentially influence friction forces.

O'Shea et al. have reported FS curves on highly oriented pyrolytic graphite (HOPG) in binary liquid mixture composed with octamethylcyclotetrasiloxane (OMCTS) and squalene (or hexadecane) using an AFM [20]. Results show that the affinity between surface and molecule determines the innermost layer. The hydration layer at the interface with substrates has been elucidated using a high-resolution frequency modulation atomic force microscope (FM-AFM) [17, 21, 22]. These results suggest that the surface property (solvophilicity vs. solvophobicity) might influence the packing density of hydration layer at the interface. The interfacial structures between solid surfaces of electrodes and ionic liquids (ILs) have shown that the ordered layers composed of ions are modified by applied potential due to the rearrangement of ions [18, 23-25]. Solvate ionic liquids (SILs) consisting of an equimolar mixture of organic lithium salts and glymes (e.g. triglyme (G3), tetraglyme (G4)) have found interest in similar studies because of their similar behavior as ILs (e.g. low volatility, high thermal stability, high ionic conductivity, and a wide potential window) [26-31]. McLean et al. reported force separation curves on highly

ordered pyrolytic graphite (HOPG) and Au(111), which varies with the anion of lithium salts and the applied potential due to the rearrangement of ions [28]. We are not aware of similar studies for organic electrolyte systems other than ILs, in particular aprotic electrolytes.

Such FS curves may also be determined using surface forces apparatus (SFA, or surface force balance, SFB). Christenson et al. have reported such FS curves in nonpolar liquids (e.g. OMCTS, cyclohexane, benzene) [32-34]. The results revealed that the number of measurable oscillations decreases with increasing molecular flexibility (e.g. rotation, asymmetry) as flexible molecules are able to pack effectively without layering. Interestingly, with adding small amounts of water in OMCTS, oscillatory forces disappear due to the strong adsorption of water on the mica surface [35]. Perkin et al. have found an oscillatory behavior when squeezing out layers of ionic liquids (ILs) on mica [31, 36, 37].

Coming back to friction, the AFM tip is ideally suited to model a single asperity of a rough surface moving across another surface. In electrolyte solutions, friction is influenced by the lubricating effect of the electrolyte, as well as that of adsorbates. In addition, the electrode potential may have a direct or an indirect (by influencing adsorption processes) impact on friction. Therefore, apart from the importance of friction on wet surfaces (and thus electrodes), electrochemistry also offers means to control friction [1-12]. For SILs, Li et al. demonstrated that friction as function of normal load correlates with the interaction between ions and the surface by varying potential. Furthermore, they observed that the behavior of friction with potential depends on substrate (HOPG and Au(111)) [29]. However, it is still unclear why the dependence of friction closely related to the arrangement of ions shows a difference between HOPG and Au(111).

In order to simplify the system, we exclude coverage effects of adsorbate on friction [38] by modifying surface of Au(111) with an iodine adlayer [14, 22, 39-48]. We demonstrate that the AFM tip can penetrate into the iodine adlayer without irreversible wear as normal load increases. The electrochemical window is chosen such that no electrochemical reaction occurs. As solvent, tetraethylene glycol dimethyl ether (G4) is used to exclude hydrogen bonding that might influence friction. This aprotic electrolyte also seemed interesting because of the similarity to the above mentioned SILs. Finally, the electrochemistry in this electrolyte is important because such ether-based electrolytes have been studied as an alternative electrolyte for the Li-O_2 battery due to their greater stability during oxygen reduction reaction (ORR) compared with organic carbonate-based electrolytes (e.g. propylene carbonate (PC)) [49-51]. G4 is also of interest for application as an electrolyte solvent for Mg deposition-dissolution processes [52-57].

Questions to be answered in this study are: Do G4 molecules order near the surface of an I-modified Au(111) electrode as in the above mentioned examples for SILs. Furthermore, would the squeezing out the innermost layer of G4 molecules have an influence on friction? Also of interest is if the tip penetration into the iodine adlayer could be observed in FS curves and whether this tip penetration leads to an increase or change of friction, as one might expect from previous studies [37, 58, 59]. Two different kinds of experiments are performed with the AFM: either measurement of friction (lateral force) when the tip is laterally moving (perpendicular to the cantilever) or force distance curves for a fixed x-y position of the tip.

6.3 Experimental

A disc type Au(111) single crystal (diameter: 10mm and thickness: 3mm) purchased from MaTecK GmbH (Germany) was used as working electrode. It was annealed by flame and cooled down above iodine crystals purged with Ar, forming a monolayer of iodine on clean surface. In the H-cell, a gold wire was used as counter electrode and silver wire in 2 mM $AgClO_4$/0.1 M $LiClO_4$/G4 was used as reference electrode. In the AFM-cell, gold and silver wires were used as counter and quasi reference electrode, respectively. For electrolytes, 0.1M $LiClO_4$ were dissolved in tetraethylene glycol dimethyl ether (G4). A coulometric KF Titrator (C20, Metler Toledo) with a diaphragm electrode was used to measure the water content.

Lateral (frictional) force measurements were performed using Agilent 5500 AFM, combined with an atmosphere chamber. Silicon tips (PPP-FM, NANOSENSORS, tip radius <10 nm) were used and the normal spring constant was individually calibrated to 1.1±0.05 N/m. Normal and torsional resonance frequency of AFM tips were measured by AFM (Agilent 5500/AC mode). The Q factor for theses resonance frequencies was obtained by fitting the equation of simple harmonic oscillation (SHO) [60]. Normal and torsional force constants were calculated using the Sader method [60, 61] and the lateral force constant was obtained by dividing torsional force constant with the square of the tip height. During the measurement, a homemade AFM cell was used, which contains a three-electrode assembly and Ar was purged through the atmosphere chamber. The lateral force vs. normal load and potential curves were measured using the silicon tip, PPP-FM, and the scan size and rate were 20 nm² and 0.47 nm/s, respectively.

When the AFM tip scans the surface, friction (F) between the tip and surface makes the cantilever twist, which results in the deflection of the laser beam. The sign of the deflection depends on the scan direction. In addition, the deflection of the laser can be caused by topography (T) (e.g. steps on the surface) and it does not depend on scan direction. Thus, the forward image and backward image contain [T+F] and [T-F], respectively. Friction force data was obtained by subtracting the backward data from the forward data and dividing it by 2 to eliminate topographic effects [62].

Atomic corrugations of the surface can be visualized in lateral force maps. To investigate structures in detail, the right or left side of the images are removed such that oscillations of the scan piezo during the change of scan directions do not disturb the image. Fast Fourier Transform (FFT) filtering was used in some images. The thermal drift was corrected by recording two subsequent images in downward and upward direction which allows calculating the drift vector [63]. The illustration of lattice shows the lattice parameters obtained after the correction of thermal drift. For highly oriented pyrolytic graphite (HOPG) in air, the discrepancy of atomic structures obtained using topography and lateral force map was negligible. Furthermore, the observed lattice parameters were approx. 10 % larger than the theoretical value, mainly due to viscous effects and errors in thermal drift correction. Therefore, we assume that the experimental value contains basically ± 10 % error and it might be slightly larger under electrochemical conditions.

Force distance curves were typically repeated approx. ten times to ensure reproducibility.

6.4 Results and discussion

6.4.1 Cyclic voltammetry (CV)

Figure 6.1 shows the cyclic voltammogram (CV) obtained in an H-cell containing 0.1M $LiClO_4$/G4 with trace amounts of water (21ppm). In this potential range, where no chemical reaction occurs, the small cathodic peak, C_1, appears only in the first sweep. Since the potential range in this measurement is far positive from the desorption potential of iodide (E = -1.2 V vs. Ag/Ag^+) [47], it is assumed that C_1 is related to the desorption of a small amount of iodine exceeding the coverage of the ordered $(\sqrt{3} \times \sqrt{3})$R30° adlayer described below. Figure S6.1 shows the second cycle of CV in AFM-cell verifying that the concentration of water has no large influence on electrochemical reaction on I-modified Au(111).

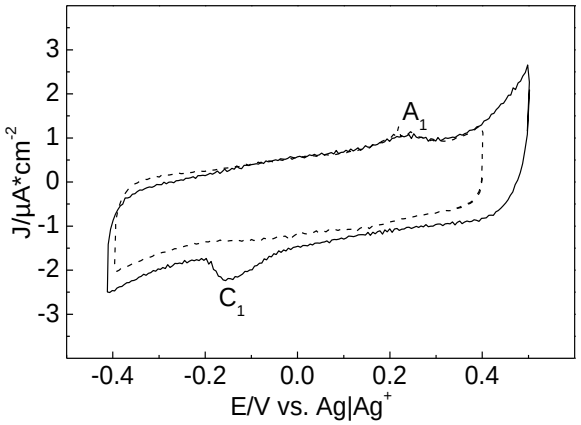

Figure 6.1 Cyclic voltammogram of I-modified Au(111) in 0.1M $LiClO_4$/G4 in H-cell. Solid line and dashed line indicate the 1st and 2nd sweep, respectively. The amount of water in electrolyte is about 21 ppm. The sweep rate is 50 mV/s.

6.4.2 Atomic corrugation

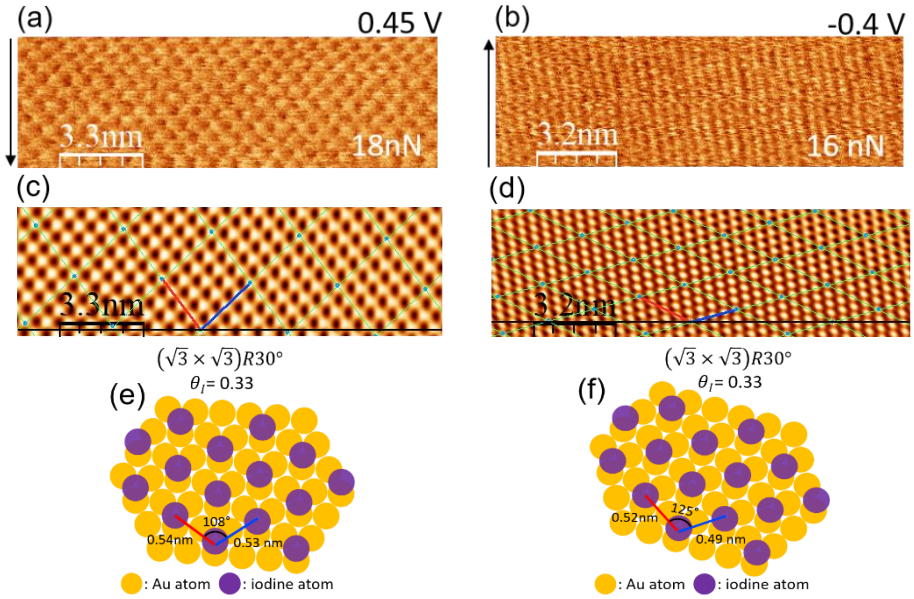

Figure 6.2 Lateral force maps at (a) 0.45 V (vs. Ag/Ag+) and (b) -0.4 V. (c) and (d) are the lattice images after Fast Fourier Transform (FFT) of (a) and (b), respectively. (e) and (f) are the illustration of the real lattice with lattice parameters after the correction of thermal drift. Applied normal loads of (a) and (b) are 18 nN and 16 nN, respectively. The water concentrations of (a) and (b) in the electrolyte are 21 ppm and 100 ppm, respectively. Scan rate is 0.47 nm/s.

At relatively low normal load (F_N < 30 nN), a $(\sqrt{3}\times\sqrt{3})$R30° structure is dominantly observed at both + 0.45 V and - 0.4 V (vs. Ag/Ag^+) on I-modified Au(111) in 0.1 M $LiClO_4$/G4, indicating that the coverage of iodine is 0.33 (Figure 6.2) over the whole potential range; therefore, the small peak, C_1, observed in the first sweep of CV is not related to a phase transition. With increasing normal load above 50 nN, the revealed atomic corrugations correspond to a $Au(111)(1\times1)$ structure as shown in Figure 6.3. Therefore, we conclude that at a sufficiently high normal load the tip penetrates the iodine adlayer and this behavior (visibility of the iodine structure for F_N < 30 nN and of the gold structure for F_N > 50 nN) is independent of potential. No clear structure was observed for intermediate normal loads. The thermal drift correction and procedure for obtaining the lattice parameters for the two potentials can be found in the SI (Figure S6.2-5).

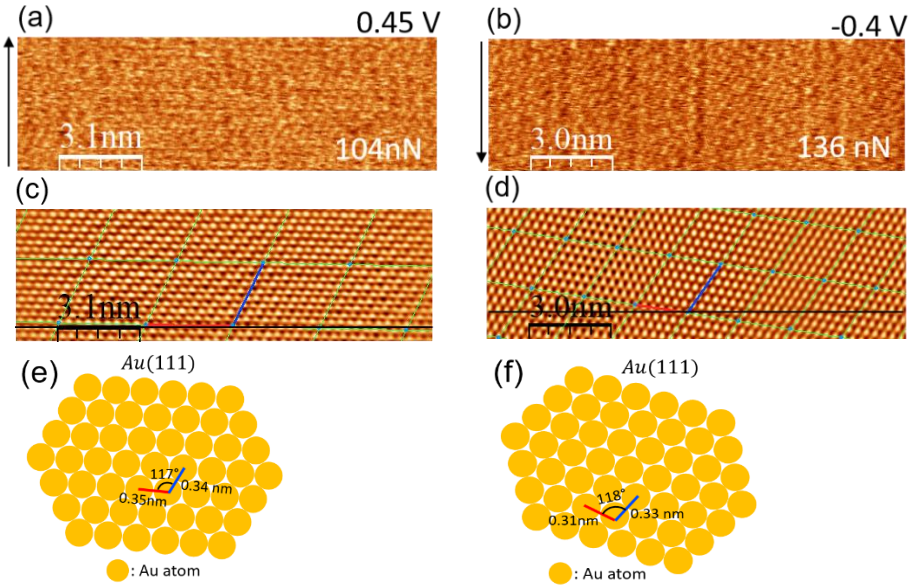

Figure 6.3 Lateral force maps at (a) 0.45 V (vs. Ag/Ag+) and (b) -0.4 V. (c) and (d) are the lattice images after Fast Fourier Transform (FFT) of (a) and (b), respectively. (e) and (f) are the illustration of the real lattice with lattice parameters after the correction of thermal drift. Applied normal loads of (a) and (b) are 104 nN and 136 nN, respectively. The water concentrations of (a) and (b) in the electrolyte are 21 ppm and 100 ppm, respectively. Scan rate is 0.47 nm/s.

Figure 6.4 directly shows the transition of the atomic stick-slip structure with increasing and decreasing normal load in one lateral force map for two different potentials: The $(\sqrt{3} \times \sqrt{3})$R30° structure is also observed, when the normal load is reduced again. Obviously, this structural transition for changing normal loads is reversible. Therefore, we presume that there is no, or at least no irreversible wear, possibly due to strong interaction between iodine and the surface of Au(111).

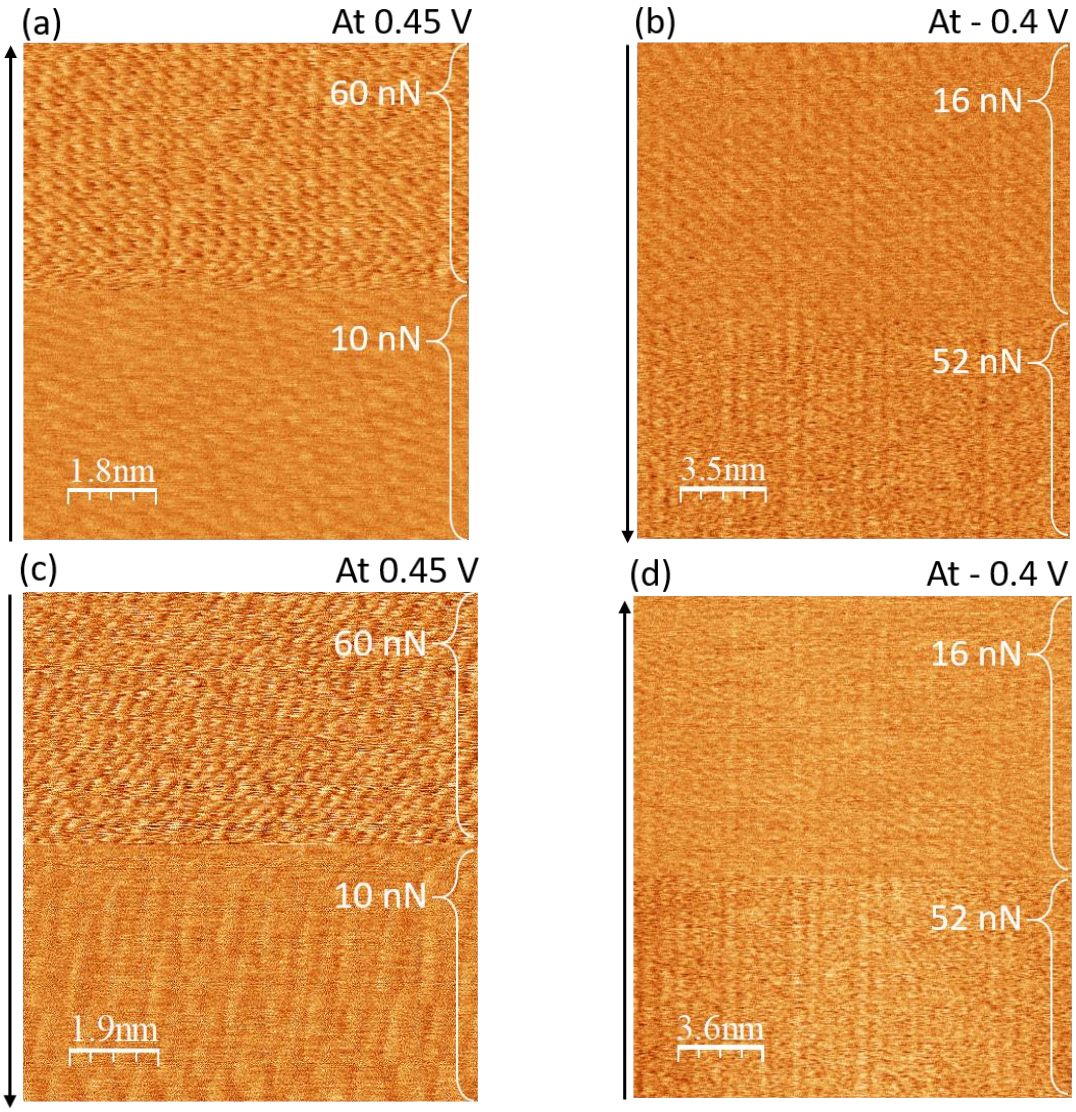

Figure 6.4 Lateral force maps on I-modified Au(111) in 0.1 M $LiClO_4$/G4 with increasing normal load at (a) 0.45 V and (b) -0.4 V and with decreasing normal load at (c) 0.45 V and (d) – 0.4 V. Black arrow indicates the scan direction.

It is interesting to note that the 'stick-slip lateral force loops' show no energy dissipation for low normal loads (cf. Figure 6.5). This is expected according to the Tomlinson model as described in [64, 65]; this will also be discussed below.

On bare Au(111) in 0.1 M $LiClO_4$/G4, atomic corrugation shows constantly the lattice structure of Au(111) at low and high normal loads, as shown in Figure S6.6 together with the cyclic voltammetry in the AFM-cell. As for I-modified Au(111), in the potential range between -0.4 V to 0.45 V there is no electrochemical reaction. This result confirms that the transition of structures is caused by the penetration of AFM tip into the iodine adlayer.

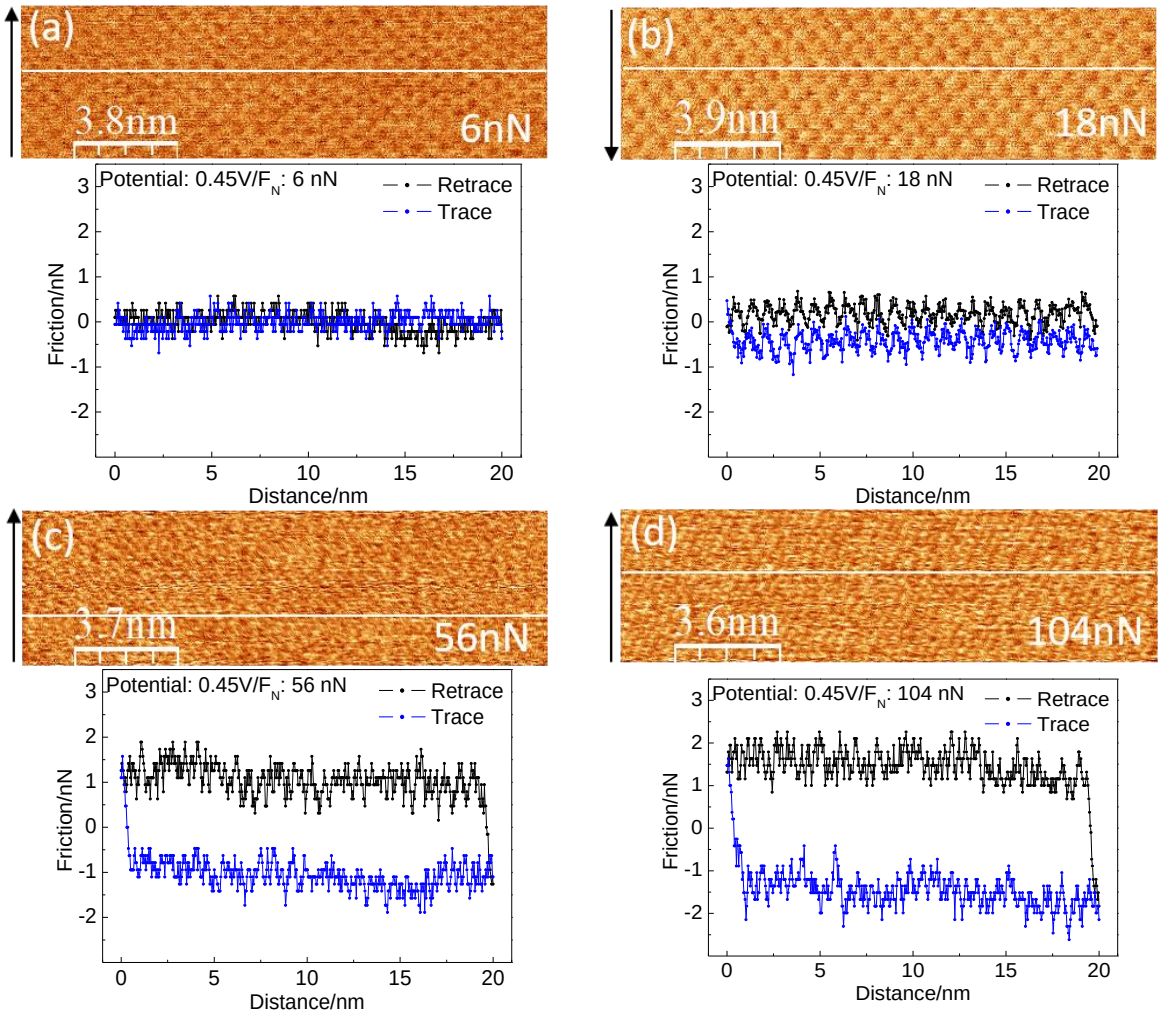

Figure 6.5 Lateral force loops at 0.45 V and stick-slips at the normal load of (a) 6 nN, (b) 18 nN, (c)56 nN, and (d) 104 nN. The water concentration is 21 ppm. Scan rate is 0.47 nm/s.

As shown in Figure S6.7-9 (at 0.45 V) and Figure S6.10-12 (at –0.4 V), an increased water content (300 ppm) in the electrolyte has no influence on the structure of adsorbed iodine and the penetration of tip into this adlayer at high normal load.

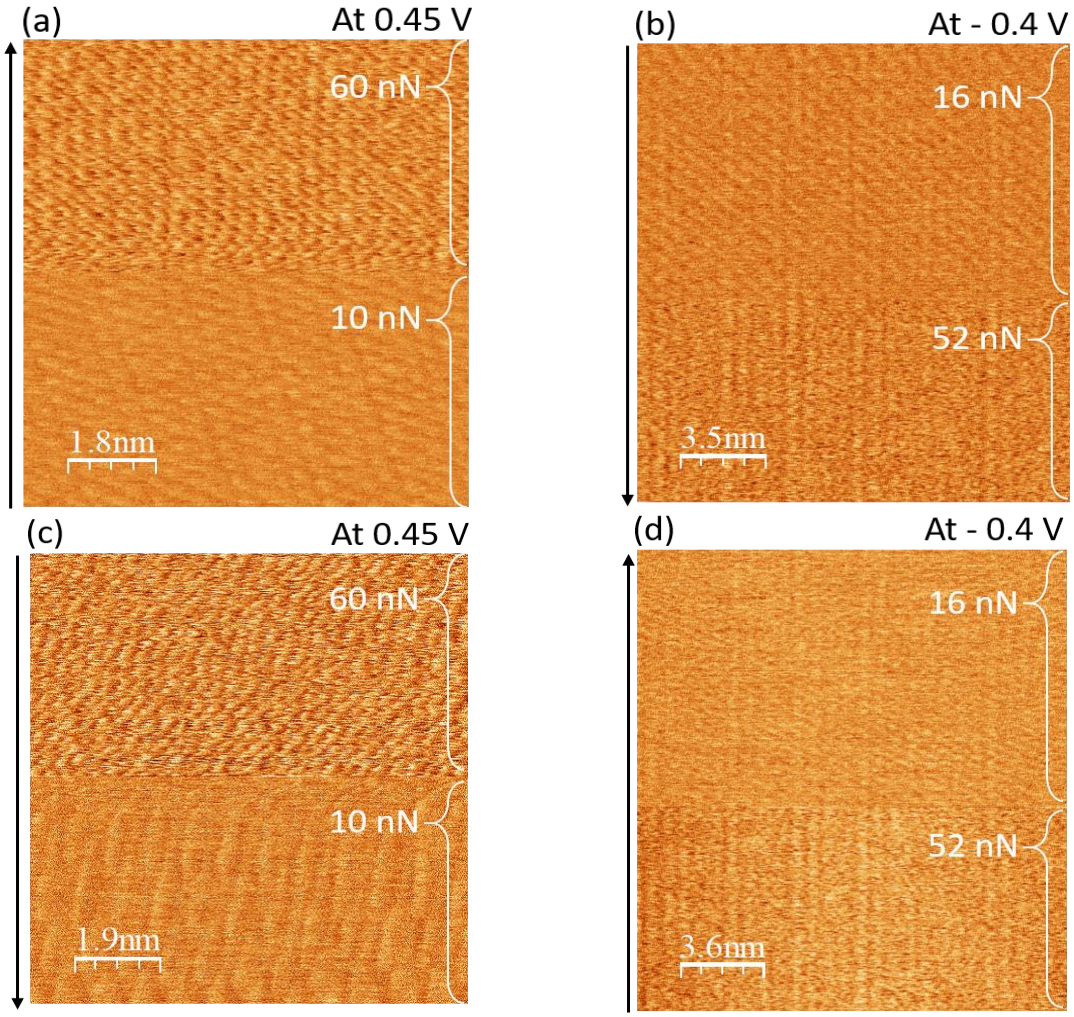

Figure 6.6 Lateral force maps on I-modified Au(111) in 0.1 M $LiClO_4$/G4 with increasing normal load at (a) 0.45 V and (b) -0.4 V and with decreasing normal load at (c) 0.45 V and (d) – 0.4 V. Black arrow indicates the scan direction.

6.4.3 Interfacial structure: ordered solvent layers on the surface

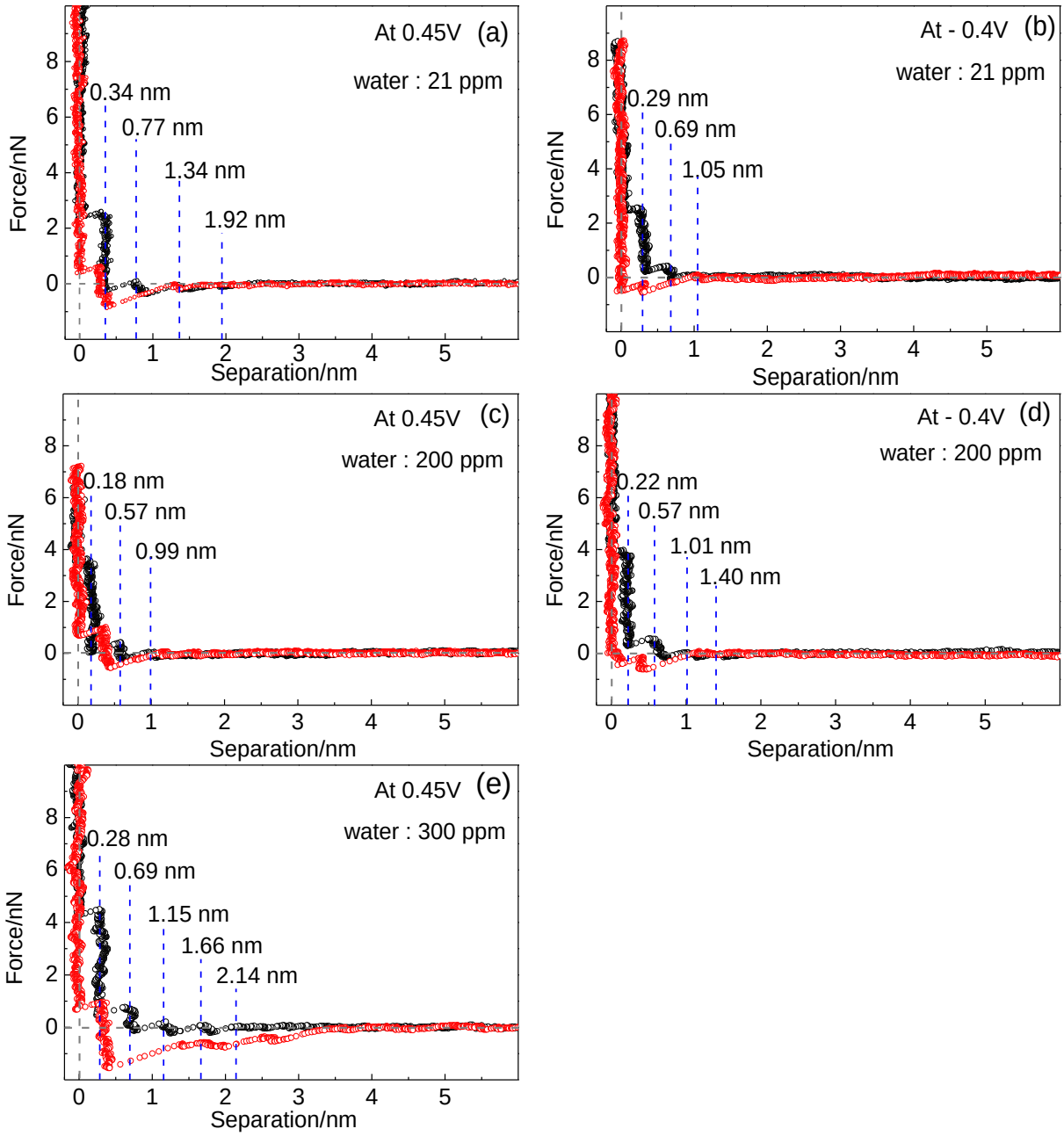

Figure 6.7 Force separation profiles obtained on the I-modified Au(111) in 0.1M $LiClO_4$/G4 containing water (a) and (b) 21 ppm, (c) and (d) 209 ppm, and (e) 300 ppm . The applied potential for (a), (c), and (e) is 0.45 and for (b) and (d) is -0.4 V. All profiles show the approach of AFM tip to the working electrode and approaching speed of tip is 80±10 nm/s.

To further probe the penetration of the iodine adlayer, force versus separation (FS) curves have been acquired. FS-curves are recorded at 0.45 V and -0.4 V on I-modified Au(111) for different concentrations of water in the electrolyte. Typical FS-curves are shown in Figure 6. A clear layering structure is revealed by the stepwise increase of normal force upon approach. Ordered

layers of electrolyte require an additional force for disruption by the AFM tip moving toward the surface, resulting in discrete steps in FS curves [16]. The force required to rupture a layer is referred to as the 'push-through force' [30].

Zero force is measured beyond 5 nm from the surface, revealing that there the electrolyte acquires its bulk structure. As the AFM tip moves closer to the surface, several layers are detected regardless of applied potential. The highest push through force observed was ~ 5 nN. Even though the applied normal load was increased to 50 nN, a value where always the substrate lattice was already observed in the LFM images, there was no further step indicating a higher push-through force. Therefore, we presume that there is no penetration of the iodine layer by the tip during recording of the tip approach curves and thus no displacement of iodine. Probably, in addition to a high normal load a sufficient shear force might be required: The normal force provides the necessary (thermodynamic) energy for desorption and displacement of the iodine, whereas the lateral shear force helps to overcome the kinetic energy barrier for the penetration into the iodine adlayer [66]. This barrier might be rather high because desorption has to happen for a large number of atoms simultaneously.

Interestingly, no effect of the amount of water in the electrolyte was found. Christenson et al. reported that the oscillations disappear when small amounts of water were added to nonpolar liquids due to the preferred adsorption of water on the mica surface [32, 67]. In contrast to this observation, the hydrophobic character of the adsorbed iodine adlattice in the system studied here prevents the incorporation of water to the interface. It is worth noting that the observed FS-curves on bare Au(111) in the same electrolyte show no clear steps. Therefore, it is rather probable that adsorption and structured layering of G4 molecules is preferred on hydrophobic I-modified Au(111).

The push-through force for outer layers is relatively small and independent of the applied potential but the distance of outer layers is slightly smaller at - 0.4 V (~ 0.44 nm) than 0.45 V (~ 0.6 nm). Figure S6.12 shows FS curves obtained on I-modified Au(111) in pure G4. The similarity to those obtained in presence of electrolyte suggests that the ordered layers are mostly attributed to G4 molecules preferentially oriented parallel to the surface of I-modified Au(111) [30]. Presuming that the G4 molecule can be flexibly compressed, it is not surprising that the thickness of the innermost layer varies [20, 67]. Thus, during the approach, ordered molecules are compressed by the AFM tip, leading to a slightly increased ordering. As a consequence the force required to rupture layers increase as the separation decreases as is often observed (Figure S6.12a and Figure 6.6). We assume that the low surface energy of the iodine monolayer leads

to a very low interaction with the G4 molecules of the liquid. This solvophobic behavior results in less perturbations of the G4 liquid surface structure by the solid iodine covered Au(111) surface. The required push-through force corresponds to the energy necessary for a rupture of the ordered liquid layer. This also explains the lower reproducibility of FS curves on bare Au(111), where the stronger interaction of the G4 molecules with the surface prevents such an ordering. It is instructive to compare the energy required to break the innermost layer with the tip calculated using our data from Fig. 6.7 (layer thickness: 0.3 nm and normal force: 3 nN) which is about $0.9 \times 10^{-18}\ N \cdot m$ with that calculated from the surface tension. From the surface tension of G4 of $34 \times 10^{-3}\ N/m$ [68,68] and the estimated surface area of the tip of $2.8 \times 10^{-17}\ m^2$ we obtain an energy of $0.95 \times 10^{-18}\ N \cdot m$, which is closer than one could expect from the crude approximation. (For the calculation, we simply assumed that the contact surface is a flat circle with a radius of it is 3 nm. This supports our assumption that the interaction with the solvophobic iodine layer is negligible. Occasionally, a relatively large rupture force for the innermost layer (cf. Figure S6.12b and Figure S6.13) is observed. This suggests that the strength of the interaction between the iodine adlayer and G4 molecules is somewhat varying, meaning that the strong interaction results in tightening the layer and resisting the displacement by tip.

As the AFM tip moves away from the surface the FS curves sometimes show clear steps, suggesting a fast reordering of G4 molecules on I-modified Au(111), but more often the adhesion force predominates (Figure S6.14).

6.4.4 The dependence of friction on normal load

Although the classical friction law of Amontons predicts a linear relationship between friction and normal load, in electrochemical systems often a non-linear behavior is observed [2, 4, 6]. On electrode surfaces, a sudden increase in friction or a plateau region had been ascribed to the penetration of the tip into an ionic layer. Also in ionic liquids, such a sudden, stepwise increase in friction was observed upon penetration of the tip through distinct electrolyte layers; there, penetration was confirmed by force distance curves [58, 69]. Therefore, since the atomically resolved LFM images (Fig. 6.4) showed that the AFM tip penetrates into the iodine adlayer with increasing normal load, a similar stepwise friction increase might be expected also for the iodine modified Au(111) in G4.

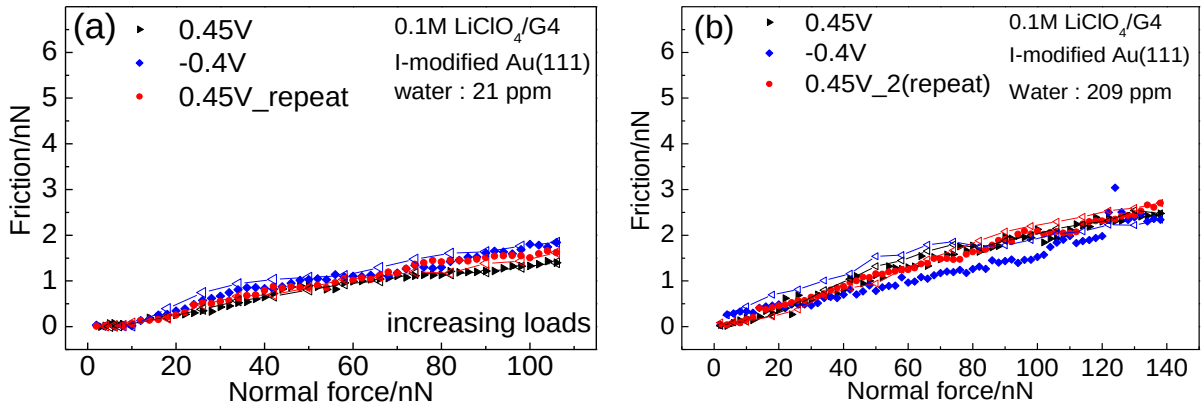

Figure 6.8 The dependence of friction on normal load at fixed potentials on I-modified Au(111) in 0.1M $LiClO_4$/G4 containing (a) 21 ppm water and (b) 209 ppm water. Solid and hollow symbols indicate friction forces obtained during increasing and decreasing load, respectively. The scan size and scan rate were 20x20 nm^2 and 0.47 nm/s, respectively.

Figure 6.8a shows friction force as function of normal load for I-modified Au(111) in 0.1 M $LiClO_4$/G4. No clear deviation from the classical linear relationship (Amontons' law) is observed. Furthermore, the slope, i.e. the friction coefficient, is independent of potential and found to be 0.02. Based on the dependence of the atomic LFM images on normal load, the independence of friction of applied potential is not astonishing; it is due to the fact that the iodine is strongly adsorbed on Au(111) in this potential window between -0.4 V and +0.45 V. However, according to the discussion above, it is astonishing that there is no clear abrupt change of friction after the penetration of the tip into the iodine adlayer, when the tip is in contact with the Au(111) substrate. Obviously, the friction coefficient for the iodine covered surface and for

the Au substrate are similar. A control experiment on a pure, i.e. iodine free Au(111) electrode shows that this is indeed the case: the resulting friction vs. normal load curve is very similar (Figure S6.16). The magnitude of energy dissipation and friction after penetration of the iodine layer therefore suggests that the iodine within the adsorbate layer is quite mobile. The independence of friction of applied potential also suggests that the adsorption strength of iodine on Au(111) (which should vary with potential) is not a decisive factor. This is opposed to the case of adsorbed sulfate, for which we assumed desorption and readsorption during scanning of the tip [2], whereas iodine atoms are only laterally shifted, always staying in contact with the Au surface. The value of the surface diffusion barrier, which may also depends on potential, seems to be too low to play a role. This does not contradict the fact that iodine is strongly adsorbed: The energy barrier for surface diffusion is completely independent of that for desorption.

In Figure 6.7a, friction remains nearly zero up to a normal load of 10 nN. This is consistent with the fact that the lateral force loop on the iodine adlayer also shows the expected transition from continuous movement without energy dissipation to stick-slip motion with an additional energy dissipation around 10 nN as shown in Figure 6.5. [64, 65].

Figure 6.7b shows the friction results when the amount of water in the electrolyte is raised to 209 ppm. Again, friction increases linearly with normal load, independent of potential and resembles the results as shown in Figure 6.7a for a water content of 21 ppm. This result demonstrates that even after the penetration of the iodine adlayer, the water has a minor influence on friction forces.

6.4.5 Conclusion

We investigated the frictional behavior of I-modified Au(111) for different potentials and normal loads. At low normal loads (F_N < 30 nN), the atomic structures show that the adsorbed iodine atoms form a $(\sqrt{3} \times \sqrt{3})$R30° adlattice at both potentials. At high normal loads, (F_N>50 nN), the revealed LFM structure and atomic stick-slip indicate that the tip slides directly on the Au(111) surface. It is noteworthy that with increasing normal load, the AFM tip penetrates into iodine layer without irreversible wear. Such structural image changes are often observed in STM when increasing the setpoint of the tunneling current [14, 70, 71]. However, we are not aware of similar structural transitions observed by AFM upon increasing load. FS curves show that several ordered solvent layers (~5 layers) are formed in the electrolyte in front of I-modified Au(111) independent of potential and the amount of water. The stepwise push-through forces and distance between layers resemble the results observed in pure G4. Therefore, the vertically ordered layers on I-modified Au(111) are attributed to G4 molecules. Considering that we did not observe clear stepwise FS curves on bare Au(111), we assume that the lower surface energy of the iodine monolayer leads to negligible interaction between G4 molecules and iodine adlayer. Thus, G4 molecules form stable ordered layers to minimize the surface energy of the liquid phase and that of the interface. Two different push-through forces for the innermost layer may indicate different ordering. These forces seem to be too small to show up in the friction vs. load curves. In the present measurements, the effect of water was negligible, in contrast to previous reports in literature [32, 33]. A reasonable assumption is that due to the unfavorable adsorption of water on the hydrophobic iodine adlayer, water has no influence on the arrangement of G4 molecules.

Astonishingly, we did not observe a push-through force corresponding to the structural change and the penetration of the tip into the iodine adlayer. It seems that a larger push though force is needed in the absence of a lateral tip movement. The dependence of friction forces as function of normal load shows a monotonic increase independent of potential and the concentration of water. This implies that the strength of the iodine adsorbed on Au(111) has no variation with potential in this potential region and it is a minor effect on friction. Moreover, a stepwise increase of friction upon increasing the normal load and upon the structural transition caused by penetration of the tip into either solvent layers or the adsorbate layer, as found in other cases

[2, 4, 6, 58, 69], was not observed. Therefore we assume that the adsorbed iodine is quite mobile, and no extra energy is dissipated to push it away in front of the sliding tip.

Acknowledgment

The authors gratefully acknowledge the DFG (Deutsche Forschungsgemeinschaft) for funding this work (BA1008/21-1).

6.5 Supporting information

6.5.1 CV in AFM-cell with increasing the concentration of water

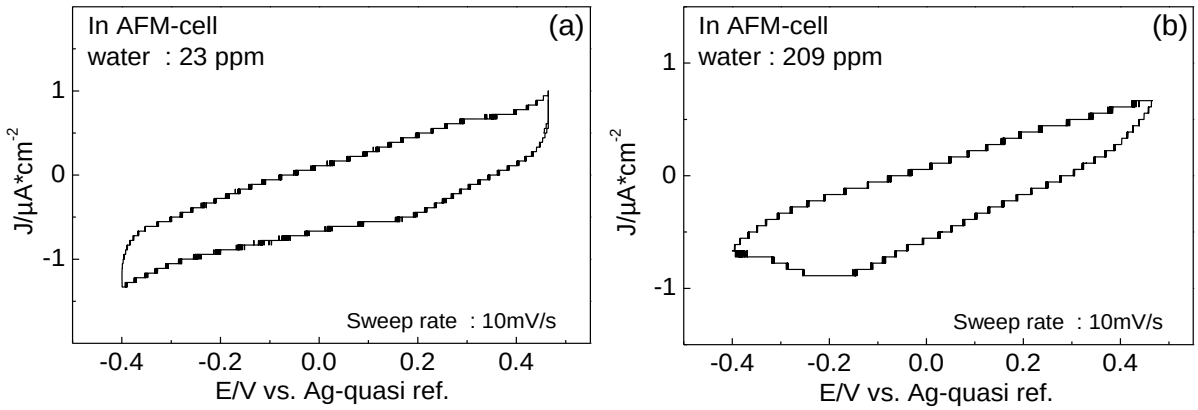

Figure S 6.1 Cyclic voltammetry (second sweep) in AFM-cell for I-modified Au(111) in 0.1M $LiClO_4$/G4 containing (a) 23 ppm water and (b) 209 ppm. The sweep rate is 10mV/s.

6.5.2 Thermal drift correction

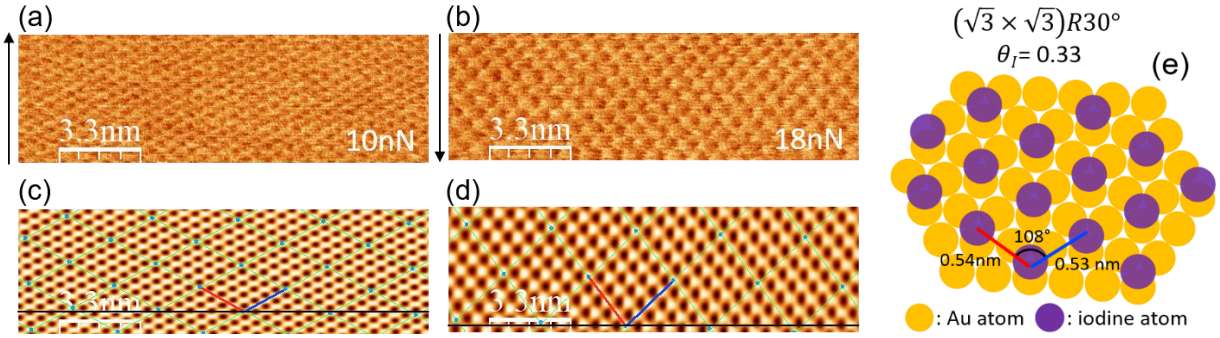

Figure S 6.2 Lateral force maps at 0.45 V (vs. Ag/Ag^+) in (a) upward scan and (b) downward scan. Black arrow indicates scan direction. (c) and (d) are the lattice images after Fast Fourier Transform (FFT) of (a) and (b), respectively. (e) is the illustration of the real lattice with lattice parameters after the correction of thermal drift. Applied normal loads of (a) and (b) are 10 and 18 nN. Scan rate is 0.47 nm/s. The amount of water in the electrolyte is 21 ppm.

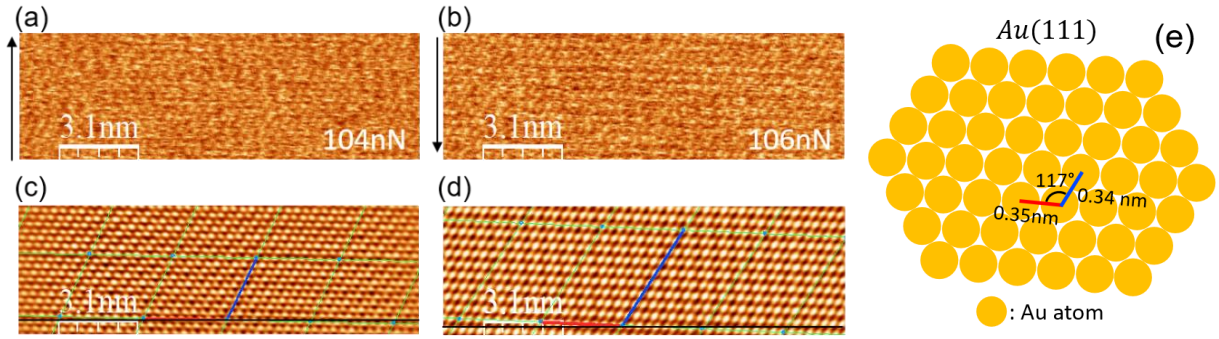

Figure S 6.3 Lateral force maps at 0.45 V (vs. Ag/Ag^+) in (a) downward scan and (b) upward scan. Black arrow indicates scan direction. (c) and (d) are the lattice images after Fast Fourier Transform (FFT) of (a) and (b), respectively. (e) is the illustration of the real lattice with lattice parameters after the correction of thermal drift. Applied normal loads of (a) and (b) are 104 and 106 nN, respectively. Scan rate is 0.47 nm/s. The amount of water in the electrolyte is 21 ppm.

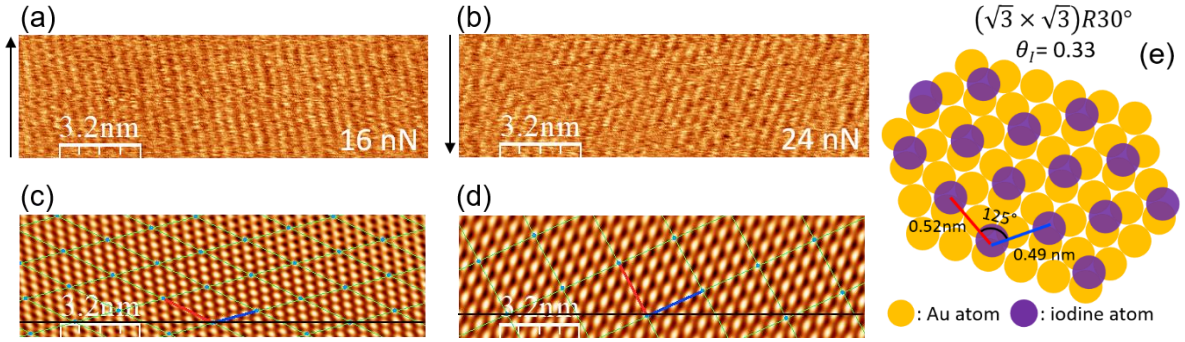

Figure S 6.4 Lateral force maps at -0.4 V (vs. Ag/Ag^+) in (a) upward scan and (b) downward scan. Black arrow indicates scan direction. (c) and (d) indicate the lattice images after Fast Fourier Transform (FFT) of (a) and (b), respectively. (e) The illustration of the real lattice with lattice parameters after the correction of thermal drift. Applied normal loads of (a) and (b) are 16 and 24 nN. Scan rate is 0.47 nm/s. The amount of water in the electrolyte is 100 ppm.

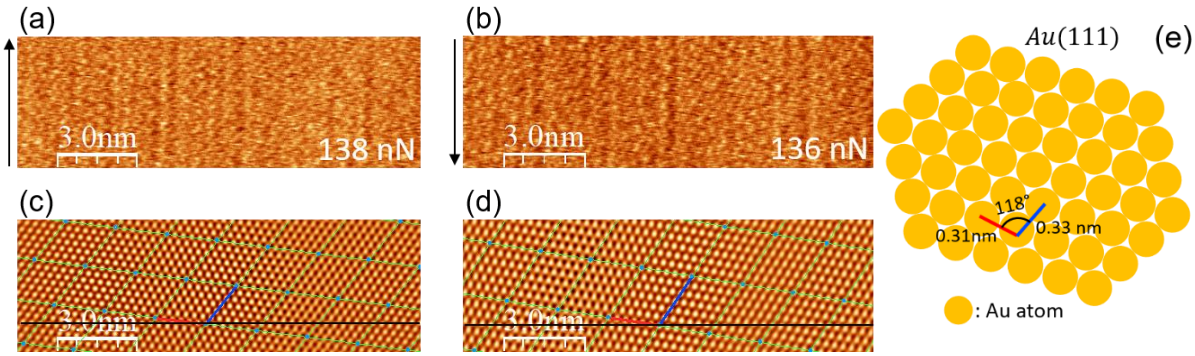

Figure S 6.5 Lateral force maps at -0.4 V (vs. Ag/Ag^+) in (a) upward scan and (b) downward scan. Black arrow indicates scan direction. (c) and (d) indicate the lattice images after Fast Fourier Transform (FFT) of (a) and (b), respectively. (e) The illustration of the real lattice with lattice parameters after the correction of thermal drift. Applied normal loads of (a) and (b) are 138 and 136 nN. Scan rate is 0.47 nm/s. The amount of water in the electrolyte is 100 ppm.

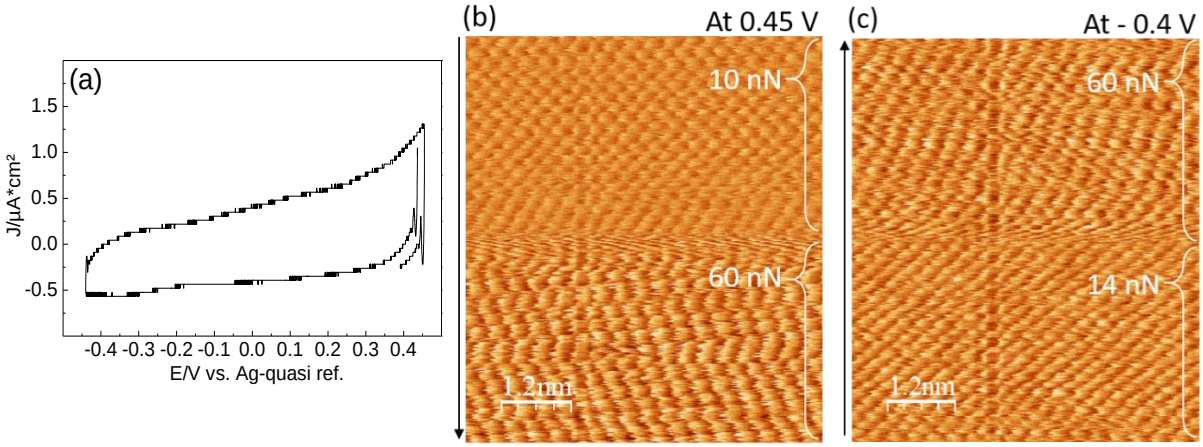

Figure S 6.6 (a) cyclic voltammogram in AFM-cell for Au(111) in 0.1M $LiClO_4$/G4. The sweep rate of CV is 15 mV/s. Lateral force maps on Au(111) in 0.1 M $LiClO_4$/G4 with increasing normal load at (b) 0.45 V and (c) -0.4 V. The scan size is 7x7 nm². Black arrow indicates the scan direction.

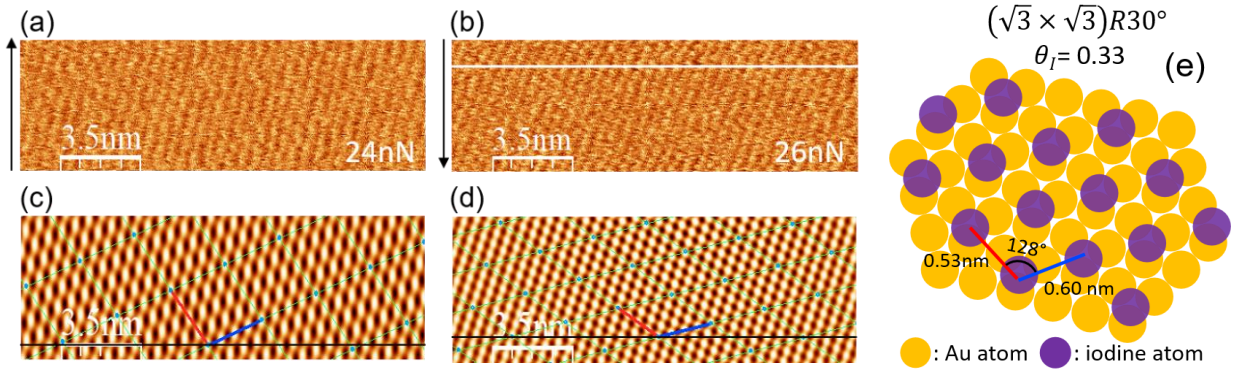

Figure S 6.7 Lateral force maps at 0.45 V (vs. Ag/Ag^+) in (a) upward scan and (b) downward scan. Black arrow indicates scan direction. (c) and (d) are the lattice images after Fast Fourier Transform (FFT) of (a) and (b), respectively. (e) is the illustration of the real lattice with lattice parameters after the correction of thermal drift. Applied normal loads of (a) and (b) are 10 and 18 nN. Scan rate is 0.47 nm/s. The amount of water in the electrolyte is 300 ppm.

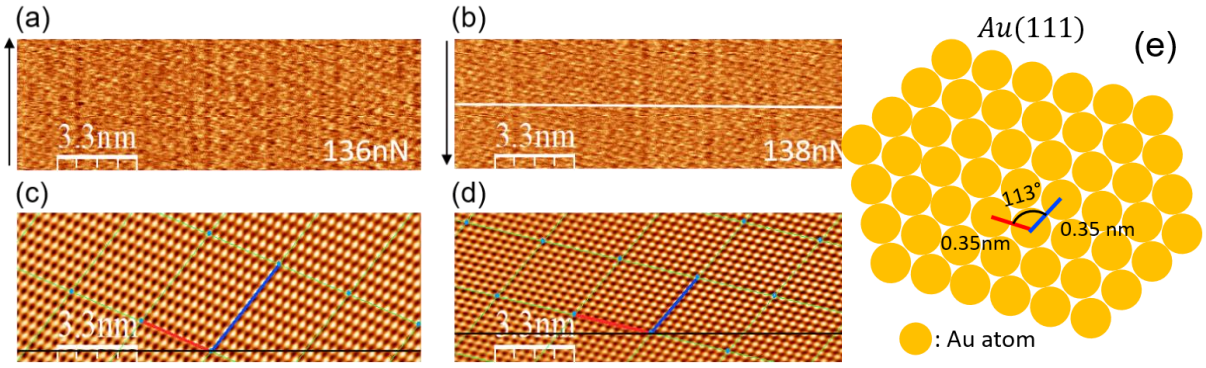

Figure S 6.8 Lateral force maps at 0.45 V (vs. Ag/Ag^{+}) in (a) downward scan and (b) upward scan. Black arrow indicates scan direction. (c) and (d) are the lattice images after Fast Fourier Transform (FFT) of (a) and (b), respectively. (e) is the illustration of the real lattice with lattice parameters after the correction of thermal drift. Applied normal loads of (a) and (b) are 104 and 106 nN, respectively. Scan rate is 0.47 nm/s. The amount of water in the electrolyte is 300 ppm.

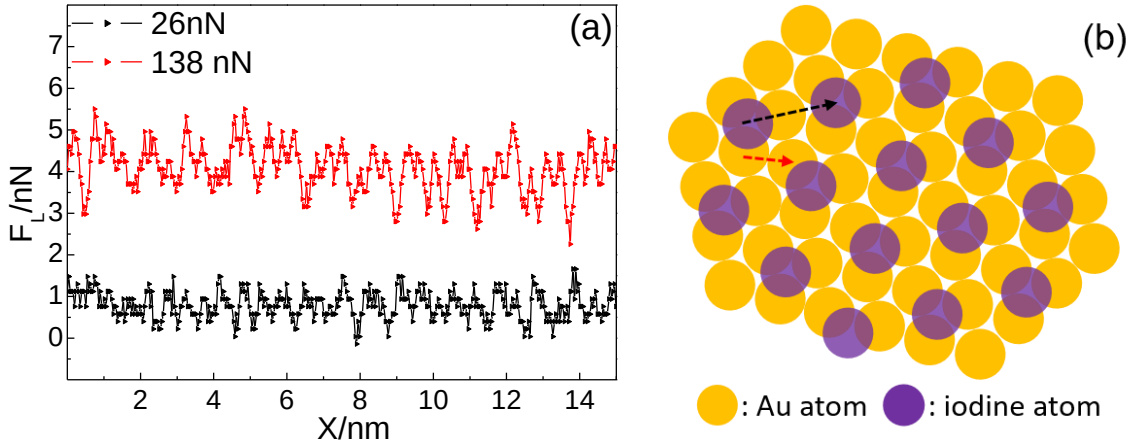

Figure S 6.9 (a) Atomic stick-slip at the white line marked in Figure S7b (26 nN) and Figure S8b (138 nN). (b) possible way for the atomic stick-slip. Scan rate is 0.47 nm/s.

Figure S6.7 and S6.8 shows atomic corrugations at 0.45V with increasing normal load in the electrolyte containing 300 ppm water. When the applied normal load is relatively low, the observed structure is $(\sqrt{3} \times \sqrt{3})$R30° structure representing the iodine structure. With increasing the normal load, the revealed structure corresponds to Au(111)(1×1). The results of atomic stick-slip at 26 nN and 138 nN are shown in Figure S6.9. At 26 nN and 138 nN, the distances between sticks are about 0.5 nm and 0.34 nm, respectively. Together with atomic corrugations, Figure S6.9b shows the possible way for the atomic stick-slip.

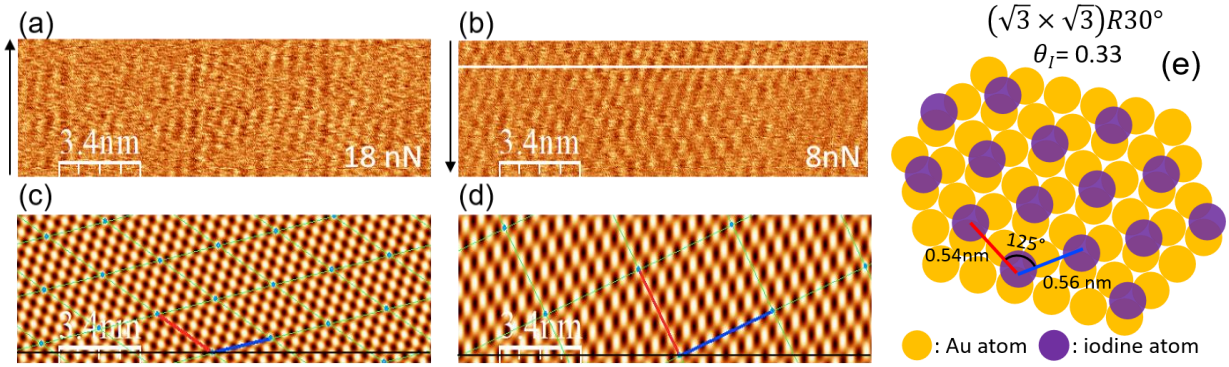

Figure S 6.10 Lateral force maps at - 0.4 V (vs. Ag/Ag^+) in (a) upward scan and (b) downward scan. Black arrow indicates scan direction. (c) and (d) are the lattice images after Fast Fourier Transform (FFT) of (a) and (b), respectively. (e) is the illustration of the real lattice with lattice parameters after the correction of thermal drift. Applied normal loads of (a) and (b) are 10 and 6 nN. Scan rate is 0.47 nm/s. The amount of water in the electrolyte is 300 ppm.

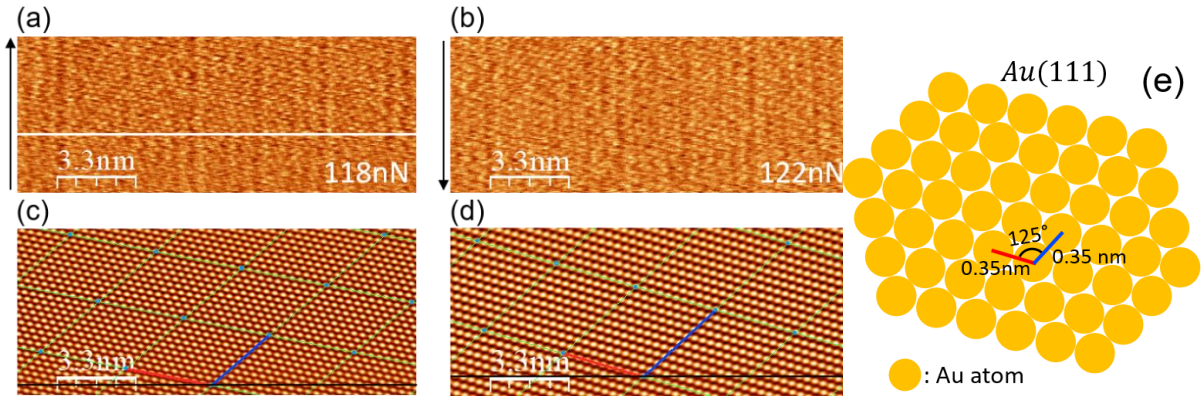

Figure S 6.11 Lateral force maps at - 0.4 V (vs. Ag/Ag^+) in (a) downward scan and (b) upward scan. Black arrow indicates scan direction. (c) and (d) are the lattice images after Fast Fourier Transform (FFT) of (a) and (b), respectively. (e) is the illustration of the real lattice with lattice parameters after the correction of thermal drift. Applied normal loads of (a) and (b) are 118 and 122nN, respectively. Scan rate is 0.47 nm/s. The amount of water in the electrolyte is 300 ppm.

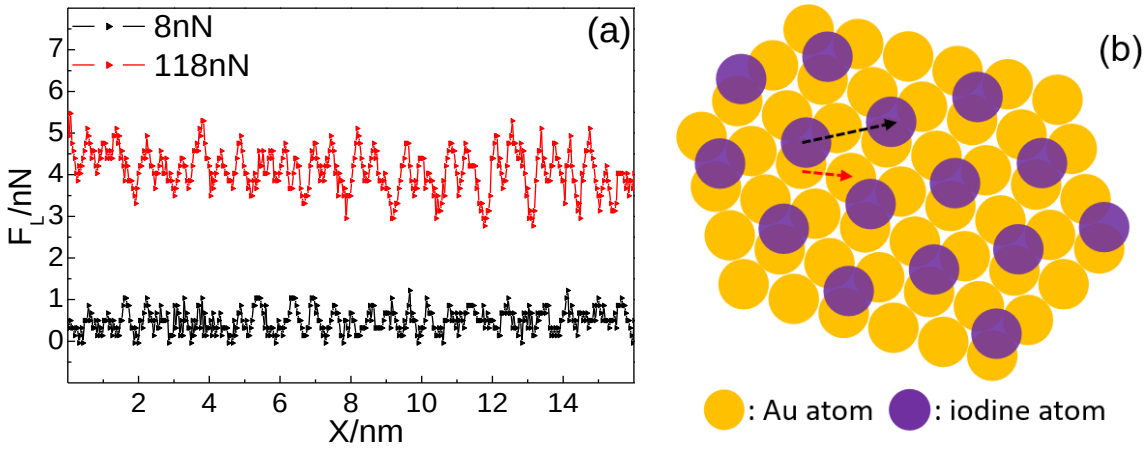

Figure S 6.12 (a) Atomic stick-slip at the white line marked in Figure S6.10b (8 nN) and Figure S6.11a (118 nN). (b) a possible way for the atomic stick-slip. Scan rate is 0.47 nm/s.

Figure S6.10 and S6.11 shows the atomic corrugation at -0.4 V in the electrolyte containing 300 ppm water. The overserved $(\sqrt{3} \times \sqrt{3})$R30° structure indicates that the iodine is still adsorbed on the surface. With increasing the normal load, the structure changes to Au(111), which confirms that the AFM tip penetrates into iodine layer. The results of atomic stick-slip at 8 nN and 118 nN are shown in Figure S6.12. At 8 nN and 118 nN, the distances between sticks are about 0.54 nm and 0.37 nm, respectively. Together with atomic corrugations, Figure S6.12b shows the possible way for the atomic stick-slip.

6.5.3 Force separation curve

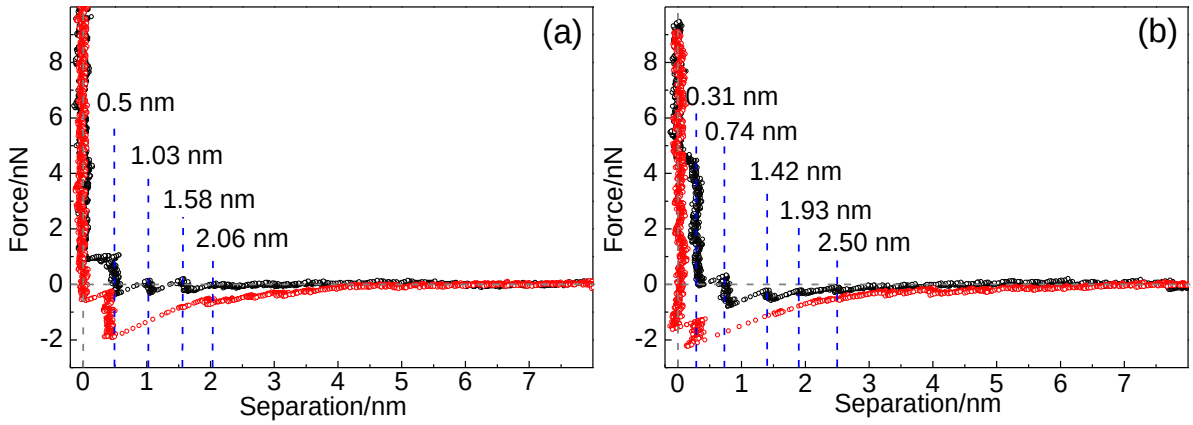

Figure S 6.13 Force separation profiles obtained on the I-modified Au(111) in G4. Black and red curves show the approach and retract of AFM tip, respectively. The speed of tip is 125 nm/s.

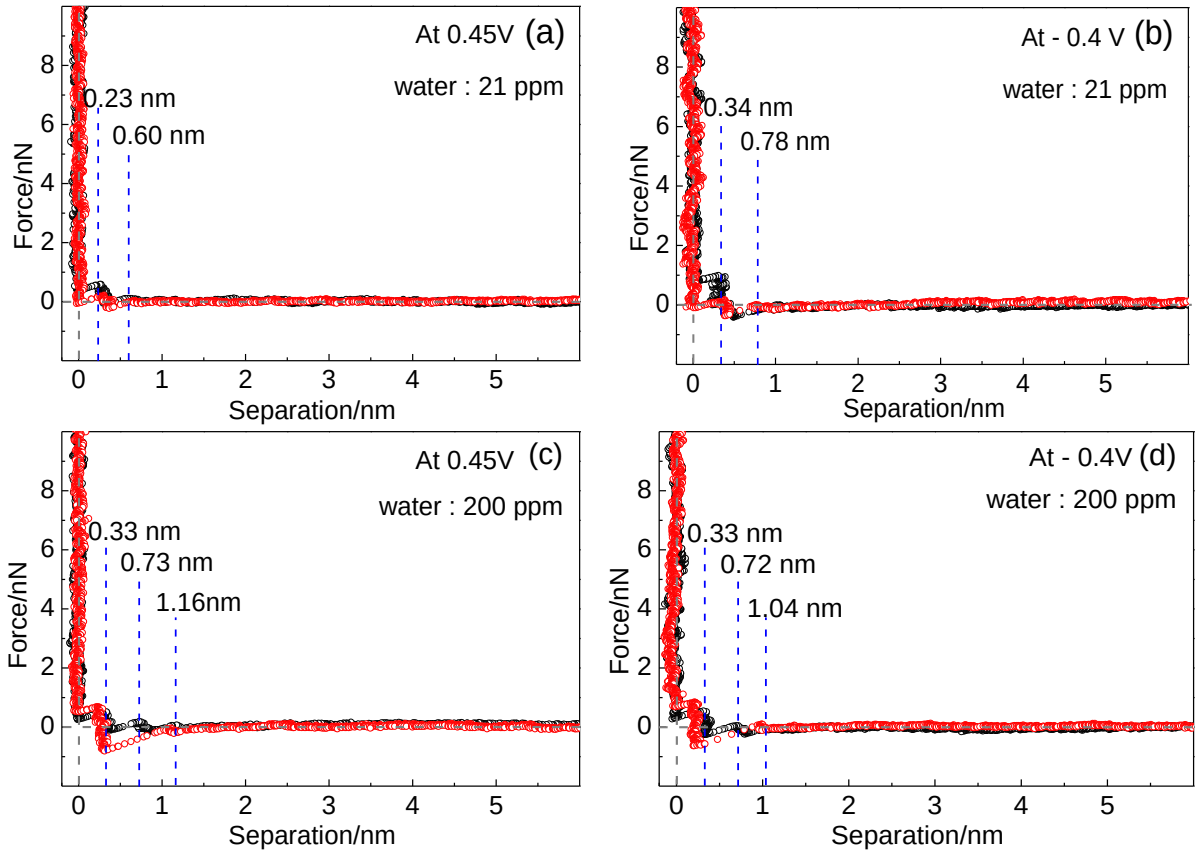

Figure S 6.14 Different type of force separation profiles of Figure 6.7.

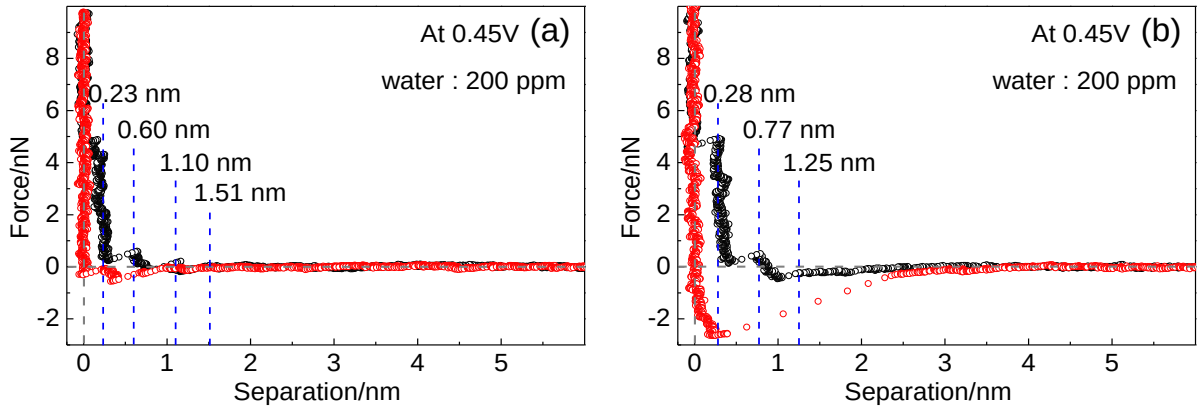

Figure S 6.15 Force separation profiles obtained at 0.45 V on the I-modified Au(111) in 0.1M $LiClO_4$/G4 (water: 200 ppm). Black and red curves indicate approach and retract curves, respectively. The approach (or retract) speeds are (a) 50 nm/s and (b) 83 nm/s.

6.5.4 Dependence of friction on normal load

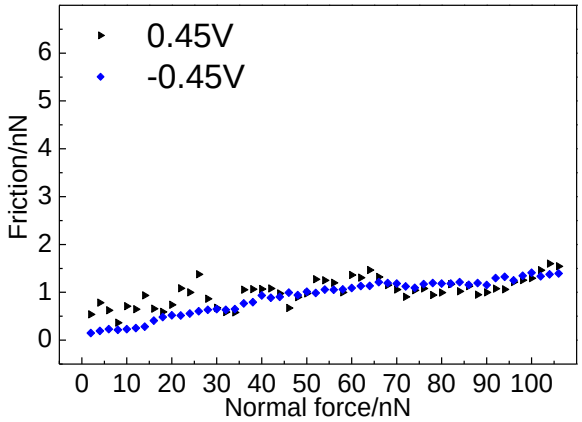

Figure S 6.16 Friction forces on normal load for Au(111) in 0.1 M $LiClO_4$/G4. The amounts of water in the electrolyte is 21 ppm. The scan size and scan rate were 20x20 nm^2 and 0.47 nm/s, respectively.

Reference

[1] M. Nielinger, H. Baltruschat *Phys. Chem. Chem. Phys.* **2007**, *9*, 3965-3969.

[2] F. Hausen, M. Nielinger, S. Ernst, H. Baltruschat *Electrochim. Acta*. **2008**, *53*, 6058-6063.

[3] M. Nielinger, F. Hausen, N. Podghainiy, H. Baltruschat in *Nanotribology at electrodes: Influence of adsorbates and potential on friction forces studied with atomic force microscopy, Vol.* (Eds.: A. Fischer, K. Bobzin), Wiley-VCH, Weinheim, **2009**, pp.178-184.

[4] N. Podgaynyy, S. Iqbal, H. Baltruschat *Surf. Sci.* **2015**, *631*, 67-72.

[5] N. Podgaynyy, S. Wezisla, C. Molls, H. Baltruschat *Beilstein J. Nanotechnol.* **2015**, *6*, 820-830.

[6] I. Park, H. Baltruschat *ChemPhysChem*. **2021**, *7*, 1-9.

[7] N. N. Gosvami, T. Filleter, R. Bennewitz *Tribol. Lett.* **2010**, *39*, 19-24.

[8] A. Labuda, W. Paul, B. Pietrobon, R. B. Lennox, P. H. Grutter, R. Bennewitz *Rev. Sci. Instrum.* **2010**, *81*, 083701.

[9] A. Labuda, F. Hausen, N. N. Gosvami, P. H. Grütter, R. B. Lennox, R. Bennewitz *Langmuir*. **2011**, *27*, 2561-2566.

[10] F. Hausen, N. N. Gosvami, R. Bennewitz *Electrochim. Acta*. **2011**, *56*, 10694-10700.

[11] R. Bennewitz, F. Hausen, N. N. Gosvami *J. Mater. Res.* **2013**, *28*, 1279.

[12] F. Hausen, J. A. Zimmet, R. Bennewitz *Surf. Sci.* **2013**, *607*, 20 - 24.

[13] A. A. Gewirth, V. B. Elings, J. Massie, P. K. Hansma, S. Manne *Science*. **1991**, *251*, 183-186.

[14] B. C. Schardt, S. L. Yau, F. Rinaldi *Science*. **1989**, *243*, 1050-1053.

[15] R. Vogel, I. Kamphausen, H. Baltruschat *Ber. Bunsenges. Phys. Chem.* **1992**, *96*, 525.

[16] R. Lim, S. O'Shea *Phys. Rev. Lett.* **2002**, *88*, 246101.

[17] K.-I. Fukui, T. Utsunomiya, Y. Yokota *Jpn. J. Appl. Phys.* **2017**, *56*, 08LA03.

[18] H. Li, F. Endres, R. Atkin *Phys. Chem. Chem. Phys.* **2013**, *15*, 14624-14633.

[19] J.-W. Yan, Z.-Q. Tian, B.-W. Mao *Curr. Opin. Electrochem.* **2017**, *4*, 105-111.

[20] R. Y. Lim, S. O'Shea *Langmuir*. **2004**, *20*, 4916-4919.

[21] K. Suzuki, N. Oyabu, K. Kobayashi, K. Matsushige, H. Yamada *Appl. Phys. Express*. **2011**, *4*, 125102.

[22] T. Utsunomiya, S. Tatsumi, Y. Yokota, K.-I. Fukui *Phys. Chem. Chem. Phys.* **2015**, *17*, 12616-12622.

[23] R. Hayes, G. G. Warr, R. Atkin *Phys. Chem. Chem. Phys.* **2010**, *12*, 1709-1723.

[24] J. Sweeney, F. Hausen, R. Hayes, G. B. Webber, F. Endres, M. W. Rutland, R. Bennewitz, R. Atkin *Phys. Rev. Lett.* **2012**, *109*, 155502.

[25] N. Borisenko, A. Lahiri, G. Pulletikurthi, T. Cui, T. Carstens, J. Zahlbach, R. Atkin, F. Endres *Faraday Discuss.* **2017**, *206*, 459-473.

[26] K. Yoshida, M. Nakamura, Y. Kazue, N. Tachikawa, S. Tsuzuki, S. Seki, K. Dokko, M. Watanabe *J. Am. Chem. Soc.* **2011**, *133*, 13121-13129.

[27] K. Dokko, N. Tachikawa, K. Yamauchi, M. Tsuchiya, A. Yamazaki, E. Takashima, J.-W. Park, K. Ueno, S. Seki, N. Serizawa *J. Electrochem. Soc.* **2013**, *160*, A1304.

[28] B. McLean, H. Li, R. Stefanovic, R. J. Wood, G. B. Webber, K. Ueno, M. Watanabe, G. G. Warr, A. Page, R. Atkin *Phys. Chem. Chem. Phys.* **2015**, *17*, 325-333.

[29] H. Li, M. W. Rutland, M. Watanabe, R. Atkin *Faraday Discuss.* **2017**, *199*, 311-322.

[30] A. Cook, K. Ueno, M. Watanabe, R. Atkin, H. Li *J. Phys. Chem. C.* **2017**, *121*, 15728-15734.

[31] S. W. Coles, M. Mishin, S. Perkin, M. V. Fedorov, V. B. Ivaništšev *Phys. Chem. Chem. Phys.* **2017**, *19*, 11004-11010.

[32] H. Christenson, R. Horn, J. Israelachvili *J. Colloid Interface Sci.* **1982**, *88*, 79-88.

[33] H. K. Christenson *J. Chem. Phys*. **1983**, *78*, 6906-6913.

[34] H. K. Christenson, C. E. Blom *J. Chem. Phys*. **1987**, *86*, 419-424.

[35] R. Horn, D. Evans, B. Ninham *J. Phys. Chem.* **1988**, *92*, 3531-3537.

[36] S. Perkin, T. Albrecht, J. Klein *Phys. Chem. Chem. Phys.* **2010**, *12*, 1243-1247.

[37] A. M. Smith, K. R. J. Lovelock, N. N. Gosvami, T. Welton, S. Perkin *Phys. Chem. Chem. Phys.* **2013**, *15*, 15317-15320.

[38] W. Ouyang, A. S. de Wijn, M. Urbakh *Nanoscale*. **2018**, *10*, 6375-6381.

[39] R. Oelgeklaus, J. Rose, H. Baltruschat *J. Electroanal. Chem.* **1994**, *376*, 127-133.

[40] F. Lu, G. N. Salaita, H. Baltruschat, A. T. Hubbard *J. Electroanal. Chem.* **1987**, *222*, 305-320.

[41] J. Albers, H. Baltruschat, I. Kamphausen *J. Electroanal. Chem.* **1995**, *395*, 99-105.

[42] N. J. Tao, S. M. Lindsay *J. Phys. Chem.* **1992**, *96*, 5213-5217.

[43] W. Haiss, J. K. Sass, X. Gao, M. J. Weaver *Surf. Sci.* **1992**, *274*, L593-L598.

[44] B. M. Ocko, J. Wang, G. M. Watson *J. Phys. Chem.* **1994**, *98*, 897-906.

[45] T. Yamada , N. Batina, K. Itaya *Surface Science*. **1995**, *335*, 204-209.

[46] X. P. Gao, M. J. Weaver *J. Am. Chem. Soc.* **1992**, *114*, 8544-8551.

[47] A. S. Shatla, P. P. Bawol, H. Baltruschat *ChemElectroChem*. **2020**, *7*, 4782-4793.

[48] A. S. Shatla, A. A. Abd-El-Latif, S. Ayata, D. Demir, H. Baltruschat *Electrochimica Acta*. **2020**, *334*, 135556.

[49] S. A. Freunberger, Y. Chen, N. E. Drewett, L. J. Hardwick, F. Barde, P. G. Bruce *Angew Chem Int Ed Engl*. **2011**, *50*, 8609-8613.

[50] R. Wen, M. Hong, H. R. Byon *J. Am. Chem. Soc.* **2013**, *135*, 10870-10876.

[51] H. M. A. Amin, C. Molls, P. P. Bawol, H. Baltruschat *Electrochim. Acta*. **2017**, *245*, 967-980.

[52] P. Hegemann, M. Hegemann, L. Zan, H. Baltruschat *J. Electrochem. Soc.* **2019**, *166*, A245-A250.

[53] L. Zan, D. Xing, A. Abd-El-Latif, H. Baltruschat *Beilstein J. Nanotechnol.* **2019**, *10*, 2541–2552.

[54] Da.Xing, P. P. Bawol, A.-E.-A. A. A. Abd-El-Latif, L. Zan, H. Baltruschat *ChemElectroChem*. **2021**, *in press*.

[55] P. K. R. Kottam, S. Dongmo, M. Wohlfahrt-Mehrens, M. Marinaro *Energies :*. **2020**, *13*, 1470.

[56] M. Marinaro, S. K. E. Moorthy, J. Bernhard, L. Jörissen, M. Wohlfahrt-Mehrens, U. Kaiser *Beilstein J. Nanotechnol.* **2013**, *4*, 665-670.

[57] N. Amir, Y. Vestfrid, O. Chusid, Y. Gofer, D. Aurbach *J. Power Sources*. **2007**, *174*, 1234-1240.

[58] H. Li, T. Niemann, R. Ludwig, R. Atkin *J. Phys. Chem. Lett.* **2020**, *11*, 3905-3910.

[59] C. S. Perez-Martinez, S. Perkin *Langmuir*. **2019**, *35*, 15444-15450.

[60] J. E. Sader, J. W. M. Chon, P. Mulvaney *Rev. Sci. Instrum.* **1999**, *70*, 3967-3969.

[61] C. P. Green, H. Lioe, J. P. Cleveland, R. Proksch, P. Mulvaney, J. E. Sader *Rev. Sci. Instrum.* **2004**, *75*, 1988-1996.

[62] S. Sundararajan, B. Bhushan *J. Appl. Phys.* **2000**, *88*, 4825-4831.

[63] S. Iqbal, L. Zan, E. Nardi, H. Baltruschat *Phys. Chem. Chem. Phys.* **2018**, *20*, 6176-6186.

[64] A. Socoliuc, R. Bennewitz, E. Gnecco, E. Meyer *Phys. Rev. Lett.* **2004**, *92*, 134301.

[65] N. N. Gosvami, P. Egberts, R. Bennewitz *J. Phys. Chem. A.* **2011**, *115*, 6942-6947.

[66] Z. B. Milne, R. A. Bernal, R. W. Carpick *Langmuir*. **2019**, *35*, 15628-15638.

[67] H. Christenson, R. Horn *Chem. Phys. Lett.* **1983**, *98*, 45-48.

[68] H. Manchanda, M. Kumar *Renewables: Wind, Water, and Solar*. **2015**, *2*, 1-24.

[69] J. Sweeney, G. B. Webber, M. W. Rutland, R. Atkin *Phys. Chem. Chem. Phys.* **2014**, *16*, 16651-16658.

[70] S. L. Yau, C. M. Vitus, B. C. Schardt *J. Am. Chem. Soc.* **1990**, *112*, 3677-3679.

[71] P. Broekmann, M. Wilms, M. Kruft, C. Stuhlmann, K. Wandelt *J. Electroanal. Chem.* **1999**, *467*, 307-324.

CHAPTER 7

Atomic-scale friction study: Underpotential deposition (UPD) of silver on I-modified Au(111) in aprotic electrolytes

7.1 Abstract

Using lateral force microscopy (LFM), we investigate the frictional behavior on I-modified Au(111) during Ag underpotential deposition (UPD) in aprotic electrolytes. Regardless of solvents, structural transitions have been observed depending on potential and normal load, respectively. These structural transitions indicate that the structure of iodine is very sensitive to the Ag coverage and the tip penetrates the adsorbed iodine as normal load increases. Force-separation (FS) curves clearly show that the solvent forms about 3 ordered layers near the iodine adlayer independent of potential. Friction forces as function of normal load show the dependence of solvents. With increasing normal load in Ag^+ containing tetraglyme (G4), friction increases steeply as the sliding tip penetrates the iodine adsorbed on Ag adlayers, in agreement with the results in aqueous electrolyte. Furthermore, friction increases more dramatically as the concentration of water increases. Considering the high friction on Ag monolayer after the penetration into the iodine, there are two possible causes: 1) the reduced mobility of the iodine on Ag adlayer and 2) the interaction between water adsorbed on the tip and Ag adlayers. However, in Ag^+ containing PC, in spite of the penetration into the iodine adlayer, friction forces on load have no distinction between gold and silver substrates. This implies that there is an influence of solvent on friction.

KEYWORDS: friction force microscopy (FFM), interfaces, tribology, adsorbate structure, tetraglyme, propylene carbonate

7.2 Introduction

Glyme-based eletrolytes such as tetraethylene glycol dimethyl ether (G4) and other ethers are attractive candidates for metal-O_2 batteries and magnesium or calcium ion batteries due to the greater stability during the discharge and charge processes than organic carbonate-based electrolytes (e.g. propylene carbonate (PC)), which are typical component of the electrolyte used in Li-ion batteries [1-9].

Ionic liquids (ILs) composed entirely of ions have attracted tremendous interest also in tribology due to their interfacial structures [10-17]. Interestingly, the frictional behavior caused by the special ordering of these ions on the solid surface helps to understand the interfacial interactions which can be modified by applied potential and normal load. For example, in AFM force-distance profiles recorded in ILs, the width of steps indicating the physical dimensions of the cation and anion depends on the length of alkyl chain of cation and the strength of interaction between ions [10]. At the transition from the multilayer regime to the boundary regime, a protic IL containing C_3 alkyl chain shows higher friction than C_2 alkyl chain due to solvophobic interaction [11]. Furthermore, this solvophobic interaction depends on the applied potential [12].

With adding water to the solvent, the oscillatory forces for octamethylcycloterasiloxane (OMCTS) measured by a surface force apparatus (SFA) disappeared due to the strong adsorption of water on the mica surface [18]. However, in the case of IL, $[C_4C_1Pyrr][NTf_2]$, water seems to be placed between ions without disrupting the film structure of the IL resulting in the increase of the force necessary to rupture layers [19]. Furthermore, when the IL $[C_4C_1Pyrr][NTf_2]$ is diluted in the organic solvent PC at low concentrations (~2 M), the wavelength of the oscillatory structure force corresponds to the molecular size of PC [20]. The investigation of dominant interactions between surfaces and medium (e.g. solvent, ions, and water) might help to understand the tribological behavior on atomic scale contact.

Underpotential deposition (UPD) of foreign metals occurs at more positive potential than the Nernst equilibrium potential. Ag UPD has been extensively studied on Au(111) in aqueous electrolytes since it is an ideal model system due to the negligible lattice mismatch ($a_{Au} = 4.07$ Å, $a_{Ag} = 4.08$ Å). The UPD process is very sensitive to the type of anions [21-26]. Recently, M. Ehrenburg et al. have reported the Ag UPD on Au(111) in air- and water-stable ionic liquid [27]. Itaya et al. have reported the Ag UPD on I-modified Au(111) showing that the structure of

iodine changes depending on the coverage of Ag [28]. Furthermore, in chapter 3, the structural transition on I-modified Au(111) during Ag UPD in aqueous electrolyte has been investigated in detail.

In chapter 3, the atomic-scale friction has been studied on Au(111) during Ag UPD in aqueous electrolyte [29]. As suggested by W. Ouyang et al. [30], friction depends on the coverage of adsorbates (e.g. Ag and sulfate), which decides whether the tip penetrates into the adlayer or not. On I-modified Au(111), lateral force microscope (LFM) images clearly show the transition of structures as normal load increases, demonstrating that the AFM tip penetrates into iodine adlayer (see chapter 4). Furthermore, at potentials slightly negative of the 1st Ag UPD peak, where the Ag coverage is 0.44, the tip penetrates into the silver layer. We note that friction increases steeply on Ag adlayer as the tip penetrates into adsorbates. Therefore, three different regimes (α, β, γ) are defined based on the transition of atomic corrugations and frictional behavior as function of normal load: 1) in α regime, the tip slides on the iodine adlayer, 2) in β regime, tip penetrates into the adlayers, and 3) in γ regime, the tip slides on gold or silver surfaces after the penetration. In chapter 6, it has been investigated that no extra energy dissipation is required to push away adsorbed iodine on Au(111), which demonstrates that the iodine is quite mobile on Au(111). Therefore, it is assumed that the mobility of iodine varies with metals. In non-aqueous electrolyte we furthermore found that G4 molecules form ordered layers on I-modified Au(111). Even though atomic corrugations show clear transition of structures with normal load (the iodine structure is visible for F_N < 30 nN, that of the gold substrate for F_N > 50 nN), there is no change of the friction coefficient due to the penetration into the iodine adlayer, as described in chapter 4 for friction on I-modified Au(111) in aqueous electrolyte. Thus, there is no additional energy dissipation for the tip induced movement of iodine atoms on Au(111) in both cases, aqueous and non-aqueous electrolytes.

Here, we report on the frictional behavior during Ag UPD on I-modified Au(111) in aprotic solvents (i.e. PC and G4) using AFM. By introducing the stable iodine adlayer, it was our aim to understand the influence of water and solvent molecules on friction as the tip penetrates into the iodine adlayer.

7.3 Experimental

A disc type Au(111) single crystal (diameter: 10mm and thickness: 3mm) purchased from MaTecK GmbH was used as working electrode. It was annealed by flame and cooled down above iodine crystals purged with Ar to get a monolayer of iodine on the clean surface. Gold and silver wires were used as counter and reference electrodes, respectively. For electrolytes, 2 mM $AgClO_4$ and 0.1 M $LiClO_4$ were dissolved in tetraethylene glycol dimethyl ether (tetraglyme, G4) or propylene carbonate (PC). A coulometric KF Titrator (C20, Metler Toledo) with a diaphragm electrode was used to measure the water content. The electrolyte was prepared in a glovebox. The concentration of water for the freshly prepared electrolyte was around 50 ppm. While the AFM-cell transferred to the AFM chamber purged with Ar, the AFM-cell is shortly exposed to the atmosphere (for less than 1 min). It might increase the final amount of water in the electrolyte but since the exposure time is less than 1 min, we assume that the concentration of water will hardly change (A further argument for the negligible change is the drastic effect in friction results, when the water content is increased to 150 ppm on purpose).

Lateral (frictional) force measurements were performed using Agilent 5500 AFM, equipped with an atmosphere chamber. Silicon tips (PPP-FM, NANOSENSORS, tip radius <10nm) were used and the normal force constants was 1.13±0.2 N/m. Normal and torsional resonance frequency of AFM tips were measured by AFM (Agilent 5500/AC mode). Q factor for theses resonance frequencies was obtained using the equation of simple harmonic oscillation (SHO) [31]. Normal and torsional force constants were calculated using the Sader method [31, 32] and the lateral force constant was obtained by dividing torsional force constant with the square of the cantilever height. During the measurement, a homemade AFM cell was used, which contains a three-electrode assembly, and Ar was purged through the atmosphere chamber. The scan size and rate for the lateral force vs. normal load curves were 20×20 nm^2 and 0.47 nm/s, respectively.

The twisting of the cantilever during the AFM tip scans over the surface due to friction (F) is recorded as the deflection of the laser beam. The sign of the deflection depends on the scan direction. In addition, the deflection of the laser is caused by topography (T) (e.g. steps on the surface); this does not depend on scan direction. Thus, the forward image and backward image contain [T+F] and [T-F], respectively. Friction force data were obtained by subtracting the backward data from the forward data and dividing it by 2 to eliminate topographic effects [33].

Atomic structures were obtained from the corrugations in lateral force maps. The scan size and scan rate are written individually in the caption of figures. In order to minimize the noise in the image, filtering by Fast Fourier Transform (FFT) was used. Thermal drift was corrected to get the lattice parameter [34]. The discrepancy between lattice parameters obtained using lateral force maps and topography is negligible. As shown in chapter 2.3.2, the atomic corrugations on the highly oriented pyrolytic graphite (HOPG) in air showed lattice parameters being about 10 % larger than the theoretical value.

7.4 Results and discussion

7.4.1 Cyclic voltammetry (CV)

Figure 7.1 shows the cyclic voltammetry (CV) obtained for I-modified Au(111) in the AFM-cell containing 2 mM $AgClO_4$/0.1 M $LiClO_4$/G4. Regardless of the water concentration, we observed two sets of Ag UPD peaks, C_1/A_1 and C_2/A_2. The charge densities corresponding to the first (C_1) and second (C_2) UPD peaks are about 195 µC/cm² and 20 µC/cm², respectively. In aqueous electrolyte for I-modified Au(111), the Ag UPD occurs in two steps for monolayer formation and a third one before the bulk deposition for formation of a bilayer (chapter 4.4.1) [28]. However, as shown in Figure S7.1a, where we extended the negative potential limit to lower values, there is no clear separation between the bilayer formation and the bulk deposition in 2 mM $AgClO_4$/0.1 M $LiClO_4$/G4. Considering the observed charge densities, we conclude that the two UPD peaks represent the formation of a Ag monolayer.

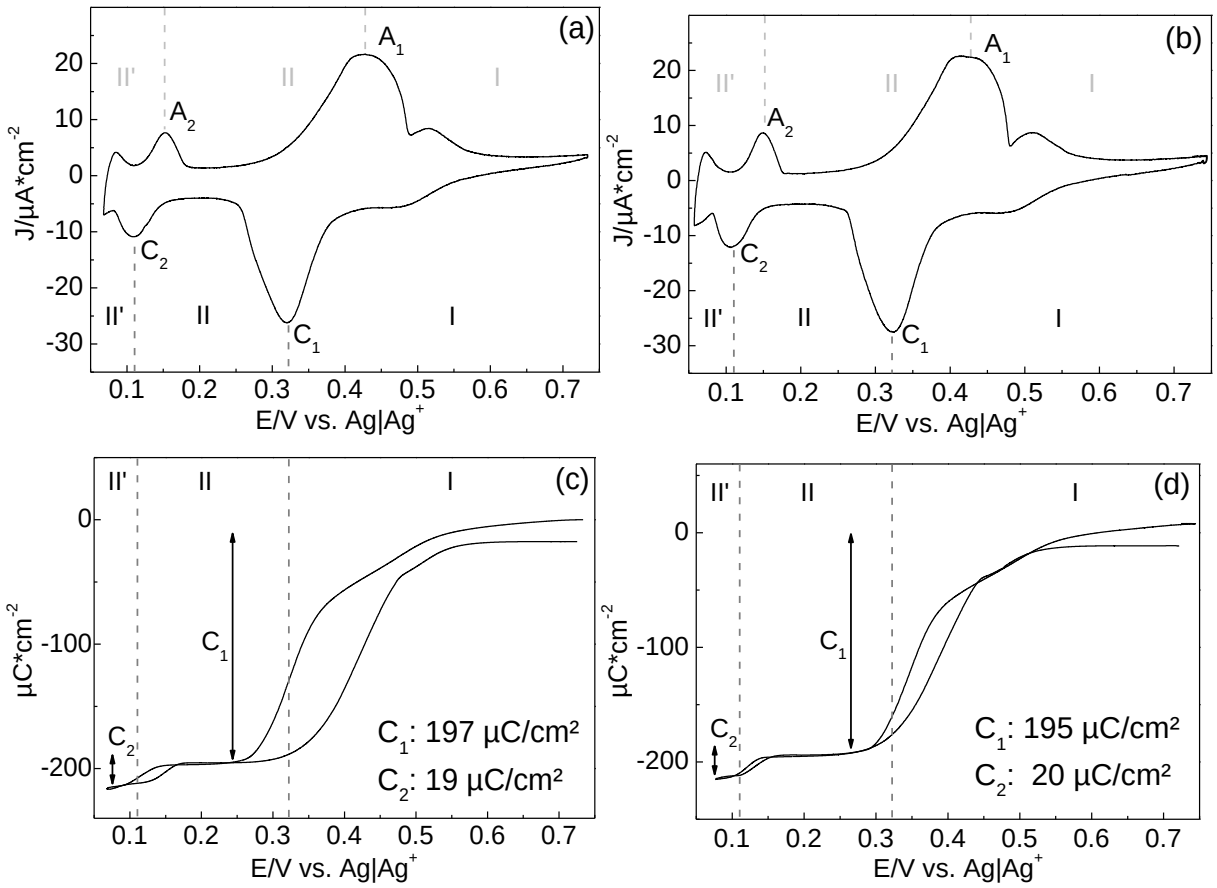

Figure 7.1 Cyclic voltammetry on I-modified Au(111) in AFM-cell filled with 2 mM $AgClO_4$/0.1 M $LiClO_4$/G4 containing (a) 51 ppm water and (b) 151 ppm water. (c) and (d) indicate the coulometric curves from (a) and (b), respectively. The sweep rate is 15 mV/s.

In contrast, we observed three peaks, C_1, C_2, and C_3, for the Ag UPD on I-modified Au(111) in Ag^+ containing propylene carbonate (PC) as shown in Figure S7.1b. However, in the extended potential window including the peak C_3, the stability of the AFM tip on the surface became an issue, which might be due to the decomposition of PC. Therefore, we focus on the two deposition steps, peak C_1 and C_2, for the Ag UPD in PC (Figure 7.2). As for Ag^+ containing G4, the concentration of water has a minor influence on the CV for the Ag UPD in PC. The charge densities corresponding to the processes in the first (C_1) and second (C_2) UPD peaks are about 182 µC/cm² and 69 µC/cm², respectively. Therefore, we suggest that the two observed peaks in PC also represent the formation of Ag monolayer. The total charge density (251 µC/cm²) is slightly higher than the theoretical value (222 µC/cm²), which might result from the double layer effects on the adsorption of silver ions on the iodine layer prior to further deposition.

In both cases, considering the charge densities, we classify the potential range as region I, II, and II´ according to the extent of Ag deposition.

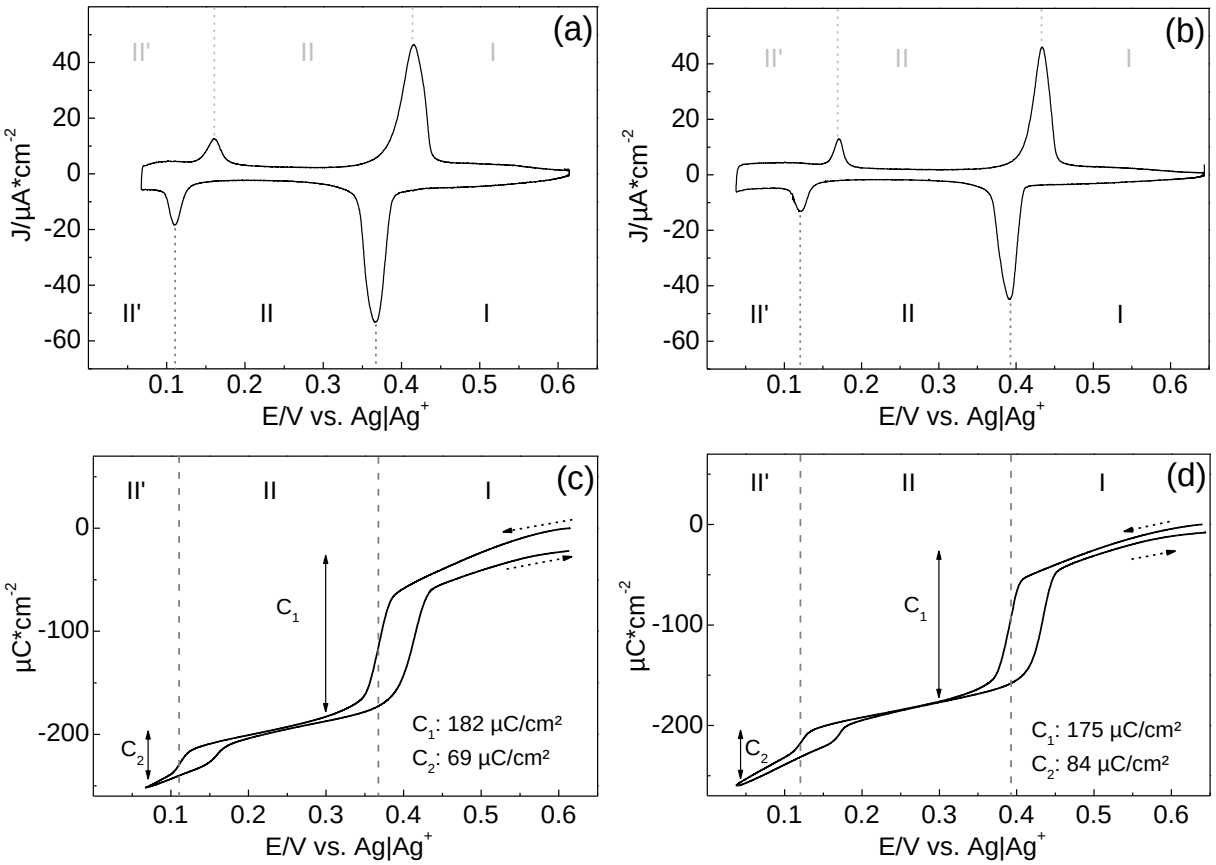

Figure 7.2 Cyclic voltammetry on I-modified Au(111) in AFM-cell filled with 2 mM $AgClO_4$/0.1 M $LiClO_4$/PC containing (a) < 100 ppm water and (b) > 500 ppm water. (c) and (d) indicate the coulometric curves from (a) and (b), respectively. The sweep rate is 15 mV/s.

7.4.2 Atomic corrugation

In chapter 4.4.2 and chapter 6.4.2, the transition of structures with increasing normal load for I-modified Au(111) has been studied in aqueous and aprotic electrolytes, respectively, which indicates that the AFM tip penetrates into the iodine adlayer without irreversible wear. Similar to that, regardless of the potential regions and the concentration of water, we observed the transition of structures with increasing normal load for I-modified Au(111) in Ag^+ containing G4 (Figure 7.3).

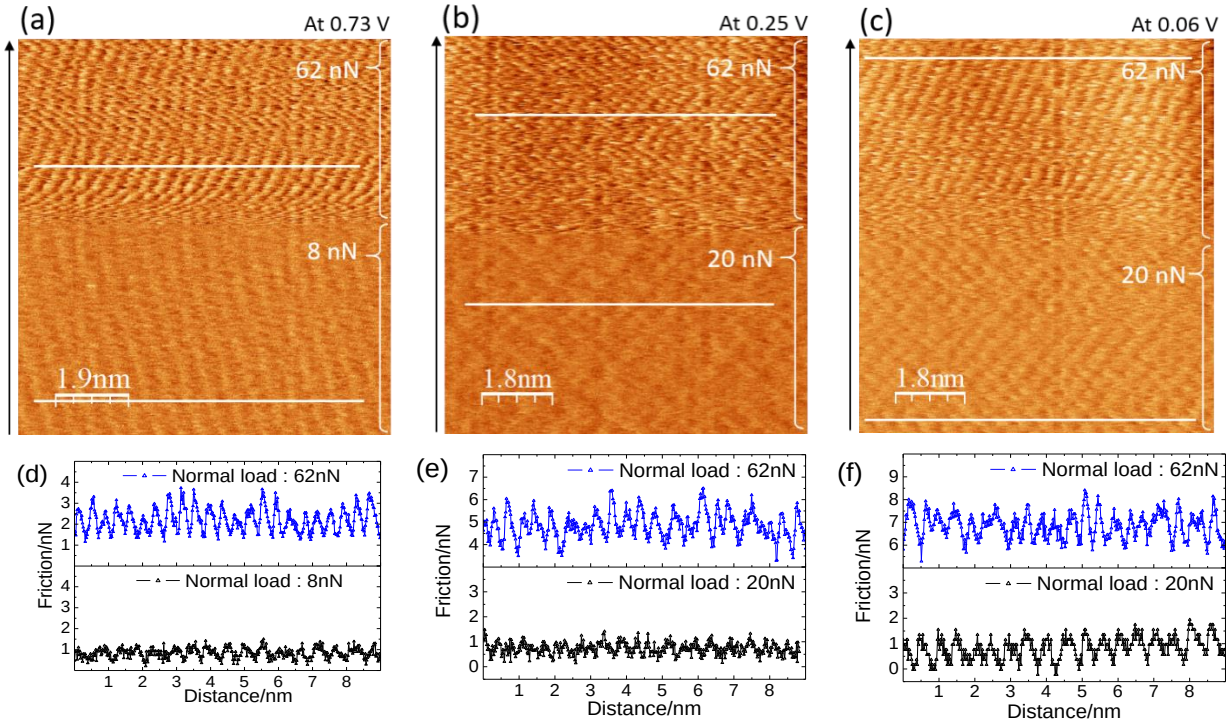

Figure 7.3 AFM lateral force maps at (a) 0.73 V, before the Ag UPD, (b) 0.25 V, after the 1st Ag UPD, and (c) 0.06 V, after the 2nd Ag UPD. (d)-(f) Cross-section of the lateral force along the line indicated in (a)-(c). The arrow indicates the scan direction and the scan size is 10x10 nm^2.

The results of atomic stick-slip demonstrate that at low normal load the tip slides on the iodine adlayer (d_{sticks}: 0.51 nm (0.73 V), 0.45 nm (0.25 V), and 0.5 nm (0.06 V)) and at high normal load where the tip penetrates into the iodine adlayer, the tip slides on the surface of gold or silver monolayer (d_{sticks}: 0.37 nm). (Note that these distances do not simply correspond to the atomic distances because of the angle between scan direction and lattice vector.)

Figure 7.4 and 7.5 show atomic corrugations in potential region I (0.73 V) at a normal load of 10 nN and 50 nN, respectively. As expected from atomic stick-slips, we observed a $(\sqrt{3} \times \sqrt{3})R30°$ structure and a $Au(111)(1 \times 1)$ structure at low (F_N < 10 nN) and high (F_N > 50 nN) normal loads, respectively. In potential region II (0.25 V), it was hard to get well-resolved atomic corrugation at low normal load (F_N < 40 nN). At high normal load (F_N > 50 nN), the observed structure is close to that expected for Ag(111), which means that a Ag monolayer completes after the 1st Ag UPD peak as expected from the charge density. When the potential was swept to potential region II´, 0.06 V, structures obtained at low normal load (F_N < 20 nN) and high normal load (F_N > 50 nN) together with atomic stick-slips suggest that the iodine forms a $(\sqrt{3} \times \sqrt{3})R30°$ structure on the Ag(1×1) monolayer (Figure 7.7 and 8).

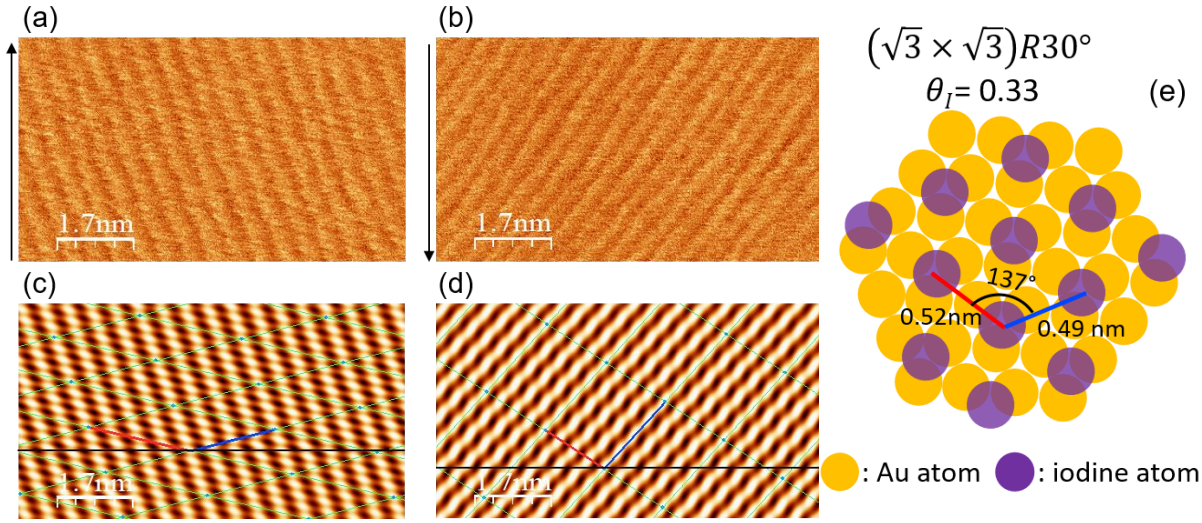

Figure 7.4 Lateral force maps at 0.73 V (vs. Ag/Ag^+) in 2 mM $AgClO_4$/0.1 M $LiClO_4$/G4 (a) upward scan and (b) downward scan. Arrow indicates scan direction. (c) and (d) are the lattice images after Fast Fourier Transform (FFT) of (a) and (b), respectively. (e) is the illustration of the real lattice with lattice parameters after the correction of thermal drift. The concentration of water in the electrolyte is 50 ppm. Applied normal is 10nN. Scan rate is 0.235 nm/s.

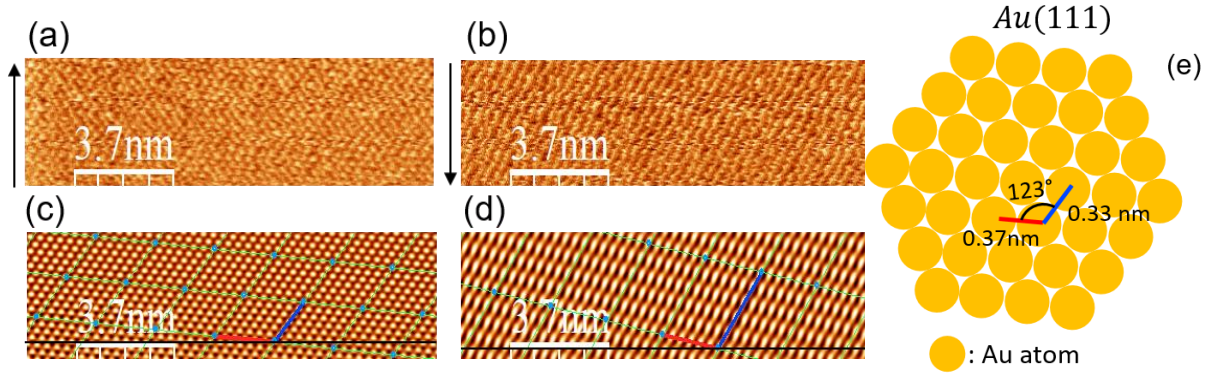

Figure 7.5 Lateral force maps at 0.73 V (vs. Ag/Ag^{+}) in 2 mM $AgClO_4$/0.1 M $LiClO_4$/G4 (a) upward scan and (b) downward scan. Arrow indicates scan direction. (c) and (d) are the lattice images after Fast Fourier Transform (FFT) of (a) and (b), respectively. (e) is the illustration of the real lattice with lattice parameters after the correction of thermal drift. The concentration of water in the electrolyte is 50 ppm. Applied normal load is 50 nN. Scan rate is 0.235 nm/s.

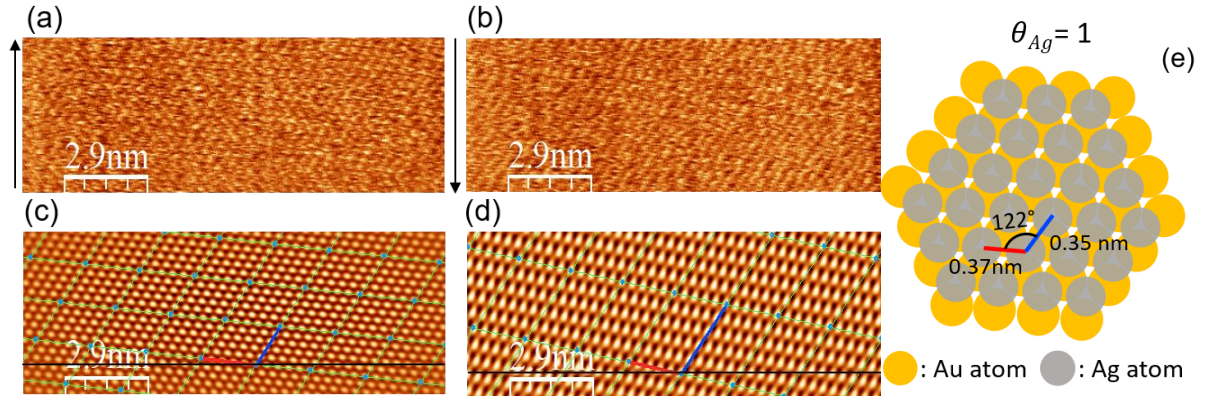

Figure 7.6 Lateral force maps at 0.25 V (vs. Ag/Ag^{+}), after the 1st Ag UPD in 2 mM $AgClO_4$/0.1 M $LiClO_4$/G4 (a) upward scan and (b) downward scan. Arrow indicates scan direction. (c) and (d) are the lattice images after Fast Fourier Transform (FFT) of (a) and (b), respectively. (e) is the illustration of the real lattice with lattice parameters after the correction of thermal drift. The concentration of water in the electrolyte is 50 ppm. Applied normal load is 62 nN. Scan rate is 0.235 nm/s.

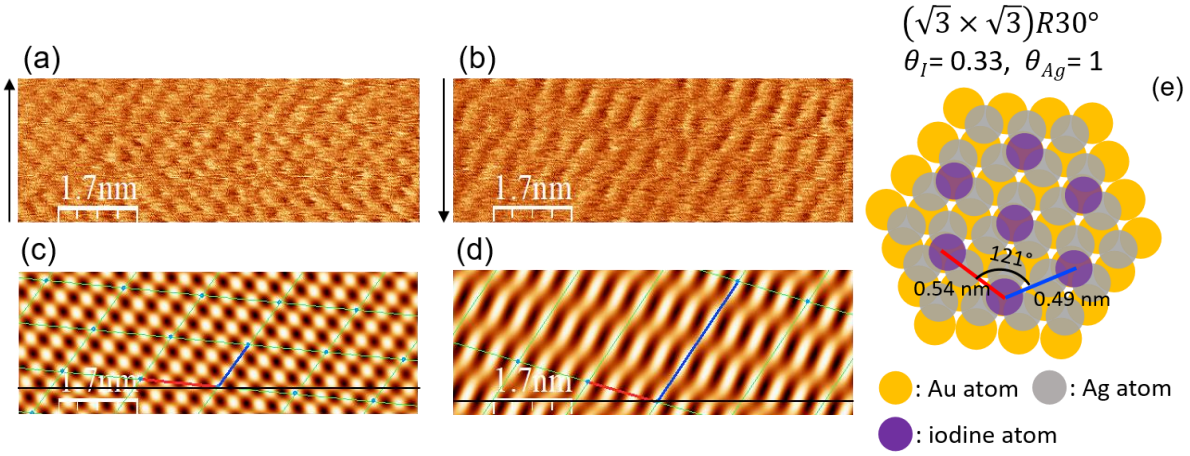

Figure 7.7 Lateral force maps at 0.06 V (vs. Ag/Ag^+), after the 2nd Ag UPD in 2 mM $AgClO_4$/0.1 M $LiClO_4$/G4 (a) upward scan and (b) downward scan. Arrow indicates scan direction. (c) and (d) are the lattice images after Fast Fourier Transform (FFT) of (a) and (b), respectively. (e) is the illustration of the real lattice with lattice parameters after the correction of thermal drift. The concentration of water in the electrolyte is 50 ppm. Applied normal load is 18 nN. Scan rate is 0.235 nm/s.

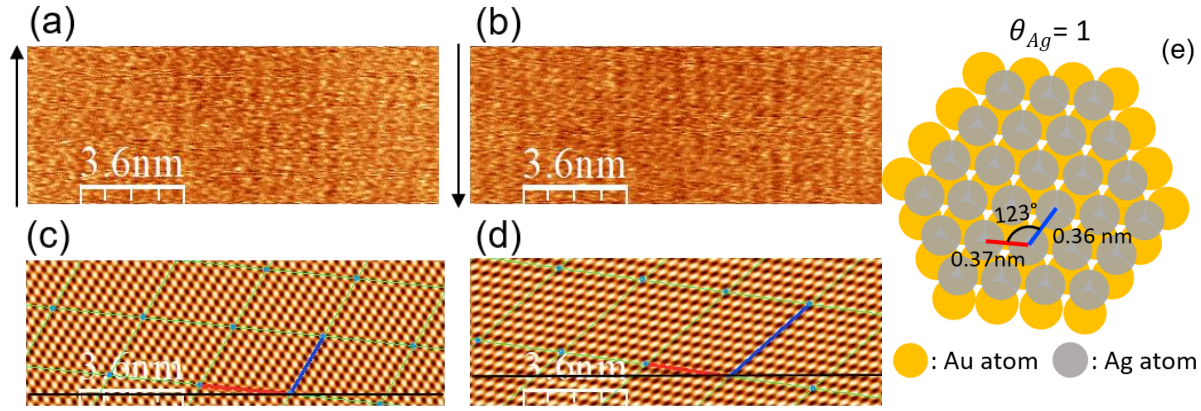

Figure 7.8 Lateral force maps at 100 nN for I-modified Au(111) in 2 mM $AgClO_4$/0.1 M $LiClO_4$/G4 at 0.06 V (vs. Ag/Ag^+), after the 2nd Ag UPD (a) upward scan and (b) downward scan. Arrow indicates scan direction. (c) and (d) are the lattice images after Fast Fourier Transform (FFT) of (a) and (b), respectively. (e) is the illustration of the real lattice with lattice parameters after the correction of thermal drift. The concentration of water in the electrolyte is 50 ppm. Applied normal load is 100 nN. The scan rate is 0.235 nm/s.

The concentration of water in the electrolyte has no influence on the atomic corrugation as shown in Figure S7.2-7. When the concentration of water is about 150 ppm, we also observed the iodine structure in potential region II (0.25 V) at low normal load, showing a $p(3 \times 3)$ structure on Ag monolayer. Therefore, we suggest that the iodine forms a $p(3 \times 3)$ structure ($\theta_I = 0.44$) in potential region II. Considering the charge density for the 1st Ag UPD peak, we assume that there are some defect regions or steps where the Ag coverage is less than 1, which might be unfavorable to iodine adsorption. This also signifies that the peak C_2 corresponds – at

least in part - to Ag deposition at such defect sites. Thus, due to such defect regions and possibly also domain boundaries between differently oriented iodine domains, the coverage of iodine on Ag monolayer may slightly increase making it possible to form a $p(3 \times 3)$ structure in the region where the silver completes a monolayer.

Figure 7.9-11 show the atomic corrugations in lateral force at different potential regions for I-modified Au(111) in 2 mM $AgClO_4$/0.1 M $LiClO_4$/PC (water < 100 ppm). The concentration of water in the electrolyte was below 100 ppm. Even though we didn't get clear atomic corrugations at low normal load, based on the preparation and the above results, we assume that the iodine forms a $(\sqrt{3} \times \sqrt{3})R30°$ structure also in this case. At high normal load, where the tip penetrates into the iodine adlayer, the atomic structures in potential region I, II, and II´ show similar structures, demonstrating that silver forms a monolayer underneath the tip at potentials negative of the 1st Ag UPD peak. Interestingly, during the friction measurement as function of potential, we observed a $p(3 \times 3)$ structure in potential region II, which disappears at high normal load (F_N > 50 nN) (Figure 7.12). Therefore, as mentioned above for the tetraglyme electrolyte, the iodine possibly forms a $p(3 \times 3)$ structure on Ag monolayer due to the defect regions ($\theta_{Ag} < 1$) of Ag deposition. When the concentration of water was above 500 ppm, it was hard to get well resolved atomic corrugation. However, based on the results in Ag^+ containing G4, we presume that there is a minor influence of water on the structure.

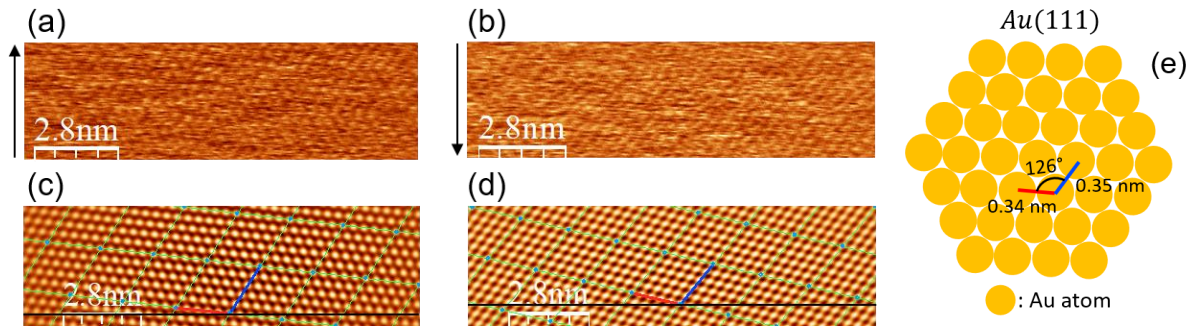

Figure 7.9 Lateral force maps at 0.61 V (vs. Ag/Ag^{+}) in 2 mM $AgClO_4$/0.1 M $LiClO_4$/PC (a) upward scan and (b) downward scan. Arrow indicates scan direction. (c) and (d) are the lattice images after Fast Fourier Transform (FFT) of (a) and (b), respectively. (e) is the illustration of the real lattice with lattice parameters after the correction of thermal drift. The concentration of water in the electrolyte is below 100 ppm. Applied normal loads for (a) and (b) are 92 nN and 104 nN, respectively. Scan rate is 0.235 nm/s.

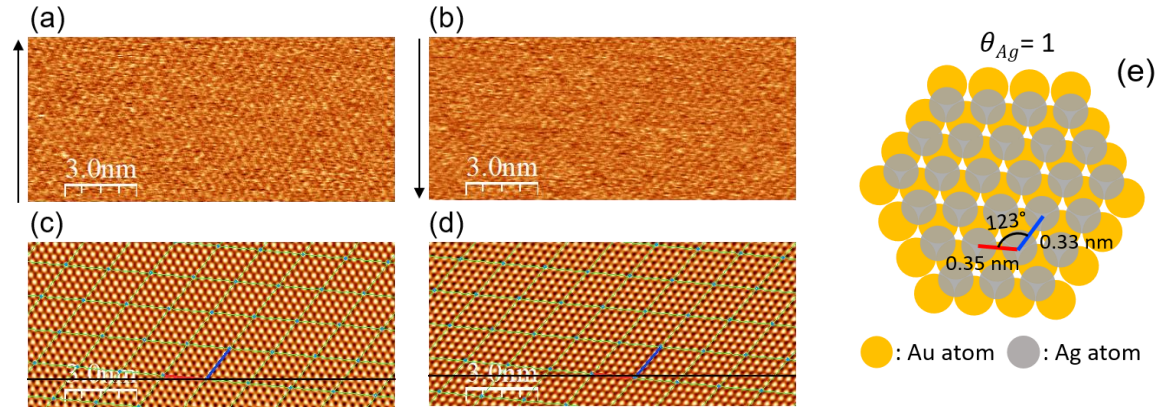

Figure 7.10 Lateral force maps at 0.30 V (vs. Ag/Ag^{+}) in 2 mM $AgClO_4$/0.1 M $LiClO_4$/PC (a) upward scan and (b) downward scan. Arrow indicates scan direction. (c) and (d) are the lattice images after Fast Fourier Transform (FFT) of (a) and (b), respectively. (e) is the illustration of the real lattice with lattice parameters after the correction of thermal drift. The concentration of water in the electrolyte is below 100 ppm. Applied normal loads for (a) and (b) are 32 nN and 52 nN, respectively. Scan rate is 0.235 nm/s.

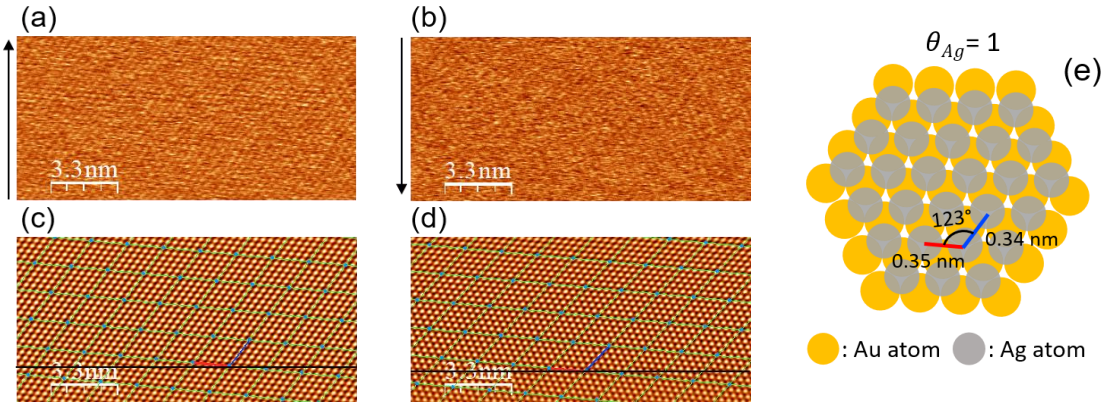

Figure 7.11 Lateral force maps at 0.08 V (vs. Ag/Ag^{+}) in 2 mM $AgClO_4$/0.1 M $LiClO_4$/PC (a) upward scan and (b) downward scan. Arrow indicates scan direction. (c) and (d) are the lattice images after Fast Fourier Transform (FFT) of (a) and (b), respectively. (e) is the illustration of the real lattice with lattice parameters after the correction of thermal drift. The concentration of water in the electrolyte is below 100 ppm. Applied normal loads are 44 nN and 48 nN, respectively. Scan rate is 0.235 nm/s.

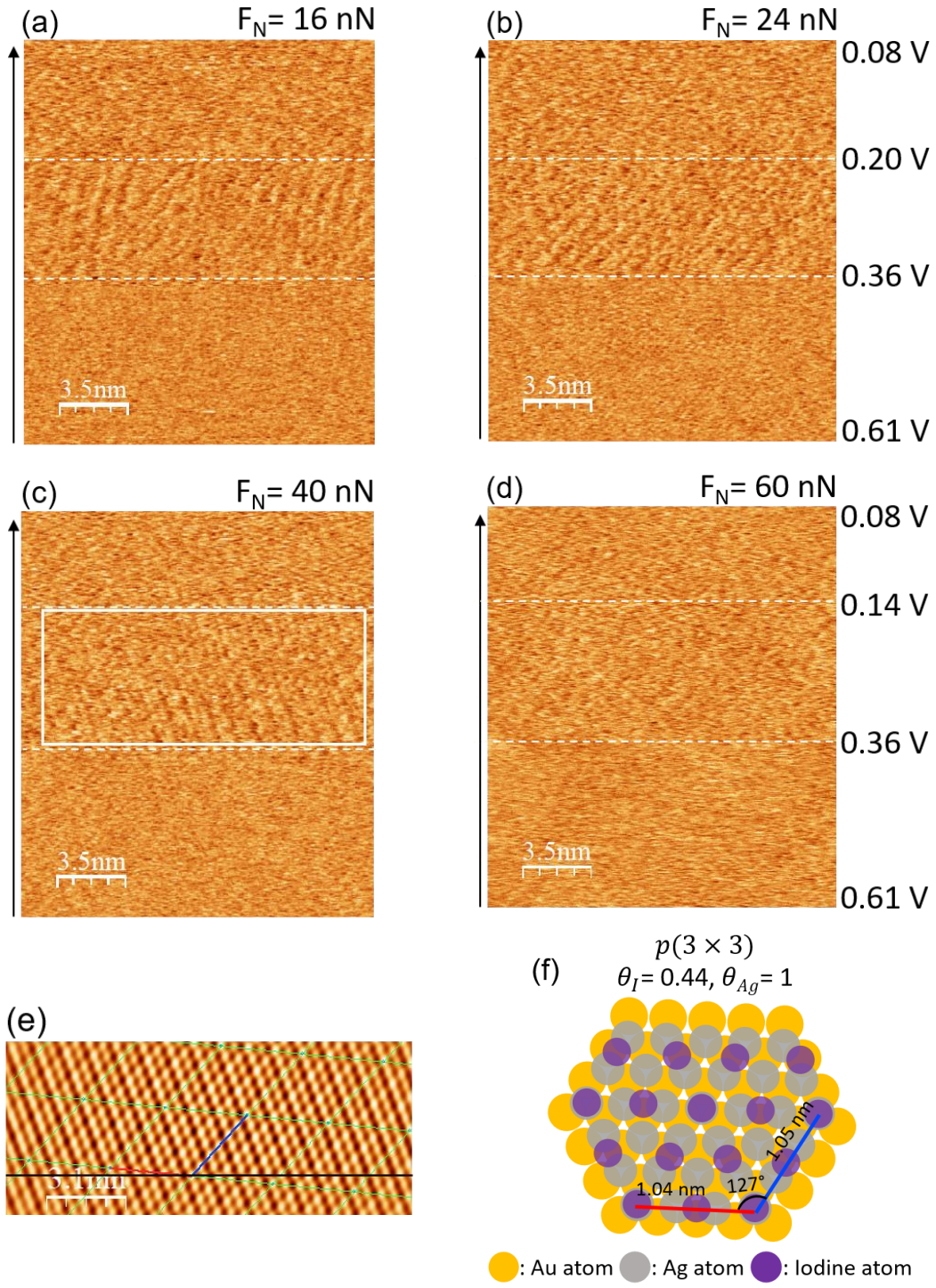

Figure 7.12 Lateral force maps as function of potential (0.6 V → 0.06 V) for I-modified Au(111) in 2 mM $AgClO_4$/0.1 M $LiClO_4$/PC at the normal loads of (a) 16 nN, (b) 24 nN, (c) 40 nN, and (d) 60 nN. The concentration of water in the electrolyte was below 100 ppm. The arrow indicates the scan direction and also potential sweep direction. (e) and (f) show FFT filtered image and illustration of structure of (c) marked with white box (potential region II). The scan rate is 0.235 nm/s.

7.4.3 Interfacial electrolyte layer structure

We investigate the interfacial structure using the force separation (FS) curves. Christenson et al. have reported that at small separations there are oscillations in the FS curves observed with the SFA on mica in nonpolar liquids (e.g. octamethylcyclotetrasiloxane (OMCTS), cyclohexane, benzene), indicating that molecular packing effects become dominant [18, 35-38]. Smith et al., have reported that when an IL is diluted in a solvent, at low concentrations the wavelength of oscillatory structural forces corresponds to the pure solvent [20]. In chapter 6.4.3, we also have shown that the solvent molecules dominate the FS curves in dilute electrolyte. Thus, the solvent molecules are adsorbed and ordered near the surface, which causes the repulsion while the AFM tip moves closer to the surface. Furthermore, based on these results, we presumed that the shear force is required for the penetration into the iodine adlayer meaning that there is no replacement of iodine during the measurement of FS curves.

Figure 7.13 shows FS curves for I-modified Au(111) in 2 mM $AgClO_4$/0.1 M $LiClO_4$/G4 at 3 different potentials (0.71 V, 0.20 V, and 0.06 V) corresponding to region I, II, and II´, respectively. Unlike atomic corrugations, FS curves are quite independent of the applied potential and also the concentration of water in the electrolyte. The results in nonpolar liquids have shown that the strength of interaction between molecule and surface is a decisive factor for the innermost layer [18, 36, 39]. If water is placed between G4 molecules, it might influence on the force to rupture layers as observed in IL [19]. The insensitivity to water is therefore certainly due to the hydrophobic character of the iodine layer (chapter 6.4.3) [40]. Zero force is measured beyond 3 nm, indicating that the electrolyte attains the bulk structure at that distance. As the tip moves toward the surface, ~3 layers are detected. Considering the atomic corrugations, the required forces to rupture the layers near the surface are too small to penetrate into the iodine adlayer, in good agreement with the friction data observed in chapter 6. Even though the forces (~1 nN) to rupture layers are very small, the force decreases slightly with separation. Moreover, the innermost layer is thinner than outer layers. In some cases, we observed relatively high force (~5 nN) to rupture the innermost layer as shown in Figure S7.8.

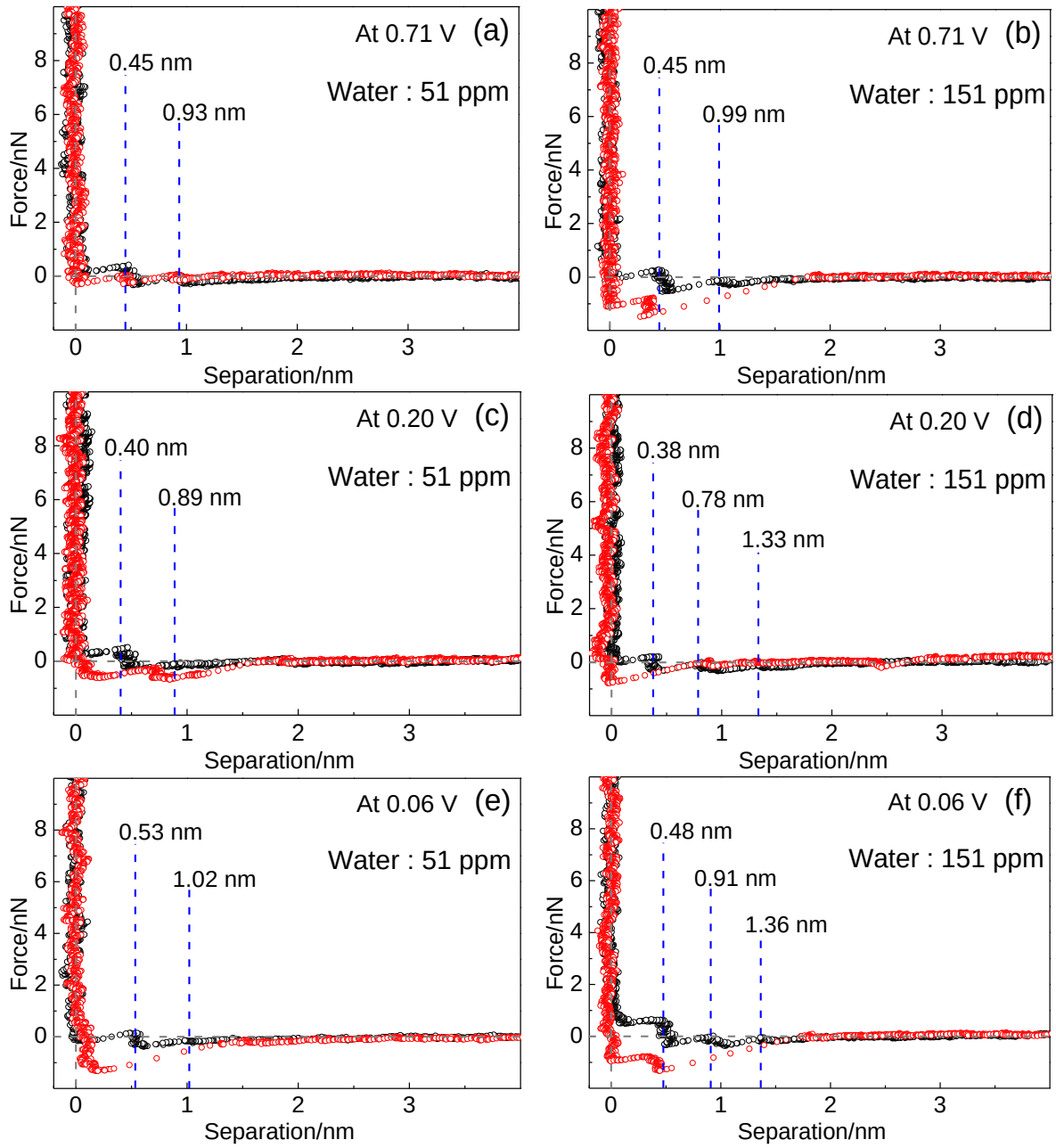

Figure 7.13 Force separation profiles for I-modified Au(111) obtained in 2 mM $AgClO_4$/0.1 M $LiClO_4$/G4 at the potential of (a) and (b) 0.71 V, before Ag UPD, (c) and (d) 0.20V, after the 1st Ag UPD peak, and (e) and (f) 0.06V, after the 2nd UPD peak. The concentrations of water for the left hand side ((a), (c), and (e)) and right hand side ((b), (d), and (f)) are 51 ppm and 151 ppm, respectively. All profiles show the approaching (black) and retracting (red) curves and the approaching speed is between 75 and 125 nm/s. PPP-FM (k_N =1.13±0.2 N/m) was used.

A similar behavior for I-modified Au(111) is observed in pure G4 and 0.1 M $LiClO_4$/G4 (see chapter 6.4.3). Thus, during the approach ordered molecules are compressed by the AFM tip, leading to a slight increase in ordering, which results in the slight increase of force required to rupture layers as the separation decreases. A large force for the innermost layer indicates that

the strength of the interaction between the iodine adlayer and G4 molecules is somewhat varying.

Figure 7.14 shows FS curves for I-modified Au(111) in Ag^+ containing PC at 3 different potentials corresponding to region I, II, and II´. As observed above in G4 (cf. Fig.13 and S8), the coverage of adsorbates (iodine and Ag) varying with potential has a minor effect on FS curves in Ag^+ containing PC. While the tip is approaching the surface, 3 layers (~1 nN) are detected and the thickness of the innermost layer is about 0.4 nm in all potential regions. In some cases, as shown in Figure S7.9, we observed slightly higher forces and lower thickness for the innermost layer. Since a similar behavior on I-modified Au(111) is observed in pure PC (Figure S7.10) and because of the potential independence, the orientation of PC molecules might dominate the FS curves. Figure S7.11 shows that the thickness of the second layer is similar to that of the innermost layer. Propylene carbonate is an asymmetric and dipolar molecule with a planar ring. Thus, it is assumed that there are more possible arrangements for smaller PC molecules compared to G4 molecules, which might be modified during the FS measurement.

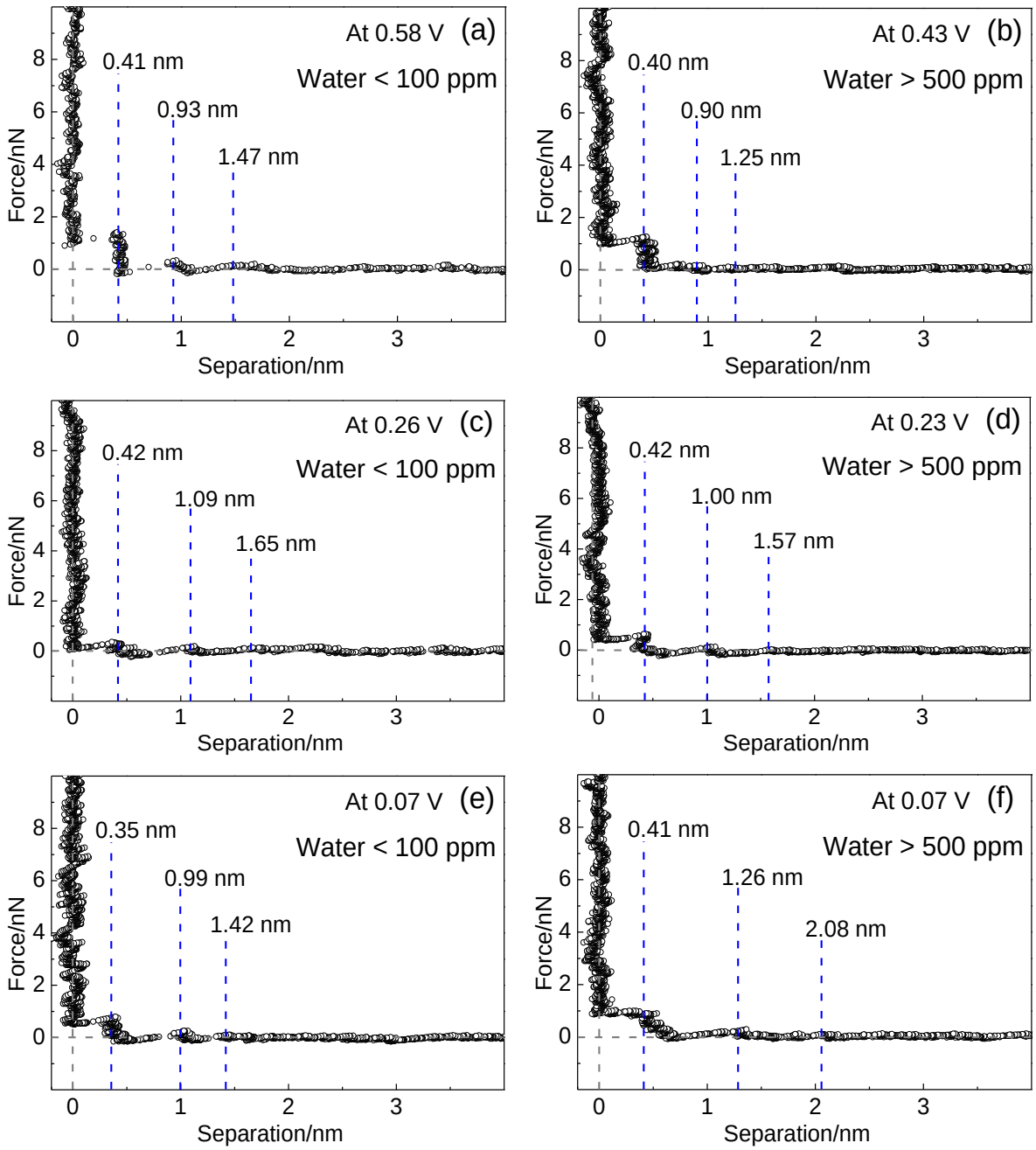

Figure 7.14 Force separation profiles for I-modified Au(111) obtained in 2 mM $AgClO_4$/0.1 M $LiClO_4$/PC at the potential region I, before Ag UPD, ((a): 0.58 V and (b): 0.43 V), the potential region II, after the 1st Ag UPD peak, ((c): 0.26 V and (d): 0.23 V), and the potential region II´, after the 2nd UPD peak, ((e): 0.07 V and (f): 0.09V). The concentrations of water for the left hand side ((a), (c), and (e)) and right hand side ((b), (d), and (f)) are below 100 ppm and above 500 ppm, respectively. All profiles show the approaching curves and the approaching speeds for the left and right images are ~ 50nm/s and 125 nm/s, respectively. PPP-FM (k_N =1.13±0.2 N/m) was used.

7.4.4 Dependence of friction on normal load

Based on FS curves, the influence of water is negligible due to the weak interaction with the iodine adlayer. However, as obvious from the atomic corrugations measurements, the tip penetrates into the iodine adlayer at high normal load, which means the effect of water might change when the tip is sliding on the metal substrates. Therefore, we investigate the friction behavior as function of normal load depending on potential regions and the concentration of water in the electrolyte.

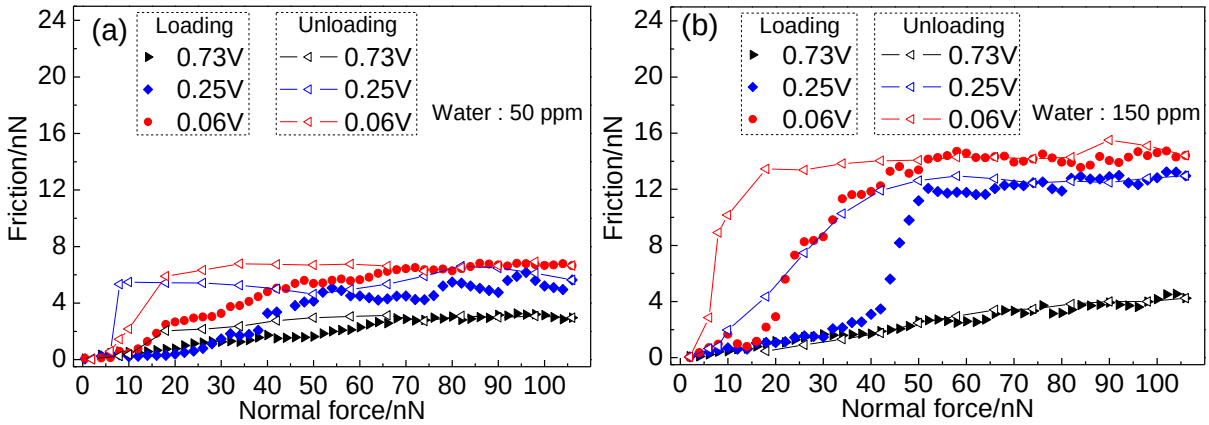

Figure 7.15 Friction on normal load depending on potential region for I-modified Au(111) in 2mM $AgClO_4$/0.1M $LiClO_4$/G4. The concentrations of water are (a) 50 ppm and (b) 150 ppm, respectively. Symbol indicates friction forces during loading and symbol with line indicates friction forces during unloading. PPP-FM (k_N =1.13±0.2 N/m) was used. The scan size and rate were 20x20 nm² and 0.47 nm/s, respectively.

Figure 7.15 shows the friction forces as function of normal load for I-modified Au(111) in Ag^+ containing G4. As we suggested in chapter 4.4.5, there are three different regimes where the coefficient of friction (COF) changes resulting from the penetration into the iodine adlayer. At low normal load, α regime, (F_N < 15 nN (0.73 V), F_N < 25 nN (0.25 V), and F_N < 15 nN (0.06 V)), the tip slides on the iodine adlayer, with a low COF (0.05 (0.73 V), 0.015 (0.25 V), and 0.05 (0.06 V)). In this regime, the stick-slip loops (Figure S7.12) as normal load increases show that even though the energy dissipation is low, it is not negligible [41].

In the β regime (15 nN < F_N < 30 nN (0.73 V), 25 nN < F_N < 50 nN (0.25 V), and 15 nN < F_N < 50 nN (0.06 V)), the observed atomic corrugations suggest that the tip penetrates into the iodine adlayer at all potentials, but the extent of friction increase caused by penetration depends on the

metal in contact with the tip. At 0.73 V (potential region I), the increase of friction during the penetration into the iodine adsorbed on Au(111) is insignificant (COF: 0.05) and the hysteresis of friction forces between loading and unloading normal load is small as observed in aqueous electrolyte (see chapter 4.4.5) and in G4-electrolyte (see chapter 6.4.4) [42]. In chapter 6.4.4, it is suggested that the sliding tip pushes away iodine adsorbed on Au(111) without a significant additional energy dissipation independent of potential, which hints to a high mobility of adsorbed iodine on Au(111). However, here at 0.25 V and 0.06 V, where Ag forms a monolayer, friction forces increase steeply with normal load (COF: 0.15 (0.25 V) and 0.13 (0.06 V)) as observed before in aqueous electrolyte (Figure 7.15a) (see chapter 4.4.5). Furthermore, increasing the concentration of water from 50 ppm to 150 ppm in Ag^+ containing G4 causes further increase of friction in β regime (COF: 0.83 (0.25 V) and 0.40 (0.06 V)) as shown in Figure 7.15b. However, further increase of water from 150 ppm to 550 ppm has a minor influence on friction in β regime (Figure S13). In contrast, the negligible effect of water on friction is observed on Au(111) in aqueous (chapter 4.4.5) and aprotic (chapter 6.4.4) electrolytes, which confirms that no extra energy dissipation is required for the sliding tip on Au(111) even though there is an interaction where the water is involved.

Therefore, there are two possible explanations. The first is that the mobility of the iodine adsorbed on Ag adlayers is lower than that on Au(111) as suggested in aqueous electrolyte. In addition to this, another possible influence is that the water adsorbed on the tip interacts with the metal surfaces after the penetration. Thus, before the saturation of tip with water, the friction increases as the concentration of water in the electrolyte increases but whenever the tip is saturated with water the increase of friction is somehow constant.

In ionic liquids where the tip cannot penetrate the innermost ion adsorbed on the electrode, the influence of water on the boundary-film lubrication depends on the features of the thin film composed with ions (e.g. solid-like, liquid-like) [43, 44]. For example, R. Espinosa-Marzal et al. reported that the friction increases for [EMIM][$EtSO_4$], [EMIM][FAP], and [HMIM][FAP] when the liquids are exposed to the ambient humidity [32, 45]. A. Smith et al. showed that friction clearly increases for 2 bilayers of [$C_{10}C_1$Pyrr][NTf_2] in the wet system [15]. In these cases, the films were determined to be solid-like, meaning that the increase of friction results from the enhanced structuring effect of ionic liquids by adding water. In the case of liquid-like films, C. Perez-Martinez et al. showed that in a dicationic ionic liquid, [$C_{10}(C_1Im)_2$][NTf_2]$_2$, the addition of water still increases the strength of layering but this enhances the lubrication effect due to the reduction of the viscosity [44].

Hence, it is expected that the contribution of interactions to friction is different even though there is an interaction between water adsorbed on the tip and silver or gold surfaces. It is generally assume that the *pzc* of the bare substrate changes gradually during UPD to more negative values and acquires the *pzc* of silver when the monolayer is completed [21, 46]. Due to the difference of the *pzc* between gold and silver, 1 V, it is reasonable that the interaction with water is enhanced on the substrate of silver compared to that of gold [47]. Therefore, the increased interaction between the tip and water on Ag monolayer causes the steep increase of friction in β regime.

At high normal load (30 nN < F_N (0.73 V) and 50 nN < F_N (0.25 V and 0.06 V)), corresponding to γ regime, the friction increases linearly (COF: 0.025).

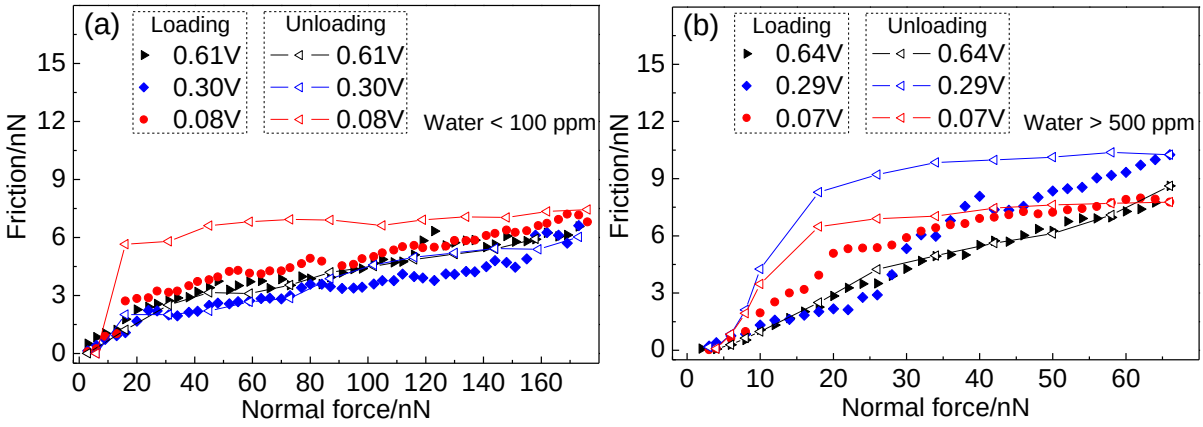

Figure 7.16 Friction on normal load depending on potential region for I-modified Au(111) in 2mM $AgClO_4$/0.1M $LiClO_4$/PC. The concentrations of water are (a) below 100 ppm and (b) above 500 ppm, respectively. PPP-FM (k_N =1.13±0.2 N/m) was used. The scan size and rate were 20x20 nm² and 0.47 nm/s, respectively.

Figure 7.16 shows the friction as function of normal load for I-modified Au(111) in Ag^+ containing PC, which is different from the behavior in Ag^+ containing G4. Thus, the clear transition of friction in β regime observed on I/Ag/Au(111) in Ag^+ containing G4 disappears in this system. Comparing the features of molecule (e.g. polarity, symmetry, size) between G4 and PC, a possible situation is that the PC molecules interact with the tip, which cancels out the influence of water on silver. Furthermore, friction forces increases as the concentration of water increases, in good agreement with the effect of water adsorbed on the tip observed in Ag^+ containing G4.

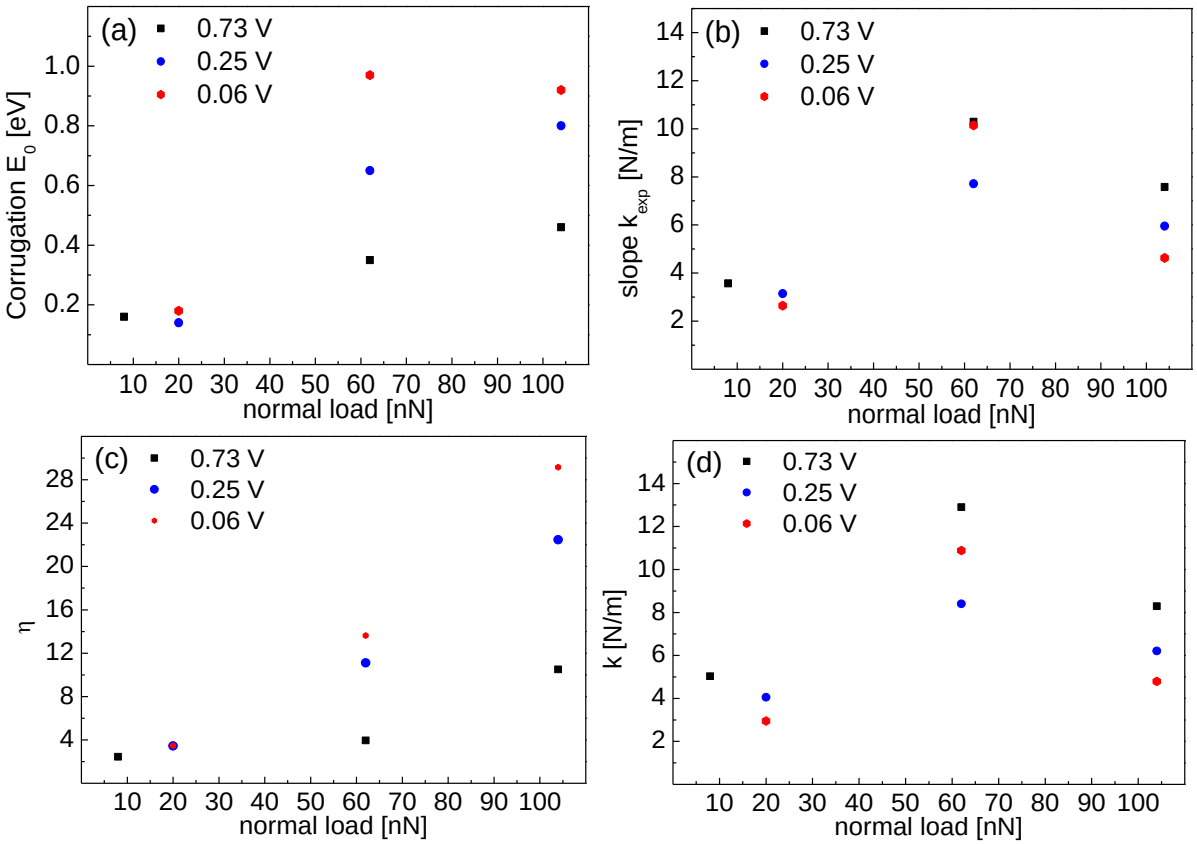

Figure 7.17 Evaluated from Figure 7.3d~f. (a) the corrugation of the surface potential E_0, (b) an experimental spring constant k_{exp}, (c) a parameter indicating the relation between corrugation energy and elastic energy η, and (d) an effective spring constant k are plotted as function of normal load.

As shown in the paper by A. Socoliuc et al. [41], the corrugation height E_0 of the surface potential energy from the maxima of the stick-slip curves can be calculated depending on the potential (Figure 7.17). Furthermore, from the experimental spring constant k_{exp} (the slope of the stick-slip curves) the effective spring constant k and η, the parameter indicating the relation between corrugation energy and elastic energy can be calculated. These are plotted as function of normal load in Figure 7.17. For $\eta < 1$, the movement is continuous without energy dissipation; for $\eta >> 1$, the tip 'jumps' into the minima and k is directly given by k_{exp}. When the tip penetrates into the iodine adlayer, the difference in corrugation energies between gold and silver surfaces is obvious, in agreement with the increase of friction on the silver layer. Furthermore, the increase of η is larger on Ag monolayer than Au(111), which implies that the interaction between tip and surface of Ag monolayer is much larger than that of Au(111). We assume that the interaction between tip and surface have influence on the corrugation energy E_0. Figure S7.13a demonstrates our assumption that the penetration into the iodine adlayer and the interaction between water and gold surface have a minor effect on friction. As shown in Figure S7.13b, the

interaction between tip and surface increases on Ag monolayer as the concentration of water increases. Unfortunately, when the concentration of water was 550 ppm, we didn't get clear atomic stick-slip on Ag monolayer.

7.5 Conclusion

Ag UPD on I-modified Au(111) in aprotic electrolyte was investigated from a frictional point of view using LFM.

Charge densities together with the atomic corrugations show that the formation of Ag monolayer takes place as two steps, C_1 and C_2, in both electrolytes and there is a minor influence of water. Interestingly, slightly negative of the 1st Ag UPD peak, C_1, there is a transition of iodine structures from a $(\sqrt{3} \times \sqrt{3})R30°$ structure to a $p(3 \times 3)$ structure at low normal load due to incomplete of Ag ($\theta_{Ag} < 1$). It confirms that the structure of iodine reflects the coverage of Ag layer. At high normal load, the atomic corrugations clearly show the gold or silver structures depending on potential meaning that the AFM tip penetrates into the iodine adlayer. Even though there is a hysteresis of load to get the iodine structure between loading and unloading, no irreversible wear is observed.

As we reported in our previous chapter 6.4.3, G4 molecules are ordered on the surface, which results in steped FS curves. It is noteworthy that we observed two different push-through forces for the innermost layer indicating that the strength of the interaction between G4 molecules and the iodine adlayer varies. In Ag^+ containing PC, as observed in G4, PC molecules are also ordered on the surface. Since we observed the atomic corrugations of iodine structure at the normal load beyond the push-through force for the innermost layer, we presume that the displacement of iodine requires shear force.

Friction forces as function of normal load is the combined result of interactions between tip, solvent, adsorbates (iodine and silver), and water. In Ag^+ containing G4, the dependence of the

friction force on normal load shows clear transitions (α, β, and γ regimes), especially when the silver forms a monolayer. In α regime, where the tip slides on the iodine adlayer, friction forces are independent of substrate (gold or silver) and the concentration of water. In β regime, where the tip penetrates the iodine adlayer, friction forces depend on substrates (gold or silver) and the concentration of water. As mentioned in our previous chapter 6.4.4, we presume that iodine on Au(111) can be easily pushed away without large energy dissipation. The remarkable effect of water on friction in aqueous and aprotic electrolytes implies that the water adsorbed on the tip dominantly contributes to the steep increase of friction when the tip penetrates into the iodine adlayer. In γ regime where the tip slides on substrate (gold or silver), friction forces show moderate increase. In Ag^+ containing PC, the steep increase of friction in β regime for Ag monolayer observed in G4 disappears. Considering properties of PC (e.g. asymmetric structure, polar), we suggest that PC molecules are involved in the interaction between tip, water, and substrate.

Acknowledgement

The authors gratefully acknowledge the DFG (Deutsche Forschungsgemeinschaft) for funding this work (BA1008/21-1).

7.6 Supporting information

7.6.1 Cyclic voltammetry (CV)

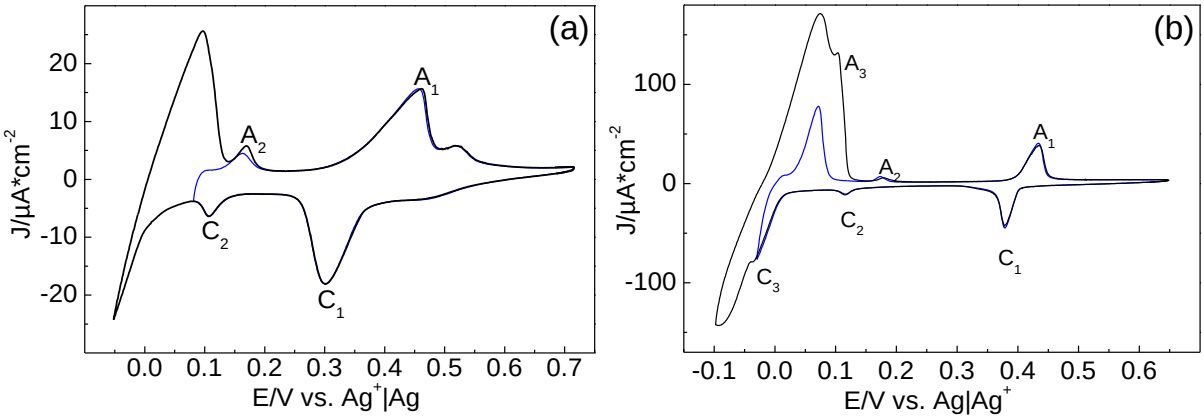

Figure S 7.1 Cyclic voltammetry on I-modified Au(111) in H-cell filled with (a) 2 mM $AgClO_4$/0.1 M $LiClO_4$/G4 and (b) 2 mM $AgClO_4$/0.1 M $LiClO_4$/PC. The concentration of water in electrolyte is 51 ppm. The sweep rate of CV is 10 mV/s.

7.6.2 Atomic corrugation

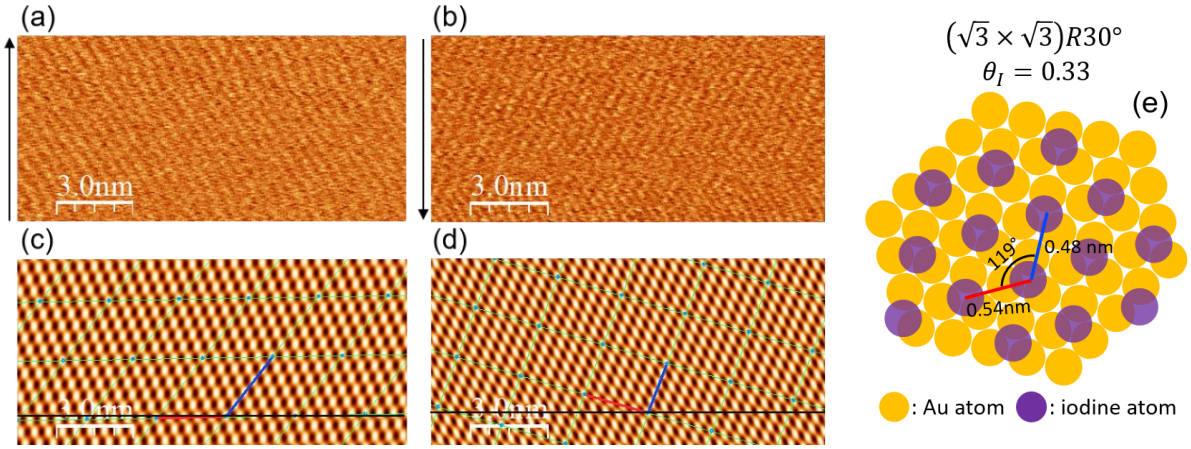

Figure S 7.2 Lateral force maps at 0.73 V (vs. Ag/Ag^+) in 2 mM $AgClO_4$/0.1 M $LiClO_4$/G4 (a) upward scan and (b) downward scan. Arrow indicates scan direction. (c) and (d) are the lattice images after Fast Fourier Transform (FFT) of (a) and (b), respectively. (e) is the illustration of the real lattice with lattice parameters after the correction of thermal drift. The concentration of water in the electrolyte is 150 ppm. Applied normal loads for (a) and (b) are 18 nN and 30 nN, respectively. Scan rate is 0.235 nm/s.

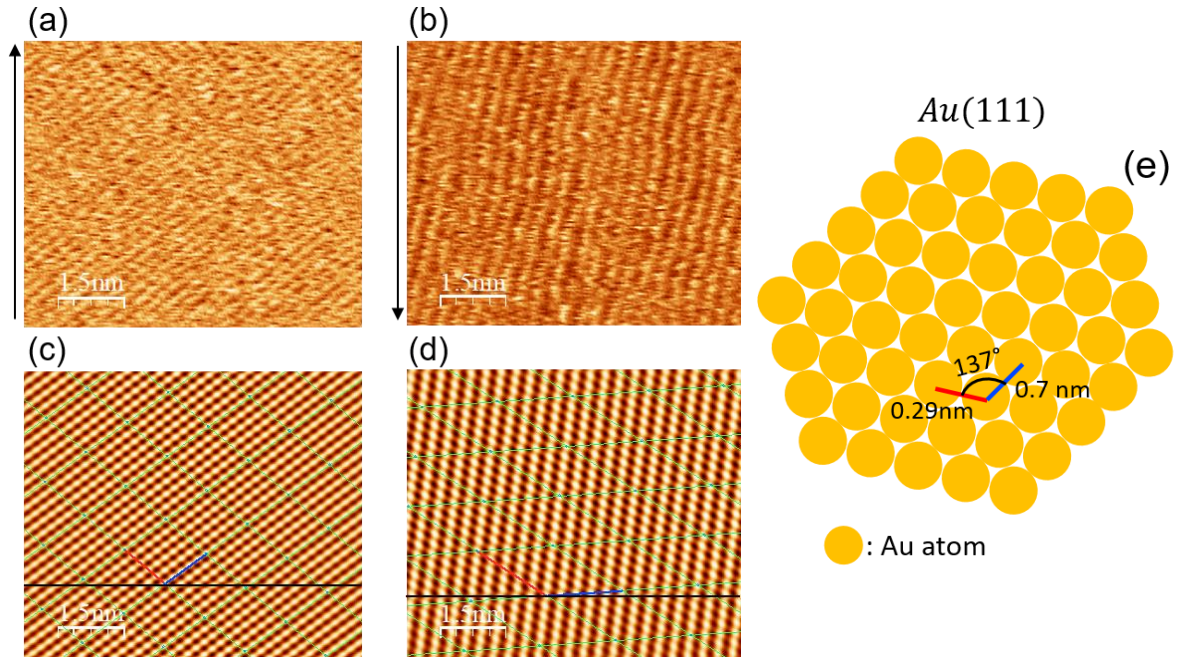

Figure S 7.3 Lateral force maps at 0.73 V (vs. Ag/Ag^+) in 2 mM $AgClO_4$/0.1 M $LiClO_4$/G4 (a) upward scan and (b) downward scan. Arrow indicates scan direction. (c) and (d) are the lattice images after Fast Fourier Transform (FFT) of (a) and (b), respectively. (e) is the illustration of the real lattice with lattice parameters after the correction of thermal drift. The concentration of water in the electrolyte is 150 ppm. Applied normal loads for (a) and (b) are 54 nN and 56 nN, respectively. Scan rate is 0.235 nm/s.

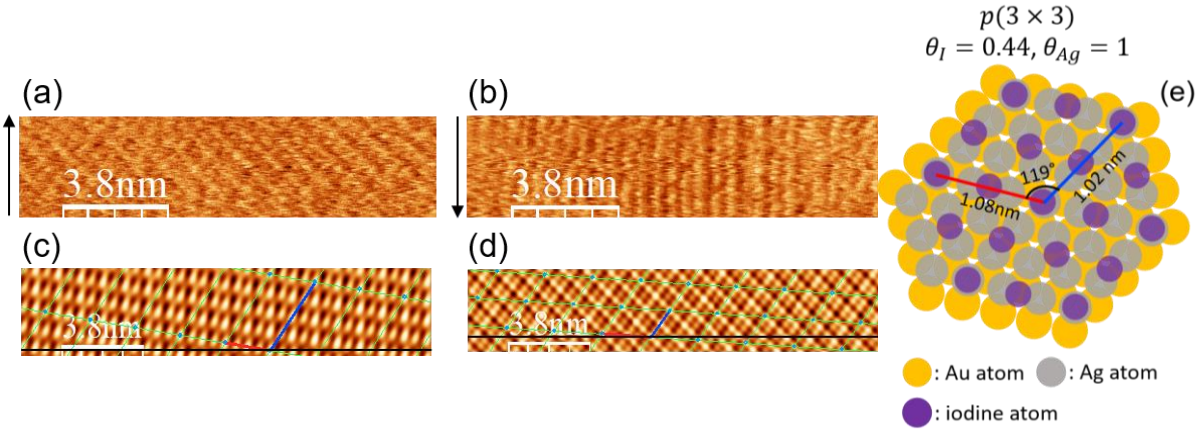

Figure S 7.4 Lateral force maps at 0.25 V (vs. Ag/Ag^+) in 2 mM $AgClO_4$/0.1 M $LiClO_4$/G4 (a) upward scan and (b) downward scan. Arrow indicates scan direction. (c) and (d) are the lattice images after Fast Fourier Transform (FFT) of (a) and (b), respectively. (e) is the illustration of the real lattice with lattice parameters after the correction of thermal drift. The concentration of water in the electrolyte is 150 ppm. Applied normal loads for (a) and (b) are 26 nN and 34 nN, respectively. Scan rate is 0.235 nm/s.

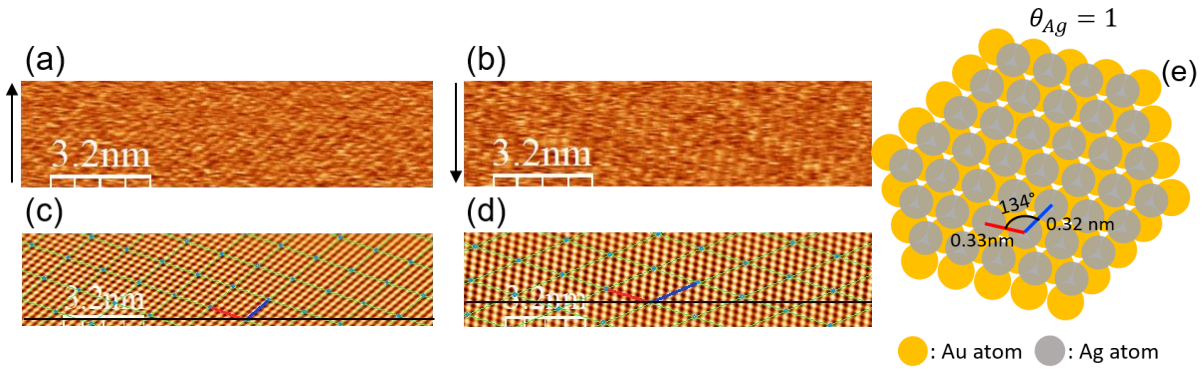

Figure S 7.5 Lateral force maps at 0.25 V (vs. Ag/Ag^+) in 2 mM $AgClO_4$/0.1 M $LiClO_4$/G4 (a) upward scan and (b) downward scan. Arrow indicates scan direction. (c) and (d) are the lattice images after Fast Fourier Transform (FFT) of (a) and (b), respectively. (e) is the illustration of the real lattice with lattice parameters after the correction of thermal drift. The concentration of water in the electrolyte is 150 ppm. Applied normal loads for (a) and (b) are72 nN and 70 nN, respectively. Scan rate is 0.235 nm/s.

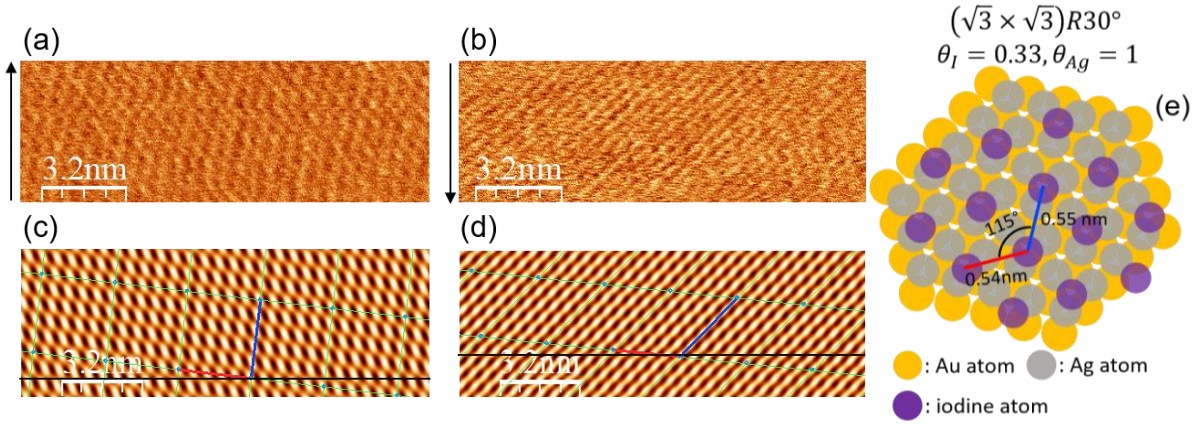

Figure S 7.6 Lateral force maps at 0.06 V (vs. Ag/Ag^+) in 2 mM $AgClO_4$/0.1 M $LiClO_4$/G4 (a) upward scan and (b) downward scan. Arrow indicates scan direction. (c) and (d) are the lattice images after Fast Fourier Transform (FFT) of (a) and (b), respectively. (e) is the illustration of the real lattice with lattice parameters after the correction of thermal drift. The concentration of water in the electrolyte is 150 ppm. Applied normal loads for (a) and (b) are 22 nN and 8 nN, respectively. Scan rate is 0.235 nm/s.

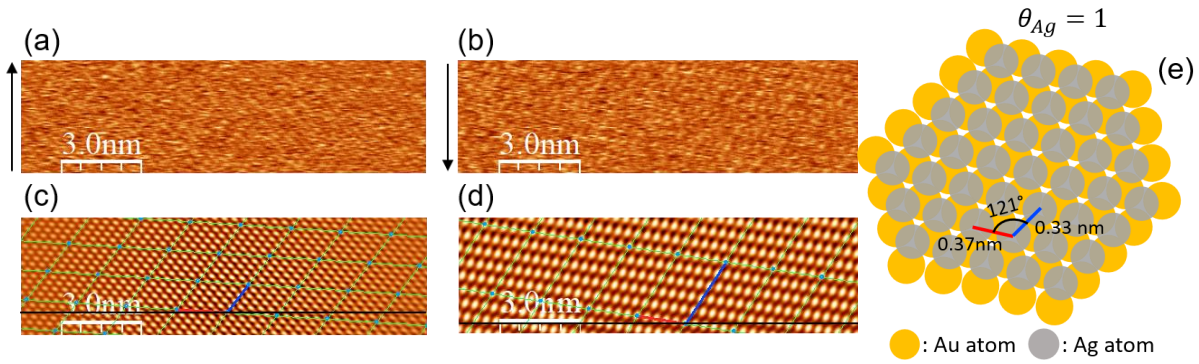

Figure S 7.7 Lateral force maps at 0.06 V (vs. Ag/Ag^{+}) in 2 mM $AgClO_4$/0.1 M $LiClO_4$/G4 (a) upward scan and (b) downward scan. Arrow indicates scan direction. (c) and (d) are the lattice images after Fast Fourier Transform (FFT) of (a) and (b), respectively. (e) is the illustration of the real lattice with lattice parameters after the correction of thermal drift. The concentration of water in the electrolyte is 150 ppm. Applied normal loads are 94 nN and 96 nN, respectively. Scan rate is 0.235 nm/s.

7.6.3 Force separation curves

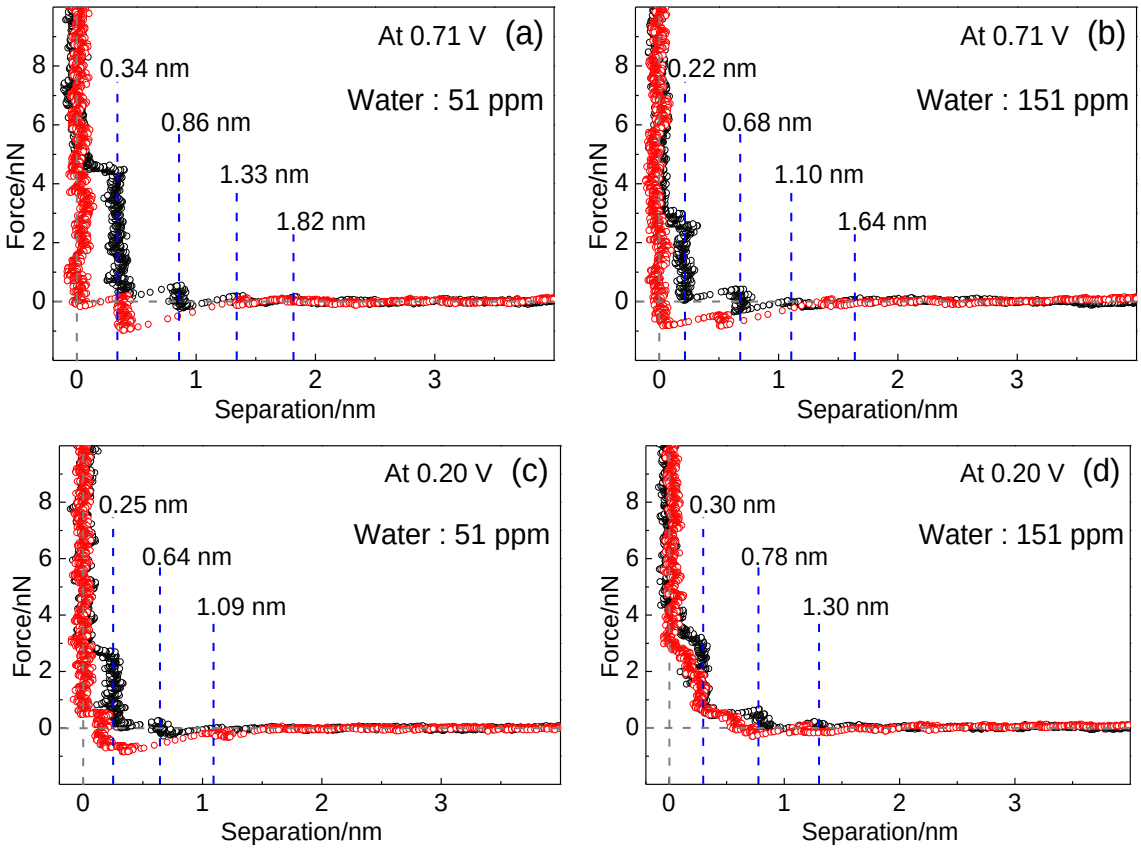

Figure S 7.8 Different type of force separation profiles compared to Figure 7.13 for I-modified Au(111) obtained in 2 mM $AgClO_4$/0.1 M $LiClO_4$/G4

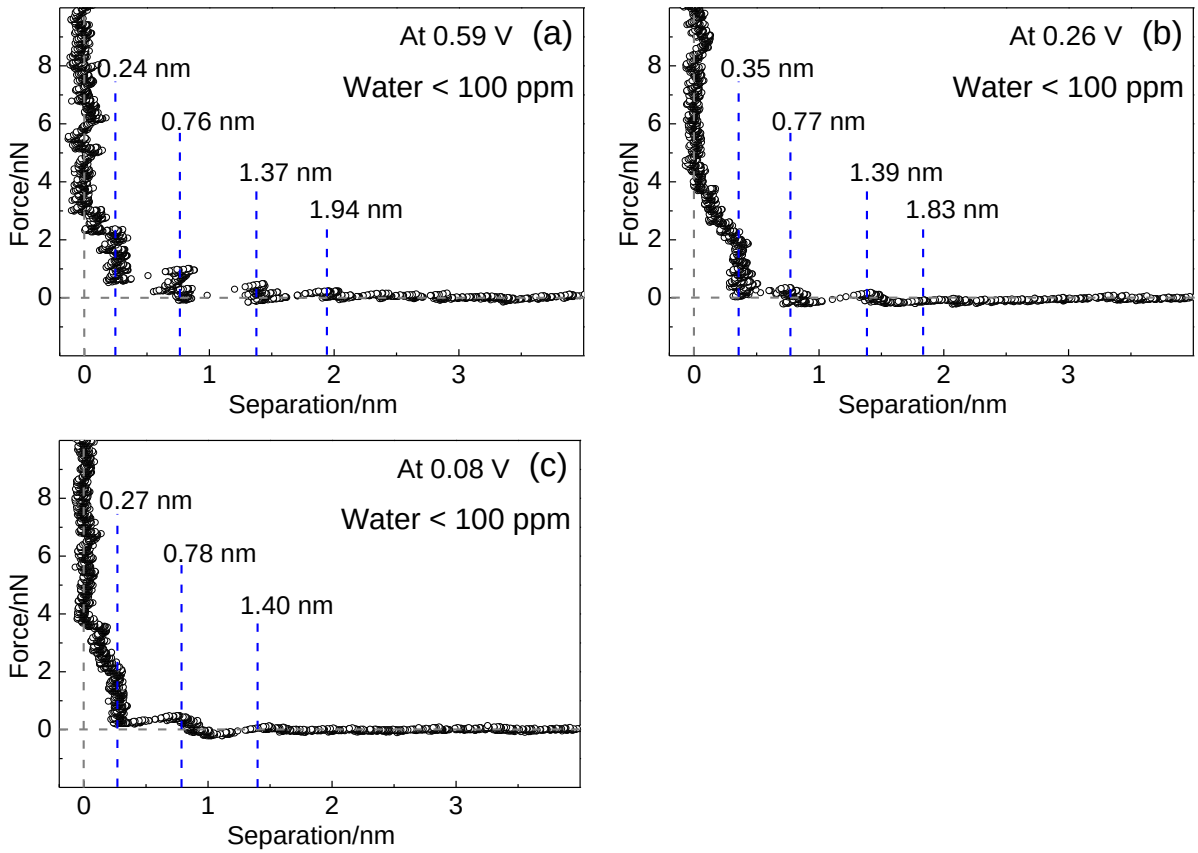

Figure S 7.9 Different type of force separation profiles compared to Figure 7.14 in 2 mM $AgClO_4$/0.1 M $LiClO_4$/PC. The concentration of water in the electrolyte is below 100 ppm. All profiles show the approaching curves and the approaching speed is ~ 50 nm/s. PPP-FM (k_N =1.13±0.2 N/m) was used.

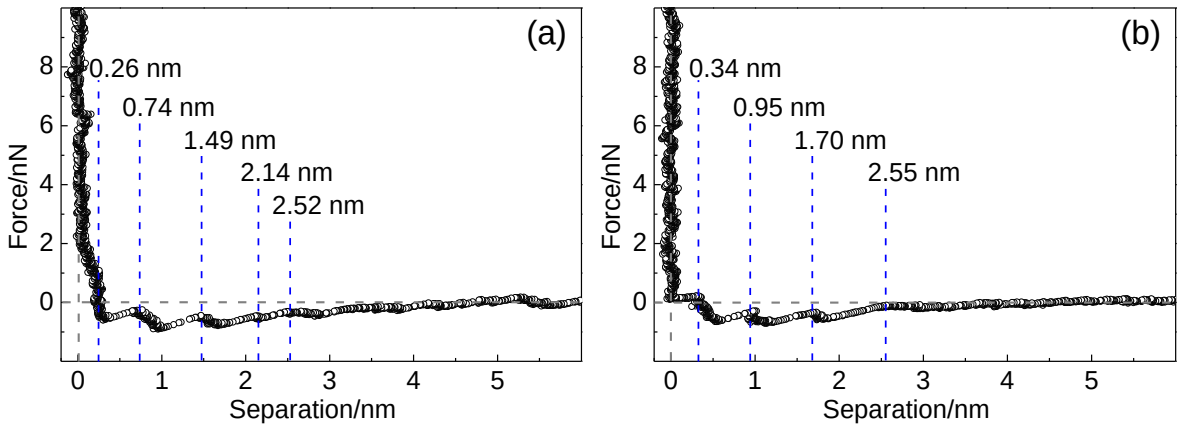

Figure S 7.10 Force separation profiles obtained on I-modified Au(111) in pure PC. All profiles show the approaching curves and the approaching speed is 75 nm/s. PPP-FM (k_N =1.13±0.2 N/m) was used.

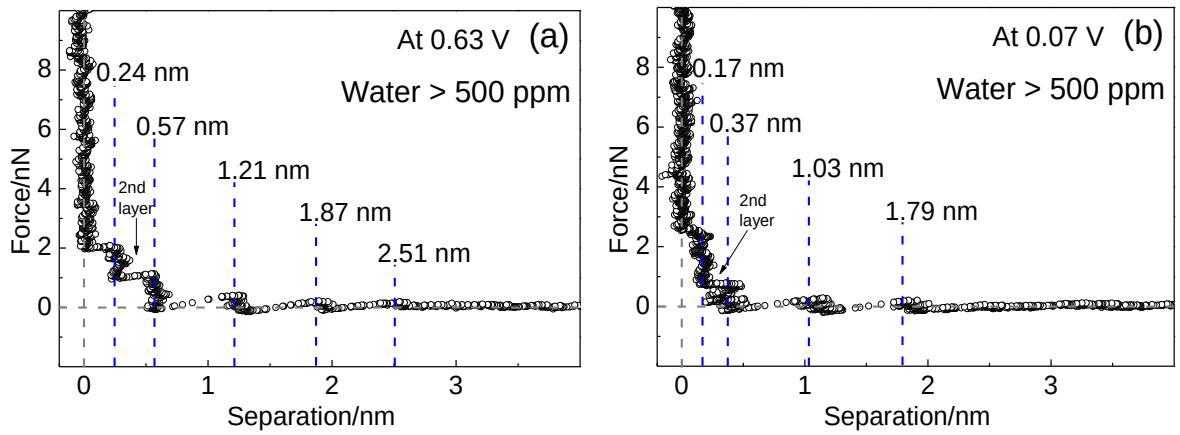

Figure S 7.11 Different type of force separation profiles compared to Figure 7.14 in 2 mM $AgClO_4$/0.1 M $LiClO_4$/PC. The concentration of water in the electrolyte is above 500 ppm. All profiles show the approaching curves and the approaching speed is 125 nm/s. PPP-FM (k_N =1.13±0.2 N/m) was used.

7.6.4 Atomic stick-slip loops

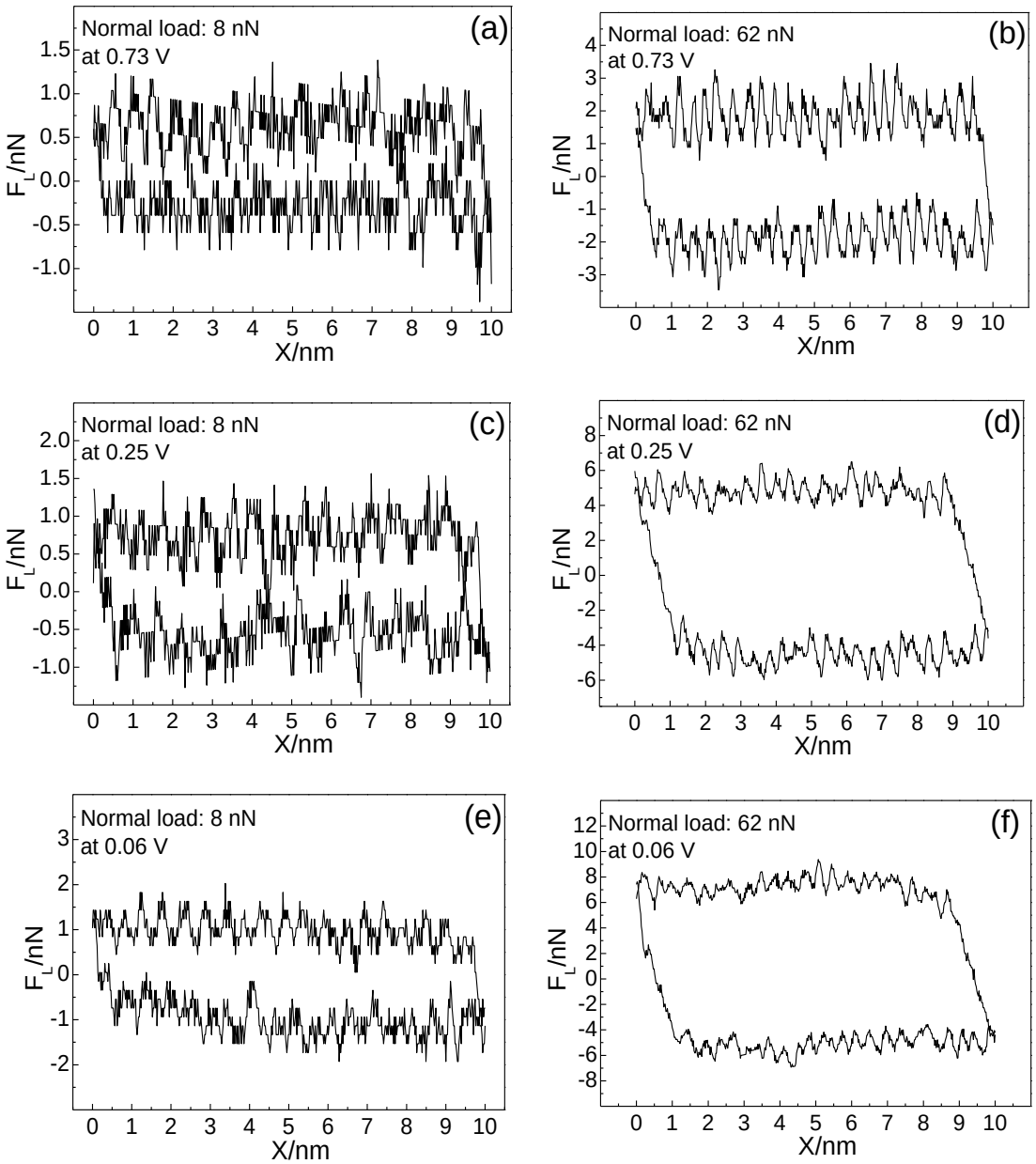

Figure S 7.12 Atomic stick-slip loops in 2 mM $AgClO_4$/0.1 M $LiClO_4$/G4 on iodine adlayers ((a) 0.73 V, (c) 0.25 V, and (e) 0.06 V) and after the penetration into iodine adlayers ((b) 0.73 V, (d) 0.25 V, and (f) 0.06 V).

7.6.5 Dependence of friction on normal load

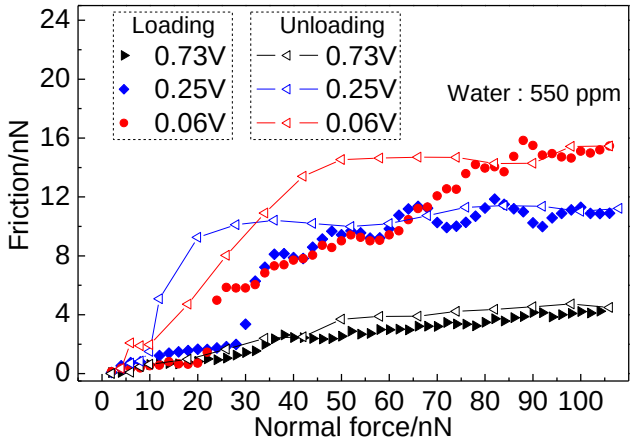

Figure S 7.13 Friction on normal load depending potential region for I-modified Au(111) in 2 mM $AgClO_4$/0.1M $LiClO_4$/G4. The concentration of water is 550 ppm water. PPP-FM (k_N =1.13±0.2 N/m) was used. The scan size and rate were 20x20 nm² and 0.47 nm/s, respectively.

7.6.6 Evaluation of the corrugation of the surface potential E_0

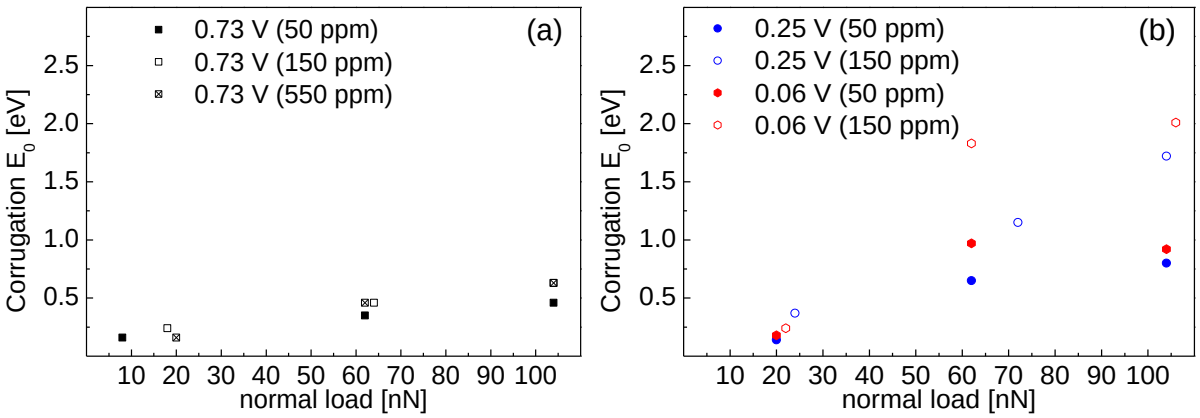

Figure S 7.14 The corrugation of the surface potential E_0 as function of normal load at (a) 0.73 V and (b) 0.25 V and 0.06 V, Ag ML as the concentration of water increases.

Reference

[1] H. M. A. Amin, C. Molls, P. P. Bawol, H. Baltruschat *Electrochim. Acta*. **2017**, *245*, 967-980.

[2] P. Hegemann, M. Hegemann, L. Zan, H. Baltruschat *J. Electrochem. Soc.* **2019**, *166*, A245-A250.

[3] L. Lutz, W. Yin, A. Grimaud, D. Alves Dalla Corte, M. Tang, L. Johnson, E. Azaceta, V. Sarou-Kanian, A. J. Naylor, S. Hamad *J. Phys. Chem. C*. **2016**, *120*, 20068-20076.

[4] M. Hegemann, P. Bawol, A. Köllisch-Mirbach, H. Baltruschat *Electrocatalysis*. **2021**, 1-15.

[5] N. Amir, Y. Vestfrid, O. Chusid, Y. Gofer, D. Aurbach *J. Power Sources*. **2007**, *174*, 1234-1240.

[6] Da.Xing, P. P. Bawol, A.-E.-A. A. A. Abd-El-Latif, L. Zan, H. Baltruschat *ChemElectroChem*. **2021**, *in press*.

[7] L. Zan, D. Xing, A. Abd-El-Latif, H. Baltruschat *Beilstein J. Nanotechnol.* **2019**, *10*, 2541–2552.

[8] E. M. Erickson, E. Markevich, G. Salitra, D. Sharon, D. Hirshberg, E. de la Llave, I. Shterenberg, A. Rozenman, A. Frimer, D. Aurbach *J. Electrochem. Soc.* **2015**, *162*, A2424-A2438.

[9] Y. L. Jie, Y. S. Tan, L. M. Li, Y. H. Han, S. T. Xu, Z. C. Zhao, R. G. Cao, X. D. Ren, F. Y. Huang, Z. W. Lei, G. H. Tao, G. Q. Zhang, S. H. Jiao *Angewandte Chemie-International Edition*. **2020**, *59*, 12689-12693.

[10] H. Li, F. Endres, R. Atkin *Physical Chemistry Chemical Physics*. **2013**, *15*, 14624-14633.

[11] J. Sweeney, G. B. Webber, M. W. Rutland, R. Atkin *Physical Chemistry Chemical Physics*. **2014**, *16*, 16651-16658.

[12] H. Li, R. Atkin, A. J. Page *Physical Chemistry Chemical Physics*. **2015**, *17*, 16047-16052.

[13] J. Sweeney, F. Hausen, R. Hayes, G. B. Webber, F. Endres, M. W. Rutland, R. Bennewitz, R. Atkin *Physical review letters*. **2012**, *109*, 155502.

[14] S. Perkin, T. Albrecht, J. Klein *Physical Chemistry Chemical Physics*. **2010**, *12*, 1243-1247.

[15] A. M. Smith, M. A. Parkes, S. Perkin *J. Phys. Chem. Lett.* **2014**, *5*, 4032-4037.

[16] M. A. Gebbie, M. Valtiner, X. Banquy, E. T. Fox, W. A. Henderson, J. N. Israelachvili *Proceedings of the National Academy of Sciences*. **2013**, *110*, 9674-9679.

[17] M. A. Gebbie, A. M. Smith, H. A. Dobbs, G. G. Warr, X. Banquy, M. Valtiner, M. W. Rutland, J. N. Israelachvili, S. Perkin, R. Atkin *Chem. Commun.* **2017**, *53*, 1214-1224.

[18] H. K. Christenson, C. E. Blom *The Journal of chemical physics*. **1987**, *86*, 419-424.

[19] R. Lhermerout, S. Perkin *Physical Chemistry Chemical Physics*. **2020**, *22*, 455-466.

[20] A. M. Smith, S. Perkin *Physical review letters*. **2017**, *118*, 096002.

[21] M. Espladiu, M. Schneeweiss, D. Kolb *Physical Chemistry Chemical Physics*. **1999**, *1*, 4847-4854.

[22] T. Hachiya, K. Itaya *Ultramicroscopy*. **1992**, *42*, 445-452.

[23] K. Ogaki, K. Itaya *Electrochimica acta*. **1995**, *40*, 1249-1257.

[24] V. Rooryck, F. Reniers, C. Buess-Herman, G. A. Attard, X. Yang *Journal of electroanalytical chemistry*. **2000**, *482*, 93-101.

[25] C. H. Chen, S. M. Vesecky, A. A. Gewirth *Journal of the American Chemical Society*. **1992**, *114*, 451-458.

[26] P. Mrozek, Y.-e. Sung, M. Han, M. Gamboa-Aldeco, A. Wieckowski, C.-h. Chen, A. A. Gewirth *Electrochimica acta*. **1995**, *40*, 17-28.

[27] M. R. Ehrenburg, E. B. Molodkina, P. Broekmann, A. V. Rudnev *ChemElectroChem*. **2019**, *6*, 1149-1156.

[28] S. Sugita, T. Abe, K. Itaya *The Journal of Physical Chemistry*. **1993**, *97*, 8780-8785.

[29] I. Park, H. Baltruschat *ChemPhysChem*. **2021**, *7*, 1-9.

[30] W. Ouyang, A. S. de Wijn, M. Urbakh *Nanoscale*. **2018**, *10*, 6375-6381.

[31] J. E. Sader, J. W. M. Chon, P. Mulvaney *Rev. Sci. Instrum.* **1999**, *70*, 3967-3969.

[32] R. Espinosa-Marzal, A. Arcifa, A. Rossi, N. Spencer *The journal of physical chemistry letters*. **2014**, *5*, 179-184.

[33] S. Sundararajan, B. Bhushan *J. Appl. Phys.* **2000**, *88*, 4825-4831.

[34] S. Iqbal, L. Zan, E. Nardi, H. Baltruschat *Phys. Chem. Chem. Phys.* **2018**, *20*, 6176-6186.

[35] H. Christenson, R. Horn, J. Israelachvili *J. Colloid Interface Sci.* **1982**, *88*, 79-88.

[36] H. K. Christenson *The Journal of chemical physics*. **1983**, *78*, 6906-6913.

[37] H. Christenson, R. Horn *Chem. Phys. Lett.* **1983**, *98*, 45-48.

[38] H. K. Christenson, R. G. Horn *J. Colloid Interface Sci.* **1985**, *103*, 50-55.

[39] R. Y. Lim, S. O'Shea *Langmuir*. **2004**, *20*, 4916-4919.

[40] F. Lu, G. N. Salaita, H. Baltruschat, A. T. Hubbard *J. Electroanal. Chem.* **1987**, *222*, 305-320.

[41] A. Socoliuc, R. Bennewitz, E. Gnecco, E. Meyer *Physical review letters*. **2004**, *92*, 134301.

[42] I. Park, H. Baltruschat *CehmElectroChem*. **2022**, *9*.

[43] R. Lhermerout, C. Diederichs, S. Perkin *Lubricants*. **2018**, *6*, 9.

[44] C. S. Perez-Martinez, S. Perkin *Langmuir*. **2019**, *35*, 15444-15450.

[45] R. Espinosa-Marzal, A. Arcifa, A. Rossi, N. Spencer *The Journal of Physical Chemistry C*. **2014**, *118*, 6491-6503.

[46] T. Langkau, H. Baltruschat *Electrochimica Acta*. **2002**, *47*, 1595 - 1599.

[47] M. F. Toney, J. N. Howard, J. Richer, G. L. Borges, J. G. Gordon, O. R. Melroy, D. G. Wiesler, D. Yee, L. B. Sorensen *Surface Science*. **1995**, *335*, 326-332.

CHAPTER 8

Summary and Outlook

This dissertation deals with atomic scale frictional behaviors under different electrochemical conditions. Therefore, in the following, the findings observed will be compared and summarized together.

The influence of the adsorbate on friction during Ag UPD in aqueous electrolytes

In chapter 3, the frictional behavior including the transition of structures on Au(111) has been studied during Ag UPD in aqueous electrolyte. In this case, sulfate was a co-adsorbed anion. In chapter 4, a monolayer of iodine ($\theta_I = 0.33$) was pre-adsorbed on Au(111) and the frictional behavior has been investigated on I-modified Au(111) during Ag UPD in aqueous electrolyte.

The transition of atomic structures with potential indicates that in both cases the structures of co-adsorbed anions are very sensitive to the coverage of Ag. For example, on Au(111), sulfate forms a $(\sqrt{3} \times \sqrt{7})R19.1°$ structure but it forms a $(\sqrt{3} \times \sqrt{3})R30°$ structure when Ag forms a monolayer or bilayer. On I-modified Au(111), the structure of iodine is changed from a $(\sqrt{3} \times \sqrt{3})R30°$ structure to a $p(3 \times 3)$ structure as the potential passes the 1st Ag UPD peak and the $p(3 \times 3)$ structure is maintained until the completion of Ag monolayer. However, when silver forms a bilayer, the iodine forms again a $(\sqrt{3} \times \sqrt{3})R30°$ structure.

No clear structure of sulfate was reproducibly observed in the potential range where the Ag monolayer is not completed on Au(111). However, friction forces as function of potential show the dependence of potential, which indirectly indicates the continuous increase of Ag coverage with potential in this potential region. Furthermore, friction forces vs. normal load replotted from the friction vs. potential show a steep increase, which suggests the penetration into the sulfate adlayer and even Ag adlayer when the Ag coverage is less than a critical value. In contrast, on I-modified Au(111), due to strongly adsorbed iodine on Au(111) or Ag adlayer, the transition of the Ag coverage is quite clear depending on the potential. Moreover, the transition

of structures is clear as the normal load increases. Thus, as the normal load increases, it has been confirmed that the penetration into the iodine adlayer occurs in whole potential range and the penetration into the Ag adlayer only happens when the Ag coverage is 0.44. It is remarkable that friction only increases steeply when the tip penetrates the iodine adsorbed on Ag adlayer. At high normal load where the tip slides on metal surfaces after the penetration, it seems that there is a strong interaction between tip and metal surfaces in sulfate containing electrolyte, which results in the further steep increase of friction with normal load. However, on I-modified Au(111), after the penetration of the iodine adlayer (or silver adlayer), no further increase is observed. This suggests that the hydrophobic iodine adlayer reduces the interaction from the electrolyte.

The influence of the solvent on friction during Ag UPD for the I-modified Au(111)

The charge densities and atomic corrugations demonstrate that silver forms a bilayer on I-modified Au(111) during Ag UPD in aqueous electrolyte (chapter 4). In chapter 7, CV on I-modified Au(111) in Ag^+ containing tetraglyme (G4) shows a two peaks, which correspond to the formation of a monolayer. The CV in Ag^+ containing propylene carbonate (PC) shows the formation of a monolayer and a bilayer as observed in aqueous electrolyte, but the surface of the electrode was unstable in the potential region for the formation of a bilayer. Therefore, in aprotic electrolytes the frictional behavior including the transition of structures has been studied during the formation of a silver monolayer, composed with 2 peaks.

As observed in aqueous electrolyte, the pre-adsorbed iodine forms a $(\sqrt{3} \times \sqrt{3})R30°$ structure ($\theta_I = 0.33$) on Au(111) positive of the 1st Ag UPD peak in aprotic electrolytes. When the potential passes the 1st Ag UPD peak, it seems that silver already forms a monolayer underneath the tip but, the observed structure of iodine shows a $p(3 \times 3)$ structure slightly negative of the 1st Ag UPD peak. As the potentials gets close to the 2nd Ag UPD peak, the observed structure of the iodine is changed to a $(\sqrt{3} \times \sqrt{3})R30°$ structure. Interestingly, similar behavior is observed in aqueous electrolyte. Thus, the iodine forms a $p(3 \times 3)$ structure negative of the 1st Ag UPD peak where the Ag coverage is 0.44 and this structure remains even though the potential is swept to negative of the 2nd Ag UPD where silver forms a monolayer. However, when a bilayer is formed, the iodine quickly changes to a $(\sqrt{3} \times \sqrt{3})R30°$ structure. Therefore, the conclusion may be drawn that a incomplete coverage of Ag leads the iodine to form a $p(3 \times 3)$ structure.

In chapter 6, it has been shown that the G4 molecules are layered on the iodine adlayer. The concentration of water as well as supporting ions in the electrolyte have a minor effect on the layered structure of G4 on the iodine adlayer. Therefore, it is not surprising that the G4 molecules are layered on the iodine adlayer in Ag^{+} containing G4-electrolyte. In aqueous electrolyte, FS curves shows a dependence on potential, which suggests a possible adsorption of silver ions on the iodine adlayer prior to the deposition of silver. However, in G4-electrolytes, FS curves are independent of potential. Moreover, there is no influence of water on the layering of G4 molecules. In addition, FS curves in pure PC and PC-electrolyte suggest that PC molecules are also ordered on the iodine adlayer.

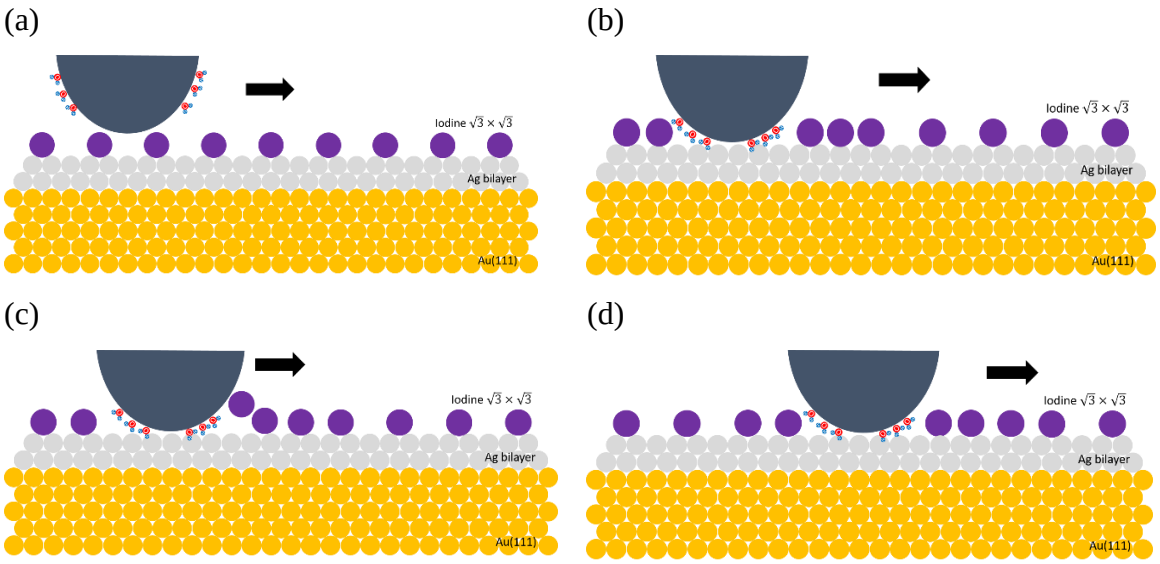

Figure 8.1 The movement of tip on I-Ag bilayer/Au(111) at (a) low normal load and (b) relatively high normal load where the tip penetrate the iodine adlayer. (c) and (d) show the sliding tip after the penetration.

In aprotic electrolytes, interestingly the frictional behavior shows the dependence of solvents. In G4-electrolyte, as observed in aqueous electrolyte, friction forces increase steeply as the tip penetrates the iodine adsorbed on the Ag adlayer. Furthermore, as the concentration of water increases from 50 ppm to 150 ppm, the friction in the region where the tip penetrates the iodine adlayer more dramatically increases. However, when the concentration of water increases further to 550 ppm, the COF seems similar as it is in 150 ppm. Therefore, together with the results in aqueous electrolyte, it is hypothesized that the water adsorbed on the tip dominantly influences on friction during the penetration as shown in Figure 8.1 and the saturation of the tip with water is closely related to the concentration of water in the electrolyte.

In addition, it has been confirmed that there is no extra energy dissipation when the tip pushes away the iodine adsorbed on Au(111) in aqueous (chapter 4) and G4-electrolyte (chapter 6). In PC-electrolyte, even though atomic corrugations show clear penetration into the iodine adlayer as the normal load increases, the influence of the penetration on friction is insignificant. Especially, the steep increase observed in G4- and aqueous electrolytes due to the penetration into the iodine adsorbed on Ag adlayer is not observed in PC-electrolyte. This implies that there is an additional interaction with PC molecules canceling out the effect of the penetration, which might correlate with the properties of PC (e.g. asymmetric structure, polar).

The influence of the lattice mismatch on friction

In chapter 5, frictional behaviors including the transition of structures during Cu UPD on Au(111) have been investigated in the presence of sulfate and pre-adsorbed iodine, respectively. Although detailed process of Cu UPD such as the coverage of copper with potential is different due to co-adsorbed anions, friction forces as function of potential, especially on a Cu monolayer (ML), somehow resemble each other. However, it is interesting that the tendency of friction forces depending on the Cu coverage is quite different compared to that observed during Ag UPD (chapter 3 and 4).

In sulfuric acid, friction forces as function of potential show that friction increases when the potential passes the 1st Cu UPD peak but it decreases again after the sulfate is ordered as a $(\sqrt{3} \times \sqrt{3})R30°$ structure on the Cu adlayer ($\theta_{Cu} = 0.67$). At high normal load, it is clear that friction forces are higher on 1 ML than 2/3 ML. When a potential is swept in the anodic direction, friction forces at a Cu ML are still larger than that at Cu 2/3 ML. In contrast, in Ag^+ containing sulfuric acid, friction forces increase as the coverage of silver increases to a critical value but it decreases again as the coverage of silver gets close to 1, meaning that friction forces is lower at a complete monolayer than sub-monolayer (see chapter 3). Therefore, it is reasonable to assume that there is an additional effect on friction on Cu adlayers, more dominant than the effect of the Cu coverage.

On I-modified Au(111), the frictional dependence on the Cu coverage is quite similar to that in sulfuric acid, which also contrasts with the results during Ag UPD. This confirms that a dominant effect has no relation with the co-adsorbed anions but correlates with the stretched copper adlayer due to the large mismatch with gold.

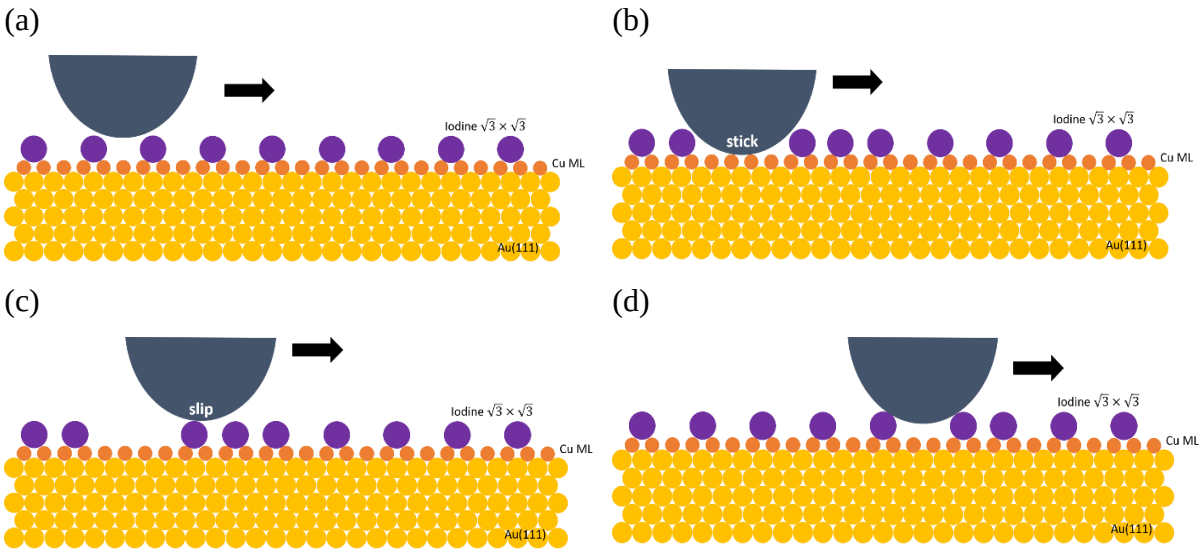

Figure 8.2 The first model for the movement of tip on I-Cu monolayer/Au(111) at (a) low normal load and (b) relatively high normal load to push away adsorbed iodine (stick). (c) indicates slip and where the tip slides on iodine adsorbed on Cu ML. (d) shows the initiation of stick after a slip.

Thus, as the coverage of copper is getting close to 1, the effect of the mismatch becomes apparent, which requires extra energy dissipation for the tip to slide on the surface of copper. Furthermore, when the normal load increases, the interaction between the tip and the Cu adlayer might increase because the tip can slightly push away or penetrate the co-adsorbed anions (Figure 8.2b and Figure 8.3b), which eventually results in the multiple stick-slips. There are two possible models for the slip event and Figure 8.2 and 8.3 show examples with the iodine adlayer. As shown in Figure 8.2c, if the adsorbates on Cu adlayer cannot be displaced during the slip event, the tip might slide on adsorbates during the slip event. However, if the cumulated energy during the stick event is strong enough to displace the adsorbed iodine, the tip might quickly displace adsorbates as shown in Figure 8.3c.

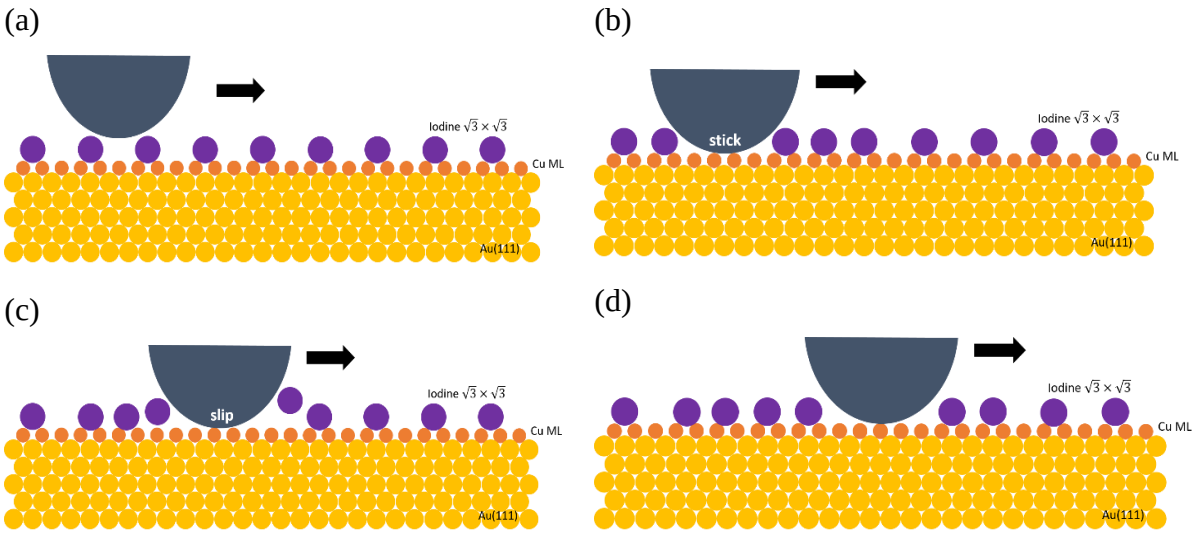

Figure 8.3 The second model for the movement of tip on I-Cu monolayer/Au(111) at (a) low normal load and (b) relatively high normal load to push away adsorbed iodine (stick). (c) indicates slip and the tip displaces iodine adsorbed on Cu ML. (d) shows the stick after the slip.

Acknowledgement

First of all, I owe a deep sense of gratitude to my research supervisor Prof. Dr. Helmut Baltruschat. I am thankful of his constant guidance and encouragement during the entire period of my research. I've learned the attitude as researcher and teacher.

I would like to thank Prof. Dr. Florian Hausen. I value his helpful suggestions and feedbacks on the friction study. I could take much more time to adjust our equipment without his help.

I´m really grateful to the members of the doctoral committee, Prof. Dr. Thomas Bredow, Prof. Dr. Sigurd Höger, and Prof. Dr. Thorsten Geisler-Wierwille.

My deepest gratitude to my research group, electrochemistry in the University of Bonn. I have learned a lot when I was working with them, Philip, Pawel, Da, Martina, Elena, Ahmed, Elke, and Dr. Siegfried Ernst.

Special thanks to Carole for her support like my mom. Her advices were always very punctual, efficient, and warm. Therefore, I could refresh my noisy mind and refocus on my research.

I would like to thank to my best friend, Aram Yeo. Because of you, I could release my anger, sadness, etc. and restart to go on. I will not forget your support and hope that we meet soon. I'm really grateful to Geunwoo Lee, who is a teacher of my life and friend. Your advice makes me think toward the future and helps me to be a better person. Furthermore, I'm thankful to Karin Kiewisch, who empathize with me and cheered me up as my sister.

My huge gratitude to my family; my father in law Christian Schäfer, my mother in law Saskia Schäfer, my sisters in law Lea and Anna Schäfer, and my grandparents in law Eika and Ernst Hay for their support, encouragement, and love.

Special thanks to my lovely husband, Nicklas Schäfer, who always shows me a future. Because of your endless belief and support, I could put the last dot in my thesis.

Publications

Parts of this thesis have already been published in international journal [2] and as preprint [1].

[1] I. Park, F. Hausen, and H. Baltruschat, *ChemElectroChem*, **2022**, 9, e202101660
Friction on I-modified Au(111) in a Tetraglyme Electrolyte
DOI: https://doi.org/10.1002/celc.202101660

[2] I. Park and H. Baltruschat, *ChemPhysChem*, **2021**, 22, 1
In situ friction study of Ag Underpotential deposition (UPD) on Au(111) in aqueous electrolyte
DOI: https://doi.org/10.1002/cphc.202100130

[3] A. Köllisch-Mirbach, I. Park, M. Hegemann, E. Thome, and H. Baltruschat, *ChemSusChem*, **2021**, 14, 2564
Electrochemical reduction of O_2 in Ca^{2+}-Containing DMSO: Role of Roughness and Single Crystal Structure
DOI: https://doi.org/10.1002/cssc.202100364

[4] A. Köllisch-Mirbach, P. Bawol, I. Park, and H. Baltruschat, *ChemElectroChem*, **2022**, 9, e202200159
Towards a Generalized ORR Mechanism in M^{2+}-Containing DMSO: Oxgen Reduction and Evolution in Ca^{2+}-Containing DMSO on Atomically Smooth and Rough Pt
DOI: https://doi.org/10.1002/celc.202200159

Conference contributions

- **Talk:** I. Park and H. Baltruschat; Atomic-scale friction study: *Underpotential deposition (UPD) of silver on I-modified Au(111) in aqueous and aprotic electrolytes*, Gordon Research Conference Tribology (GRS), 06/25/22~06/26/22, Lewiston, USA.
- **Poster:** I. Park and H. Baltruschat; Atomic-scale friction study: *Underpotential deposition (UPD) of silver on I-modified Au(111) in aqueous and aprotic electrolytes*, Gordon Research Conference Tribology, 06/26/22~07/01.22, Lewiston, USA.

- **Poster:** I. Park and H. Baltruschat; Atomic-scale friction study: *Underpotential deposition (UPD) of silver on I-modified Au(111) in aprotic electrolyte*, Friction 2021, 11/18/21~11/19/21, virtual meeting.

- **Talk:** I. Park and H. Baltruschat; Atomic-scale friction study: *Underpotential deposition (UPD) of silver on I-modified Au(111) in aprotic electrolyte*, 116th AGEF symposium: Triboelectrochemistry, 09/22/21~ 09/24/21, Bonn, Germany.

- **Poster:** I. Park and H. Baltruschat; *Friction at electrode surface: Effect of adsorbates and potential*, 71th Annual Meeting of the International Society of Electrochemistry, 08/31/20 ~ 09/01/20, virtual meeting.

- **Poster:** I. Park and H. Baltruschat; *Friction at electrode surface in aprotic electrolytes: Effect of adsorbates and potential*, International Nanotribology Forum, 01/13/2020 ~ 01/17/2020, ChiangRai, Thailand.

- **Poster:** I. Park, Philip Reinsberg, and H. Baltruschat; *Diffusion coefficient of superoxide in aprotic electrolytes containing different cations*, 60th Annual Meeting of the International Society of Electrochemistry, 09/02/18 ~ 09/07/18, Bologna, Italy.